# THE EVOLUTION OF THE CHEMICAL ABUNDANCE GRADIENTS IN THE MERGING MAGELLANIC CLOUD DWARF GALAXIES

by

Joshua Tyler Povick

A dissertation submitted in partial fulfillment
of the requirements for the degree

of

Doctor of Philosophy

in

Physics

MONTANA STATE UNIVERSITY
Bozeman, Montana

June 2023

©COPYRIGHT

by

Joshua Tyler Povick

2023

All Rights Reserved

# DEDICATION

I would like to dedicate this work to my father, Peter Michael Povick (1962 - 2000).

# ACKNOWLEDGEMENTS

I would like to thank my advisor David Nidever for his support and guidance throughout the time that I have been under his purview. Without his encouragement I would have not been able to complete my Doctor of Philosophy degree at Montana State University. I also want to thank the rest of my committee members, Dr. Anne Lohfink, Dr. Charles Kankelborg, Dr. Paul Rugheimer, and Dr. Rachel Filwett. In addition I would like to thank Margaret Jarrett, who was always there for me and other graduate students throughout her years of service as the Graduate Student Coordinator in the Physics Department. Finally, I would like to thank my friends and family in all that they have done for me.

## Funding Acknowledgment

I would like to acknowledge support for this research from the National Science Foundation (AST-1908331) and the Montana Space Grant Consortium Graduate Fellowship.

TABLE OF CONTENTS

1. INTRODUCTION ..... 1

The Magellanic Clouds ..... 1
Chemical Abundances ..... 2
Mass Fractions ..... 2
Abundance Ratios ..... 3
Abundance Measurements ..... 4
The Chemical Evolution of Galaxies ..... 5
Galactic Chemical Evolution ..... 7
Abundance Gradients ..... 10
Interacting Galaxies ..... 13

2. REVEALING THE CHEMICAL STRUCTURE OF THE MAGELLANIC CLOUDS WITH APOGEE. I. CALCULATING INDIVIDUAL STELLAR AGES OF RGB STARS IN THE LARGE MAGELLANIC CLOUD ..... 15

Contribution of Authors and Co-Authors ..... 15
Manuscript Information ..... 17
Abstract ..... 18
Introduction ..... 18
Data ..... 24
APOGEE ..... 24
Gaia EDR3 ..... 26
APOKASC ..... 31
PARSEC Isochrones ..... 31
LMC Distances ..... 32
Extinction Laws ..... 35
Cardelli Extinction Law ..... 35
Fitzpatrick Extinction Law ..... 36
Salaris Correction ..... 36
Calibrations ..... 38
Effective Temperature ..... 38
APOKASC Ages ..... 42
Extinction, Age, & Mass Calculation ..... 42
Extinction Calculation ..... 42
Age Calculation ..... 44
Interpolated Isochrone Parameters ..... 45
Mass Calculation ..... 47
Evolutionary Phase Weighting ..... 48
APOKASC Validation ..... 49

TABLE OF CONTENTS – CONTINUED

APOKASC Extinctions ..... 49
APOKASC Ages ..... 50
APOKASC Masses ..... 52
Bias Correction ..... 52
Results ..... 58
The LMC Extinction Map ..... 58
The LMC Age Map, Age-Radius Relation, & Age Distribution ..... 58
The LMC Age-Metallicity Relation ..... 63
Asymmetric Drift ..... 63
Discussion ..... 65
Summary ..... 70
Acknowledgements ..... 71
Data Availability ..... 72
*Gaia* DR3 selection ..... 72

3. REVEALING THE CHEMICAL STRUCTURE OF THE MAGELLANIC CLOUDS WITH APOGEE. II. ABUNDANCE GRADIENTS OF THE LARGE MAGELLANIC CLOUD ..... 73

Contribution of Authors and Co-Authors ..... 73
Manuscript Information ..... 75
Abstract ..... 76
Introduction ..... 76
APOGEE Data ..... 78
BACCHUS Supplemental Data ..... 80
Abundance Gradient Calculation ..... 81
LMC Geometry ..... 81
MCMC ..... 83
Stellar Age Binning ..... 84
Age-[X/Fe] Trends ..... 85
Results ..... 86
The LMC Radial Abundance Gradients ..... 87
Carbon & Nitrogen ..... 87
$\alpha$-Elements ..... 87
Odd-Z Elements ..... 89
Iron Peak Elements ..... 90
Neutron Capture Elements ..... 91
The Evolution of the LMC Abundance Gradients ..... 91
Carbon & Nitrogen ..... 92
$\alpha$-Elements ..... 97

TABLE OF CONTENTS – CONTINUED

Odd-Z Elements ..... 99
Iron Peak Elements ..... 100
Neutron Capture Elements ..... 101
Age-[X/Fe] Trends ..... 102
Carbon & Nitrogen ..... 102
$\alpha$-Elements ..... 103
Odd-Z Elements ..... 103
Iron Peak Elements ..... 105
Neutron Capture Elements ..... 106
Discussion ..... 106
LMC Metallicity Gradient ..... 107
The Evolution of Abundance Gradients of the LMC ..... 108
Summary ..... 113
Acknowledgements ..... 114
Data Availability ..... 115
$\nabla_R$[X/H] & $\nabla_R$[X/Mg] Tables ..... 120
Radius-[X/Fe]-Age Trends ..... 120
age-[X/Fe] Trends ..... 120

4. REVEALING THE CHEMICAL STRUCTURE OF THE MAGELLANIC CLOUDS WITH APOGEE. III. ABUNDANCE GRADIENTS OF THE SMALL MAGELLANIC CLOUD ..... 129

Contribution of Authors and Co-Authors ..... 129
Manuscript Information ..... 130
Abstract ..... 131
Introduction ..... 131
Data ..... 136
APOGEE ..... 136
Gaia Data Release 3 ..... 137
Calculating Distances and Ages ..... 138
SMC Distances ..... 138
SMC Ages ..... 142
Abundance Gradient Calculation ..... 142
SMC Radius ..... 142
Determining Abundance Gradients with MCMC ..... 143
Stellar Age Binning ..... 144
Age-[X/Fe] Trends ..... 145
Results ..... 146
The SMC Radial Abundance Gradients ..... 146

TABLE OF CONTENTS – CONTINUED


Carbon & Nitrogen ....146
$\alpha$-Elements ....146
Odd-Z Elements ....147
Iron Peak Elements ....149
Neutron Capture Element ....149
The Evolution of the SMC Abundance Gradients ....150
Carbon & Nitrogen ....155
$\alpha$-Elements ....155
Odd-Z Elements ....157
Iron Peak Elements ....158
Neutron Capture Element ....159
Age-[X/Fe] Trends ....159
Carbon & Nitrogen ....159
$\alpha$-Elements ....160
Odd-Z Elements ....162
Iron Peak Elements ....163
Neutron Capture ....164
Discussion ....164
SMC Metallicity Gradient ....164
Evolution of Abundance Gradients of the SMC ....168
Comparing the SMC to the LMC and MW ....169
Summary ....171
Gaia ADQL Query ....175
$\nabla_R$[X/H] & $\nabla_R$[X/Mg] Tables ....176
Radius-Abundance-Age Trends ....181
Age-[X/Fe] Trends ....181
Comparing to the LMC and MW Extra Plots ....181

5. CONCLUSION ....190

REFERENCES CITED ....194

# LIST OF TABLES

Table Page

2.1 A table of positional data for each of the APOGEE LMC fields including the number of RGB stars observed. R and PA are the projected radius and position angle respectively. $N_{Brt}$ is the number of identified bright RGB stars while $N_{Fnt}$ is the number of faint sources (see Section 2). ..... 28

3.1 Values of the different age bins used throughout this work. ..... 85

3.2 A table of overall gradients for the abundant metals carbon and nitrogen using Fe, H, and Mg as fiducials. The [C/N] gradient is also included at the bottom. ..... 88

3.3 A table of overall gradients for the $\alpha$-elements. The $[\alpha_h/\alpha_{ex}]$ gradient is included at the bottom. ..... 89

3.4 Gradients for the odd-Z elements. ..... 90

3.5 Gradients for the iron peak elements. ..... 91

3.6 Gradients for the neutron capture elements. ..... 92

3.7 A table of the gradients for each of the age bins. Horizontal lines have been added marking the division of the previously defined groups of elements. In general descending down the table corresponds to an increase in atomic number. Each age bin has its own separate column. This table also includes the evolution of the [Fe/H], [C/N] and $[\alpha_h/\alpha_{ex}]$. ..... 95

3.8 Table of literature values for the LMC [Fe/H] gradient. In the last column, RR Eq 1 and RR Eq 2 refer to two different period-[Fe/H] which are Equations 1 and 2 in Feast et al. (2010) respectively. Also for Choudhury et al. (2021) VMC corresponds to the gradient using the VMC survey data and Calibration is the gradient derived for the dataset used to calibrate the [Fe/H]-RGB slope relation. Grady et al. (2021) derives the gradient from [Fe/H] isochrones and calibrates them with APOGEE. ..... 109

LIST OF TABLES – CONTINUED

Table Page

3.9 A table of the gradients for each of the age bins using H as the fiducial element. Horizontal lines have been added marking the division of the previously defined groups of elements. In general descending down the table corresponds to an increase in atomic number. Each age bin has its own separate column. ....116

3.10 A table of the gradients for each of the age bins using H as the fiducial element. Horizontal lines have been added marking the division of the previously defined groups of elements. In general descending down the table corresponds to an increase in atomic number. Each age bin has its own separate column. ....118

4.1 Table showing the different age bins used throughout this work. These are the same age bins from Povick et al. 2023b. ....145

4.2 Radial gradients for the abundant metals carbon and nitrogen. ....147

4.3 Table of radial abundance gradients for the $\alpha$-elements. ....148

4.4 Table of radial abundance gradients for the odd-Z elements. ....149

4.5 Table of radial abundance gradients for the iron peak elements. ....150

4.6 Table of radial abundance gradients for cerium. ....150

4.7 Table of the [X/Fe] gradients for each of the age bins. Horizontal lines have been added marking the division of the previously defined groups of elements. In general descending down the table corresponds to an increase in atomic number. Each age bin has its own separate column. This table also includes the evolution of the [Fe/H], [C/N] and $[\alpha_{\rm h}/\alpha_{\rm ex}]$....153

4.8 Table of literature values for the [Fe/H]-gradient of the SMC. All but Li et al. (2023) and Choudhury et al. (2020) use CaT equivalent widths to the [Fe/H]. ....166

LIST OF TABLES – CONTINUED

Table Page

4.9 Table of the [X/H] gradients for each of the age bins. Horizontal lines have been added marking the division of the previously defined groups of elements. In general descending down the table corresponds to an increase in atomic number. Each age bin has its own separate column. .....177

4.10 Table of the [X/H] gradients for each of the age bins. Horizontal lines have been added marking the division of the previously defined groups of elements. In general descending down the table corresponds to an increase in atomic number. Each age bin has its own separate column. .....179

# LIST OF FIGURES

Figure Page

1.1 A figure from Nidever et al. (2020) that shows how stellar spectra are sensitive to different parameters. (Top) The observed stellar spectra are shown in black and best fit stellar spectra are shown in red around different elemental absorption lines for five different stars with various metallicities, $\alpha$ abundances, $T_{eff}$, and $\log g$ values. The blue vertical lines are to help guide the eye to the position of the absorption lines. This shows how spectra are generally sensitive to different physical parameters of a star. (Bottom) An observed APOGEE spectrum for a single star is shown in black with spectra fit using different $\alpha$ abundance values in color. This plot shows how changing the $\alpha$ abundance affects the goodness of fit to the observed spectrum. The measured $\alpha$ abundance will be the abundance value of the best fit spectrum. ..... 6

1.2 Adapted from McWilliam (1997). A schematic of how the GCE can be sensitive to the SFH in the [$\alpha$/Fe]–[Fe/H] plane. The GCE trend is shown in red with arrows on it denoting the direction of time. An increase in the IMF will raise the trend to higher [$\alpha$/Fe] at the metal-poor end while an increase in the SFR will pull the "knee" to higher [Fe/H]. The "knee" is the point at which type Ia SNe turn on in the system. A late burst will raise up the metal-rich end due to an increase in $\alpha$-element production. Inflows of material will drive the [Fe/H] down causing the trend to become more metal-poor. Outflows do the exact opposite of inflows in this diagram. ..... 11

2.1 Map of the APOGEE-2 Magellanic Cloud fields filled circles) and the background showing the density of MC RGB stars selected with Gaia. The LMC fields analyzed here are shown as purple filled circles. For some basic statistics on the LMC fields see Table 2. ..... 23

LIST OF FIGURES – CONTINUED

Figure Page

2.2 (*Left*) A 2MASS color magnitude diagram of the selected APOGEE LMC RGB stars colored by [Fe/H]. The tip of the RGB is assumed to be at $H$ ∼12.35 for the LMC (Nidever et al., 2020). (*Right*) A Kiel diagram for the APOGEE LMC RGB stars colored by [Fe/H]. ..... 27

2.3 A reproduction of the magnitude error curve for Gaia EDR3 calculated using the Gaia photometry and equation 2.1. The blue, green, and red curves represent the BP, G, and RP bands respectively. The curves here match qualitatively to the curves in Riello et al. (2021)..... 30

2.4 An HR diagram for the selected APOKASC RGB stars colored by [Fe/H]. ..... 32

2.5 The resulting distance map for the LMC using Equation 2.3. The contours show lines of constant "elliptical" radius starting at 1 kpc for the center contour out to 8 kpc calculated using equation 6 from Choi et al. (2018b) ..... 34

2.6 The relative extinction curve of $A_\lambda/E(B-V)$ from both CM89 and F99. The top axis shows the different photometric filters used in this work..... 37

2.7 (*Left*) The residuals of the photometric and uncalibrated ASPCAP $T_{eff}$ values with the spline used to temperature correct the uncalibrated $T_{eff}$. (*Right*) The residuals after the $T_{eff}$ correction has been applied. There is a clear trend in [M/H] and so a second spline as a function of [M/H] has been applied (see the text and Figure 2.8). ..... 39

2.8 (*Left*) A plot of the residuals between the photometric and $T_{eff}$–corrected spectroscopic $T_{eff}$ values ($T_{eff}$ spline applied) with the spline used to [M/H] correct the $T_{eff}$ values. (*Right*) The residuals after the [M/H] correction has been applied. The median residual after the [M/H] has been applied is −1.72 K with a scatter of 23.75 K. ..... 39

2.9 An example of how the intrinsic colors are determined from the isochrone photometry–$T_{eff}$ relations. ..... 44

LIST OF FIGURES – CONTINUED

Figure Page

2.10 (*Left*) The $G$–$T_{eff}$ relationship for [Fe/H] = −0.14 for the RGB isochrone points. There is a lot of degeneracy in the magnitude–$T_{eff}$ relation, but clearly broken with age. This is the basis for using the interpolations in Section 2 to get the ages. (*Right*) The same as the left panel, but for the AGB isochrone points. The AGB points mostly cover the gap in the RGB isochrone points between the young branch the rest of the points. ..... 45

2.11 (Left) $A_G$ extinction map converting the Schlegel et al. (1998) reddening values using Schlafly et al. (2010) and Fitzpatrick (1999). (Center) $A_G$ map using the values calculating using the method in this work. (Right) The residuals between the Schlegel and calculated $A_G$ values with a median residual of 0.043 mag. ..... 50

2.12 (Left) Age map of the Kepler field using APOKASC 3 masses and PARSEC isochrones. (Center) Age map of the Kepler field calculated using our method described in Section 2. (Right) The residuals between the methods with a median residual of 0.2 Gyr. ..... 51

2.13 An age-to-age plot comparing the ages derived using the APOKASC masses and PARSEC models and ages derived using the photometric matching described in Section 2 for the APOKASC validation set colored by the number of stars in each bin. To help guide the eye the 1-to-1 line has been overplotted in black. It is clear especially for younger stars that the photometric matching ages tend to be slightly younger, though overall there is quite good agreement. ..... 53

2.14 Comparing the APOKASC 3 masses to the masses calculated using Section 2. ..... 55

LIST OF FIGURES – CONTINUED

Figure Page

2.15 (*Left*) Number of stars in the target selection box for a stellar population of $10^8$ $M_\odot$ , as a function of age and metallicity. There are regions of parameter space (e.g., old, metal-poor), where no stars are expected to be observed. (*Middle*). Number of stars in the target selection box for a stellar population of $10^8$ $M_\odot$ , averaged over metallicity and showing the age dependence. There is a sharp peak around 0.15 Gyr, and a "valley" at 0.3–1.5 Gyr. (*Right*) The same, but averaged over age and showing the metallicity dependence..... 56

2.16 (*Left*) The $G$ band extinction map for the LMC with the Gaia source number density in the background. In the map there is clearly a band of low extinction between ∼2 to ∼6 kpc in the north. (Center) The dispersion in extinction for each of the bins using MAD also with the Gaia background. (*Right*) The extinction errors as a function of the extinction colored by the $T_{eff}$ of each star. There is a definite correlation between the $T_{eff}$ of a star and calculate extinction error probably due to the steepness in the color–teff relations. ..... 59

2.17 (*Left*) The age map for the LMC with the Gaia source number density in the background. (*Center*) The dispersion in age for each of the bins using MAD also with the Gaia background. (*Right*) The age errors as a function of the age colored by the [Fe/H] of each star. Most derived LMC have uncertainties that are <10% suggesting great accuracy. There is a band of stars with uncertainties that appear to approach zero, but based on the visible envelop, the best course of action is to inflate any errors for these stars to at least 2.5%..... 60

LIST OF FIGURES – CONTINUED

Figure Page

2.18 (*Left*) The age-radius relation for the LMC represented with the black solid line (see Equation 2.20). Individual LMC stars are shown in the background as light grey dots. The median ages for each of the LMC fields are overplotted as dots and xs colored in function of position angles. Northern fields are represented by dots while southern fields are represented by xs. It is clear that for inner radii that the northern fields are slightly younger than the southern fields at corresponding radii. (*Right*) The residuals of the quartic function fit. The MAD of the residuals is -0.19 for the clusters compared to 2.17 for the individual stars. ..... 61

2.19 (*Top*) A histogram of the ages calculated for the individual stars in the sample. The peak at 0 Gyr is made mostly of blue loop stars with some potentially bad results where stars could be assigned younger ages than they should be. The peaks less than 10 Gyr may suggest different star forming events while the peak at ∼17 corresponds to the age of the oldest isochrone. (*Bottom*) A histogram showing the stellar population mass corresponding to the calculated ages corrected for the bias according to Section 2. The first two peaks in the plateau between ∼2.5–5.0 Gyr do not appear to be temporally separated, but the third peak is. The supposed separation between the first two peaks may be an unphysical artefact. ..... 62

2.20 (*Top*) The AMR of the LMC calculated with the individual stars shown as the black dashed line. The APOGEE stars themselves are grey. The grey region shows the $1\sigma$ limit around the AMR. The blue points with error bars represent the 85 LMC clusters from HZ09. The grey points at the bottom show the characteristic error in the grey points. Clearly the largest disagreement with clusters happens for the oldest ages where measurements get donimated by noise. (*Bottom*) The same as the top, but with a log scale which highlights younger ages. ..... 64

LIST OF FIGURES – CONTINUED

Figure Page

2.21 (*Left*) The different components of the velocity as functions of age. The $v_r$ and $v_z$ are shown in red and blue respectively. These two velocity components use the black axis on the left. The 0.0 km/s for this is included as a dashed line. Both $v_r$ and $v_\phi$ components stay close to zero. The $v_r$ curve shows that there is an increase starting around ages of 5 Gyr, though for even the oldest ages this component does not get above 10 km/s. The $v_\phi$ velocity is shown as a green curve and uses the green axis on the right. For ages $\lesssim$2.5 Gyr there is a large increase in $v_\phi$ and then from 2.5–5.0 Gyr there is a decrease down to about $\sim$67 km/s and then an increase for the oldest stars. (*Right*) The different components of the velocity dispersion as functions of age. ..... 66

2.22 (*Left*) The $G$ band extinction map for the LMC. This is the same map as seen in Figure 2.16. (*Center*) The extinction map of LMC using $A_G$ derived from Choi et al. (2018a) and the CCM89 extinction law. (*Right*) The residuals between the converted Choi et al. (2018a) $A_G$ and the calculated $A_G$ from this work with a median residual of 0.093 mag suggesting a slight offset. ..... 67

3.1 A Kiel-diagram for the whole sample of the LMC RGB stars with associated uncertainties. The color of each of the stars in the plot represent their respective metallicities. ..... 80

3.2 The resulting distance map for the LMC using Equation 3.1 with the color indicating distance in kpc. The contours show lines of constant "elliptical" radius starting at 1 kpc for the center contour out to 8 kpc calculated using Equation 6 from Choi et al. (2018b). For reference the center of the map, (X, Y) = (0, 0), is at ($\alpha$, $\delta$) = (05:27:36,−69:52:00)..... 82

LIST OF FIGURES – CONTINUED

Figure Page

3.3 A plot showing the radial bins used to calculate the age-[X/Fe] relations. The dashed black line shows the boundary between the North and South LMC using the position angle of a star. This line amounts to a delineation in declination at $\sim -70°$. The solid black lines show the boundary of the different annular bins. Each of the annuli contain the same number of stars. ..... 86

3.4 A figure showing each of the calculated [X/Fe] gradients are shown for each element. Also included here are [Fe/H], [C/N], [$\alpha_{\rm h}$/Fe], [$\alpha_{\rm ex}$/Fe] and [$\alpha_{\rm h}/\alpha_{\rm ex}$]. The abundances have been broken up into different groups of like elements with atomic number generally increasing to the right. The color of each dot corresponds to the different age bins for which a gradient was calculated. Black lines have also been added to make the trends in the gradients more clear. The value of each gradient here can be seen in Table 3. ..... 93

3.5 Same as Figure 3.4, but for the [X/H] gradients. The [Fe/H] has also been included here. The value of each gradient is given in Table 3. ..... 93

3.6 Same as Figure 3.4, but for the [X/Mg] gradients. The [Mg/H] gradient has also been included here. The value of each gradient is given in Table 3. ..... 94

LIST OF FIGURES – CONTINUED

Figure Page

3.7 The radial abundance trends for the measured C and N abundances in the LMC. The particular abundance can be seen in the left more panel of each row. For each row, age increases from left to right with colored lines representing the linear model fits to the binned values. A correspondingly colored dashed line represents the binned median abundance value with the band showing the dispersion. A black line in a panel shows the overall radial abundance trend without age binning and functions as a fiducial here. These plots show that different C and N abundances increase over time in the galaxy, with the trends below the fiducial for older age bins and above for younger age bins. Also the [C/N] gradient clearly inverts for the youngest age bin. The range for each panel for a row is based on the fiducial line and does result in some trends being cut off in an effort to capture the overall differences among panels. ..... 98

3.8 The age-[X/Fe] trends for the LMC for C and N. The top row in each panel shows the age-[X/Fe] trends for the northern part of the LMC and the bottom row shows the trends in the south. The LMC is split into three radial bins that contain an equal number of stars. For each subpanel the age-[X/Fe] trend is included with a band of $1\sigma$ in addition the black fiducial line shows the age-[X/Fe] trend without any binning. Clearly the [N/Fe] and [(C+N)/Fe] have a sharp increase for recent times. ..... 104

LIST OF FIGURES – CONTINUED

Figure Page

3.9 A comparison of the overall metallicity gradient found in this work for various literature values. The vertical black line represents the overall metallicity gradient and the black band represents the calculated error in the gradient. The gradient for each of the age bins is similarly shown. Choudhury et al. (2021); Cioni (2009); Feast et al. (2010) show agreement with the overall gradient, while other sources agree with the gradients found with different age bins in this work. In many cases, many of these sources calculate the gradient multiple ways. For more information see Section 3 and the references therein. ....110

3.10 The same as for Figure 3.7, but with the individual $\alpha$-element abundances....121

3.11 The radial abundance trends for the composite $\alpha$-element abundances....122

3.12 The radial abundance trends for the odd-Z abundances. ....122

3.13 The radial abundance trends for the iron peak abundances. ....123

3.14 The radial abundance trends for the neutron capture abundances....123

3.15 The age-[X/Fe] trends for the individual $\alpha$-elements. ....124

3.16 The age-[X/Fe] trends for the composite $\alpha$-elements. ....125

3.17 The age-[X/Fe] trends for the odd-Z elements. ....126

3.18 The age-[X/Fe] trends for the ironpeak elements. ....127

3.19 The age-[X/Fe] trends for the neutron capture elements....128

4.1 Stellar density map of the Gaia DR3 RGB with SMC-like proper motions in and SMC-centric coordinate system. The 14 APOGEE-2S SMC fields are highlighted in gray. ....135

4.2 A schematic showing the relationship between true velocity ($v$), radial velocity ($v_r$), and tangential velocity ($v_t$). The time derivative of the angle $\theta$ is the proper motion. An observer would be at the bottom point in this diagram. ....139

LIST OF FIGURES – CONTINUED

Figure Page

4.3 (*Left*) A map of the APOGEE SMC fields showing the mean distance in each spatial bin determined using our "proper motion distance" method. (*Right*) A dispersion map for the calculated distances. The larger line-of-sight depth is clearly visible on the eastern side of the galaxy.....141

4.4 The distribution of calculated ages for the SMC stars. A large portion of the stars formed within the last ∼7.5 Gyr in the SMC with a peak ∼3–4 Gyr ago. This is similar to Figure 19 in Paper I, where most star formation happens .....142

4.5 A figure showing each of the calculated gradients are shown for each element. The difference abundances have been broken up into different groups of like elements. The color of each dot corresponds to the different age bins that contain the same number of stars previously mentioned. The value of each gradient here can be seen in Table 4.....151

4.6 A figure showing each of the calculated gradients are shown for each element. The difference abundances have been broken up into different groups of like elements. The color of each dot corresponds to the different age bins that contain the same number of stars previously mentioned. The value of each gradient here can be seen in Table 4.....151

4.7 A figure showing each of the calculated gradients are shown for each element. The difference abundances have been broken up into different groups of like elements. The color of each dot corresponds to the different age bins that contain the same number of stars previously mentioned. The value of each gradient here can be seen in Table 4.....152

LIST OF FIGURES – CONTINUED

Figure Page

4.8 The radial abundance trends for the carbon and nitrogen abundances. For each row, age increases from left to right. The solid colored line is the fitted linear model, the dashed line follows the median abundance value for a given radius, and the color band shows the dispersion around the median. The black line is the fit to all the data without any age binning and serves as a fiducial. These plots show that the each of the different abundances increase over time, with the fit trend below the fiducial for older age bins and above for younger age bins. The youngest [N/Fe] and [C/N] trends standout showing much larger gradients than the other age bins. Also the [C/N] gradient clearly inverts for the youngest age bin.....156

4.9 The age-[X/Fe] trends for the SMC for carbon and nitrogen. The top row in each panel shows the age-[X/Fe] trends for the northern part of the SMC and the bottom row shows the trends in the south. The SMC is split into two radial bins that contain an equal number of stars. For each sub-panel the age-[X/Fe] trend is included with a band of $1\sigma$ in addition the black fiducial line shows the age-[X/Fe] trend without any binning. Clearly the [N/Fe] and [(C+N)/Fe] have a sharp increase for recent times.....161

4.10 A comparison of the [Fe/H] gradients found in this work to multiple literature values. The vertical lines and bands correspond to the gradients for each of the age bins with the associated errors. The literature values are shown as points. The gradients calculated by De Bortoli et al. (2022) out to 3.4° overlap with the overall gradient as well as values found by Dobbie et al. (2014) and Parisi et al. (2016). Around half of the literature gradients overlap with any of the gradients calculated in this work.....167

LIST OF FIGURES – CONTINUED

Figure Page

4.11 A comparison of the overall radial abundance gradients for the SMC, LMC and the MW. The LMC is shown in blue, the SMC in orange, and the MW in green. (*Top*) [X/H] gradients which show a clear separation between the MW and the dwarf galaxies. The MW has median abundance gradients (dotted horizontal lines) almost 50% larger then ($-1.20$ dex/$R_d$) than the MCs ($-0.80$ dex/$R_d$). (*Bottom*) [X/Fe] gradients where all three galaxies show much more consistent patterns and almost no difference in the median gradients. .....172

4.12 The same as for Figure 4.8, but with the individual $\alpha$-element abundances.....182

4.13 The radial abundance trends for the composite $\alpha$-element abundances.....183

4.14 The radial abundance trends for the odd-Z abundances. .....183

4.15 The radial abundance trends for the iron peak abundances. .....184

4.16 The radial abundance trends for the neutron capture abundances.....184

4.17 The age-[X/Fe] trends for the SMC for the individual $\alpha$-element abundances.....185

4.18 The age-[X/Fe] trends for the SMC for the composite $\alpha$-element abundances.....186

4.19 .....187

4.20 The age-[X/Fe] trends for the SMC for the individual iron peak abundances.....188

4.21 The age-[X/Fe] trend for the SMC for the neutron capture element cerium.....189

4.22 The same as Figure 4.11, but for the [X/Mg] gradients only. The median gradient value all three galaxies is quite similar. .....189

# NOMENCLATURE

| | |
|---|---|
| AGB | Asymptotic giant branch |
| AGN | Active Galactic Nucleus/Nuclei |
| AMR | Age-metallicity relation |
| APO | Apache Point Observatory |
| APOGEE | Apache Point Observatory Galactic Evolution Experiment |
| $B_{MS}$ | Magellanic Stream latitude |
| CMD | Color magnitude diagram |
| Clouds | Magallenic Clouds |
| dec (or $\delta$) | Declination |
| GC | Globular Cluster |
| GCE | Galactic chemical evolution |
| GMC | Giant molecular cloud |
| HR | Hertzsprung-Russell |
| IMF | Initial mass function |
| ISM | Interstellar medium |
| LCO | Las Campanas Observatory |
| LMC | Large Magellanic Cloud |
| $L_{MS}$ | Magellanic Stream longitude |
| MCs | Magellanic Clouds |
| MW | Milky Way |
| NS | Neutron star |
| OC | Open cluster |
| PN/PNe | Planetary nebula(e) |
| ra (or $\alpha$) | Right ascension |
| RGB | Red giant branch |
| SDSS | Sloan Digital Sky Survey |
| SFE | Star formation efficiency |
| SFH | Star formation history |
| SFR | Star formation rate |
| SMASH | Survey of the Magellanic Stellar Periphery |
| SMC | Small Magellanic Cloud |
| SN/SNe | Supernova(e) |
| TRGB | Tip of the red giant branch |
| WD | White dwarf |
| $\mu$ | proper motion |
| $\mu_\alpha$ | Right ascension proper motion |
| $\mu_\delta$ | Declination proper motion |
| $\varpi$ | Parallax |
| $\Sigma_g$ | Gas (surface) density |
| $\Sigma_{SFR}$ | Star formation rate (surface) density |

# ABSTRACT

Dwarf galaxies are some of the most abundant objects in the Universe, but most of them are very distant and very faint. While observing these galaxies does pose some challenges, they are important to study because it is believed that larger galaxies, such as the Milky Way (MW), form from a series of dwarf mergers in a process called hierarchical merging. As if by chance, the Magellanic Clouds (MCs) are both bright enough and close enough to resolve individual stars. These two dwarf satellites of the MW are also in the process of merging together, presenting a great opportunity to examine how the abundance gradients of galaxies are impacted by intergalactic interactions. A great tool to study the MCs is the Apache Point Galactic Evolution Experiment (APOGEE). APOGEE is an H-band near infrared survey commissioned to measure chemical abundances and accurate radial velocities of the MW and its neighborhood. In the MCs, APOGEE was able to observe 6130 red giant branch (RGB) stars in the Large Magellanic Cloud (LMC) and 2062 RGB stars in the Small Magellanic Cloud (SMC). Individual stellar ages are derived using multi-band photometry and spectroscopic parameters to compare to stellar isochrones. Using the abundance measurements of 20+ elements and the derived stellar ages, abundance gradients and their evolutions are extracted from radial abundance trends. The stellar ages in the LMC reveal that recent star formation has been concentrated in the center of that galaxy. The fields that overlay a spiral arm in the north of the LMC reveal median ages of $\gtrsim$2 Gyr. The age-metallicity relation (AMR) remains mostly flat with the exception of an increase in overall metallicity $\sim$2 Gyr ago. Looking at the evolution of many abundance gradients in the LMC there is a U-shaped trend with an extremum around the same time as the increase in metallicity. Additionally, the SMC also shows a U-shaped trend in its abundance gradient evolutions albeit a few billion years earlier than the LMC. These results all correspond to a conjectured close interaction between the LMC and SMC in the recent past.

# 1

# INTRODUCTION

## The Magellanic Clouds

The Magellanic Clouds, also known as the MCs or just the Clouds, have been two ever-present smudges in the southern night sky since before man walked on Earth. Ancient accounts of these two galaxies have been preserved in the oral histories of indigenous peoples of the South American continent that survive to this day including that of the Tupi-Guaraní (Afonso, 2006) and Mapuche (Pozo Menares et al., 2015).

The earliest confirmed written firsthand accounts of the Clouds that still survive to the present day began with the era of European exploration by the Portuguese in the 16th century (Dennefeld, 2020). One of the more detailed early passages come from Andrea Corsali in a letter he wrote in 1516, which was translated into English by Richard Eden in 1555 and published by Arber et al. (1885) is as follows:

> Here we sawe a marueylous order of starres, so that in the parte of heauen contrary to owre northe pole, to know in what place and degree the south pole was, we tooke the day with the soonne, and obserued the nyght with the Astrolabie, and sawe manifestly twoo clowdes of reasonable bygnesse mouynge abowt the place of the pole continually now rysynge and nowe faulynge, so keepynge theyr continuall course in circular mouying, with a starre euer in the myddest which is turned abowt with them abowte xi degrees from the pole.

Here Corsali gives a brief description of the position and the kinematics of the clouds, which he measured with an astrolabe. Many other "contemporary" sources are even more terse and

lack information about the motion of the Clouds (Dennefeld, 2020). But this shows there has been some sort of scientific interest since the 1500s.

In the centuries since, we have learned a lot more about the Clouds. While they may not be the closest, they are definitely the largest satellites of the Milky Way (MW) and so they pose a great opportunity to study dwarf galaxies. The larger of the two galaxies that make up the Clouds is called the Large Magellanic Cloud (LMC) and can be found at a distance of 49.9 kpc (De Grijs et al., 2014; van der Marel & Cioni, 2001) with a total mass of $\sim 1.8 \times 10^{11}$ $M_\odot$ (Erkal et al., 2019; Vasiliev et al., 2021). The stellar mass of this galaxy comes out to $3.2 \times 10^{10}$ $M_\odot$ (van der Marel et al., 2008). The accordingly-named Small Magellanic Cloud is at a distance of 62.44 kpc (Graczyk et al., 2020) with a slightly smaller mass of $\sim 10^9$ $M_\odot$ (Bekki & Stanimirović, 2009), and only $\sim 3$–$3.5 \times 10^8$ $M_\odot$ is made up of stars (Skibba et al., 2012).

In addition to their close distance and size, the Clouds are also very bright. The LMC and the SMC have apparent V band magnitudes of $0.4 \pm 0.1$ and $2.2 \pm 0.2$ respectively (McConnachie, 2012) and can be seen with the naked eye. To put this in perspective apparent magnitude is a logarithmic scale that describes how bright objects appear in the sky. A change of 1 dex (degree exponent) in magnitude is a change in brightness by a factor of 2.512. Rather unintuitively, a larger numeric value for apparent magnitude means an object is dimmer. The human eye can see down to an apparent magnitude of $\sim 7.0$, so quantitatively the Clouds are extremely bright.

## Chemical Abundances

### Mass Fractions

The mass fractions of a star are a convenient shorthand that describe its composition. The mass fractions X, Y, and Z are defined such that:

$$X + Y + Z = 1 \qquad \text{and} \qquad X > Y > Z, \tag{1.1}$$

where $X$, $Y$, $Z$ are the mass fractions of hydrogen, helium, and metals respectively. It is important to point out that in the field of Astronomy, "metal" refers to a chemical species that is not hydrogen or helium. Hydrogen and helium are assigned their own symbol because matter in the universe is almost exclusively made up of these elements. Along with trace amounts of lithium, hydrogen and helium were the first elements produced in the universe (Alpher et al., 1948). It is no coincidence that these are also the elements with the simplest atomic structure. All other elements were created later through stellar nucleosynthesis (Burbidge et al., 1957).

Abundance Ratios

Though mass fraction are sometimes used, most of the time astronomers opt for using abundance ratios (or more colloquially abundance) in their place. The abundance ratio is the logarithm of the ratio of the number of one atomic species to another, which is given as:

$$[A/B] \equiv \log\left(\frac{N_A}{N_B}\right)_\star - \log\left(\frac{N_A}{N_B}\right)_\odot, \tag{1.2}$$

where $N_A$ is the number of atoms of species A and $N_B$ is the number of atoms of species B (often referred to as the fiducial). Here $\star$ denotes the star of interest. From the above definition, [A/B] = 0.0 means that the ratio of the number of atoms of A to B in a particular star is the same as it is in the sun.

Since atoms of a particular species have an established mass, the ratio of the number of atoms of two atomic species is related to ratio of their stellar mass fractions by:

$$\frac{N_A}{N_B} = \frac{X_A}{X_B}, \tag{1.3}$$

where $X_{\rm A}$ ($=M_{\rm A}/M_{\rm tot}$) is the mass fraction of species A and $X_{\rm B}$ ($=M_{\rm B}/M_{\rm tot}$) is the mass fraction of species B. More explicitly, as an example the relationship between the iron abundance ratio and the iron mass fraction is:

$$Z_{\rm Fe,\star} = Z_{\rm Fe,\odot} \times 10^{\rm [Fe/H]} \quad \text{or more appropriately} \quad \left(\frac{Z_{\rm Fe}}{X_H}\right)_\star = \left(\frac{Z_{\rm Fe}}{X_H}\right)_\odot \times 10^{\rm [Fe/H]} \tag{1.4}$$

where $Z_{\rm Fe,\star}$ is the iron mass fraction of the star, $Z_{\rm Fe,\odot}$ is the mass fraction of iron in the sun, $X_H$ is the hydrogen mass fraction of the star or sun depending on the subscript above, and [Fe/H] is the abundance ratio of iron for the star using hydrogen as the fiducial.

Composite abundance ratios can be calculated from single species abundance ratios using:

$$\left[\left(\sum_A A\right)/B\right] = \log\left(\frac{\sum_A 10^{\log \epsilon_{X_A} - 12.0 + [A/B]}}{\sum_A 10^{\log \epsilon_{X_A} - 12.0}}\right) \quad \text{and} \quad \log \epsilon_{X_A} \equiv \log\left(N_{X_A}/N_H\right) + 12.0, \tag{1.5}$$

where $\log \epsilon_{X_A}$ is the logarithmic solar abundance, with $\log \epsilon_{X_H}$ defined to be 12.0, and $[A/B]$ is the individual constituent abundance ratios as defined in equation 1.2.

The abundance ratio that represents the total metal content of star is called metallicity and is normally denoted as [M/H]. Often times iron is used as a proxy for all metals because [M/H] $\approx$ [Fe/H]. Throughout this work I will use [Fe/H] for metallicity to be in line with modern convention unless otherwise specified.

Abundance Measurements

While it is possible to get some abundance information from photometry (mainly metallicity), spectroscopy is primarily used for measuring chemical abundances since it generally produces more accurate results (Favata et al., 1997; Lianou et al., 2011). Spectroscopy measures the flux of a source across a large range of wavelengths creating a spectrum. The largest component of a stellar spectrum is the continuum. Spectral lines

represent deviations from the continuum and can be caused by either emission or absorption at the discrete energies of atomic electron transitions. Emission lines will appear as an excess of flux at certain wavelengths above the continuum while absorption lines will appear as flux that is missing creating dips below the continuum.

Historically it was not immediately obvious that spectral lines of stars corresponded to different transitions. The first spectra of a star (the sun) were taken in the early 1800s by Wollaston (1802) and Fraunhofer (1817). It was not until a few decades after this that Kirchhoff (1860) made the connection which laid the ground work for spectroscopy and eventually abundance analysis in Astronomy.

It has been long established that the shape of a spectrum is sensitive to many different parameters such as effective temperature ($T_{\rm eff}$), the logarithm of the surface gravity ($\log g$), total metallicity ([M/H]), total $\alpha$ abundance ([$\alpha$/M][1]), etc. Of course this also includes different abundances not just [M/H] and [$\alpha$/M]. An example how spectra are sensitive affected by the listed parameters can be seen in the top panel of Figure 1.1. The bottom panel of the same Figure demonstrates how changing the [$\alpha$/M] affects a spectrum. Different abundance values affect the width and depth of a line in a similar fashion.

## The Chemical Evolution of Galaxies

A galaxy is a complex object made up of many different components and not just stagnant conglomerations of stars, even though the timescales of their evolutions make them appear as such. It is only possible to gain an understanding of how galaxies evolve through indirect measurements.

[1] [$\alpha$/M] is defined as the multi-element abundance that represents the total $\alpha$ abundance relative to the total metals of a star. For more on $\alpha$-elements see the next section.

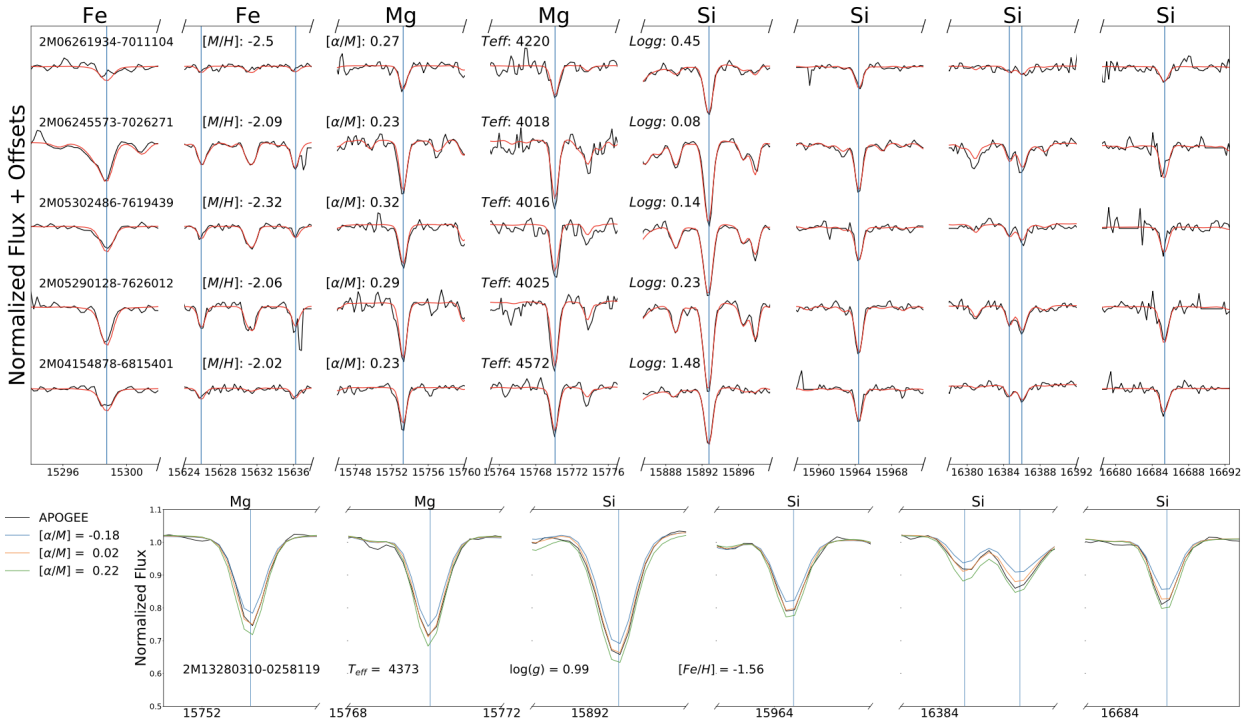



Figure 1.1: A figure from Nidever et al. (2020) that shows how stellar spectra are sensitive to different parameters. (Top) The observed stellar spectra are shown in black and best fit stellar spectra are shown in red around different elemental absorption lines for five different stars with various metallicities, $\alpha$ abundances, $T_{\rm eff}$, and $\log g$ values. The blue vertical lines are to help guide the eye to the position of the absorption lines. This shows how spectra are generally sensitive to different physical parameters of a star. (Bottom) An observed APOGEE spectrum for a single star is shown in black with spectra fit using different $\alpha$ abundance values in color. This plot shows how changing the $\alpha$ abundance affects the goodness of fit to the observed spectrum. The measured $\alpha$ abundance will be the abundance value of the best fit spectrum.

Galactic Chemical Evolution

Stars form from the collapse of giant molecular clouds (GMCs) made up of the interstellar medium (ISM). As a GMC collapses, it fragments, creating groups of similar stars that will have compositions indicative of the material in the GMC (Lada & Lada, 2003). This means we can use the compositions of stars in the present day as a fossil record of the original GMC composition. Major contributors to the composition of star forming gas in galaxies include the following: Supernovae (SNe), asymptotic giant branch (AGB) winds, neutron star mergers, inflows, and outflows. Instead of looking just at a single star in isolation, this can be scaled up to explore galactic chemical evolution (GCE) by combining observations of all the stars in a galaxy. GCE uses the present day abundances of stars to determine how galaxies evolved in the past to end up where they are today. The GCE of a galaxy is highly sensitive to its star formation history (SFH).

The SNe that have the largest effect on GMC composition are type Ia and type II. Type Ia SNe do not have Balmer lines, but they do contain ionized silicon. Stars with masses between 0.5–8 $M_\odot$ will go through a type Ia SNe. These SNe start as a binary system containing at least one white dwarf (WD) and once enough mass is transferred to the WD to make it more massive than the Chandrasekhar mass of 1.4 $M_\odot$, a thermal runaway leads to a supernova explosion (Khokhlov et al., 1993). Because these SNe require a WD, which is an evolved star, there is a delay between when a galaxy forms and when type Ia SNe typically begin. These SNe contribute iron peak elements, which include: chromium, manganese, iron, cobalt, nickel, vanadium, copper, and zinc (Nomoto et al., 2013). Type II SNe have Balmer lines and result from the core collapse of massive stars (Woosley & Janka, 2005). Here massive is anything above 8 $M_\odot$. Type II SNe can almost be thought of as instantaneous compared to type Ia SNe because more massive stars evolve faster and these SNe do not require an evolved stellar companion. These type II SNe inject carbon and nitrogen into the ISM (Kobayashi et al., 2006) as well as the $\alpha$-elements including oxygen,

magnesium, silicon, sulfur, calcium, titanium, and neon as well as the odd-Z elements sodium and aluminium (Nomoto et al., 2013; Weinberg et al., 2019). It is important to keep in mind that many elements can be released or created through both types of SNe, but here only the primary SNe products for each is stated.

Stellar winds results from the forceful removal of material from the outer layer of a star. One common type of stellar wind that contributes material to the ISM is an AGB wind (Ferrarotti & Gail, 2006; Höfner & Olofsson, 2018). AGB stars are giants that have started to burn helium, which initially moves the star to a warmer part of the Hertzsprung-Russell (HR) diagram[2] and then move back toward the red giant branch (Vassiliadis & Wood, 1993). AGB stars can appear quite similar to red giant branch (RGB) stars, hence the asymptotic in their name. It is thought that intermediate mass stars, such as AGB, produce a large portion of carbon and nitrogen (Kobayashi et al., 2006; Ventura et al., 2013).

Neutron stars (NS) in binaries have been observed to merge, with the first confirmed instance being Abbott et al. (2017). Neutron capture elements are heavy atoms produced through the rapid neutron capture process ($r$-process) and slow neutron capture process (s-process). Many $r$-process elements are thought be produced in neutron-rich environments such as jets from some core collapse supernovae (Thielemann et al., 2011) and neutron star mergers (Chen et al., 2021; Thielemann et al., 2011). On the other hand $s$-process elements can be created in less violent neutron-rich environments such as normal AGB stars (Karakas & Lattanzio, 2014). The neutron capture elements explored in this work are cerium and neodymium. Both of these are produced in the $r$- and $s$-processes with substantial fractions created by $r$-process (Prantzos et al., 2020). A large amount of these elements probably formed from neutron star mergers.

The last major contributors to ISM enrichment are inflows and outflows of gas (Bouché

[2]An HR diagram is much like a color magnitude diagram (CMD), but it uses $T_{\rm eff}$ and $\log g$ instead of color and magnitude respectively.

et al., 2010; Davé et al., 2011, 2012; Lilly et al., 2013; Peng & Maiolino, 2014). An inflow is the accretion of extragalactic low-metallicity gas onto a galaxy. This new alien material mixes with the in situ ISM and will go on to create stars. An outflow is the opposite of an inflow and is the forceful ejection of gas from a galaxy. Two major causes of outflows in galaxies include active galactic nucleus (AGN) jets (e.g. Bower et al., 2006; Santoro et al., 2020) and ram pressure stripping (e.g. Cayatte et al., 1994; Treyer et al., 2018). A galaxy moving through a medium will experience ram pressure, which under the right conditions can remove material Gunn & Gott (1972). Hence the name ram pressure stripping.

There are also two "internal" parameters of a galaxy that can affect chemical abundances. These are the star formation rate (SFR) and the initial mass function (IMF). The SFR is, as the names suggest, the birth rate at which stars form and it is generally measured in solar masses per year ($M_\odot$/yr). This is closely related to the star formation efficiency (SFE), which is the SFR surface density ($\Sigma_{\rm SFR}$) divided by the surface density of gas ($\Sigma_{\rm g}$) so SFE = $\Sigma_{\rm SFR}/\Sigma_{\rm g}$. An increase in the SFR means that more stars were able to be formed in the past while an increase in SFE means that the galaxy was more efficient in the past at creating stars from gas. An increase in SFR or SFE will result in more stars forming at higher [Fe/H] before type Ia SNe ignite. This is because more stars will be born earlier including higher mass stars, which release their material faster than low mass stars into the ISM. On the other hand the IMF is a probability distribution that describes the initial overall mass distribution of a population of stars or the probability a star having a certain mass. The mass of a star will determine the evolutionary path that it takes over its lifetime, such as what type of supernova it has and what elements it will primarily enrich the ISM with.

A nice way to illustrate and summarize the above outlined processes is to look at how the abundance of the $\alpha$-elements change in relation to [Fe/H] in a galaxy (see Figure 1.2). As previously mentioned the $\alpha$-elements enrich the ISM through type II SNe, which are

caused by the explosion of single very massive stars that die quickly without the need for a companion WD. This means that initially the [$\alpha$/Fe] will be higher due to its dependence on SNe that happen early on in a galaxy's lifetime. How high the [$\alpha$/Fe] will be depends on the IMF of the system. More higher mass stars initially will mean more type II SNe which in turn means higher $\alpha$ abundance in the past. How long the [$\alpha$/Fe] remains high compared to [Fe/H] is controlled by the SFR (or SFE) for the reasons given in the previous paragraph. Once type Ia SNe turn on there will be a decrease in the [$\alpha$/Fe] with respect to [Fe/H]. As galaxies age there is a general trend for increasing metallicity, but if gas accretes onto the galaxy as an inflow, then the metallicity will be driven down causing the GCE trend to turn back and appear like time has reversed somewhat. A starburst will cause an increase in the [$\alpha$/Fe] for the same reason that it is elevated early on in a galaxy. And finally an outflow will remove gas quenching star formation and allowing more metal-rich material to form and/or prevail. In this example it is clear that many of the different mechanisms listed above are related to each other and they all affect the general GCE.

Abundance Gradients

From the previous section, we established that there are many different processes that lead to change in the composition of the ISM and stars. Since there is no requirement that these processes are homogeneous throughout a galaxy, star formation and evolution will progress at different rates across a galaxy. This results in the formation of abundance gradients (Pagel & Edmunds, 1981; Tinsley, 1980). An abundance gradient is simply the slope with respect to radius of an abundance trend for any measured elemental abundance ratio. Metallicity gradients have been shown to be sensitive to mass (e.g. Belfiore et al., 2017) and angular momentum of a galaxy (e.g. Schroyen et al., 2013). This should also be true for other abundance gradients not just for metallicity. While the formation of a metallicity gradient or other abundance gradients is complicated, these have the ability to summarize a

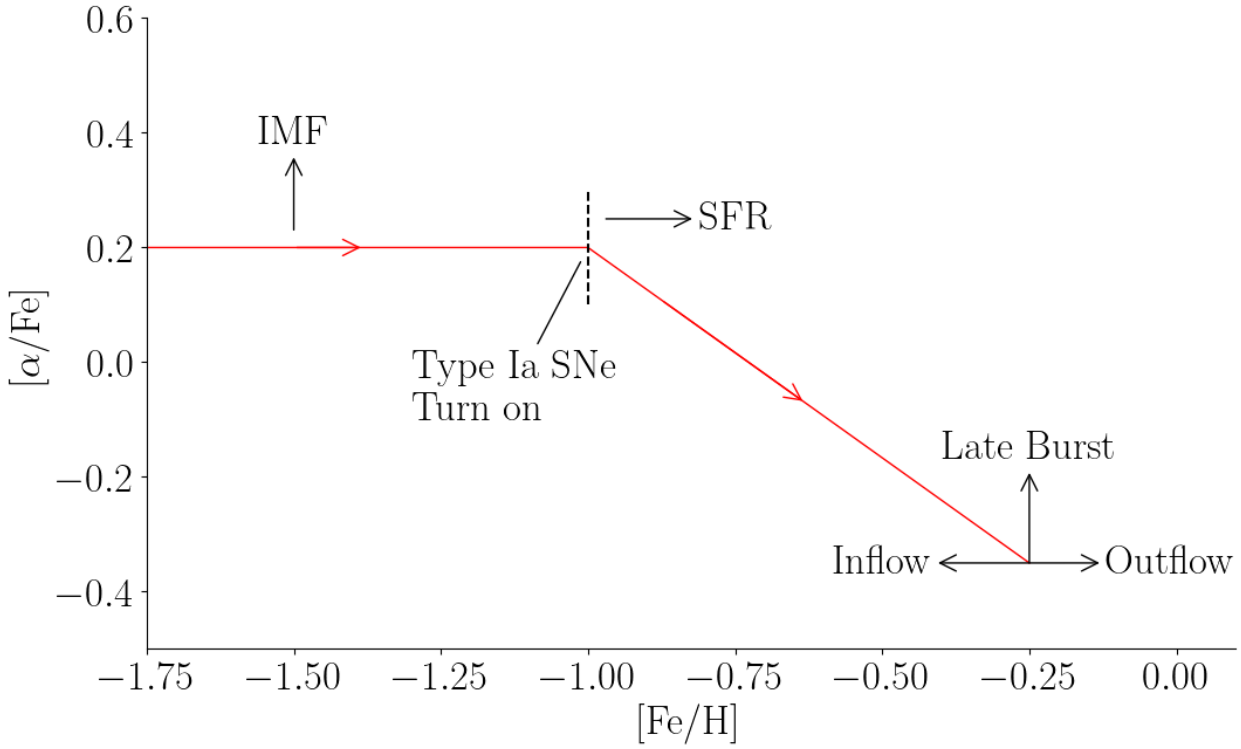



Figure 1.2: Adapted from McWilliam (1997). A schematic of how the GCE can be sensitive to the SFH in the [$\alpha$/Fe]–[Fe/H] plane. The GCE trend is shown in red with arrows on it denoting the direction of time. An increase in the IMF will raise the trend to higher [$\alpha$/Fe] at the metal-poor end while an increase in the SFR will pull the "knee" to higher [Fe/H]. The "knee" is the point at which type Ia SNe turn on in the system. A late burst will raise up the metal-rich end due to an increase in $\alpha$-element production. Inflows of material will drive the [Fe/H] down causing the trend to become more metal-poor. Outflows do the exact opposite of inflows in this diagram.

large part of GCE because certain processes are responsible for different abundances.

Abundance gradients can be measured for a myriad of different types of sources such as the ISM or groups/individual stars. The choice will depend on each particular study. ISM gradients can be found using HII regions by measuring the compositions of the gas (e.g. Searle, 1971). As for groups of stars, gradients have been derived using both globular clusters (GCs, e.g. Cohen et al., 1998) and open clusters (OCs, e.g. Andreuzzi et al., 2011; Donor et al., 2020; Twarog et al., 1997) by measuring the average abundance over a cluster. In the case for individual stars, gradients can be measured with O/B stars (e.g. Cunha & Daflon, 2003; Daflon & Cunha, 2004), Cepheids (e.g. Luck et al., 2003), red giant branch stars (RGB stars, e.g. Escala et al., 2021), planetary nebulae (PNe, e.g. Henry et al., 2010; Maciel & Koppen, 1994), etc. Throughout this work the focus will be on individual RGB field stars.

Abundances and their gradients can change over time, becoming either steeper or shallower, via the same processes that form the gradients as well as through the kinematics of the system. Kinematic mechanisms that lead to changes in abundance gradients include churning (Bilitewski & Schönrich, 2012; Sellwood & Binney, 2002; Vickers et al., 2021) and blurring (Jia et al., 2018; Sellwood, 2014). Churning happens when a spiral arm feature interacts with a star which, in response, changes its galactic radius to conserve angular momentum. If this happens on a large scale then the distribution of elements will change and so will the corresponding gradients, at least if using stars. Blurring occurs due to the slight oscillations around the galactic radius of a star. The distribution of stars will appear to smooth out causing less apparent variation in the abundances across a galaxy leading to flatter gradients. With temporal information, it becomes possible to track the evolution of abundance gradients. Because of the complicated and broad nature of gradient evolution, this work only considers the effects of galaxy interactions on abundance gradients measured with individual stars.

Interacting Galaxies

Currently, the most accepted paradigm of galaxy formation is known as hierarchical merging, or sometimes, hierarchical clustering (Searle, 1971; White & Rees, 1978). The main idea is that in the early universe dark matter began to clump together forming dark matter halos and then baryonic matter fell into them due to gravity, creating dwarf galaxies. As these first galaxies moved throughout the universe, they interacted with other galaxies, sometimes even fully merging with them. These new galaxies then went on to merge with other galaxies. Thus studying interacting (dwarf) galaxies is key to filling in the gaps of our knowledge about galaxy formation.

Close galactic interactions or collisions are violent events that lead to the rapid inflow of material onto a galaxy, which in combination with shocks (e.g. Saitoh et al., 2009), and tidal compressions (e.g. Renaud et al., 2009) lead to starbursts (Knapen & Cisternas, 2015; Larson & Tinsley, 1978; Schweizer, 2005; Toomre & Toomre, 1972). In hydrodynamics, a shock is a discontinuity in pressure that propagates through a medium. Unlike an acoustic wave in a fluid, a shock propagates at a speed faster than the speed of sound in the medium. This means that a fluid parcel is blissfully unaware that a change to its state will happen until the front of the shock reaches it. The shock will cause areas of higher density gas which can collapse to form stars. Similarly, with tidal compression the interactions between galaxies can squeeze the ISM leading to higher density pockets and creating conditions ripe for star formation. The chemical evolution of a galaxy will be marred by the ignition of these starburst events, which will be reflected in the distribution of abundances and hence the abundance gradients of the system

The organization of this work is as follows. Chapter 2 presents the method used to calculate the ages of individual RGB stars. Next, Chapter 3 explores the gradients and the variations of abundances over time for the LMC. Chapter 4 explores the evolution of the SMC abundance gradients using a similar analysis to the LMC. Finally, Chapter 5 offers

some concluding remarks.

# REVEALING THE CHEMICAL STRUCTURE OF THE MAGELLANIC CLOUDS WITH APOGEE. I. CALCULATING INDIVIDUAL STELLAR AGES OF RGB STARS IN THE LARGE MAGELLANIC CLOUD

## Contribution of Authors and Co-Authors

Manuscript in Chapter 2

Author: Joshua T. Povick

Contributions: Lead author of the manuscript who carried out the calculation of the stellar extinctions, ages, and masses.

Author: David L. Nidever

Contributions: Provided general advice, architect of the bias correction, helped edit the manuscript, and gave comments on the manuscript.

Author: Pol Massana

Contributions: Provided comments and helped edit the manuscript.

Author: Jamie Tayar

Contributions: Engaged in valuable discussion of the results especially for the APOKASC validation dataset. Provided comments and feedback on the draft of the manuscript.

Author: Knut Olsen

Contributions: Created and ran the LMC kinematic models as well as helped write the asymmetric drift section. Provided comments and feedback on the draft of the manuscript.

Author: Sten Hasselquist

Contributions: Provided comments and feedback on the draft of the manuscript.

Author: Maria-Rosa L. Cioni

Contributions: Provided comments and feedback on the draft of the manuscript.

Author: Christian Nitschelm

Contributions: Provided comments and feedback on the draft of the manuscript.

Author: Ricardo Carrera

Contributions: Provided comments and feedback on the draft of the manuscript.

Author: Yumi Choi

Contributions: Provided comments and feedback on the draft of the manuscript.

Author: Alexandre Roman-Lopes

Contributions: Provided comments and feedback on the draft of the manuscript.

Author: Steven R. Majewski

Contributions: Provided comments and feedback on the draft of the manuscript.

Author: Andrés Almeida

Contributions: Lead observer for the APOGEE-2S survey. Provided comments and feedback on the draft of the manuscript.

Author: Katia Cunha

Contributions: Provided comments and feedback on the draft of the manuscript.

Author: Verne Smith

Contributions: Provided comments and feedback on the draft of the manuscript.

Manuscript Information

Joshua T. Povick, David L. Nidever, Pol Massana, Jamie Tayar, Knut Olsen, Sten Hasselquist, Maria-Rosa L. Cioni, Christian Nitschelm, Ricardo Carrera, Yumi Choi, Alexandre Roman-lopes, Steven R. Majewski, Andrés Almeida, Katia Cunha, Verne Smith

Monthly Notices of the Royal Astronomical Society

Status of Manuscript:
____ Prepared for submission to a peer-reviewed journal
_X_ Officially submitted to a peer-reviewed journal
____ Accepted by a peer-reviewed journal
____ Published in a peer-reviewed journal

Oxford Academic, Oxford University Press Monthly Notices of the Royal Astronomical Society
11 May 2023

## Abstract

Stellar ages are critical for understanding the temporal evolution of a galaxy. We calculate the ages of over 6000 red giant branch stars in the Large Magellanic Cloud (LMC) observed with SDSS-IV / APOGEE-S. Ages are derived using multi-band photometry, spectroscopic parameters ($T_{\rm eff}$, $\log g$, [Fe/H], and [$\alpha$/Fe]) and stellar isochrones and the assumption that the stars lie in a thin inclined plane to get accurate distances. The isochrone age and extinction are varied until a best match is found for the observed photometry. We perform validation using the APOKASC sample, which has asteroseismic masses and accurate ages, and find that our uncertainties are $\sim$20% and range from $\sim$1$-$3 Gyr for the calculated age values. Here we present the LMC age map as well as the age-radius relation and an accurate age-metallicity relation (AMR). The age map and age-radius relation reveal that recent star formation in the galaxy was more centrally located and that there is a slight dichotomy between the north and south with the northern fields being slightly younger. The northern fields that cover a known spiral arm have median ages of $\gtrsim$ 2 Gyr, which is the time when an interaction with the SMC is suggested to have happened. The AMR is mostly flat especially for older ages although recently (about 2.0–2.5 Gyr ago) there is an increase in the median [Fe/H]. Based on the time frame, this might also be attributed to the close interaction between the LMC and SMC.


## Introduction

The ages of stars is very important for understanding galaxy evolution and galactic archaeology. Without temporal information it becomes much more difficult to pinpoint how galaxies evolved to what we see today. Unfortunately, determining ages is not without its challenges as we rely on indirect means to find ages. Often times limited photometry or low resolution spectra make ages nearly impossible to determine because there is not enough

information to constrain the ages of stars provided by these methods.

Stellar clusters have been accurately age-dated for many decades, taking advantage of the age-sensitivity of turnoff and subgiant branch stars (e.g. Flower et al., 1983; Sandage, 1970; Sarajedini, 2008). It is substantially more challenging to measure the ages of individual field stars. However, there are several methods that have been developed to calculate ages of individual stars. Some of the more popular methods include: nucleocosmochronometry, gyrochronology, asteroseismology, chemical abundance ratios, and using isochrones. Nucleocosmochronometry relies on measuring the abundance of radioactive nuclides and their daughter products and is much like the analog of radiocarbon dating, but for stars (Frebel et al., 2007; Hill et al., 2002). Very high signal-to-noise and high resolution spectra are required to make these measurements and even then the relevant absorption lines may not exist in the spectrum. In general, nucleocosmochronometry has only been performed for a small number of stars. Gyrochronology uses the rotation rate of a star to calculate its age because as a star ages its rotational speed decreases (Barnes, 2007; Mamajek & Hillenbrand, 2008). This requires precise, time-series photometry of cool, main-sequence stars which can be challenging to obtain for external galaxies like the LMC. Asteroseismology uses scaling relations and the oscillations inside of a star to obtain precise masses and then ages using isochrones (Cunha et al., 2007; Pinsonneault et al., 2014). Since mass and age are strongly anticorrelated on the giant branch, measuring mass accurately also allows for an accurate age to be determined. However, very precise and high-cadence photometry is required to derive good asterseismologic masses and this is currently only available for small portions of the sky (i.e., Kepler, K2, CoRoT, TESS). More recently, spectroscopic chemical abundances have been used to determine masses of RGB stars with [C/N] and [$C^{12}/C^{13}$] ratios (Ness et al., 2016a). These ratios are sensitive to the mass-dependent dredge-up that happens on the giant branch and pulls up nuclear-processed material from the interior. Currently, this technique only works for metal-rich populations ([Fe/H] $\gtrsim -0.5$), and, therefore, is

not applicable for the relatively metal-poor LMC stars. Arguably one of the most popular methods to find ages is using isochrones. Isochrone-fitting involves fitting theoretical stellar models to either individual or groups of stars. Many of these methods rely on comparing to stellar evolutionary models and to be able to truly do this we need many photometric bands that constrain the spectral energy distribution (SED) or high resolution spectra. The `BEAST` (Gordon et al., 2016) compares a grid of isochrones to multi-band photometry to determine mass, age, metallicity, $T_{\rm eff}$, and $\log g$ on a star-by-star basis. This has been used successfully in M31 using the PHAT survey (Dalcanton et al., 2012). All of these methods come with their own set of pros and cons and the choice of which one to use is often dictated by context.

Previous work of finding ages using isochrones for giant stars include works such as Feuillet et al. (2016). In that work ages are found two different ways: 1) calculating the mass from measured stellar parameters from which the mass–age relation can be used to get age and 2) using a Bayesian isochrone matching technique with a constant star formation history (SFH) to derive an age probability distribution for each star. Through mock data tests it was found that this method shows that decent ages can be derived for individual stars using a combination of photometry and spectroscopy with isochrones using a probabilistic approach.

This work uses isochrones to determine the age of individual red giant branch (RGB) stars using photometric and spectroscopic observations through direct calculation that is non-probabilistic. We take advantage of the fact that the absolute magnitude of giant stars vary substantially with age for fixed $T_{\rm eff}$, by as much as 0.8 magnitudes between 1 Gyr and 10 Gyr at an average LMC metallicity of [Fe/H]$=-0.5$. One potential drawback of using isochrones is the age-metallicity degeneracy of RGB stars, but we overcome this by using the metallicity measured with high-resolution spectroscopy.

The method presented in this work finds the age by calculating the model photometry age in six different passbands spanning both optical and infrared wavelengths using a single

common trial and comparing to the observed photometry of a star. This method is possible due to accurate distances, which are needed to constrain the absolute magnitude of a star.

There are two main reasons for studying the ages of red giant branch (RGB) stars in the LMC. The first reason is that the literature is scant on the spatial distribution of ages in the galaxy especially using individual stars. The LMC is a relatively close satellite galaxy of the Milky Way (MW) at 49.9 kpc (De Grijs et al., 2014; van der Marel & Cioni, 2001) and so it makes sense to analyze it as it does not pose as many challenges compared to galaxies which are farther away that may or may not be resolved. The second reason is that accurate ages are needed on a star-to-star basis to study the chemical evolution of the LMC at very high resolution.

Galaxies are the sum of their parts and stars make up a large portion of them. With a large enough sample of stars with good spatial coverage, it becomes possible to study the chemical evolution of a galaxy. When a star "dies", material is ejected into the interstellar medium (ISM) making it available to form newer stars. Thus enriching the reservoir of gas in the ISM to higher metallicities through the yields of the now deceased star. This leads to new stars having elevated chemical abundances and hence higher metallicities. It is also well known that metallicity is a proxy for age. While the particular age-metallicity (AMR) for galaxies will differ, they are an extremely useful tool to study galaxy evolution. The AMR reveals how a galaxy evolved over time. Generally the AMR is measured using clusters or field stars.

Studies of the star formation history (SFH) of a galaxy have the potential to yield AMRs. Usually, observations of resolved stellar population observations are fit with stellar evolutionary models using a combination of distance, age and metallicity parameters. This means that as a result one ends up having a relation between the age and metallicity of stars in the galaxy. Normally though, this method gives very approximate results. For the LMC, there are very few examples where these results are used to draw conclusions about

the galaxy's evolution. Harris & Zaritsky (2009) used the MCPS survey (Zaritsky et al., 1997) to derive SFH across the main-body of the LMC. Because of the shallow nature of the photometric survey, the study was limited to younger ages and only four metallicity bins per single age stellar population. The general conclusions were that the LMC seemed to remain at a constant metallicity in the old ages until around $\approx 4$ Gyr ago, when it started to increase to the present day value. A more recent approach with larger photometric depths was used by Meschin et al. (2014), covering three small fields in the LMC. The AMR derived from the SFH results had a good fit with spectroscopic results from field stars by Carrera et al. (2008), but the spatial scope of the study was still relatively small. Furthermore, Weisz et al. (2013) used deep *HST* imaging to derive the SFH in eight fields in the LMC (as well as seven more in the SMC), but released no metallicity information due to the focus being on the comparison of star formation between the two galaxies. In Monteagudo et al. (2018), SFHs for several small fields in the central parts of the LMC were released, but again contained no metallicity information. Ruiz-Lara et al. (2020) used the deep, multi-band, contiguous SMASH data (Nidever et al., 2017) in the LMC to derive spatially-resolved SFHs. The paper was focused on the formation of the LMC's spiral arm and also did not include any metallicity information. Finally, Mazzi et al. (2021) used infrared VMC data Cioni et al. (2011) covering the entire main body of the LMC. Unfortunately, infrared photometry is even less well suited than optical photometry for metallicity determination because it is less sensitive to metallicity, and the study does not include any AMR results. But they state that populations of stars made up of younger ages should have a lower metallicity than what is predicted from Carrera et al. (2008). This is not to say that infrared photometry should not be used in studies of metallicity. In Choudhury et al. (2021) it was shown that metallicities derived from NIR photometry can be useful in exploring variations across the LMC. Therefore, establishing a precise and reliable source for an LMC AMR will benefit the current literature. Our goal is to take advantage of the precision in our metallicities and

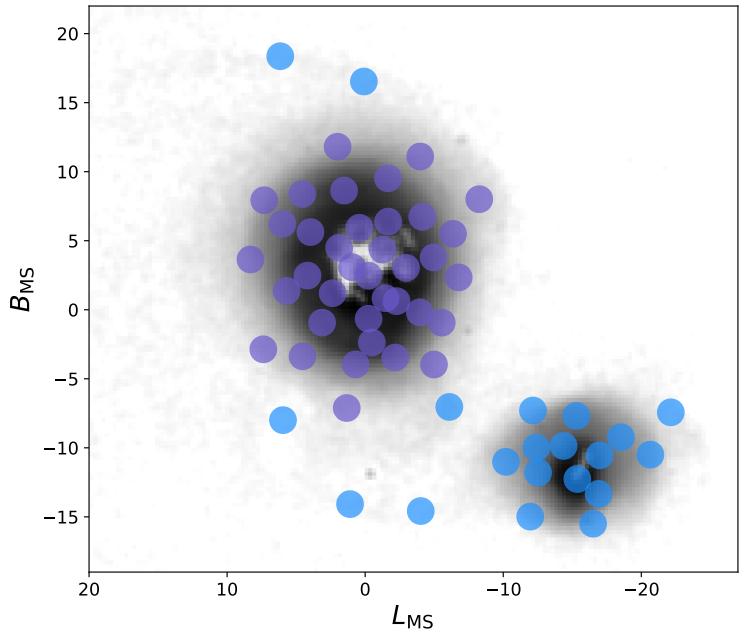



Figure 2.1: Map of the APOGEE-2 Magellanic Cloud fields filled circles) and the background showing the density of MC RGB stars selected with Gaia. The LMC fields analyzed here are shown as purple filled circles. For some basic statistics on the LMC fields see Table 2.

the extent of our data to generate an AMR that will cover more areas of the LMC to an unprecedented precision.

Alternatively, there have been many different studies of the LMC that specifically target the calculation of the AMR in the past. For example Dirsch et al. (2000); Grocholski et al. (2006); Olszewski et al. (1991) derive the AMR using clusters, while some papers such as Carrera et al. (2008) derive the AMR using spectroscopy of field stars. Most previous studies have a preference for clusters instead of individual stars and so with the derived individual ages and the known metallicities, we also explore the AMR of the LMC.

One drawback with using clusters for AMR and other age studies is that an age gap exists creating a bimodal cluster age distribution (Da Costa, 1991; Geisler et al., 1997). Only two clusters in the LMC have been confirmed having ages between $\sim$3$-$12 Gyr old. These being ESO 121-SC 03 (Mateo et al., 1986; Olszewski et al., 1991) and KMHK 1592

(Piatti, 2022) respectively. Having only two clusters for such a wide range of ages leads to large uncertainties in the behavior of the LMC for intermediate ages. However, Gatto et al. (2020) make the claim using YMCA (Gatto et al. in prep) and STEP Ripepi et al. (2014) data that the gap is observational bias. That work finds 16 candidate intermediate age clusters, which if confirmed will change our understanding of how star clusters formed in the LMC. Currently the only way to get data for intermediate ages is to use field stars to fill in the age gap where clusters are not present or to confirm the existence of more so called age gap clusters.

This paper starts in Section 2.2 by presenting the four datasets used. Sections 2.3, 2.4, and 2.5 introduce how distances to the individual LMC stars are calculated, the extinction laws used, and the Salaris correction to the metallicity, respectively. Next, Section 2.7 outlines how the extinctions, ages, and masses are calculated for each star with the validation explained in Section 2.8. In Section 2.9, the bias correction applied to the LMC stars is discussed. Finally, the LMC results are presented in Section 2.10 and discussed in Section 2.11.

## Data

### APOGEE

The Apache Point Observatory Galactic Evolution Experiment (APOGEE, Majewski et al. 2017) is a valuable tool to study the LMC. APOGEE is part of the broader Sloan Digital Sky Survey (SDSS IV, Blanton et al. 2017). APOGEE's main goal is to accurately and extensively study the chemistry and kinematics of the Milky Way (MW). It does this with two identical $H$-band spectrographs (Wilson et al., 2019) in the northern and southern hemispheres. For the northern hemisphere the spectrograph (APOGEE-N) is located at the Apache Point Observatory (APO) and takes data on the Sloan 2.5 m (Gunn et al., 2006) and NMSU 1.0 m (Holtzman et al., 2010) telescopes. As for the southern hemisphere,

the spectrograph (APOGEE-S) is located at the Las Campanas Observatory (LCO) and connected to the du Pont 2.5 m telescope (Bowen & Vaughan, 1973).

The raw APOGEE are processed with the data processing pipeline (Nidever et al., 2015) producing 1-D extracted and wavelength calibrated spectra with accurate radial velocities (RVs) determined with `Doppler` (Nidever, 2021). Spectral parameters and abundances are then determined with the APOGEE Stellar Parameters and Chemical Abundances Pipeline (ASPCAP, García-Pérez et al. 2016). This compares the normalized observed spectra with a large grid of synthetic spectra using `FERRE` (Allende Prieto et al., 2006). The most up-to-date version of the data used in this work is part of SDSS-IV Data Release 17 (Abdurro'uf et al., 2022). In particular for DR17, the APOGEE spectral grid was created using `synspec` (Hubeny et al., 2021). Updates specific to DR17 can be found in Holtzmann et al. (in prep).

The main ASPCAP spectral fitting determines the "spectral parameters" which affect a significant fraction of the spectrum: $T_{\rm eff}$, $\log g$, $v_{\rm micro}$, [M/H], [C/M], [N/M], [$\alpha$/M], and $v_{\rm macro}$ for giant stars. Individual elemental abundances are then determined from the same spectral grid by holding the spectral parameters constant but varying [M/H] (or [$\alpha$/M], depending on the element) with the use of narrow spectral windows specific to each element. Chemical abundances provided in DR17 from ASPCAP are: C, CI, N, O, Na, Mg, Al, Si, S, K, Ca, Ti, TiII, V, Cr, Mn, Fe, Co, Ni, and Ce. For this work we extensively use $T_{\rm eff}$, [Fe/H], and [$\alpha$/Fe] (=[$\alpha$/M]+[M/H]-[Fe/H]) derived by ASPCAP. Uncalibrated $T_{\rm eff}$, $\log g$, vmicro, [M/H], [C/M], [N/M], [$\alpha$/M], and v sini can be found in each star's `FPARAM` array in the data catalog.

There are both systematic and statistical errors present in the APOGEE data. To minimize the effect of systematic errors, stars with known solar-like metallicity in the solar neighborhood were observed. From these stars offsets were derived and corrected for in the APOGEE data. Statistical uncertainties were calculated by performing multiple visits of single stars and fitting function of $T_{\rm eff}$, [M/H], and SNR to the observed scatter. More

information on $\alpha$-abundance uncertainties can be found in Nidever et al. (2020).

The LMC selection for DR17 is almost identical to that described in Nidever et al. (2020) for DR16. The biggest difference is the coverage that has been extended to roughly twice the previous size (compare Fig. 2.1 here to Fig. 1 in Nidever et al. 2020). The quality cuts applied to each field star were:

- `Teff_BAD`, `LOGG_BAD`, `VMICRO_BAD`, `ALPHAFE_BAD`, `CFE_BAD`, `NFE_BAD`, `NO_ASPCAP_RESULT` flags are not set
- $T_{\rm eff} < 5200\,{\rm K}$
- $\log g < 3.4$
- S/N $> 20$.

After the membership selection and applying the above quality cuts, the total number of stars in the LMC sample is 6130. A CMD and HR diagram for the LMC RGB star sample can be seen in Figure 2.2.

Detailed information on the APOGEE-1/-2 targeting can be found in Zasowski et al. (2013) and Zasowski et al. (2017). APOGEE DR17 has excellent spatial coverage of a significant portion of the LMC as seen in Figure 2.1 out to a radius $\sim$10° (or $\sim$8 kpc). More information on the fields can be seen in Table 2.

Gaia EDR3

The Gaia mission (Gaia Collaboration et al., 2016, 2021a) is an extensive space-based all-sky survey. We use both photometric and astrometric data from the early data release 3 (Gaia EDR3), which contains over 1.8 billion sources. Gaia obtains photometric data in three optical bands: denoted $BP$, $G$, and $RP$. All of the Gaia EDR3 data are publicly available online from the Gaia Archive[1]. The APOGEE DR17 catalog includes the corresponding

[1] `https://gea.esac.esa.int/archive/`

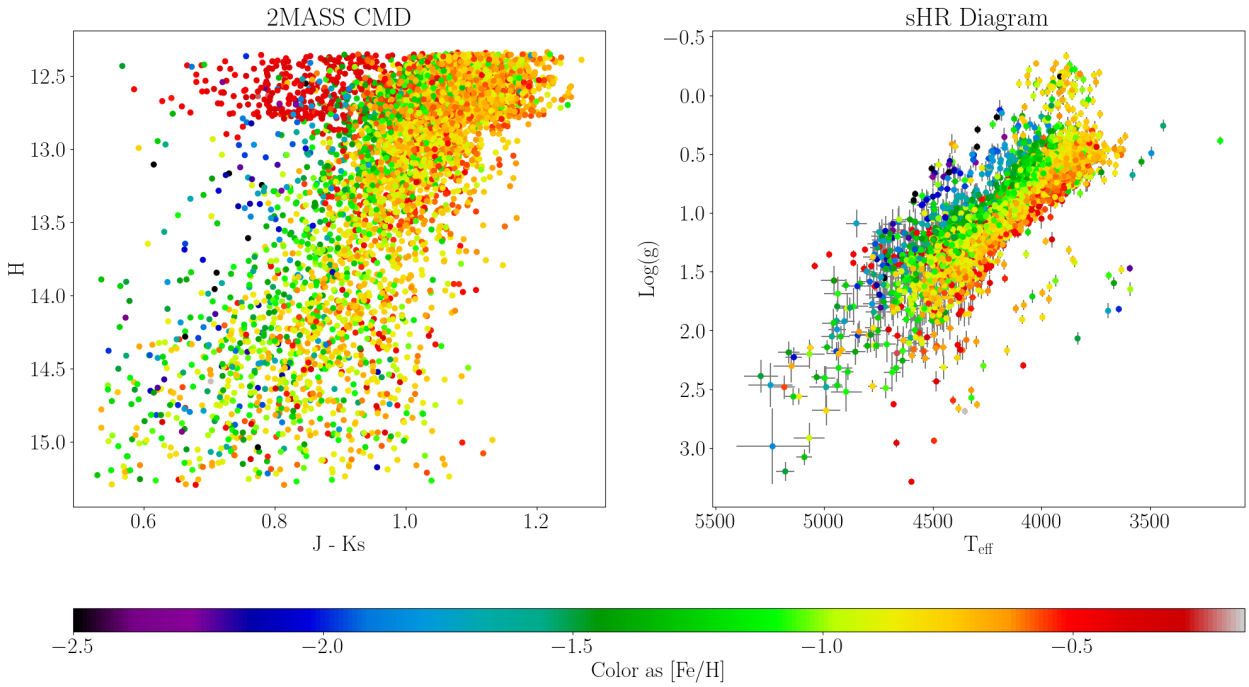



Figure 2.2: (*Left*) A 2MASS color magnitude diagram of the selected APOGEE LMC RGB stars colored by [Fe/H]. The tip of the RGB is assumed to be at $H$ ∼12.35 for the LMC (Nidever et al., 2020). (*Right*) A Kiel diagram for the APOGEE LMC RGB stars colored by [Fe/H].

Table 2.1: A table of positional data for each of the APOGEE LMC fields including the number of RGB stars observed. R and PA are the projected radius and position angle respectively. $N_{Brt}$ is the number of identified bright RGB stars while $N_{Fnt}$ is the number of faint sources (see Section 2).

| Name | R.A. (J2000.0) | Decl. (J2000.0) | R (deg) | PA (deg) | $N_{RGB}$ | $N_{Brt}$ | $N_{Fnt}$ |
|---|---|---|---|---|---|---|---|
| 30Dor | 05:34:3.30 | -69:21:6.40 | 0.8 | 52.0 | 41 | 41 | 0 |
| LMC1 | 04:14:32.0 | -71:59:22.2 | 6.3 | 242.0 | 169 | 10 | 159 |
| LMC2 | 04:13:14.9 | -68:28:21.6 | 6.7 | 272.0 | 148 | 9 | 139 |
| LMC3 | 04:49:10.2 | -75:11:48.9 | 6.1 | 204.0 | 188 | 26 | 162 |
| LMC4 | 04:54:54.6 | -68:48:6.80 | 3.1 | 287.0 | 254 | 254 | 0 |
| LMC5 | 04:57:10.3 | -71:08:54.2 | 2.9 | 240.0 | 236 | 236 | 0 |
| LMC6 | 05:10:55.5 | -65:46:21.7 | 4.4 | 337.0 | 200 | 200 | 0 |
| LMC7 | 05:14:46.4 | -62:43:22.3 | 7.3 | 349.0 | 171 | 62 | 109 |
| LMC8 | 05:20:48.5 | -72:32:48.2 | 2.8 | 191.0 | 220 | 220 | 0 |
| LMC9 | 05:22:15.7 | -69:48:1.30 | 0.7 | 260.0 | 143 | 143 | 0 |
| LMC10 | 05:30:28.3 | -75:53:11.2 | 6.1 | 178.0 | 171 | 35 | 136 |
| LMC11 | 05:41:49.0 | -63:37:17.1 | 6.4 | 14.0 | 195 | 128 | 67 |
| LMC12 | 05:44:9.90 | -60:38:40.1 | 9.4 | 13.0 | 138 | 17 | 121 |
| LMC13 | 05:44:24.1 | -67:41:59.7 | 2.7 | 38.0 | 173 | 173 | 0 |
| LMC14 | 05:50:34.4 | -70:58:29.1 | 2.2 | 122.0 | 152 | 152 | 0 |
| LMC15 | 06:08:2.80 | -63:47:24.5 | 7.3 | 38.0 | 175 | 47 | 128 |
| LMC16 | 06:29:7.50 | -75:04:58.8 | 6.9 | 145.0 | 131 | 13 | 118 |
| LMC17 | 06:29:59.5 | -70:17:23.1 | 5.3 | 102.0 | 176 | 44 | 132 |
| LMC18 | 06:06:28.4 | -66:26:29.5 | 5.0 | 51.0 | 192 | 192 | 0 |
| LMC19 | 06:12:35.8 | -69:27:47.4 | 4.0 | 90.0 | 182 | 182 | 0 |

| | | | | | | | |
|---|---|---|---|---|---|---|---|
| LMC20 | 05:14:31.3 | -74:25:36.5 | 4.7 | 191.0 | 208 | 208 | 0 |
| LMC21 | 04:35:3.80 | -67:39:8.40 | 5.3 | 289.0 | 205 | 118 | 87 |
| LMC22 | 04:35:47.4 | -71:37:2.20 | 4.7 | 242.0 | 205 | 167 | 38 |
| LMC23 | 07:07:56.0 | -73:45:55.5 | 8.6 | 128.0 | 86 | 4 | 82 |
| LMC24 | 05:44:24.8 | -79:06:12.0 | 9.3 | 175.0 | 70 | 4 | 66 |
| LMC25 | 06:33:14.1 | -63:39:58.6 | 8.9 | 54.0 | 170 | 15 | 155 |
| LMC26 | 04:15:7.10 | -62:35:31.7 | 10.1 | 307.0 | 65 | 4 | 61 |
| LMC27 | 05:12:55.0 | -67:59:33.1 | 2.3 | 321.0 | 152 | 152 | 0 |
| LMC28 | 04:56:36.5 | -60:48:53.1 | 9.6 | 337.0 | 185 | 11 | 174 |
| LMC29 | 06:23:21.8 | -65:40:18.9 | 6.7 | 58.0 | 210 | 79 | 131 |
| LMC30 | 04:50:5.40 | -65:11:22.6 | 5.9 | 318.0 | 205 | 125 | 80 |
| LMC31 | 05:31:58.7 | -66:27:10.7 | 3.5 | 13.0 | 152 | 152 | 0 |
| LMC32 | 04:27:18.9 | -65:41:49.5 | 7.1 | 299.0 | 221 | 24 | 197 |
| LMC33 | 06:51:56.5 | -67:24:9.50 | 8.1 | 83.0 | 180 | 12 | 168 |
| LMC34 | 06:05:43.3 | -72:55:21.2 | 4.4 | 140.0 | 201 | 201 | 0 |
| LMC35 | 04:06:26.5 | -74:54:2.80 | 7.9 | 221.0 | 160 | 7 | 153 |

Gaia photometry and astrometry columns and much of Gaia EDR3 and Gaia DR3 (Gaia Collaboration et al., 2022) are the same for the LMC stars in this work.

Our age calculations in Section 2 require uncertainties in the photometric magnitudes. We calculate these from the relative flux uncertainties provided in the data release catalog. Flux and magnitude are related by $m_\lambda = -2.5\log(F_\lambda)$, where $m_\lambda$ is the magnitude and $F_\lambda$ is the flux. Using general error propagation methods and taking into account the zero point for each Gaia band, the magnitude error is given by

$$\sigma_{m\lambda} = \sqrt{\left(\frac{1.085}{F_\lambda/\sigma_\lambda}\right)^2 + zp_\lambda^2} \tag{2.1}$$

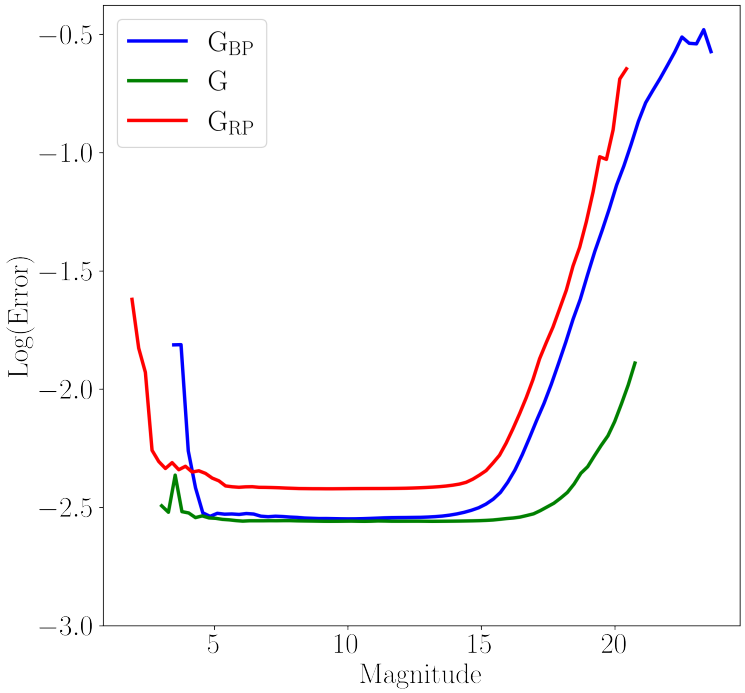



Figure 2.3: A reproduction of the magnitude error curve for Gaia EDR3 calculated using the Gaia photometry and equation 2.1. The blue, green, and red curves represent the BP, G, and RP bands respectively. The curves here match qualitatively to the curves in Riello et al. (2021).

where $\sigma_{m\lambda}$ is the magnitude uncertainty for the $\lambda$ Gaia band, $F_\lambda/\sigma_\lambda$ is the flux over its error provided by Gaia, and $zp_\lambda$[2] is the zero point offset for the band. Plotting the calculated error as a function of the magnitude produces the curve in Figure 2.3. This was created by taking a large selection of stars and interpolating the error as a function of magnitude. Qualitatively this figure closely resembles the analogous figure in Riello et al. (2021).

Gaia EDR3 includes very accurate proper motions ($\mu$) and parallaxes ($\varpi$). The reciprocal of the Gaia parallax is used to calculate distances of stars in the APOKASC validation set (see Section 2). While taking the parallax reciprocal is non-optimal for low-S/N values, the large majority of stars in the APOKASC sample have S/N$\gtrsim$70 where this

[2]See `https://www.cosmos.esa.int/web/gaia/dr3-passbands` for these values

is less of a problem.

APOKASC

APOKASC is a joint spectroscopic and asteroseismic dataset created by combining APOGEE and *Kepler* data (Pinsonneault et al., 2014, 2018). The APOKASC stars have well-determined masses, radii and ages. We use the APOKASC 3 (Pinsonneault et al. in prep) catalog to validate our estimated ages and masses.

The following selection criteria are applied to the APOKASC data to best match the APOGEE data for the LMC sample:

- `APOKASC3_CONS_EVSTATES` = 1
- $\varpi/\sigma_{\varpi} > 3.0$

where `APOKASC3_CONS_EVSTATES` denotes RGB stars in the 6.7.4 version of the APOKASC dataset (in contrast to red clump stars). The parallax cut is performed to ensure accurate distances can be found by taking the reciprocal. After the selection criteria is applied, there are 4058 RGB stars left in the APOKASC sample that span $T_{\rm eff}$ from 3712 to 5345. A Kiel diagram of the final selection is shown in Figure 2.4.

PARSEC Isochrones

In order to derive extinction, age, and mass estimates of stars we rely on the use of PARSEC (Bressan et al. 2012; Marigo et al. 2017) isochrones, which are available online[3]. These contain $T_{\rm eff}$, $\log g$, metallicity, initial mass, the photometric absolute magnitudes, as well as a convenient stellar evolutionary phase label (`LABEL`). We downloaded a finely-spaced grid of isochrones in age and metallicity for the Gaia EDR3 and 2MASS bands. The ages span 25 Myr to 17 Gyr in steps of 50 Myr, and the metallicities span [M/H]=−2.3 to +0.5 in steps of 0.02 dex.

[3] `http://stev.oapd.inaf.it/cgi-bin/cmd`

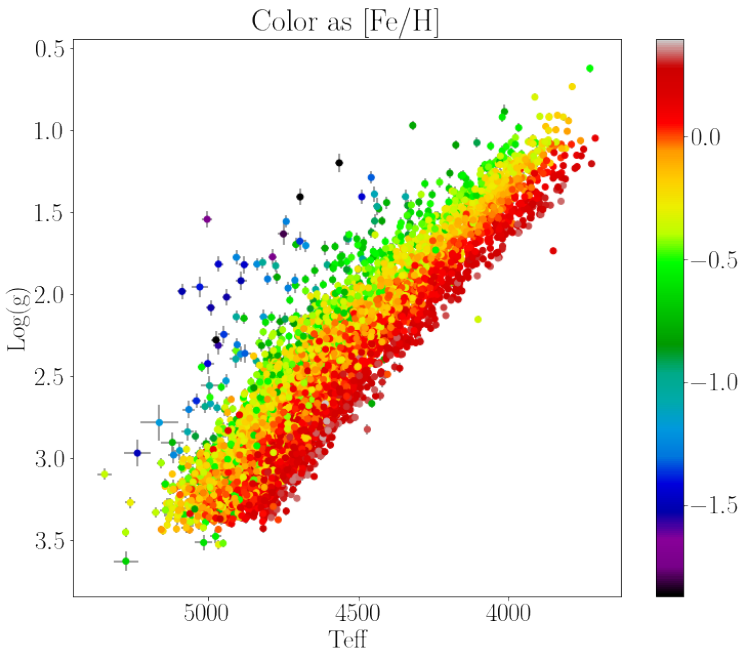



Figure 2.4: An HR diagram for the selected APOKASC RGB stars colored by [Fe/H].

## LMC Distances

The geometry of the LMC disk is well-modeled as a thin, inclined plane. Using this simple model and well-constrained observational parameters, the distances for the LMC disk stars can be calculated. The mathematical basis of this model comes from van der Marel & Cioni (2001) and Choi et al. (2018b).

To calculate the distance in the inclined disk model, the first step is to convert the $(\alpha, \delta)$ celestial coordinates to a cylindrical coordinate system $(\rho, \phi)$. These coordinates are defined such that $\rho$ is the angular distance from the LMC center (radius) and $\phi$ is the position angle (east of north). This is analogous to polar coordinates in 2D, but on the celestial sphere.

The coordinate conversion to the cylindrical coordinates is:

$$\begin{aligned}
\cos\rho &= \cos\delta_0\cos\delta\cos(\alpha-\alpha_0)+\sin\delta_0\sin\delta,\\
\sin\rho\cos\phi &= -\cos\delta\sin(\alpha-\alpha_0),\\
\sin\rho\sin\phi &= \cos\delta_0\sin\delta-\sin\delta_0\cos\delta\cos(\alpha-\alpha_0),
\end{aligned} \tag{2.2}$$

where $(\alpha_0, \delta_0) = (82.25°, -69.50°)$ is from van der Marel & Cioni (2001).

The distance can be calculated by projecting the angular coordinates onto a plane which means the distance is the given by

$$D = \frac{D_0\cos i}{\cos i\cos\rho-\sin i\sin\rho\sin(\phi-\theta)}, \tag{2.3}$$

where $D_0 = 49.9$ kpc (De Grijs et al., 2014; van der Marel & Cioni, 2001) is the distance from the Sun to the center of the LMC, $i = 25.87°$ is the inclination of the LMC disk, and $\theta = 149.23°$ is the position angle of the line of nodes. Both the inclination and position angle of the line of nodes comes from the Choi et al. (2018b) analysis of the SMASH (Nidever et al., 2021) red clump stars. When using equation 2.3, it is important to note that many angle are measured from North and not East, so 90° is added to $\theta$ in practice.

We take the equation for finding the radius directly from Choi et al. (2018b), which is

$$r(x,y)^2 = (x\cos\psi - y\sin\psi)^2 + \left(\frac{x\sin\psi + y\cos\psi}{b/a}\right)^2, \tag{2.4}$$

where $\psi\,(= 227.24°)$ is the position angle of the semi-major axis, and $b/a\,(= 0.836)$ is ratio of the semi-minor axis to the semi-major axis. For angles measured from the north, 90° must be added to $\psi$ just like with $\theta$ above. A distance map of the LMC with the added elliptical radius contours (annuli) can be seen in Figure 2.5.

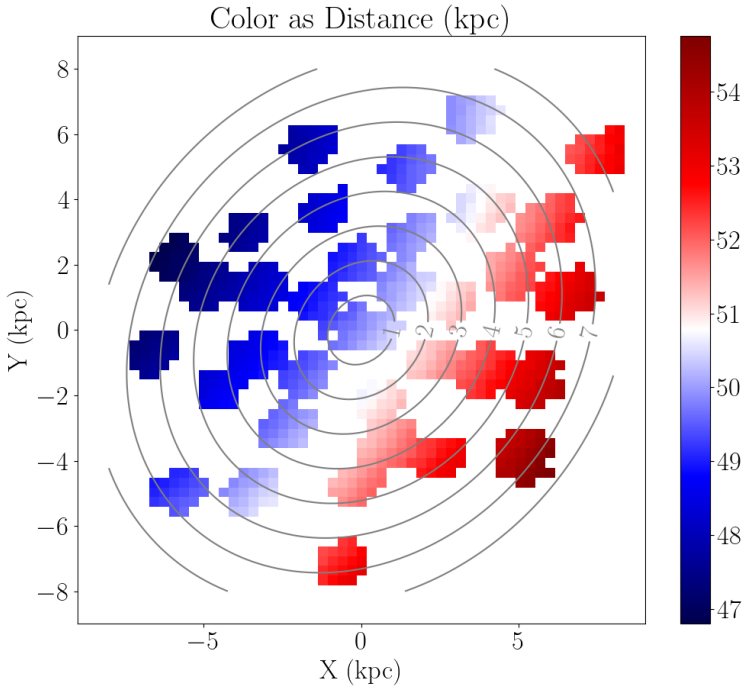



Figure 2.5: The resulting distance map for the LMC using Equation 2.3. The contours show lines of constant "elliptical" radius starting at 1 kpc for the center contour out to 8 kpc calculated using equation 6 from Choi et al. (2018b)

.

## Extinction Laws

### Cardelli Extinction Law

In order to calculate and constrain the extinction across multiple bands, we adopt the extinction law directly from Cardelli et al. (1989, hereafter CCM89) for calculating the extinction coefficients.

The extinction relative to the $V$ band can be found with

$$\mathrm{A}_\lambda/\mathrm{A}_V = a_{\mathrm{CCM}}(x) + b_{\mathrm{CCM}}(x)/R_V, \tag{2.5}$$

where $a_{\mathrm{CCM}}(x)$ and $b_{\mathrm{CCM}}(x)$ are functions of wavelength ($x = 1/\lambda$) with functional forms that vary with the particular wavelength regime (i.e. IR, Optical) and $R_V \equiv \mathrm{A}_V/\mathrm{E}(B-V)$.

For the IR regime ($0.3 \leq x \leq 1.1\,\mu m^{-1}$), $a_{\mathrm{CCM}}(x)$ and $b_{\mathrm{CCM}}(x)$ are simply

$$a_{\mathrm{CCM}}(x) = 0.574x^{1.61} \tag{2.6a}$$

$$b_{\mathrm{CCM}}(x) = -0.527x^{1.61}. \tag{2.6b}$$

For the NIR and Optical regime ($1.1 \leq x \leq 3.3\,\mu m^{-1}$), $a_{\mathrm{CCM}}(x)$ and $b_{\mathrm{CCM}}(x)$ are

$$y(x) = x - 1.82 \tag{2.7a}$$

$$\begin{aligned} a_{\mathrm{CCM}}(y) = {} & 1 + 0.17699y - 0.50477y^2 - 0.02427y^3 \\ & + 0.72085y^4 + 0.01979y^5 - 0.77530y^6 \\ & + 0.32999y^7 \end{aligned} \tag{2.7b}$$

$$\begin{aligned} b_{\mathrm{CCM}}(y) = {} & 1.41338y + 2.228305y^2 + 1.07233y^3 \\ & - 5.38434y^4 - 0.62251y^5 + 5.30280y^6 \\ & - 2.09002y^7 \end{aligned} \tag{2.7c}$$

As noted in CCM89, a value of 3.1 for $R_V$ reproduces what would be expected for the diffuse interstellar medium and only starts to substantially deviate from this value in the UV regime ($\lambda < 0.303$ $\mu$ m). Since we are only considering the optical and IR regimes, $R_V = 3.1$ is used throughout this work unless, otherwise specified.

In this work, the $G$ band extinction ($A_G$) is taken as the fiducial instead of $A_V$ and this is accomplished by simply dividing Equation 2.5 by $A_G/A_V$. A figure of extinctions of all six photometric bands relative to $A_G$ can be seen in Figure 2.6. The CCM89 extinction law is included in the `dust_extinction`[4] Python package, which is used throughout this work for the actual calculation of the extinction coefficients.

Fitzpatrick Extinction Law

We make use of a second extinction law to validate the extinctions from Fitzpatrick (1999, hereafter F99). For a more detailed discussion on why F99 is used see Section 2. Also, as with CCM89, we make use of `dust_extinction` to calculate the extinction coefficients. While similar to CCM89, F99 gives slightly different results (see Figure 2.6).

Salaris Correction

Most stellar isochrone models are based on a scaled solar composition, but in actuality stars have a variety of chemical compositions. One solution that allows the use of the solar scaled isochrones for stars with a more complex composition is to shift the [Fe/H] of the isochrone based on the star's [$\alpha$/Fe] abundance. Stars that are enhanced in $\alpha$-elements will appear to have a cooler $T_{\rm eff}$ than expected. This can result in an older age being assigned to the star. Salaris et al. (1993) determined that an $\alpha$-abundance correction of the following form would fix this:

$$[\mathrm{Fe/H}]_{\rm sal} = [\mathrm{Fe/H}] + \log(a_{\rm sal} f_\alpha + b_{\rm sal}), \tag{2.8}$$

[4] `https://dust-extinction.readthedocs.io/en/stable/#`

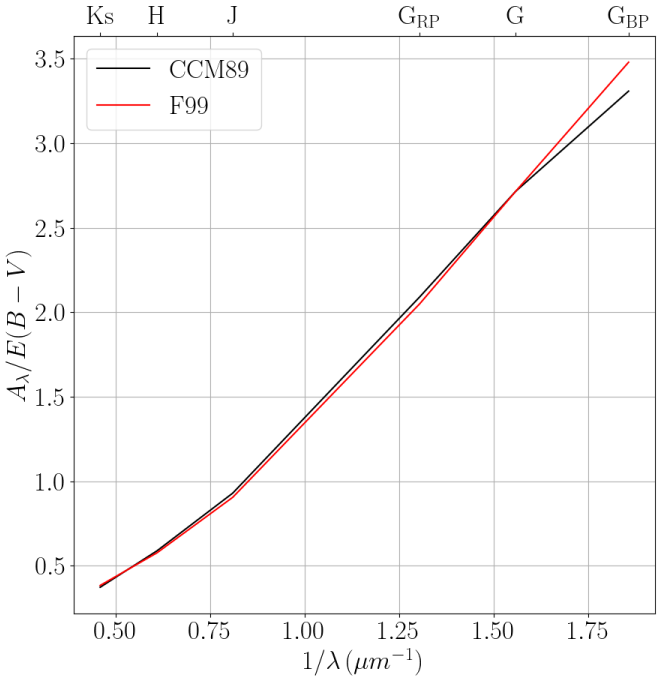



Figure 2.6: The relative extinction curve of $A_\lambda/E(B-V)$ from both CM89 and F99. The top axis shows the different photometric filters used in this work.

where [Fe/H] is the uncorrected metallicity, $a_{\rm sal}$ and $b_{\rm sal}$ are coefficients and $f_\alpha = 10^{[\alpha/{\rm Fe}]}$. The original values for $a_{\rm sal}$ and $b_{\rm sal}$ are 0.638 and 0.362, respectively (Salaris et al., 1993).

For this work we recalculate the $a_{\rm sal}$ and $b_{\rm sal}$ using the solar composition from Asplund et al. (2021). Calculating the coefficients is done using

$$a_{\rm sal} \equiv \sum_{\rm X} \left(\frac{\rm X}{\rm Z}\right) = \sum_{\rm X} 10^{\log \epsilon_X - 12.0} \frac{A_{\rm X}}{A_{\rm H}} \left(\frac{\rm Z}{\rm X}\right)_\odot^{-1} \tag{2.9a}$$

$$b_{\rm sal} = 1 - a_{\rm sal} \tag{2.9b}$$

where $\log \epsilon_X$ is the value reported in Asplund et al. (2021), $A_X/A_H$ is the atomic mass ratio of element $X$ to hydrogen from IUPAC[5] (not to be confused with the relative extinction coefficients used elsewhere in this work), and $(Z/X)_\odot$ is the Asplund et al. (2021) value of $0.0187 \pm 0.0009$. The sum is over the exact same elements used in Salaris et al. (1993) (i.e. O, Ne, Mg, Si, S, Ca). The new updated values for the correction are $a_{\rm sal} = 0.659$ and $b_{\rm sal} = 0.341$.

## Calibrations

### Effective Temperature

Having an accurate temperature for a star is critical as the calculation of ages and extinctions in Section 2 relies heavily on this value. It is also important that the observed $T_{\rm eff}$ and isochrone $T_{\rm eff}$ values agree with each other. We find that the results from our age validation sample is greatly improved when the temperatures provided by APOGEE are recalibrated and the "named" `TEFF` values are not used directly.

Here we outline how the recalibration was performed with the stars in a two step process by using PARSEC isochrones and low extinction RGB stars in the full APOGEE `allStar`

[5] `https://iupac.qmul.ac.uk/AtWt/`

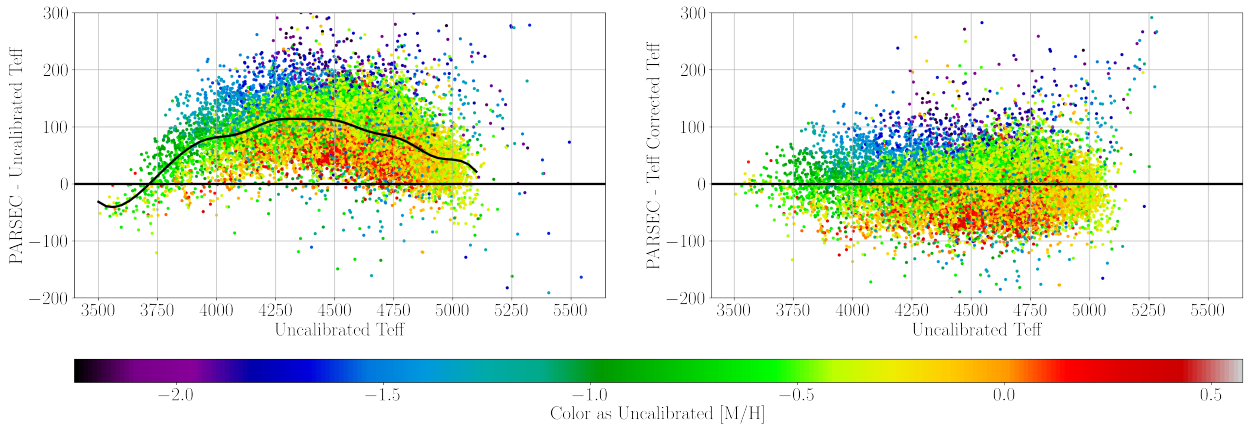



Figure 2.7: (*Left*) The residuals of the photometric and uncalibrated ASPCAP $T_{eff}$ values with the spline used to temperature correct the uncalibrated $T_{eff}$. (*Right*) The residuals after the $T_{eff}$ correction has been applied. There is a clear trend in [M/H] and so a second spline as a function of [M/H] has been applied (see the text and Figure 2.8).

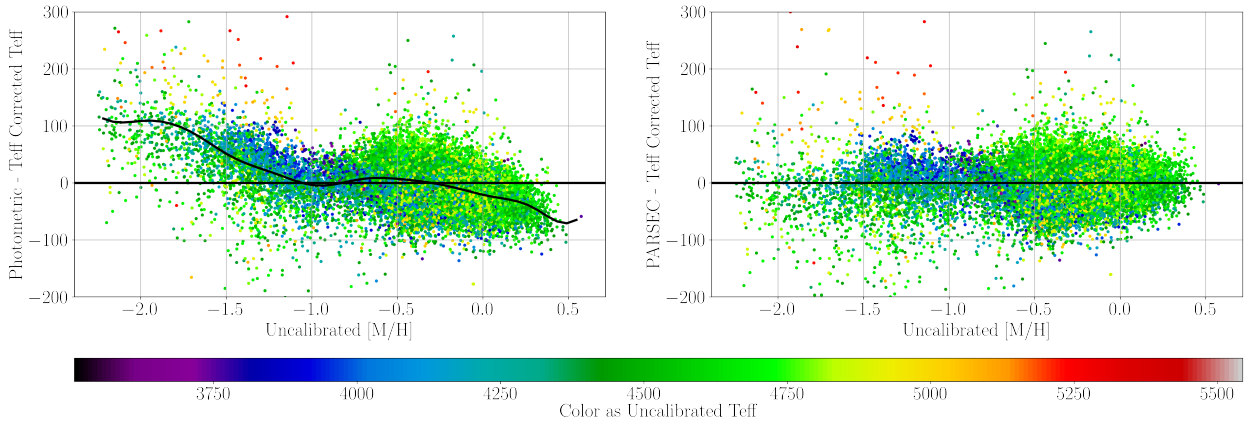



Figure 2.8: (*Left*) A plot of the residuals between the photometric and $T_{eff}$–corrected spectroscopic $T_{eff}$ values ($T_{eff}$ spline applied) with the spline used to [M/H] correct the $T_{eff}$ values. (*Right*) The residuals after the [M/H] correction has been applied. The median residual after the [M/H] has been applied is $-1.72$ K with a scatter of 23.75 K.

summary file[6]. RGB stars were used for the calibration as the LMC stars should be RGB. First, the RGB stars were selected using the criteria

- uncalibrated log(g) $< 3.5$
- uncalibrated $T_{eff} < 6000$ K

where the uncalibrated log(g) and $T_{eff}$ values can be found in the `FPARAM` column in the `allStar` file. This selection does not remove red clump (RC) stars, which were identified and removed using

- $2.38 <$ uncalibrated log(g) $< 3.5$
- [C/N] $>$ 0.04 - 0.46[M/H] - 0.0028$\cdot dT$

where

$$dT = \mathrm{Teff_{spec}} - (4400 - 552.6 \cdot (\log \mathrm{g_{spec}} - 2.5) - 324.6 \cdot [\mathrm{M/H}]) \tag{2.10}$$

where $T_{eff,spec}$, and $\log \mathrm{g_{spec}}$ are `Teff_SPEC` and `LOGG_SPEC` in the `allStar` file, respectively. These are the same RGB selection criteria from DR16 used for the $T_{eff}$ calibration (Jönsson et al., 2020). Any star with a non-zero `ASPCAPFLAG` value was removed to create a "pristine" sample of RGB stars. The pristine sample overlaps the RGB stars in both the APOKASC and the selected LMC RGB datasets in $T_{eff}$ –$\log g$ –[Fe/H].

Once the RGB stars were selected, low extinction stars were picked out such that `SFD_EBV` $\leq 0.03$, where `SFD_EBV` is the $E(B-V)$ value from Schlegel et al. (1998). In actuality, the value of the cutoff is unimportant so long as it is small so that the attenuation due to the reddening is negligible when calculating the intrinsic color for calibration. There are some regions where the Schlegel map does not give accurate values for reddening, such as the center of the LMC. It is assumed that the calibration RGB stars cover enough of the

[6] `https://www.sdss.org/dr17/irspec/spectro_data/`

sky where the Schlegel map is accurate that stars in places where this is not true can still be calibrated with the method in this section.

Even after making the necessary cuts to create a sample of RGB stars, there are still some RC stars remaining. These stars are easily removed because they do not follow the expected RGB trend in $\log g$–$T_{\rm eff}$ –[Fe/H] space.

Next, the photometric temperatures were calculated for the sample of low extinction RGB stars using the PARSEC isochrones through the following process:

1. Pick all isochrones with the Salaris corrected metallicity of the star.

2. Remove extremely old (10 Gyr $<$ age) or young ages (age $>$ 0.5 Gyr). Age in itself does not greatly impact the color–$T_{\rm eff}$ relation for the isochrones.

3. The isochrone color–$T_{\rm eff}$ relation is interpolated using a B-spline for each of the colors (i.e., $BP - G$, $G - RP$, $G - J$, $G - H$, and $G - K_{\rm s}$).

4. The "photometric $T_{\rm eff}$" for each star is then calculated using the weighted mean of the $T_{\rm eff}$ values from the individual colors.

Calibrating the $T_{\rm eff}$ values involves fitting residuals between the photometric and spectroscopic temperatures. We find the best way to calibrate the $T_{\rm eff}$ values is a two-step process. The first step is fitting a spline as a function of the uncalibrated spectroscopic $T_{\rm eff}$ values to the median residuals (photometric $T_{\rm eff}$ − uncalibrated spectroscopic $T_{\rm eff}$). In this case, the spline is fit to the binned median values. Figure 2.7 shows the $T_{\rm eff}$ residuals before and after of this first step. After this initial correction there is a trend in [M/H] that is still present and, therefore, the second step is to fit a second spline as a function of uncalibrated [M/H] to the median residuals of the photometric $T_{\rm eff}$ and the $T_{\rm eff}$–corrected spectroscopic $T_{\rm eff}$. Figure 2.8 illustrates this second step. In the end, the final photometric and calibrated spectroscopic $T_{\rm eff}$ residuals have a median of $-1.72$ K and scatter of 23.75 K.

The splines derived from fitting the residuals were then used to calculate the $T_{eff}$ values for the datasets on this work.

APOKASC Ages

The ages presented in the APOKASC catalog were derived using isochrones from the Yale Rotating Evolution Code (YREC, Pinsonneault et al., 1989; Van Saders & Pinsonneault, 2012) or the Garching Stellar Evolution Code (GARSTEC, Weiss & Schlattl, 2008) not the PARSEC isochrones as we use here. For consistency's sake, we re-derive ages for the APOKASC stars using their APOKASC-determined mass, the star's Salaris corrected metallicity, and the PARSEC isochrones using the following procedure:

1. All isochrones with the two closest metallicity values to the star's own Salaris corrected metallicity are selected.

2. For both the lower and higher metallicities, the age is interpolated as function of mass for the APOKASC-mass value of the star.

3. The ages for the lower and higher metallicites are linearly interpolated to the star's Salaris corrected metallicity giving its final age.

The calculation of the APOKASC ages using the PARSEC models and the APOKASC 3 masses versus the original APOKASC 3 ages do differ slightly. On average the re-derived APOKASC ages tend to be younger. The youngest ages remain relatively unchanged while for the oldest ages the deviation is $\sim$1.75 Gyr.

## Extinction, Age, & Mass Calculation

Extinction Calculation

Extinction is the attenuation of the flux of a star due to dust and gas between the observer and the star. This needs to be accounted for in order to produce accurate absolute

photometry as the age method described in Section 2 depends sensitively on the photometry.

An important quantity directly related to the extinction is the reddening. The reddening of a stars is the color excess due to different amounts of extinction in two different bands.

$$E(G - K_{\rm s}) = (G - K_{\rm s})_{\rm obs} - (G - K_{\rm s})_{\rm int} = A_{\rm G} - A_{\rm Ks} \tag{2.11}$$

Using the $G$ band as the fiducial, all other reddenings for each of the colors are coupled. The reddening equations than be re-framed as a linear algebra problem and solved for $A_{\rm G}$:

$$A_G = \frac{\mathbf{A}'(\lambda) \cdot \mathbf{E}(\lambda)}{|\mathbf{A}'(\lambda)|^2} \tag{2.12a}$$

$$\mathbf{A}'(\lambda) = \begin{cases} \frac{A_{BP}}{A_G} - 1 & \text{if } \lambda = BP \\ 1 - \frac{A_\lambda}{A_G} & \text{if } \lambda \neq BP \end{cases} \tag{2.12b}$$

$$\mathbf{E}(\lambda) = \begin{cases} E(BP - G) & \text{if } \lambda = BP \\ E(G - \lambda) & \text{if } \lambda \neq BP \end{cases} \tag{2.12c}$$

where the $\frac{A_\lambda}{A_{\rm G}}$ can be found using an extinction law such as CCM89, and the components of $\mathbf{E}(\lambda)$ are the reddenings for each color.

The intrinsic color of a star can be found by interpolating isochrones with the following process:

1. Pick isochrones with the Salaris corrected [Fe/H] of the star.
2. Select all isochrone points with a temperature within 200 K of the star's $T_{\rm eff}$.
3. The isochrone colors for $BP - G$, $G - RP$, $G - J$, $G - H$, and $G - K_{\rm s}$ are interpolated as functions of temperature using a B-spline.
4. Plugging in the $T_{\rm eff}$ value of the star gives the expected intrinsic value for each of four

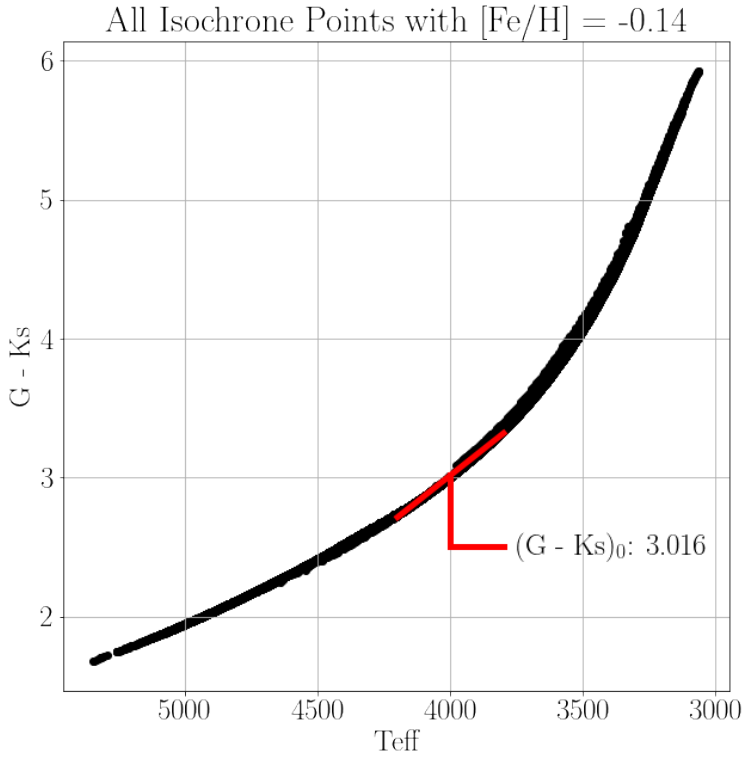



Figure 2.9: An example of how the intrinsic colors are determined from the isochrone photometry–$T_{eff}$ relations.

colors previously mentioned and reddening is found. A pictorial example of calculating the $G - K_s$ intrinsic color can be seen in Figure 2.9.

Once $A_G$ is calculated for a star, the chosen extinction law is used to calculate the extinction for all the other bands. The age of a star has a negligible effect on the color–$T_{eff}$ relationship, therefore, it is not considered when determining the extinction.

Age Calculation

The age of a star can be determined by comparing the observed photometric and spectroscopic parameters to stellar isochrones. Specifically, the absolute multiband photometry is the most sensitive parameter to age. Given a star's $T_{eff}$ and Salaris-corrected [Fe/H], we compare the observed multiband absolute magnitudes and surface gravity to the

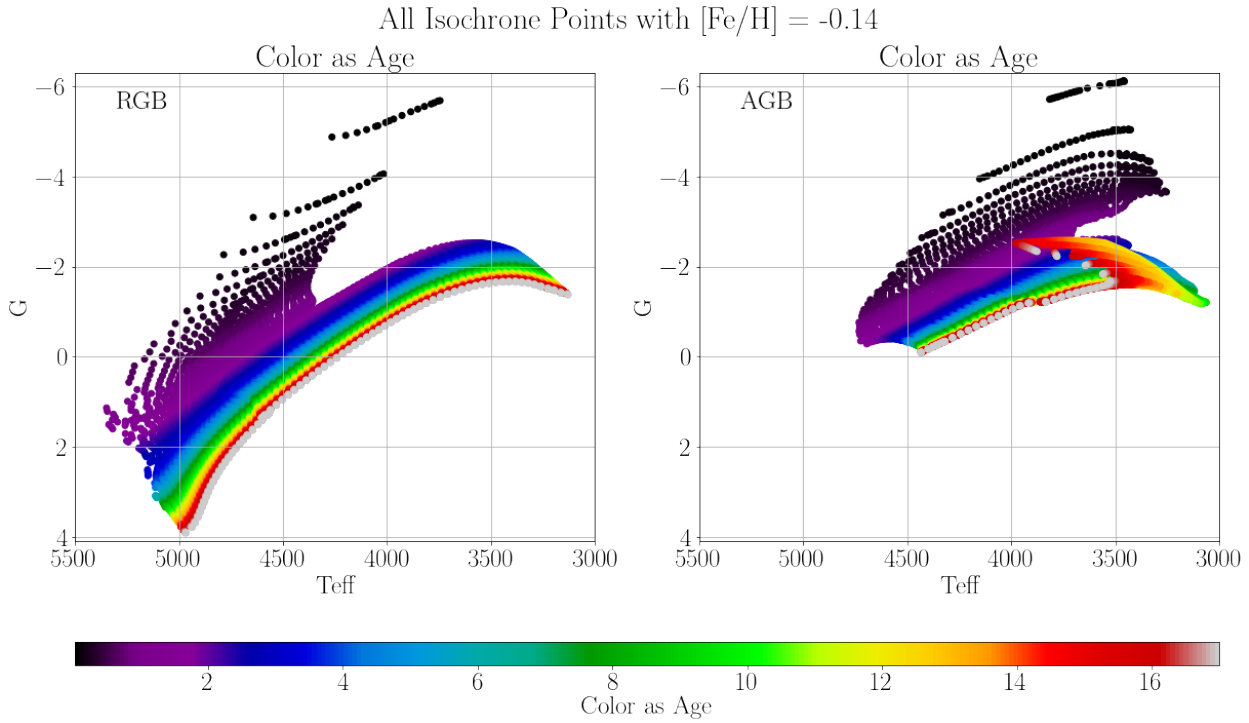



Figure 2.10: (*Left*) The $G$–$T_{\rm eff}$ relationship for [Fe/H] $= -0.14$ for the RGB isochrone points. There is a lot of degeneracy in the magnitude–$T_{\rm eff}$ relation, but clearly broken with age. This is the basis for using the interpolations in Section 2 to get the ages. (*Right*) The same as the left panel, but for the AGB isochrone points. The AGB points mostly cover the gap in the RGB isochrone points between the young branch the rest of the points.

isochrones to determine age.

Interpolated Isochrone Parameters Within our isochrone grid, which is finely-sampled in [Fe/H] and age, we must interpolate a number of properties both "along" the isochrone (i.e., in mass) or between the grid points (in [Fe/H] and age). The PARSEC isochrones provide an `int_IMF`[7] column which is the indefinite integral of the IMF (initial mass function) by number from zero to the current mass. The difference in `int_IMF` between two neighboring isochrone points ($\Delta$`int_IMF`) provides the number of stars occupying that isochrone segment (or stellar mass) per unit mass of the total initial stellar population. For our purposes,

[7]Previously called `FLUM`.

$\Delta$`int_IMF` essentially gives the expected number of RGB versus AGB stars or their relative probability. More information about why $\Delta$`int_IMF` is important see Section 2.

The isochrone absolute magnitudes, $\log g$, and $\Delta$`int_IMF` for a given age are interpolated through the following process:

1. Pick all isochrone points with the Salaris-corrected [Fe/H] of the star regardless of age.

2. Determine an initial guess for the age by calculating $\chi^2$ using $BP$, $G$, $RP$, $J$, $H$, $K_\mathrm{s}$, $T_\mathrm{eff}$, and $\log g$ (see Eq. 2.13) for all selected isochrone points and picking the one with the lowest $\chi^2$ value.

3. Determine the closest two adjacent ages of the initial guess age. If no isochrone points exist for the chosen age and [Fe/H], then pick the next closest age.

4. Remove all isochrone points outside a specified $T_\mathrm{eff}$ range as these points should not affect the interpolations. For most stars this amount to keeping isochrone points within 200 K of the measured $T_\mathrm{eff}$ of the star.

5. For each of the two ages the $T_\mathrm{eff}$–magnitude relationship for each band, $T_\mathrm{eff}$–$\log g$, and $T_\mathrm{eff}$–$\Delta$`int_IMF` relationships are used to interpolate these quantities for the star's observed $T_\mathrm{eff}$.

6. Finally, the two sets of interpolated isochrone quantities are linearly interpolated in age for the desired age.

Normally, the $T_\mathrm{eff}$–magnitude relationship for any given [Fe/H] exhibits a large degeneracy. However, this degeneracy can be broken with age as seen in Figure 2.10. This work exploits this to obtain the age of a star because the photometry and $T_\mathrm{eff}$ are known. Also the boundary between the RGB and AGB phases can be blurred due to uncertainty in the $T_\mathrm{eff}$ or magnitude values of a star as well as the close proximity of RGB and AGB

isochrone points. The overlap is illustrated in Figure 2.10. This means that it is possible either RGB or AGB isochrones points could potentially describe a star due to overlap and the true evolutionary phase of a star is uncertain (see Figure 2.10).

If the age is considered a free parameter, then it can be found by fitting the isochrone absolute magnitudes, and $\log g$ and matching to the observed absolute magnitudes and surface gravity. To accomplish this we make use of `scipy.optimize.curve_fit` (hereafter `curve_fit`). We limit the maximum number of iterations in `curve_fit` to 5000.

The best age is determined by looking at the $\chi^2$ value for the final photometry and $\log g$ determined by `curve_fit`. Here the $\chi^2$ value is calculated by

$$\chi^2 = \sum_{\lambda} \left( \frac{m_{\lambda,\mathrm{iso}} - m_{\lambda,\mathrm{obs}}}{\sigma_{\lambda,\mathrm{obs}}} \right)^2 + \left( \frac{\log g_{\mathrm{iso}} - \log g_{\mathrm{obs}}}{\sigma_{\log g,\mathrm{obs}}} \right)^2, \tag{2.13}$$

where $m_{\lambda,\mathrm{iso}}$ is the isochrone apparent magnitude for the $\lambda$ band (i.e., $BP$, $G$ $RP$, $J$, $H$ or $K_\mathrm{s}$), $m_{\lambda,\mathrm{obs}}$ is the observed apparent magnitude, and $\sigma_{\lambda,\mathrm{obs}}$ is the measured uncertainty in the observed $\lambda$ band magnitude. The second term is the $\log g$ contribution to the $\chi^2$ where $\log g_{\mathrm{iso}}$ is the value predicted from the isochrone interpolation, $\log g_{\mathrm{obs}}$ is the observed surface gravity, and $\sigma_{\log g,\mathrm{obs}}$ is the uncertainty in the observed value of the surface gravity. The additional $\log g$ term in $\chi^2$ produces improved fits and uses all of the observed information.

Mass Calculation

The mass and age of a star are highly anti-correlated on the RGB, which means it is generally straightforward to calculate the mass of a star if its age is known and vice versa. There is a slight degeneracy in the age-mass relationship that is broken with [Fe/H], which is a known quantity for our stars. At an age of 10 Gyr the isochrones mass can vary up to about $\pm$ 0.28 $\mathrm{M}_\odot$ and at an age of 1 Gyr the isochrones mass can vary up to about $\pm$ 0.33 $\mathrm{M}_\odot$. To determine the mass for a star, it is interpolated as a function of age for a given Salaris-corrected [Fe/H].

Evolutionary Phase Weighting

While most of the stars in our sample are RGB stars, there should also be a small amount of "contamination" from other phases of evolution such as the AGB. The tip of the APOGEE RGB (TRGB) selection is at a magnitude of $H$ ∼12.35, but there can be overlap between the AGB and RGB regions in color magnitude space close to this magnitude (Nidever et al., 2020). Figure 2.10 shows [Fe/H]=−0.14 isochrones in the $G$–$T_{eff}$ plane for a range of ages. Only the RGB phase is displayed in the left panel which shows a sizeable gap between the older ages (> 1.0 Gyr) and very young ages ($\lesssim$ 1 Gyr). There are stars in our APOGEE sample that fall in that gap. As can be seen in the right panel, this gap is "filled" with the AGB phase with some overlap with the RGB. Since there is no easy way to separate the RGB and AGB stars in our sample, we take a weighted sum between the ages calculated for RGB and AGB points.

This phase weighting is done through the following process:

1. The age and mass for each star is calculated for each phase (RGB and AGB) separately without allowing for extrapolating outside the specified $T_{eff}$ range as described in Sections 2 and 2.

2. If a star is covered by only one phase, then that age and mass are used. If a star is covered by both phases, then the mean of the RGB and AGB mass and age values are calculated weighted by each phase's $\Delta$`int_IMF`.

3. If neither phase covers the star within the specified $T_{eff}$ range, then the code is allowed to extrapolate up to a limit of 200 K. A star is assigned a "bad" value if it is beyond this 200 K extrapolation limit.

$\Delta$`int_IMF` represents the number of stars in a 1 solar mass total stellar population between the two points of the integrated IMF (`int_IMF`). This can be thought of as a the probability of detecting a star in this phase.

The `int_IMF` is provided as part of the isochrone table from PARSEC and we use the Kroupa IMF (Kroupa, 2001; Kroupa, 2002). The $\Delta$`int_IMF` is chosen for the weighting factor as it naturally encodes the fact that there should be more RGB stars compared to AGB stars.

## APOKASC Validation

We use the APOKASC dataset to validate and calibrate our ages since it has highly accurate asteroseismic ages and uses an independent technique. The method used by APOKASC to derive ages relies on calculating the mass using temperature and asteroseismic scaling relations to obtain a measured surface gravity with APOGEE [M/H] and [$\alpha$/M]. An evolutionary track is then used for the corresponding mass, [M/H] and [$\alpha$/M]. The age of a star is then found by determining the point on the evolutionary track that has a $\log g$ value equal to the asteroseismic $\log g$. While the APOKASC method does rely on measured APOGEE DR16 (Ahumada et al., 2020) values of $T_{\rm eff}$, [M/H], and [$\alpha$/M], the rest of the method is completely independent. This method applies to the APOKASC 3 ages in the `A3P_AGEMOD_JT` column. For more on previously calculated ages included with the APOKASC catalog, which may rely on slightly different methods, please see Serenelli et al. (2017) or Pinsonneault et al. (2018).

### APOKASC Extinctions

Accurate photometry is required to calculate the age of a star and, therefore, is important that the star's extinction is well-determined. The APOGEE catalog includes the Schlegel et al. (1998) $E(B-V)$ value for every star. We follow Schlafly et al. (2010) in

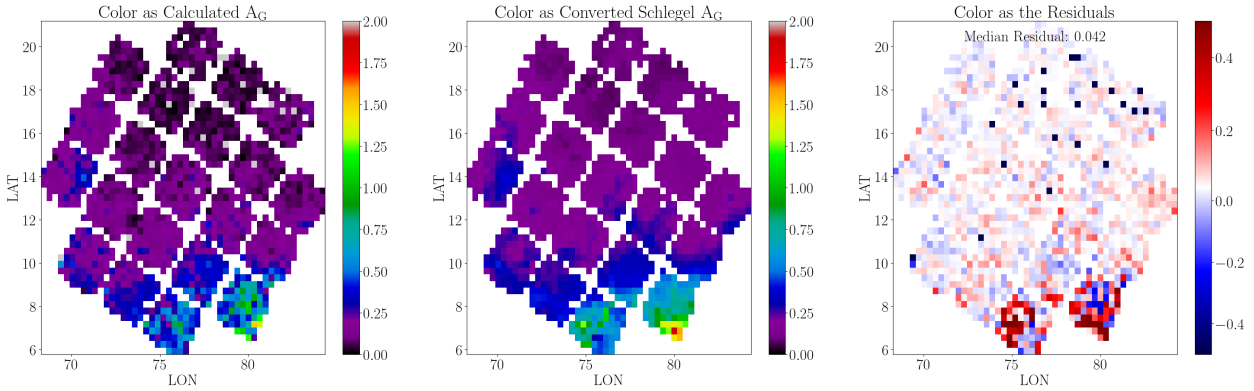



Figure 2.11: (Left) $A_G$ extinction map converting the Schlegel et al. (1998) reddening values using Schlafly et al. (2010) and Fitzpatrick (1999). (Center) $A_G$ map using the values calculating using the method in this work. (Right) The residuals between the Schlegel and calculated $A_G$ values with a median residual of 0.043 mag.

converting the Schlegel reddening values to extinctions for any band with a correction factor:

$$A_\lambda = \begin{cases} 0.78/1.32 \times E(B-V)_{\rm SFD} \times \frac{\rm F99(\lambda)}{\rm F99(1\mu m)} & \text{if } E(B-V) > 1 \\ 0.78 \times E(B-V)_{\rm SFD} & \text{if } E(B-V) < 1 \end{cases} \tag{2.14}$$

where $E(B-V)_{\rm SFD}$ is the Schlegel reddening value, F99($\lambda$) is the value of the Fitzpatrick (1999) extinction law for the $\lambda$ band and F99($1\mu m$) is the Fitzpatrick (1999) extinction law value for a wavelength of 1 $\mu$m.

Comparing the $A_G$ expected from Schlegel et al. (1998) to the calculate $A_G$ in Figure 2.11 shows good agreement with a slight offset of about 0.043 mag. The part of the Kepler field nearest the MW plane tends to agree less well than the rest of the field. However, this is a good validation of the extinction values derived from our method.

APOKASC Ages

While our derived ages rely on using the PARSEC isochrones, the APOKASC method did not use PARSEC models in their calculations to convert mass to age. This means that

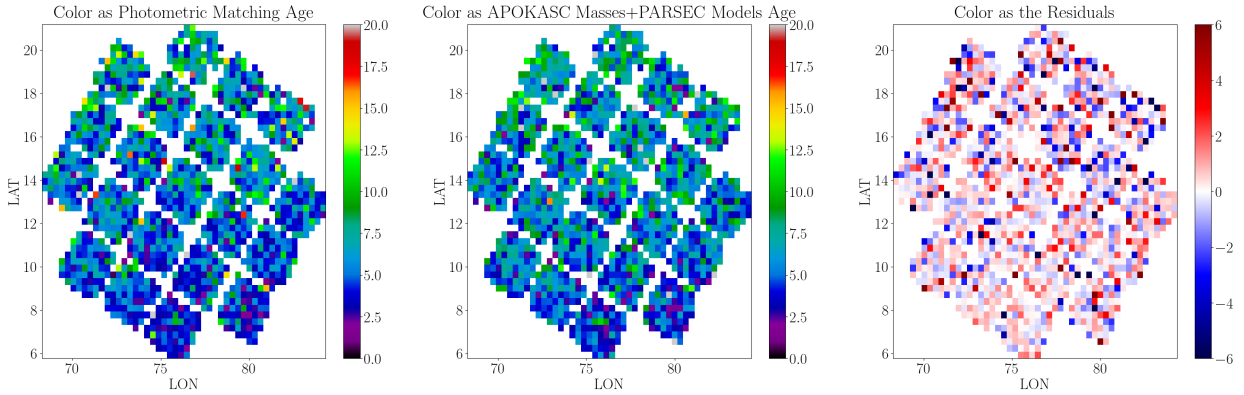



Figure 2.12: (Left) Age map of the Kepler field using APOKASC 3 masses and PARSEC isochrones. (Center) Age map of the Kepler field calculated using our method described in Section 2. (Right) The residuals between the methods with a median residual of 0.2 Gyr.

a direct comparison of our ages to the APOKASC catalog ages might have discrepancies because of the use of different models. Instead, we use the Salaris-corrected [Fe/H] and the APOKASC mass to determine the ages by interpolating the PARSEC isochrones. This is very similar to the mass calculation described in Section 2, but essentially in reverse. From now on, we shall call these ages derived from the APOKASC mass and PARSEC isochrone the "APOKASC ages".

Comparing the APOKASC ages and our ages calculated through the photometric matching process described in Section 2 shows quite good agreement. Figure 2.12 shows the spatial map of the Kepler field ages from the two methods as well as the difference. Visually, the maps look very similar and the right panel showing that the residuals have an average close to zero, as desired.

A direct one-to-one comparison of the APOKASC ages against our ages shows more clearly how well the two methods agree (see Figure 2.13). Overall, the locus of the stars in the 2D histogram is very close to the one-to-one line. Ages under 10 Gyr typically agree better and especially under ∼8 Gyr. This is not unexpected as older ages have larger uncertainties because the isochrones tend to stack up on each other in color–magnitude space. A curious

feature is the upturn that happens for APOKASC ages older than about 10 Gyr. While we have investigated various causes for this systematic behavior, its origin remains unclear. This is not as bad as it seems, because there are few stars older than 10 Gyr. However, it does cause a larger spread of our oldest ages.

As for systematic uncertainties, we find that the dispersion in the residuals is ∼1 Gyr for younger stars and then increase linearly up to about 3 Gyr for older stars close to the age of the universe. This is a roughly ∼20% age uncertainty.

APOKASC Masses

The mass and age of a star can be related through the mass-age relation. As another check this relation can be use to validate the ages. If the ages are correct then the masses calculated should match closely to the APOKASC catalog mass. After calculating the masses using Section 2, the mass-to-mass plot in Figure 2.14 shows good agreement. The locus of the stars in that plot match very well with the 1-to-1 black line. The number of stars in each bin quickly fall off moving from the line. The derived mass calculated from the photometric matching method appear to be slightly higher than APOKASC 3 values. Nonetheless, this is a reassuring result and suggests that the age calculation method in Section 2 works well.

## Bias Correction

There are a number of biases in our dataset that need to be corrected for to obtain reliable age-related measurements. There are two main biases that we correct for: (1) the targeting selection function, and (2) the number of expected RGB and AGB stars in our target selection box as a function of age and metallicity.

In general, one is not able to spectroscopically target and observe all of the stars in a given target selection category. This was also the case for the APOGEE-2S Magellanic Cloud fields. Our main goal was to obtain an integrated S/N=100 (over all visits) for a given star.

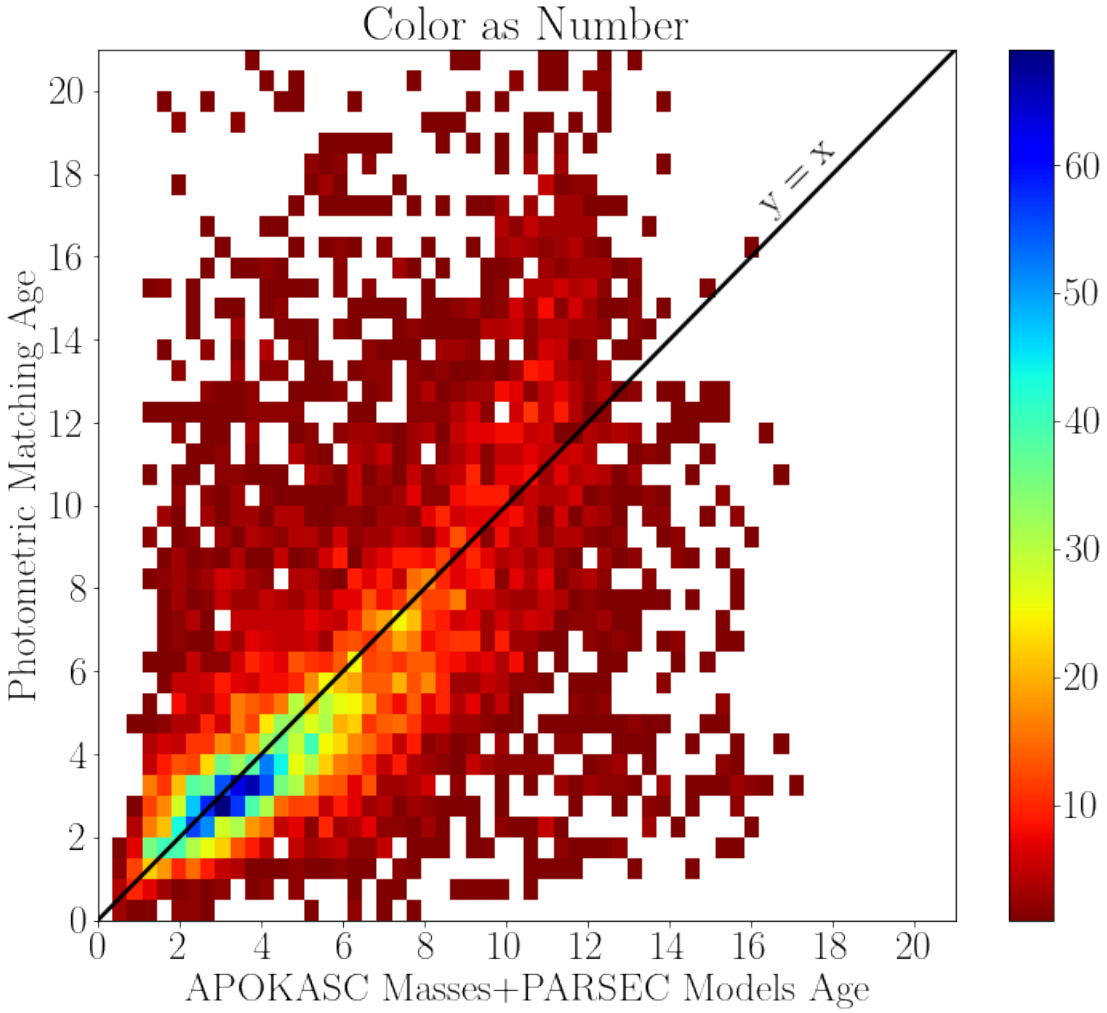



Figure 2.13: An age-to-age plot comparing the ages derived using the APOKASC masses and PARSEC models and ages derived using the photometric matching described in Section 2 for the APOKASC validation set colored by the number of stars in each bin. To help guide the eye the 1-to-1 line has been overplotted in black. It is clear especially for younger stars that the photometric matching ages tend to be slightly younger, though overall there is quite good agreement.

The LMC fields were allotted nine × ∼1 hour visits which meant that the S/N=100 could be achieved for H≤12.8 stars. Therefore, the main RGB targeting category (`BrtRGB`) was from $H$=12.0, the nominal tip of the RGB, to $H$=12.8. In the inner fields, there were many more `BrtRGB` targets than could be accommodated by the APOGEE spectrograph (∼250 science targets per plate). This required us to select a subset of the targets which was accomplished by randomly drawing 260 stars (allowing for a small buffer to account for fiber "collisions").

In the outer fields, with lower stellar density, there were often less than 260 targets in the `BrtRGB` box, and, therefore, fainter targets (`FntRGB`) were included to fill the shortfall. The faint limit was extended only as faint as was needed to fill the 260 number of targets. Therefore, the faint limit in the outer fields varies from field to field and extends in some cases to $H$=15.3. For each field we calculate an average "selection function" which is calculated as

$$\text{Selection Function} = \frac{N_{\text{potential targets}}}{N_{\text{observed targets}}} \tag{2.15}$$

For consistency and simplicity across all fields, we use $N_{\text{potential targets}}$ for all targets down to $H$=15.3. The outer fields have selection function values near unity, while the inner fields have very large values indicating that only a small fraction of the potential targets were observed.

From stellar evolution models we know that the number of RGB stars in a given magnitude range of a stellar population is not constant but varies systematically with age and metallicity. This adds a separate "astrophysical" bias, which is especially important when using age histograms, because variations are expected even if the star formation history is constant. We correct for this bias by calculating the number of stars expected in our target selection boxes for a given age and metallicity, $N_{\text{stars}}$([Fe/H],Age), using synthetic photometry generated from PARSEC isochrones. We use a total stellar population of $10^8$ $M_\odot$ and the RGB, horizontal branch, and AGB evolution stages. As described above, the

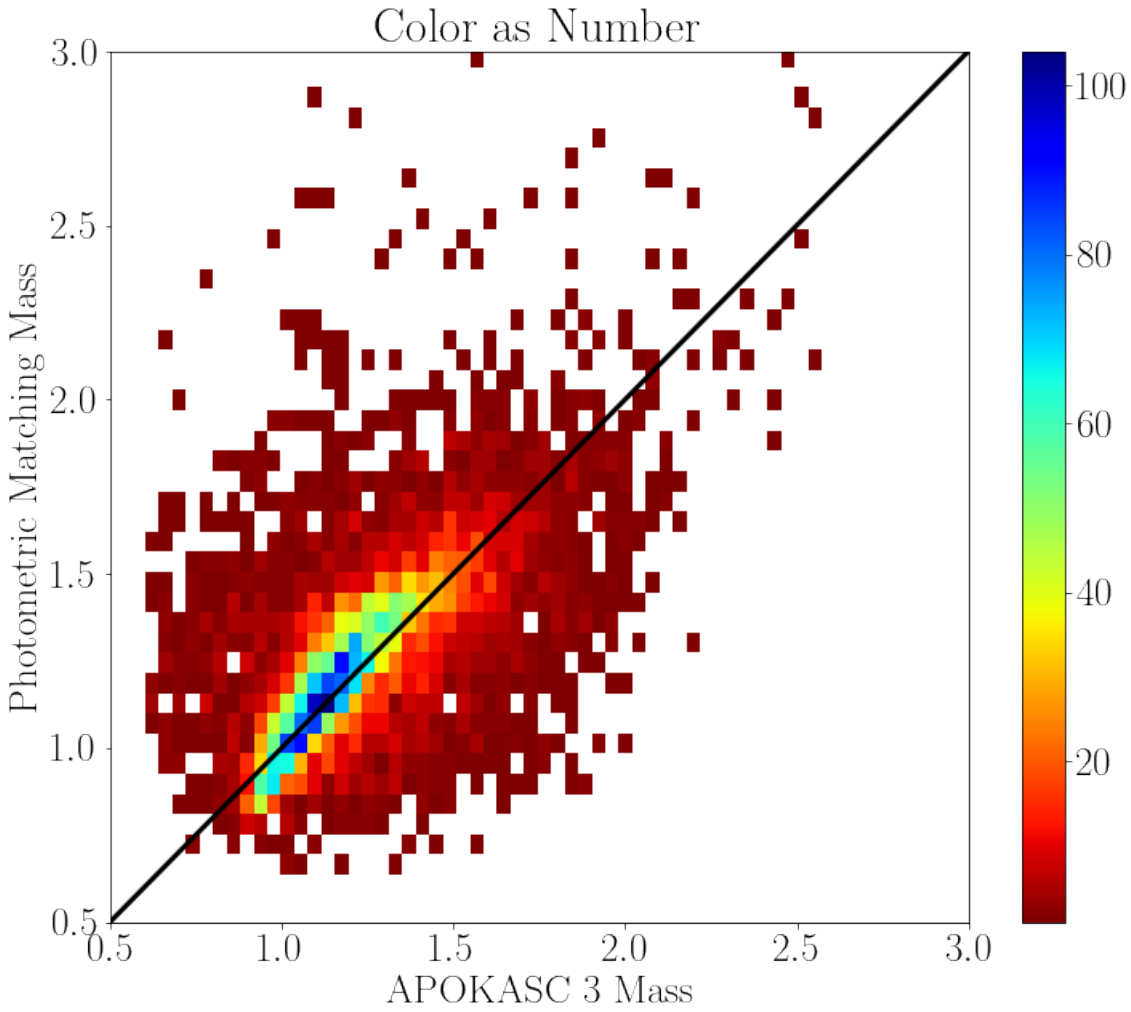



Figure 2.14: Comparing the APOKASC 3 masses to the masses calculated using Section 2.

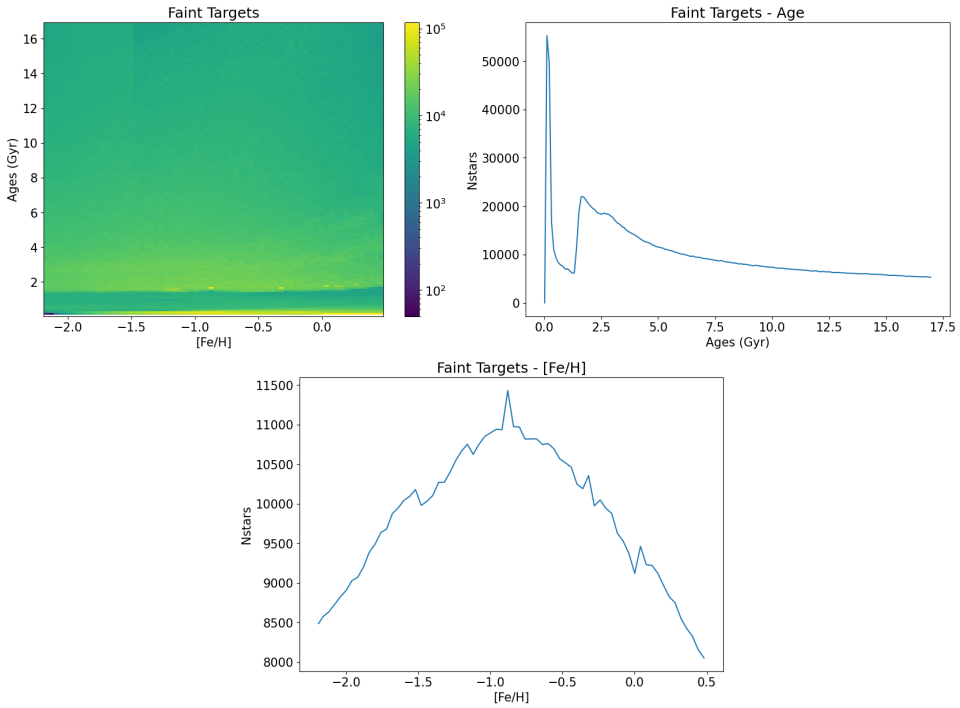



Figure 2.15: (*Left*) Number of stars in the target selection box for a stellar population of $10^8$ $M_\odot$ , as a function of age and metallicity. There are regions of parameter space (e.g., old, metal-poor), where no stars are expected to be observed. (*Middle*). Number of stars in the target selection box for a stellar population of $10^8$ $M_\odot$ , averaged over metallicity and showing the age dependence. There is a sharp peak around 0.15 Gyr, and a "valley" at 0.3–1.5 Gyr. (*Right*) The same, but averaged over age and showing the metallicity dependence.

PARSEC $\Delta$`INT_IMF` value is used to ascertain the number of synthetic stars to produce along the isochrone. The left panel of Figure 2.15 shows the number of stars falling in the target selection box as a function of metallicity and age while the middle and right panels show average values for age and metallicity, respectively. A substantial amount of structure is seen for younger ages, with a peak at $\sim$0.15 Gyr and a "valley" for 0.3–1.5 Gyr. These are significant biases that need to be accounted for.

For a given star, we want to determine the amount of stellar population mass ($M_{\rm SP}$) that this star "represents". We convert our number of stars in the target selection box as a function of age and metallicity, $N_{\rm stars}$([Fe/H],Age), into a stellar population mass by taking the total stellar mass ($10^8$ $M_\odot$) used to generate our synthetic photometry (described in the previous paragraph) and dividing by the expected number of stars in the target selection box:

$$M_{\rm SP}({\rm [Fe/H],Age}) = \frac{10^8 M_\odot}{N_{\rm stars}({\rm [Fe/H],Age})} \tag{2.16}$$

Note, that our synthetic photometry did not distinguish between RGB or AGB stars but just counted all stars falling into our target selection box. This deals nicely with the evolutionary phase ambiguity mentioned above.

When determining $M_{\rm SP}$ for a given star, we take into account the uncertainty in its age and metallicity by using a "measurement" probability distribution function ($P_{\rm meas}$([Fe/H],Age)) unique for each star and represented as a 2-D Gaussian:

$$P_{\rm meas}({\rm [Fe/H],Age}) = \mathcal{N}([{\rm Fe/H}]_0, \sigma_{\rm [Fe/H]}) \times \mathcal{N}({\rm Age}_0, \sigma_{\rm Age}) \tag{2.17}$$

where $\mathcal{N}()$ is the normalized Gaussian distribution. In addition, we can use $N_{\rm stars}$([Fe/H],Age) itself as a probability distribution function, i.e. a prior. Regions of higher values indicate that we are more likely to detect stars there than regions where the values are low or zero. We convert our distribution of number of stars into a probability by simply normalized

$N_{\rm stars}$([Fe/H],Age)

$$P_{\rm stars}([Fe/H], Age) = \frac{N_{\rm stars}([\rm Fe/H],\rm Age)}{\sum N_{\rm stars}([\rm Fe/H],\rm Age)} \tag{2.18}$$

We use this information to produce a "joint" PDF by taking the product of the two PDFs.

$$P_{\rm joint}([\rm Fe/H],\rm Age) = P_{\rm meas}([\rm Fe/H],\rm Age) \times P_{\rm stars}([\rm Fe/H],\rm Age) \tag{2.19}$$

The final $M_{\rm SP}$ value for a given APOGEE star is then calculated by taking a weighted mean of $M_{\rm SP}$([Fe/H],Age) with the joint PDF. Since the faint limit of the `FntRGB` target selection box varies from field to field, we calculated the number of stars in the `FntRGB` box for 0.1 mag intervals from 12.8 to 15.3. Finally, the $M_{\rm SP}$ value is multiplied by the "selection function" (from the first step) to calculate the final selection function-corrected "stellar population mass" $M_{\rm SP,SF}$ value for one of our stars. This is the value that is used for "weighting" in many of the following calculations.

## Results

### The LMC Extinction Map

The $G$ band extinction map for the LMC can be seen in Figure 2.16. Interestingly there appears to be a band in the northern part of the LMC with low extinction for radii between $\sim$2 kpc and $\sim$6 kpc. This contrasts the southern part and center of the galaxy especially for the western side which is closest to the Small Magellanic Cloud (SMC).

### The LMC Age Map, Age-Radius Relation, & Age Distribution

The 2-D median age map of the LMC shows that the center of the galaxy tends to be slightly younger than the outskirts with a wide range of values for the age dispersion (see Figure 2.17). A clear trend is evident in the age uncertainties, where older ages typically have larger uncertainties. The age uncertainties are calculated using standard error propagation

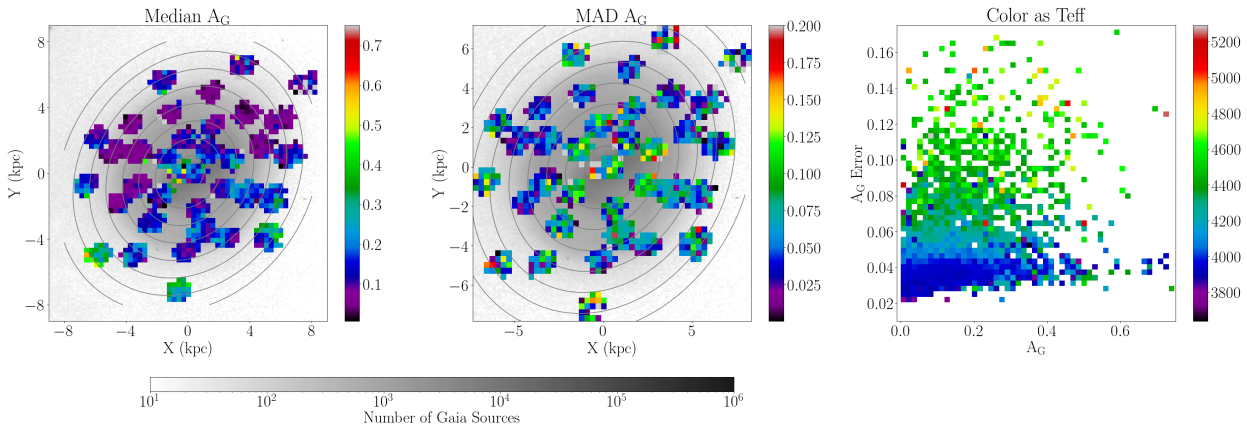



Figure 2.16: (*Left*) The $G$ band extinction map for the LMC with the Gaia source number density in the background. In the map there is clearly a band of low extinction between ∼2 to ∼6 kpc in the north. (Center) The dispersion in extinction for each of the bins using MAD also with the Gaia background. (*Right*) The extinction errors as a function of the extinction colored by the $T_{eff}$ of each star. There is a definite correlation between the $T_{eff}$ of a star and calculate extinction error probably due to the steepness in the color–teff relations.

techniques and interpolated splines. The uncertainties shown in the left panel of the age map. It is obvious that these uncertainties suggest great accuracy in the ages. When validating ages, Figure 2.13 shows that most stars fall within 10% of the 1-to-1 line reinforcing the accuracy in the LMC ages. But regardless the derived uncertainties for the LMC ages should be considered lower limits as they are statistical uncertainties and other systematic sources of uncertainties could contribute. Some uncertainties of the LMC stars appear to be very close to 0 Gyr. For these stars it is probably best to impose a minimum uncertainty of ∼2.5%. This estimation is based on clear envelop that can be seen in the left panel of Figure 2.17.

To gain another perspective on the spatial distribution of stars, we look at the age-radius relation for the median age for each field. Fitting a quartic function to the median field ages gives:

$$\text{age} = -0.03159r^4 + 0.4015r^3 - 1.443r^2 + 1.603r + 5.452 \tag{2.20}$$

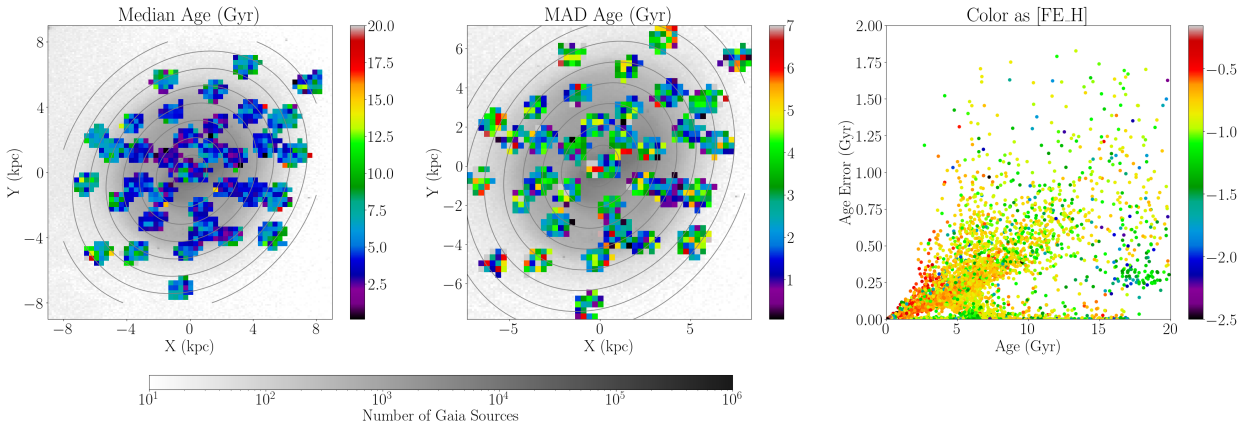



Figure 2.17: (*Left*) The age map for the LMC with the Gaia source number density in the background. (*Center*) The dispersion in age for each of the bins using MAD also with the Gaia background. (*Right*) The age errors as a function of the age colored by the [Fe/H] of each star. Most derived LMC have uncertainties that are <10% suggesting great accuracy. There is a band of stars with uncertainties that appear to approach zero, but based on the visible envelop, the best course of action is to inflate any errors for these stars to at least 2.5%.

where $r$ is the elliptical radius given by Equation 2.4. Quartic functions were chosen as visually the field points and the trends matched best without going to a higher order. A plot of the age-radius relations can be seen in Figure 2.18. In the left panel, the nonlinearity is clearly evident.

The age map suggests that young ages are widespread, but more centrally located. The top panel of Figure 2.19 shows the age distribution of individual stars and indicates that there are substantially more young stars, though this could be misleading. Using the bias correction and stellar population mass calculation from Section 2 shows that the corrected-age distribution is somewhat different (see the bottom panel of Figure 2.19). The first noticeable feature of the corrected distribution is the recent increase in stellar population mass (or star formation rate) consistent with many of the other results. Second, there is a wide peak or plateau for ages ∼3 Gyr to ∼7 Gyr.

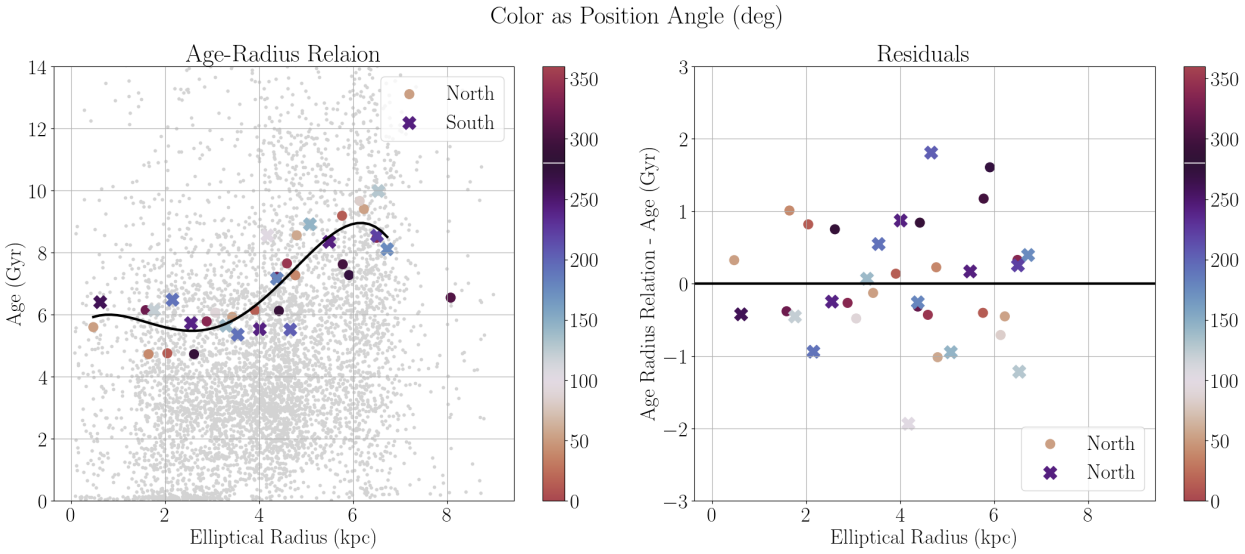



Figure 2.18: (*Left*) The age-radius relation for the LMC represented with the black solid line (see Equation 2.20). Individual LMC stars are shown in the background as light grey dots. The median ages for each of the LMC fields are overplotted as dots and xs colored in function of position angles. Northern fields are represented by dots while southern fields are represented by xs. It is clear that for inner radii that the northern fields are slightly younger than the southern fields at corresponding radii. (*Right*) The residuals of the quartic function fit. The MAD of the residuals is -0.19 for the clusters compared to 2.17 for the individual stars.

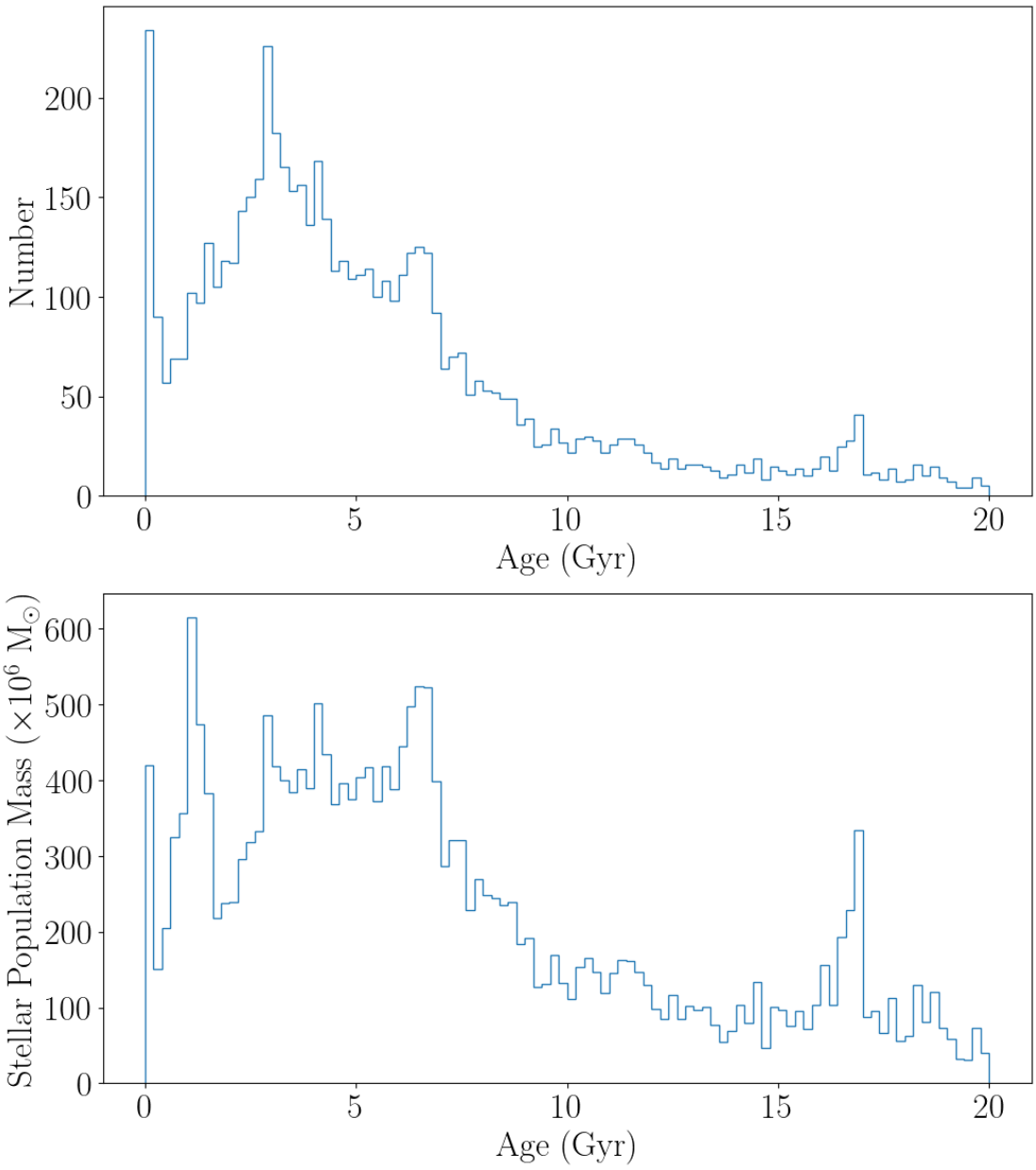



Figure 2.19: (*Top*) A histogram of the ages calculated for the individual stars in the sample. The peak at 0 Gyr is made mostly of blue loop stars with some potentially bad results where stars could be assigned younger ages than they should be. The peaks less than 10 Gyr may suggest different star forming events while the peak at ∼17 corresponds to the age of the oldest isochrone. (*Bottom*) A histogram showing the stellar population mass corresponding to the calculated ages corrected for the bias according to Section 2. The first two peaks in the plateau between ∼2.5–5.0 Gyr do not appear to be temporally separated, but the third peak is. The supposed separation between the first two peaks may be an unphysical artefact.

The LMC Age-Metallicity Relation

In Figure 2.20, the age-metallicity relation (AMR) is fairly flat between 5 and 15 Gyr. Anything younger than 5 Gyr tends to show increasing metallicity with a rapid increase for stars with ages $\lesssim$2 Gyr, most likely related to the close interaction between the Clouds mentioned before. When comparing the AMR to LMC clusters from Harris & Zaritsky (2009) (hereafter, HZ09), we find that the younger clusters tend to agree better than the older ones. Notably, the older clusters do bunch up at the age of the universe, but do not follow the AMR derived in this work.

Asymmetric Drift

We briefly investigated the LMC's kinematics as a function of our derived ages by assuming that all of our stars lie in the LMC disk plane, and applying the disk kinematic and geometric model from Choi et al. (2022) to derive the velocity components $v_\phi$, $v_r$, $v_z$, and their associated errors, from our measured proper motions and line-of-sight velocities. Figure 2.21 shows the mean values of the velocity components and their dispersions as a function of age, where we have restricted the sample to include only those stars with age<15 Gyr, velocity errors <15 km s$^{-1}$ in $v_\phi$ and $v_r$, errors <7.5 km s$^{-1}$ in $v_z$, and in-plane radius $R$ >3 kpc; the limit on the radius is to ensure that we sample only the flat portion of the rotation curve.

As seen in the figure, the mean $v_z$ is close to 0 at all ages, while its associated dispersion rises from <20 km s$^{-1}$ at the youngest ages to nearly 30 km s$^{-1}$ at 10 Gyr and beyond. This is expected behavior for a population that is dynamically heated over time. The mean $v_r$ is also small at all ages, but slowly increasing with larger age to a value of $\sim$8 km s$^{-1}$ beyond 10 Gyr. The dispersion in $v_r$ also grows with age, from $\sim$25 km s$^{-1}$ at 2.5 Gyr to $\sim$35 km s$^{-1}$ at 10 Gyr. As we also see some correlation between $v_r$ and azimuthal angle, the small but positive $v_r$ may be a sign that the disk inclination changes in the periphery, where older stars

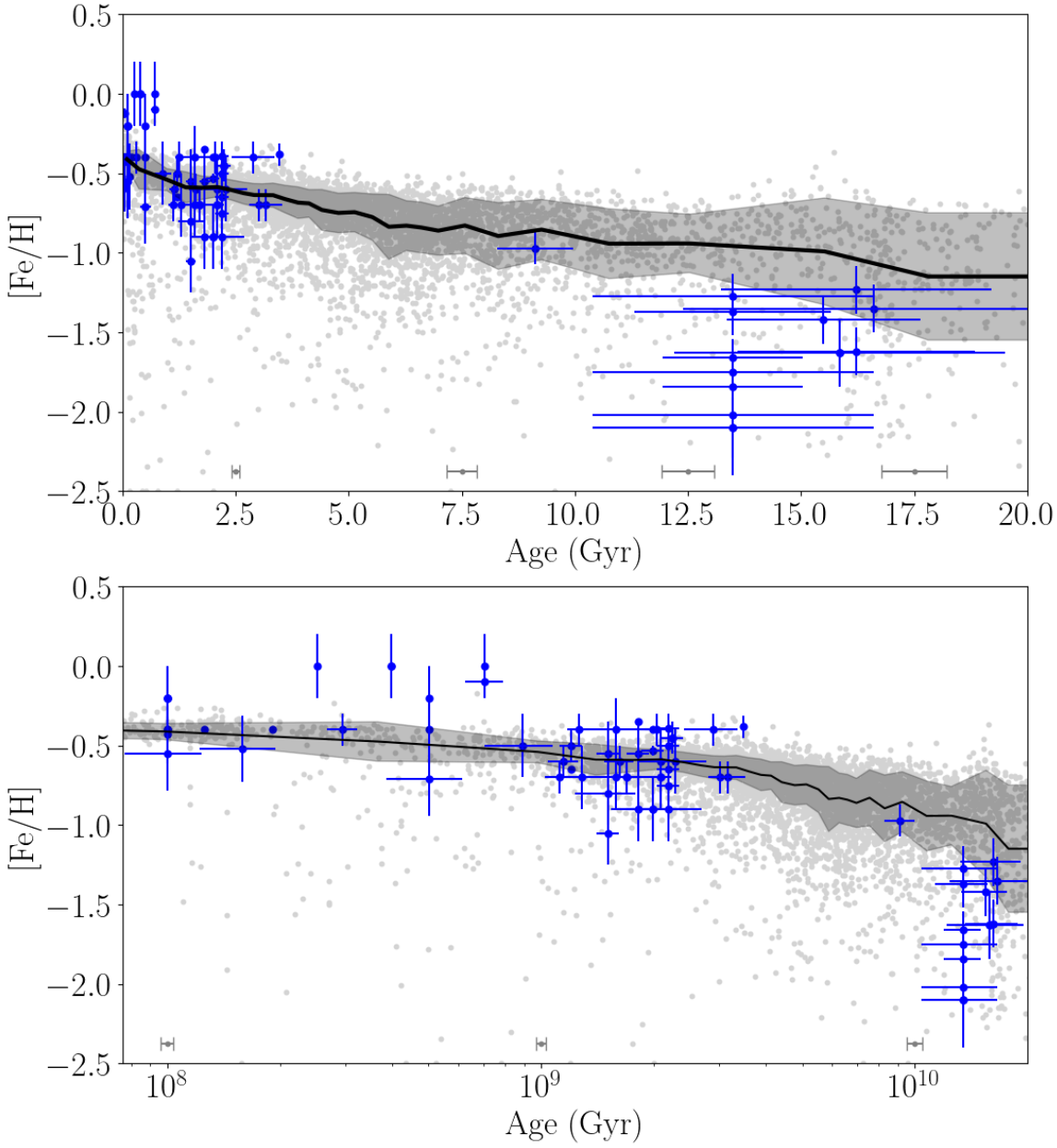



Figure 2.20: (*Top*) The AMR of the LMC calculated with the individual stars shown as the black dashed line. The APOGEE stars themselves are grey. The grey region shows the $1\sigma$ limit around the AMR. The blue points with error bars represent the 85 LMC clusters from HZ09. The grey points at the bottom show the characteristic error in the grey points. Clearly the largest disagreement with clusters happens for the oldest ages where measurements get donimated by noise. (*Bottom*) The same as the top, but with a log scale which highlights younger ages.

predominate. Finally, the mean $v_\phi$ clearly decreases with age, from a peak of $\sim$80 km s$^{-1}$ at 2.5 Gyr to a minimum of $\sim$60 km s$^{-1}$ at 10 Gyr, with roughly constant dispersion at all ages. The significant decrease in mean $v_\phi$ is evidence for asymmetric drift, in which stars which started on nearly circular orbits acquire random deflections over time, which when combined with a decreasing density distribution as a function of radius leads to a suppression of the maximum observed rotational velocity. We can use this observation of asymmetric drift to estimate the circular velocity of the LMC out to the radius limit of our sample. As shown in Binney & Tremaine (1987), we expect the magnitude of the asymmetric drift, $v_c - \overline{v_\phi}$ to be proportional to the radial velocity dispersion $\sigma_r^2$, as the effect of asymmetric drift comes from the preferential selection of stars on the slower portions of their elliptical orbits at any given radius. Thus if we can measure asymmetric drift at two different epochs $t_1$ and $t_2$, and assume that the density distribution is the same for stars with those ages, we can solve for the circular velocity $v_c$:

$$v_c = \frac{v_{\phi,1} - v_{\phi,2}\sigma_{r,1}^2/\sigma_{r,2}^2}{1 - \sigma_{r,1}^2/\sigma_{r,2}^2} \tag{2.21}$$

where $v_{\phi,1}$, $v_{\phi,2}$, $\sigma_{r,1}$, and $\sigma_{r,2}$ refer to the mean rotational velocity and radial velocity dispersion at epochs 1 and 2. Taking $v_{\phi,1} = 80$ km s$^{-1}$, $v_{\phi,2} = 60$ km s$^{-1}$, $\sigma_{r,1} = 25$ km s$^{-1}$, and $\sigma_{r,2} = 35$ km s$^{-1}$, we find $v_c \sim$100 km s$^1$. As the outermost in-plane radius of our sample is 10 kpc, we can then conclude that the mass of the LMC enclosed within 10 kpc is $2.3\times10^{10}$ M$_\odot$. If the rotation curve remains flat out to 15 kpc, as concluded by Besla (2015), then the total mass of the LMC is at least $3.5\times10^{10}$ M$_\odot$, in good agreement with the value determined therein.

## Discussion

The extinction of the LMC has been recently explored with the SMASH data (Choi et al., 2018a). In that paper, the extinction map was derived using red clump stars. This

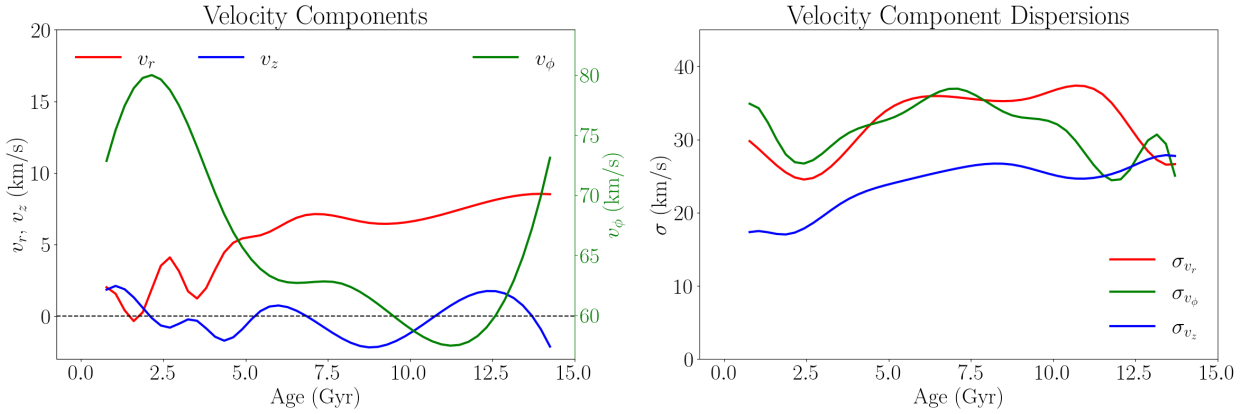



Figure 2.21: (*Left*) The different components of the velocity as functions of age. The $v_r$ and $v_z$ are shown in red and blue respectively. These two velocity components use the black axis on the left. The 0.0 km/s for this is included as a dashed line. Both $v_r$ and $v_\phi$ components stay close to zero. The $v_r$ curve shows that there is an increase starting around ages of 5 Gyr, though for even the oldest ages this component does not get above 10 km/s. The $v_\phi$ velocity is shown as a green curve and uses the green axis on the right. For ages $\lesssim$2.5 Gyr there is a large increase in $v_\phi$ and then from 2.5–5.0 Gyr there is a decrease down to about $\sim$67 km/s and then an increase for the oldest stars. (*Right*) The different components of the velocity dispersion as functions of age.

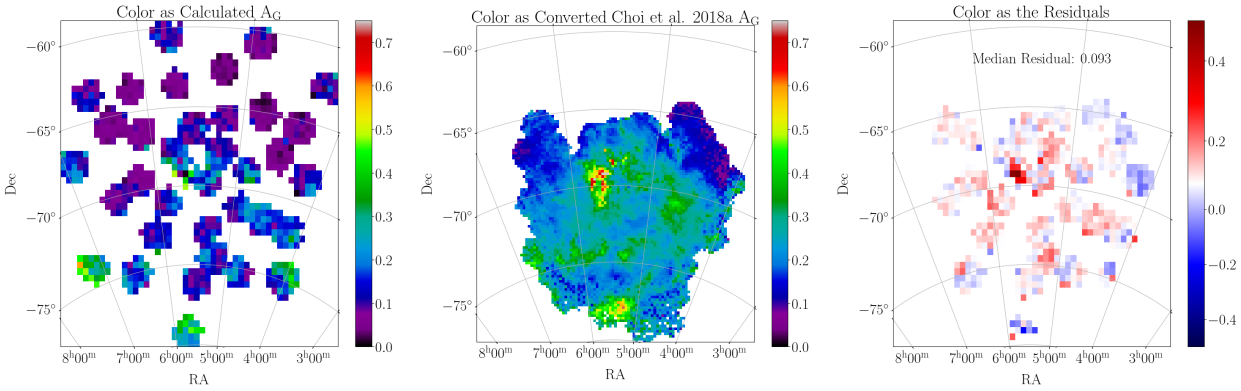



Figure 2.22: (*Left*) The $G$ band extinction map for the LMC. This is the same map as seen in Figure 2.16. (*Center*) The extinction map of LMC using $A_G$ derived from Choi et al. (2018a) and the CCM89 extinction law. (*Right*) The residuals between the converted Choi et al. (2018a) $A_G$ and the calculated $A_G$ from this work with a median residual of 0.093 mag suggesting a slight offset.

map was chosen to compare to because it is recent and has high resolution coverage of the LMC. In addition, the Choi et al. (2018a) map agrees well with the average reddening value for the LMC found by Bell et al. (2022); Haschke et al. (2011); Zaritsky et al. (2004) and also with the Schlegel et al. (1998) map. In order to compare the derived reddening and the extinction calculated in this work, CCM89 is used to convert the SMASH values to $A_G$. In Figure 2.22, the left and right panels show the extinctions from this work and the SMASH $E(g-i)$ converted to $A_G$, respectively. The right panel of the same figure shows the residuals which reveal a median offset of 0.093 mag while with the APOKASC validation there appears to be an offset of 0.043 mag suggesting that the method in this work slightly underestimates extinction compared to previous literature results. It is not entirely clear what the cause of this could be. The discrepancies in the extinction values may come from the spread of isochrone points in the isochrone photometry–$T_{\rm eff}$ relations. The extinction method only fits to the locus of the isochrone points and the method in Section 2 essentially uses a weighted average of the across all bands, which may compound the width effect.

The age map for the LMC shows a large concentration of younger stars in the center of

the galaxy with mean age increasing towards the outskirts. Many of the central young stars are thought to have been created as the result of an interaction between the LMC and SMC as the LMC experienced a burst of star formation at that time (Nidever et al., 2020). This is one of the first times the spatial distribution of ages in the LMC has been done and so there are not many literature sources available to compare with.

The age-radius relation is consistent with this result showing a positive gradient (see the left panel of Figure 2.18). The age-radius relation is clearly not flat for the LMC nor is it simply linear, but there is a distinct increase in the median age of stars with larger radii similar to what is seen in the age map. This shows that earlier in its history the LMC experienced more widespread star formation even out to its furthest limits, while at more recent times star formation has been concentrated toward the center, as previously mentioned. This change in behavior could be due to the outer LMC gas being stripped off by the interaction of the LMC with the SMC or from the ram pressure in the Milky Way's hot halo. Another mechanism that can affect the distribution of stars in a galaxy is radial migration (e.g. Sellwood, 2014; Sellwood & Binney, 2002). Radial migration leads to changes in the metallicity gradient of a galaxy and because metallicity is a proxy for age, this should also affect the age-radius relation.

In the left of Figure 2.18, the majority of the northern fields are below the trendline for radii $< 4$ kpc, but the southern fields tend to be above it producing a north-south dichotomy. There is a single spiral arm structure present in the inner northern fields with approximately the right age to be created through a known interaction between the LMC and SMC $\sim$2 Gyr ago. Through N-body simulations it has been shown that single spiral arms can be created through intergalactic tidal interactions (e.g. Berentzen et al., 2003; Pearson et al., 2018). This suggests that the spiral arm in the north was likely created by this major event.

The AMR of the LMC is mostly flat, increasing very slowly over time. In the upper panel of Figure 2.20 there is a clear recent increase in [Fe/H] coincident with the LMC-SMC

interaction. The derived AMR shows decent agreement for the LMC globular clusters from HZ09, except close to the age of the universe. This is also true of AMRs derived using clusters such as in Olszewski et al. (1991), Dirsch et al. (2000), and Grocholski et al. (2006), which all exhibit the downturn near the age of the universe while the one derived in this work does not. The LMC AMR derived from individual RGB stars in Carrera et al. (2008) matches even better than the cluster AMRs, but the downturn is still seen. It appears that for field star derived AMRs, the metallicities for intermediate ages tends to be slightly higher than what is seen according to clusters. This could be due to a known lack of clusters for those ages Rich et al. (2001),Bekki et al. (2004), and Mackey et al. (2006). For the oldest ages, both the cluster and field star derived AMRs do show a downturn around the age of the universe that is not present in the AMR derived here. A possible reason for this is that the stars with ages >12.5 Gyr are dominated by measurement uncertainties in their parameters that get propagated through the age method. Other sources of this effect could be systematics with the PARSEC models or the interpolation favors pushing metal poor stars to older ages.

Previously the difference in the AMR for the LMC disk and bar have been investigated in (Carrera et al., 2008, 2011; Cole et al., 2005). Selecting the APOGEE bar stars in this work, it was found that there is an increase in [Fe/H] in the last $\sim$1 Gyr for the both the bar and the LMC disk. This contradicts Cole et al. (2005) and Carrera et al. (2008), which found that there is not an appreciable increase in [Fe/H] for the bar in the last Gyr or so. Though there are less stars in the bar for older ages, the AMR for the bar is largely flat for ages older than 5 Gyr. For the most part the bar AMR suggests that these stars are more metal-rich for all times.

The detection of asymmetric drift in the stellar kinematics as a function of age is expected, and thus lends support to our ability to measure ages with our method. We used the measured evolution in asymmetric drift to estimate the LMC's circular velocity and thus

its total mass out to 10 kpc; our estimate of $2.3\times10^{10}$ $M_\odot$ within 10 kpc is $\sim$10% higher than e.g. van der Marel & Kallivayalil (2014), but in overall good agreement.

## Summary

We present an isochrone based method to calculate the ages of individual RGB stars and use this to find the ages of more than 6000 stars in the LMC. This method makes use of both photometry and spectroscopy and requires the distance to be known. The "A codE to calculaTe stellAr ageS" (Aetas) code used throughout this work is available online[8]. In addition the age method can be easily adapted to find the age of any individual star under some minimal constraints. Aetas requires that the photometry, distance, [Fe/H], [$\alpha$/Fe], $T_{\rm eff}$, and $\log g$be already measured. In order to use a different set of isochrones with Aetas, the appropriate labels will need to be changed to match the input table.

- We have used accurate photometry, spectroscopy and isochrones to determine ages statistically accurate to $\sim$1–2% and systematically accurate to $\sim$1–3 Gyr of stars in the LMC disk.
- Our method determined age and extinction simultaneously. Our LMC extinction map corresponds well with other literature extinction maps (e.g., Choi et al., 2018a).
- The median age is relatively flat with radius at $\sim$4 Gyr out to $\sim$4 kpc. Then it rises to $\sim$6 Gyr until the edge of our coverage at 7 kpc.
- We see an Age dichotomy in the LMC disk, with northern fields slightly younger than same ones at the same elliptical radius.
- Exploring the relation between the derived ages and kinematics of the LMC shows evidence of asymmetric drift.

[8] `https://github.com/JoshuaPovick/aetas`

Papers II and III in this series will use the ages determined in this work and study the chemical age-radius trends in both the LMC and SMC.

## Acknowledgements

J.T.P. acknowledges support for this research from the National Science Foundation (AST-1908331) and the Montana Space Grant Consortium Graduate Fellowship. D.L.N. acknowledges support for this research from the National Science Foundation (AST-1908331)

Funding for the Sloan Digital Sky Survey IV has been provided by the Alfred P. Sloan Foundation, the U.S. Department of Energy Office of Science, and the Participating Institutions.

SDSS-IV acknowledges support and resources from the Center for High Performance Computing at the University of Utah. The SDSS website is www.sdss.org.

SDSS-IV is managed by the Astrophysical Research Consortium for the Participating Institutions of the SDSS Collaboration including the Brazilian Participation Group, the Carnegie Institution for Science, Carnegie Mellon University, Center for Astrophysics | Harvard & Smithsonian, the Chilean Participation Group, the French Participation Group, Instituto de Astrofísica de Canarias, The Johns Hopkins University, Kavli Institute for the Physics and Mathematics of the Universe (IPMU) / University of Tokyo, the Korean Participation Group, Lawrence Berkeley National Laboratory, Leibniz Institut für Astrophysik Potsdam (AIP), Max-Planck-Institut für Astronomie (MPIA Heidelberg), Max-Planck-Institut für Astrophysik (MPA Garching), Max-Planck-Institut für Extraterrestrische Physik (MPE), National Astronomical Observatories of China, New Mexico State University, New York University, University of Notre Dame, Observatário Nacional / MCTI, The Ohio State University, Pennsylvania State University, Shanghai Astronomical Observatory, United Kingdom Participation Group, Universidad Nacional Autónoma de México, University of Arizona, University of Colorado Boulder, University of Oxford, University of Portsmouth,

University of Utah, University of Virginia, University of Washington, University of Wisconsin, Vanderbilt University, and Yale University.

This work has made use of data from the European Space Agency (ESA) mission *Gaia* (`https://www.cosmos.esa.int/gaia`), processed by the *Gaia* Data Processing and Analysis Consortium (DPAC, `https://www.cosmos.esa.int/web/gaia/dpac/consortium`). Funding for the DPAC has been provided by national institutions, in particular the institutions participating in the *Gaia* Multilateral Agreement.

*Software:* Astropy (Astropy Collaboration et al., 2013, 2018), Matplotlib (Hunter, 2007), NumPy (Harris et al., 2020), SciPy (Virtanen et al., 2020)

## Data Availability

All APOGEE DR17 data used in this study is publicly available and can be found at: `https://www.sdss4.org/dr17/data_access/`. This dataset does include the corresponding Gaia and 2MASS data in addition to the spectroscopic data.

## *Gaia* DR3 selection

For Figure 2.1, we use *Gaia* DR3 data to make the background density map, which highlights some of the structures around the Clouds. We use a parallax cut of stars compatible with being more than 20 kpc away at lower than 10% uncertainty. A proper motion cut of a radius of 1.05 mas/yr centered around $(\mu_{\rm L}, \mu_{\rm B}) = (1.767, 0.451)$ in Magellanic Stream coordinates (Nidever et al., 2008a). A magnitude cut at G=19.3 and a cut around the red giant branch sequence in a colour-magnitude diagram.

# REVEALING THE CHEMICAL STRUCTURE OF THE MAGELLANIC CLOUDS WITH APOGEE. II. ABUNDANCE GRADIENTS OF THE LARGE MAGELLANIC CLOUD

## Contribution of Authors and Co-Authors

Manuscript in Chapter 3

Author: Joshua T. Povick

Contributions: Lead author of the manuscript who carried out the calculation of abundance trends and age-abundance trends.

Author: David L. Nidever

Contributions: Provided general advice as well as gave comments and feedback on the manuscript.

Author: Steve R. Majewski

Contributions: Provided general advice as well as gave comments and feedback on the manuscript.

Author: Doug Geisler

Contributions: Provided general advice as well as gave comments and feedback on the manuscript.

Author: Maria-Rosa L. Cioni

Contributions: Provided comments and feedback on the draft of the manuscript.

Author: Yuxi (Lucy) Lu

Contributions: Provided comments and feedback on the draft of the manuscript.

Author: Ricardo Muñoz

Contributions: Provided comments and feedback on the draft of the manuscript.

Author: Penélope Longa-Peña

Contributions: Provided comments and feedback on the draft of the manuscript.

Author: Richard R. Lane

Contributions: Provided comments and feedback on the draft of the manuscript.

Author: Andrés Almeida

Contributions: Lead observer for the APOGEE-2S survey. Provided comments and feedback on the draft of the manuscript.

Manuscript Information

Joshua T. Povick, David L. Nidever, Steven R. Majewski, Doug Geisler, Maria-Rosa L. Cioni, Yuxi (Lucy) Lu, Ricardo Muñoz, Penélope Longa-Peña, Richard R. Lane, Andrés Almeida

Monthly Notices of the Royal Astronomical Society

Status of Manuscript:
_X_ Prepared for submission to a peer-reviewed journal
____ Officially submitted to a peer-reviewed journal
____ Accepted by a peer-reviewed journal
____ Published in a peer-reviewed journal

## Abstract

We present the abundance gradients of the Large Magellanic Cloud (LMC) for 25 elemental abundance ratios and their respective temporal evolution as well as age-[X/Fe] trends using 6130 field red giant branch (RGB) stars observed by SDSS-IV / APOGEE-2S. APOGEE is a high resolution (R $\sim$ 22,500) $H$-band spectroscopic survey that gathered data on the LMC with an impressive radial and azimuthal range out to $\sim$10°. The overall metallicity gradient of the LMC was found to be $-0.0380 \pm 0.0022$ dex/kpc. We also find that many of the abundance gradients show a U-shaped trend with age and an extremum point at the same time in their respective evolution around $\gtrsim$2 Gyr ago. In addition, some of the age-[X/Fe] trends show an increase in abundance starting a few Gyr before the turnover in the gradient evolution. A subset of the age-[X/Fe] trends also show maxima concurrent with the gradients' extremum points, further pinpointing a major event in the history of the LMC $\sim$2 Gyr ago. This time frame is consistent with a previously-proposed interaction between the Magellanic Clouds suggesting that this is most likely the cause of the distinct trend in the gradients and age-[X/Fe] trends.


## Introduction

While much progress has been made in our understanding of galaxy formation and evolution over the past several decades, both from the observational and theoretical sides, there are still important aspects that remain to be solved. It is widely accepted that the first galaxies formed from material falling into dark matter halos creating smaller "dwarf" galaxies that later merge with other dwarfs to create larger galaxies such as the Milky Way (MW) in a process known as hierarchical galaxy formation (White & Rees 1978; Searle & Zinn 1978). Therefore, a key ingredient in understanding how larger galaxies form is by examining the properties and evolution of dwarf galaxies. An important aspect of dwarf galaxies is their

distribution and abundance of chemical elements including any radial gradients.

Dwarf galaxies are the most abundant galaxies in the universe. However, they are intrinsically faint and most are very far away, making them difficult to study. Fortunately, the Local Group is ripe with dwarf galaxies close enough to resolve stars and study in great detail (e.g., Mateo, 1998; McConnachie, 2012). The largest satellites of our own Milky Way are the Large and Small Magellanic Clouds (LMC and SMC, respectively). Both of the Magellanic Clouds (MCs) are relatively close with the LMC at 49.9 kpc (De Grijs et al., 2014; Pietrzyński et al., 2019; van der Marel & Cioni, 2001) and the SMC at 62.44 kpc (Graczyk et al., 2020). The MCs have been studied for decades with wide-field optical (e.g., Nidever et al., 2017), NIR (e.g., Skrutskie et al., 2006) and radio surveys (e.g., Staveley-Smith et al., 2003). However, wide-field, high-resolution spectroscopic surveys have only started more recently (e.g., Cullinane et al., 2020; Nidever et al., 2020; Olsen et al., 2011).

The study of the LMC abundance gradients started in the 1970s with such works as Dufour (1975) and Pagel et al. (1978), which looked at HII regions in the LMC. Although neither of these studies found a gradient, the existence of a gradient could also not be ruled out. Since then, there have been many other studies of abundance gradients in the LMC: some of them detect a gradient (e.g. Cioni, 2009; Feast et al., 2010; Kontizas et al., 1993; Wagner-Kaiser & Sarajedini, 2013), while others do not (e.g. Geisler et al., 2003; Grocholski et al., 2006; Palma et al., 2015; Peña et al., 1987; Sharma et al., 2010). The debate is still ongoing and one of the goals of this work is to show that the LMC does in fact have a measurable metallicity and abundances gradients

This work breaks new ground in the LMC by exploring radial gradients and their age-dependence of 25 elements by using high-resolution spectroscopy of thousands of field stars. While it is possible to use star clusters to accomplish something similar in galaxies such as the Milky Way (MW) (Donor et al., 2020), this is not possible in the LMC. An age gap exists in LMC star clusters between $\sim$3$-$12 Gyr (Da Costa, 1991; Geisler et al., 1997) with very

few clusters having been identified in the gap (Mateo et al., 1986; Olszewski et al., 1991; Piatti, 2022). Clearly this does not bode well for exploring the full evolution of gradients derived from clusters with so much "missing" temporal information. Fortunately, the LMC contains many field stars for which ages can be derived and this is the approach we take for our study.

In Povick et al. 2023a (in preparation; hereafter Paper I), we described our method for calculating ages for individual LMC field stars. Spectroscopic parameters ($T_{\rm eff}$, $\log g$, [Fe/H], and [$\alpha$/Fe]), multi-band photometry, and isochrones are used to accomplish this. Ages for individual RGB stars are found by calculating apparent isochrone magnitudes for a star using the spectroscopic parameters ($T_{\rm eff}$, $\log g$, [Fe/H], and [$\alpha$/Fe]), PARSEC isochrones (Girardi et al., 2002), and an inclined plane disk model (Choi et al., 2018a) for the stellar distances. The age and extinction are varied until the best match with the observed photometry is found.

In this paper, we start by discussing the APOGEE data in Section 3.2. Then, Section 3.3 outlines the inclined disk geometry and radial abundance trend calculation. Section 3.4 presents the results. From there we discuss the implications of the results in Section 3.5 and, finally, our main conclusions are summarized in Section 3.6.

## APOGEE Data

The spectroscopic data for this work comes from the Apache Point Observatory Galactic Evolution Experiment (APOGEE, Majewski et al., 2017). More precisely, the data were taken by the second component of the survey (APOGEE-2) which, for the first time, obtained data in the southern hemisphere (APOGEE-2S) and was part of the Sloan Digital Sky Survey-IV (SDSS-IV; Blanton et al. 2017). All the data are available as part of the public SDSS-IV data release 17 (DR17, Abdurro'uf et al., 2022).

The APOGEE survey was designed to study the chemical enrichment and kinematics of

the Milky Way with wide coverage. The survey is dual hemisphere with two identical $H$-band spectrographs (Wilson et al., 2019) located at the Apache Point Observatory (APO, Gunn et al., 2006; Holtzman et al., 2010) in New Mexico and at the Las Campanas Observatory (LCO, Bowen & Vaughan, 1973) in Chile. Information regarding the targeting of the telescopes for the survey can be found in Zasowski et al. (2013) and Zasowski et al. (2017).

After observations have been obtained, the stellar spectra are initially reduced with the APOGEE reduction pipeline (Nidever et al., 2015). After this first reduction, the stellar parameters were derived using the APOGEE Stellar Parameter and Chemical Abundance Pipeline (ASPCAP, Holtzman et al., 2015; Pérez et al., 2016). ASPCAP works by using the `FERRE` (Allende Prieto et al., 2006) software to compare the observed spectra to a library of synthetic spectra created using `synspec` (Hubeny et al., 2021). The library is searched for the best-matching synthetic spectrum and, thereby, the main stellar parameters that affect the global spectrum ($T_{\rm eff}$, $\log(g)$, $v_{\rm micro}$, [M/H], [C/M], [N/M], [$\alpha$/M], and $v_{\rm macro}$) are determined. Finally, ASPCAP derives abundances for C, C I, N, O, Na, Mg, Al, Si, S, K, Ca, Ti, Ti II, V, Cr, Mn, Fe, Co, Ni, and Ce by holding the stellar parameters fixed and only varying the [M/H] dimension (or [$\alpha$/M] dimension for the $\alpha$-elements) and finding the best-fitting synthetic spectrum using wavelength windows unique to each element. Most of these abundances and various abundance ratios are studied in this work. For more information on the data reduction process and updates specifically for DR17 see Holtzman et al. (in preparation).

Like all observations, APOGEE measurements suffer from statistical uncertainties as well as systematic bias, which must be accounted for. To mitigate the problems that arise due to systematic biases, APOGEE uses solar neighborhood stars with known solar-like metallicities and derived offsets that were applied to the APOGEE parameters and abundances. Statistical uncertainties were determined using multiple visits for stars and the scatter was fit as a function of $T_{\rm eff}$, [M/H], and SNR. The uncertainties were then somewhat

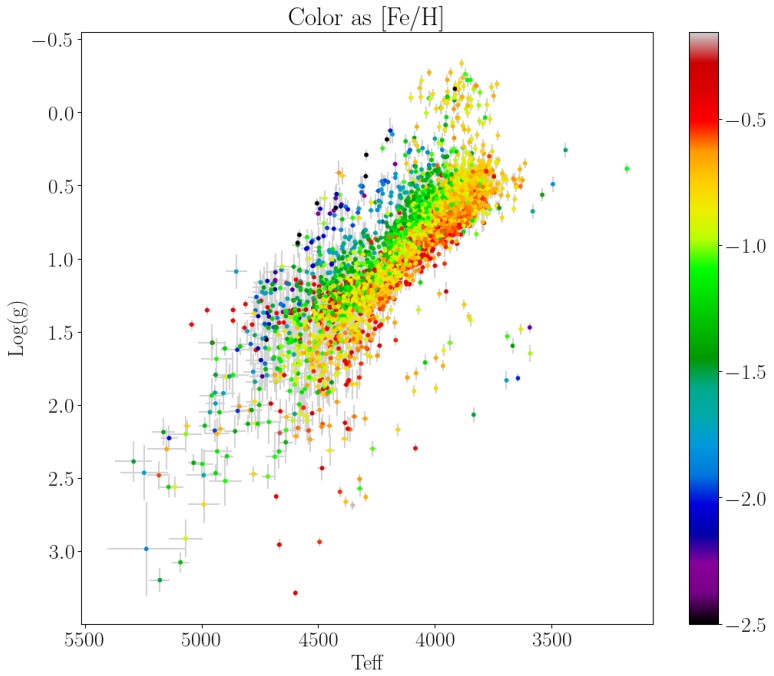



Figure 3.1: A Kiel-diagram for the whole sample of the LMC RGB stars with associated uncertainties. The color of each of the stars in the plot represent their respective metallicities.

inflated to be more in line with those seen for first generation stars in globular clusters. More details on the uncertainties specific for the Magellanic Cloud stars can be found in Nidever et al. (2020).

In the end, APOGEE was been able to observe and measure abundances for 6130 red giant branch (RGB) stars in the 36 LMC fields. A Kiel-diagram of the full APOGEE-2S LMC RGB sample is in Figure 3.1. APOGEE has wide radial and azimuthal coverage out to $\sim 10^{\circ}$ as can be seen in Figure 3.2.

BACCHUS Supplemental Data

In Hayes et al. (2022), the APOGEE DR17 spectra of 120,000 giants were reanalysed to derive abundances for elements that possess weak or blended spectral lines in the APOGEE data. Using the Brussels Automatic Code for Characterizing High-accuracy Spectra (`BACCHUS`) abundances were derived for Na, P, S, V, Cu, Ce, and Nd as well as

the $^{12}C/^{13}C$ isotopic ratio. The BACCHUS abundances for these weak-lined elements are generally more accurate than those produced by ASPCAP.

The BACCHUS catalog includes data for 763 of the LMC RGB stars. This work makes use of the Ce and Nd abundances derived with the `BACCHUS` code. While the main APOGEE catalog does derive Ce abundances for many more stars, the evolutionary trend of the Ce gradient is slightly more coherent when using the Hayes et al. (2022) abundances versus the ASPCAP ones. Though there are less stars with the `BACCHUS` Ce abundances, we use these values to derive our gradients. With the exception of Nd, none of the other BACCHUS abundances have enough stars with reliable values to calculate good gradients.

## Abundance Gradient Calculation

### LMC Geometry

The geometry of the LMC disk is well-modeled by an inclined elliptical disk. The mathematical framework was developed by van der Marel & Cioni (2001) and Choi et al. (2018b) and consists of two steps to convert equatorial coordinates to a Cartesian coordinate system with an origin at the center of the LMC. Since the LMC is elliptical, this must be considered when determining the radius. We take the equation for finding the radius of an ellipse directly from Choi et al. (2018b), which is

$$r(x,y)^2 = (x\cos\psi - y\sin\psi)^2 + \left(\frac{x\sin\psi + y\cos\psi}{b/a}\right)^2, \tag{3.1}$$

where $\psi\,(= 227.24°)$ is the position angle of the semi-major axis, and $b/a\,(= 0.836)$ is ratio of the semi-minor axis to the semi-major axis. For angles measured from the north, 90° must be added to $\psi$. Graphically, the geometry of the LMC can be seen in Figure 3.2. Also for reference the disk scale length for this model is $1.667 \pm 0.002$ kpc (Choi et al., 2018b).

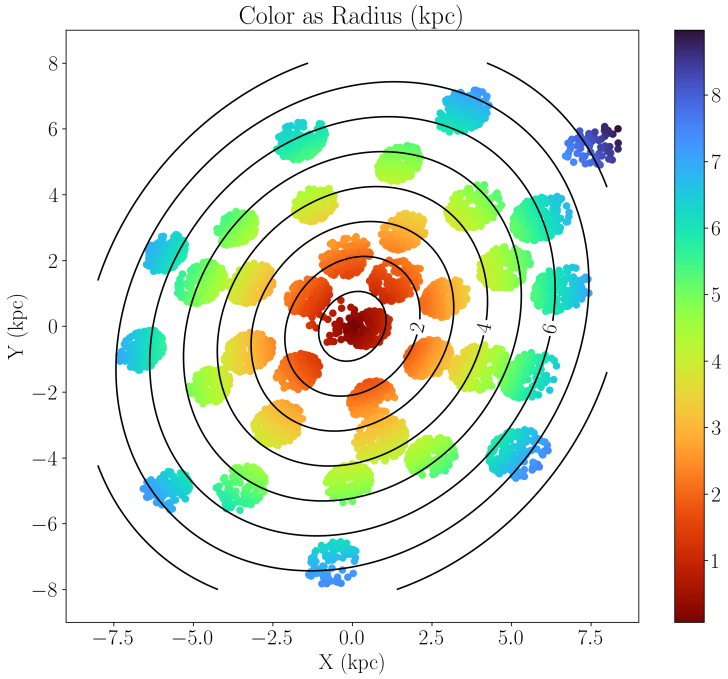



Figure 3.2: The resulting distance map for the LMC using Equation 3.1 with the color indicating distance in kpc. The contours show lines of constant "elliptical" radius starting at 1 kpc for the center contour out to 8 kpc calculated using Equation 6 from Choi et al. (2018b). For reference the center of the map, (X, Y) = (0, 0), is at ($\alpha$, $\delta$) = (05:27:36,−69:52:00).

MCMC

Radial abundance trends can be found assuming a simple, linear model that is only functionally dependent on the radius from the center of the LMC. The model used to find the abundance gradient is given by

$$[\mathrm{X/Fe}] = \nabla_R R + [\mathrm{X/Fe}]_0, \tag{3.2}$$

where $\nabla_R$ is the gradient in dex per kpc and $[\mathrm{X/Fe}]_0$ is the central abundance.

Most of the abundances measured by APOGEE use iron as the fiducial element as in the above Equation 3.2, but this is only for demonstration purposes. Gradients are also calculated using hydrogen and magnesium as fiducials. Hydrogen is an obvious choice for a fiducial as it removes any trace of a trend with another element and gives an absolute abundance gradient. Magnesium was also chosen as a fiducial because it almost entirely enriches the interstellar medium (ISM) through core collapse supernovae with only the slightest [Fe/H] dependence (Andrews et al., 2017). On the other hand, iron enriches the ISM through multiple channels and, therefore, its relationship to other elements is more complicated compared to magnesium (Weinberg et al., 2019). The abundance ratios that do not use iron, hydrogen, or magnesium as a fiducial (i.e. [C/N] and $[\alpha_{\mathrm{h}}/\alpha_{\mathrm{ex}}]$) are grouped in with the iron fiducial gradients. For future reference $[\alpha_{\mathrm{h}}/\alpha_{\mathrm{ex}}]$ is the iron free $\alpha$ abundance where $[\alpha_{\mathrm{h}}/\mathrm{Fe}]$ is the average hydrostatic $\alpha$ abundance and $[\alpha_{\mathrm{ex}}/\mathrm{Fe}]$ is the average explosive $\alpha$ abundance. More on this can be found in Section 3.

In order to find the parameters of the linear model in Equation 3.2, we use maximum likelihood estimation (MLE). MLE has advantages over methods such as ordinary least squares (OLS), because it does not assume that the uncertainties are necessarily Gaussian like OLS does. In the limit of Gaussian errors, MLE approaches OLS.

Implementing MLE requires maximizing the likelihood function, which is the same as

minimizing the negative log likelihood function. The log likelihood function for the linear model is

$$\ln \mathcal{L} = \frac{1}{2}\Bigg[\sum_i \frac{([\mathrm{X/Fe}]_i - \nabla_R R_i - [\mathrm{X/Fe}]_0)^2}{\sigma_i^2} - \ln 2\pi\sigma_i^2\Bigg], \tag{3.3}$$

where $R_i$ is the radius of an individual star, $[\mathrm{X/Fe}]_i$ is its abundance, and $\sigma_i$ is the uncertainty in the abundance of the same star.

In order to obtain the uncertainties for each of the model parameters, the `emcee` (Foreman-Mackey et al., 2013) python package is used. `emcee` implements the affine invariant Markov chain Monte Carlo ensemble sampler outlined by Goodman & Weare (2010), in pure Python. Thirty-two walkers are used with 5000 numbers of sets. The first int(max($\tau$)) + 50 steps are removed as "burn-in", where the walkers are still finding the optimal value. Here max($\tau$) is the largest of the calculated auto-correlation times for a set of parameters. Also, the chain is thinned by selecting every 15th value.

In actuality, when fitting radial trends, the individual stars are not used. Instead the stars are radially binned and the gradients are fit to the median values and the median absolute deviation (MAD) is used for the uncertainty in each bin. This is done to create a more robust fit, speed up the process, and not have the gradients weighted too highly in radial regions with many stars.

For the actual fit, stars with less reliable abundances are removed by requiring S/N > 100. Then the stars are binned into 1 kpc radial bins and the abundance trend is fit with `emcee`. After this, outlier stars more than 3 × MAD from the best-fit model are removed and the trend is refit to obtain the final abundance gradient.

Stellar Age Binning

All ages were calculated using Paper I. The age of a star is derived by finding the age and extinction that produces the best match of the model PARSEC isochrone photometry (Bressan et al., 2012; Marigo et al., 2017) for the star's $T_{\mathrm{eff}}$, $\log g$, [Fe/H], [$\alpha$/Fe] and a

Table 3.1: Values of the different age bins used throughout this work.

| Bin | Age Range (Gyr) |
|---|---|
| 1 | $t \leq 2.23$ |
| 2 | $2.23 < t \leq 3.66$ |
| 3 | $3.66 < t \leq 5.58$ |
| 4 | $5.58 < t \leq 8.36$ |
| 5 | $8.36 < t$ |

distance given by the LMC inclined disk model with the observed multi-band photometry.

Each star was placed into one of five different age bins. The bins were chosen such that the total number of stars in each bin was roughly the same. The particular age ranges of each of these bins can be seen in Table 3.1. This binning scheme has good age resolution while also mitigating the effect of stars whose calculated ages are quite large. No significant differences in abundance gradients were found when varying the age bins, unless very large deviations were attempted.

Age-[X/Fe] Trends

In addition to radial abundance trends, we also explore age-abundance trends for different positions in the LMC. This is performed for the [X/Fe] abundances as well as [C/N] and $[\alpha_{\rm h}/\alpha_{\rm ex}]$. Stars were placed into three different radial bins, or annuli, with the same number of stars in each bin. This is done because the outskirts of the LMC in the APOGEE sample has significantly less stars than in the central regions. Three bins were chosen so that the inner bin contains the central disk, the outer bin contains the "edge" of the disk, and the middle bin probes intermediate radii. The radial bins selected were: $R < 3.3$ kpc, $3.3 \leq R < 4.86$ kpc, and $R > 4.8$. The annuli were further subdivided into north

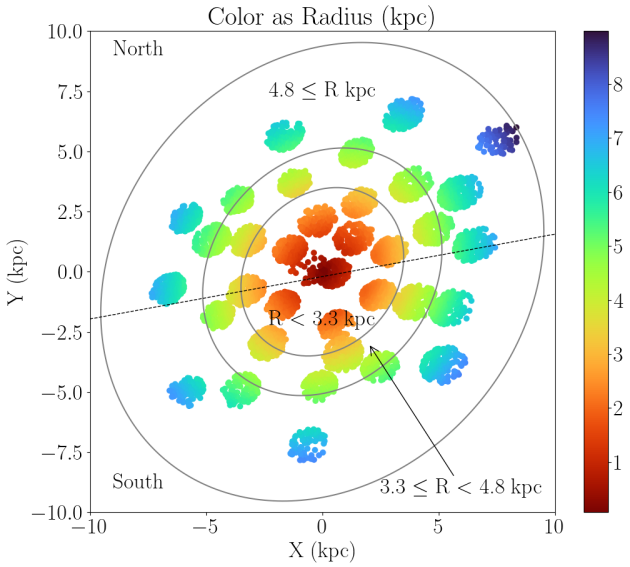



Figure 3.3: A plot showing the radial bins used to calculate the age-[X/Fe] relations. The dashed black line shows the boundary between the North and South LMC using the position angle of a star. This line amounts to a delineation in declination at $\sim -70°$. The solid black lines show the boundary of the different annular bins. Each of the annuli contain the same number of stars.

and south based on the position angle of the stars. A north-south division was chosen as the bar runs along an east-west line. Admittedly the bar is not perfectly east-west with some rotation from this axis. The different spatial regions can be seen in Figure 3.3.

For each of the positional bins, age-[X/Fe] trends were calculated by splitting the stars into age bins and determining the median abundance and MAD scatter. The number of age bins for the age-[X/Fe] trends is calculated using $N_{\text{bins}} = \left\lceil \sqrt{N_{\text{data points}}} \right\rceil$. The number of age bins varies somewhat with element and were chosen to provide fairly smooth trends but without sacrificing too much temporal resolution.

## Results

In this section we discuss the main results of the analysis carried out using the methods in Section 3. These include the [X/Fe], [X/H], and [X/Mg] gradients and their evolution as

well as the age-[X/Fe] trends.

The LMC Radial Abundance Gradients

Carbon & Nitrogen Both carbon and nitrogen are very abundant metals whose abundances are measured by APOGEE. These elements are produced in intermediate-mass stars (Ventura et al., 2013) and type II SNe (Kobayashi et al., 2006). In addition to these elements, the C+N abundance and [C/N] are also analyzed. C and N created through nuclear burning are brought up from the core of a star to the surface by dredge-up and change the observed C and N abundances through vigorous convection. However, the C+N abundance stays relatively constant in the atmosphere. In addition, the [C/N] abundance ratio has been shown to be age-sensitive (at least in relatively metal-rich stars; Ness et al., 2016b).

All the C, N, and C+N gradients show similar relative behaviour irrespective of whether the fiducial element is Fe, H, or Mg (see Table 3.2). The nitrogen gradients tend to be very flat or at least much flatter that what is seen for C and C+N, though the [N/H] gradient is decidedly not flat with a value of $-0.0540 \pm 0.0027$ dex/kpc. The similarities seen in the C and C+N gradients are most likely due to the carbon abundances dominating the weighted sum when calculating the C+N values. As for the [C/N] gradient it is very similar to the [(C+N)/Mg] gradient with a value of $-0.0115 \pm 0.0015$ dex/kpc. The radial trends for each of the [X/Fe] carbon and nitrogen and [C/N] can be seen as the black trendlines in Figure 3.7. In general, the radial trends for [X/H] and [X/Mg] are not included.

$\alpha$-Elements The $\alpha$-elements enrich the ISM primarily through type II SNe (Nomoto et al., 2013; Weinberg et al., 2019). The $\alpha$-abundances measured by APOGEE include oxygen, magnesium, silicon, sulfur, calcium, titanium, and mean $\alpha$. In addition to the elemental $\alpha$-abundances, we also inspected the ASPCAP [$\alpha$/Fe], and the average hydrostatic $\alpha$-abundance ([$\alpha_h$/Fe]=([O/Fe]+[Mg/Fe])/2) and average explosive $\alpha$-abundance ([$\alpha_{\rm ex}$/Fe] = ([Si/Fe]+[Ca/Fe]+[Ti/Fe])/3) as well as the ratio of hydrostatic and explosive $\alpha$-abundances

Table 3.2: A table of overall gradients for the abundant metals carbon and nitrogen using Fe, H, and Mg as fiducials. The [C/N] gradient is also included at the bottom.

| Element | $\nabla_R$ [X/Fe] (dex/kpc) | $\nabla_R$ [X/H] (dex/kpc) | $\nabla_R$ [X/Mg] (dex/kpc) |
|---|---|---|---|
| C | $-0.0281 \pm 0.0010$ | $-0.0676 \pm 0.0031$ | $-0.0212 \pm 0.0012$ |
| N | $-0.0028 \pm 0.0010$ | $-0.0540 \pm 0.0027$ | $-0.0002 \pm 0.0009$ |
| C+N | $-0.0232 \pm 0.0008$ | $-0.0631 \pm 0.0028$ | $-0.0129 \pm 0.0008$ |
| [C/N] | $-0.0115 \pm 0.0015$ | ... | ... |

([$\alpha_{\rm h}/\alpha_{\rm ex}$] = [$\alpha_h$/Fe]-[$\alpha_{\rm ex}$/Fe]) or "HEx ratio". The hydrostatic $\alpha$-elements are produced by nuclear fusion inside the star, while the explosive $\alpha$-elements are created through the type II SNe explosion itself (Carlin et al., 2018). The [$\alpha_{\rm h}/\alpha_{\rm ex}$] is an iron free abundance that tracks the two different modes of evolution for $\alpha$-element nucleosynthesis. (Carlin et al., 2018) performed a spectroscopic study of Sagittarius stream stars and showed that the HEx ratio of Sagattarius stars are deficient compared to Milky Way stars but are consistent with a top-light IMF.

Looking at the tabulated gradients in Table 3.3, the [X/Fe] gradients tend to be positive and shallow. Of these, the [S/Fe], [Ti/Fe], and [$\alpha_{\rm ex}$/Fe] stand out. [S/Fe] has a relatively steep positive gradient of $+0.0236 \pm 0.0028$ dex/kpc and [Ti/Fe] has a steep negative gradient of $-0.0186 \pm 0.0015$ dex/kpc. [$\alpha_{ex}$/Fe] has a slightly negative gradient of $-0.0036 \pm 0.0006$ dex/kpc, but this is most likely because it is the mean of the explosive $\alpha$-elements including Ti, which has a large negative gradient, as previously mentioned. As for the [X/H] $\alpha$-gradients there is more homogeneity with every gradient being negative and steeper than the [X/Fe] gradients, but [Ti/H] and [$\alpha_{\rm ex}$/H] stand out just like for the [X/Fe] abundance ratios. The [X/Mg] gradients for the $\alpha$-elements are similar to the [X/Fe]-gradients, though clearly not the same. The [$\alpha_{\rm h}/\alpha_{\rm ex}$] has a value of $+0.0047 \pm 0.0005$ dex/kpc. The individual $\alpha$-

Table 3.3: A table of overall gradients for the $\alpha$-elements. The $[\alpha_{\rm h}/\alpha_{\rm ex}]$ gradient is included at the bottom.

| Element | $\nabla_R$ [X/Fe] (dex/kpc) | $\nabla_R$ [X/H] (dex/kpc) | $\nabla_R$ [X/Mg] (dex/kpc) |
|---|---|---|---|
| O | $0.0023 \pm 0.0005$ | $-0.0419 \pm 0.0023$ | $0.0023 \pm 0.0004$ |
| Mg | $0.0021 \pm 0.0007$ | $-0.0475 \pm 0.0024$ | ... |
| Si | $0.0054 \pm 0.0005$ | $-0.0351 \pm 0.0022$ | $0.0039 \pm 0.0007$ |
| S | $0.0263 \pm 0.0028$ | $-0.0281 \pm 0.0027$ | $0.0283 \pm 0.0028$ |
| Ca | $0.0030 \pm 0.0004$ | $-0.0383 \pm 0.0022$ | $0.0021 \pm 0.0006$ |
| Ti | $-0.0186 \pm 0.0015$ | $-0.0931 \pm 0.0036$ | $-0.0158 \pm 0.0013$ |
| $\alpha$ | $0.0008 \pm 0.0004$ | $-0.0448 \pm 0.0024$ | $-0.0008 \pm 0.0004$ |
| $\alpha_{\rm h}$ | $0.0022 \pm 0.0006$ | $-0.0479 \pm 0.0023$ | $0.0011 \pm 0.0002$ |
| $\alpha_{\rm ex}$ | $-0.0036 \pm 0.0006$ | $-0.0816 \pm 0.0029$ | $-0.0061 \pm 0.0008$ |
| $[\alpha_{\rm h}/\alpha_{\rm ex}]$ | $0.0047 \pm 0.0005$ | ... | ... |

element radial trends are shown in Figure 3.10 as black lines, while the composite abundance trends can be seen in Figure 3.11, also in black.

Odd-Z Elements It has long been established that elements with odd atomic number are always more rare than elements with even atomic numbers except for hydrogen (Harkins, 1917; Oddo, 1914). These rarer elements with odd atomic number that do not fall neatly into any of the other groups of elements in APOGEE are called odd-Z elements. The odd-Z elements that are explored in this work include sodium, aluminium, and potassium. The odd-Z elements are mostly created by exploding massive stars. Both Na and Al are created by type II SNe with some metallicity dependence (Nomoto et al., 2013; Weinberg et al., 2019), as is the case with potassium (Weinberg et al., 2019).

Table 3.4: Gradients for the odd-Z elements.

| Element | $\nabla_R$ [X/Fe] (dex/kpc) | $\nabla_R$ [X/H] (dex/kpc) | $\nabla_R$ [X/Mg] (dex/kpc) |
|---|---|---|---|
| Na | $0.0017 \pm 0.0019$ | $-0.0527 \pm 0.0021$ | $-0.0002 \pm 0.0019$ |
| Al | $-0.0197 \pm 0.0012$ | $-0.0682 \pm 0.0036$ | $-0.0120 \pm 0.0012$ |
| K | $0.0075 \pm 0.0009$ | $-0.0412 \pm 0.0026$ | $0.0046 \pm 0.0009$ |

There is a large diversity in the gradients for the odd-Z elements (see Table 3.4). The [X/Mg] gradients are the flattest compared to the [X/Fe] and [X/H]. Also, like for other groups of elements, the [X/Mg] gradients are more similar to the [X/Fe] gradients than the [X/H] gradients. Interestingly, the [Al/H] gradient is very steep versus any other odd-Z gradient, regardless of the fiducial element, with a value of $-0.0682 \pm 0.0036$ dex/kpc. The full radial trends for the odd-Z [X/Fe] can be seen as black lines in Figure 3.12.

Iron Peak Elements Chromium, manganese, iron, cobalt, nickel, and vanadium are the iron peak elements investigated in this study. These elements typically enrich the ISM through type Ia SNe, though some enrichment does happen with type II SNe (Kobayashi et al., 2006). Fe tends to be more robustly measured than many other elements, with many good lines in stellar spectra. Therefore, it is often used as the main fiducial element used to track the overall "metallicity" of a star.

Comparing the three different fiducials, in general the gradients become large for increasing atomic number until Mn or Fe, where the gradients become shallower (see Table 3.5). As with the other groups of elements, the [X/Mg] elements are in between the [X/Fe] and [X/H] gradients. The [Mn/H] is the steepest gradient out of all of the elements with a value of $-0.1024 \pm 0.0040$ dex/kpc. The black lines in Figure 3.13 show the overall radial [X/Fe] trends for the odd-Z elements.

Table 3.5: Gradients for the iron peak elements.

| Element | $\nabla_R$ [X/Fe] (dex/kpc) | $\nabla_R$ [X/H] (dex/kpc) | $\nabla_R$ [X/Mg] (dex/kpc) |
|---|---|---|---|
| V | $-0.0079 \pm 0.0012$ | $-0.0466 \pm 0.0028$ | $-0.0105 \pm 0.0013$ |
| Cr | $-0.0032 \pm 0.0011$ | $-0.0666 \pm 0.0024$ | $-0.0077 \pm 0.0014$ |
| Mn | $-0.0247 \pm 0.0009$ | $-0.1024 \pm 0.0040$ | $-0.0228 \pm 0.0013$ |
| Fe | ... | $-0.0380 \pm 0.0022$ | $-0.0862 \pm 0.0042$ |
| Co | $-0.0081 \pm 0.0009$ | $-0.0528 \pm 0.0023$ | $-0.0075 \pm 0.0000$ |
| Ni | $0.0010 \pm 0.0004$ | $-0.0445 \pm 0.0022$ | $-0.0013 \pm 0.0000$ |

Neutron Capture Elements Neutron capture elements are created through two processes: the rapid process ($r$-process) and the slow process ($s$-process). The $s$-process takes place inside massive stars in late stages of their evolution by the slow absorption of neutrons by heavy atoms, while the $r$-process happens in supernovae on the timescale of seconds. In this work, we explore two neutron capture elements, namely Ce and Nd. These elements are created through both the $r$- and $s$-processes (Prantzos et al., 2020). Note that there are reliable Ce and Nd abundance values only for a fraction of our LMC RGB sample, as previously mentioned in Section 3.

For the LMC, we find that the Nd gradient is always flatter than the Ce gradient for all three fiducials (see Table 3.6). The black lines in Figure 3.14 represent the overall radial trend for the neutron capture elements.

The Evolution of the LMC Abundance Gradients

Radial abundance gradients are sensitive to the particular formation history of a galaxy Pagel & Edmunds (1981). If star formation proceeds at a higher rate at one radius compared to another, then this will be detectable in the radial abundances gradients. With the addition

Table 3.6: Gradients for the neutron capture elements.

| Element | $\nabla_R$ [X/Fe] (dex/kpc) | $\nabla_R$ [X/H] (dex/kpc) | $\nabla_R$ [X/Mg] (dex/kpc) |
|---|---|---|---|
| [Ce/Fe] | $-0.0091 \pm 0.0042$ | $-0.0642 \pm 0.0078$ | $-0.006 \pm 0.0039$ |
| [Nd/Fe] | $0.0054 \pm 0.0038$ | $-0.0259 \pm 0.0053$ | $0.0012 \pm 0.0046$ |

of stellar age information (see Section 3), it is possible to track the evolution of the abundance gradients over time. The values for the [X/Fe], [X/H], and [X/Mg] for each of the age bins are tabulated in Tables 3, 3, and 3 respectively. However, it is worth noting that stars move away from their birth location overtime via radial migration (e.g. Sellwood & Binney, 2002). This process flattens the abundance gradient overtime (e.g. Minchev et al., 2013). As a result, even though the gradients in mono-age populations contain memories of the birth gradients and thus reflect some information of the birth environment of the stars, gradients in mono-age populations do not necessarily provide such information without taking radial migration into account. The temporal behavior of the gradients is described in more detail below.

Carbon & Nitrogen The evolution in the C and N abundances is varied. For the [X/Fe] gradients, [C/Fe] flattens out with age showing an upward trend in Figure 3.4. This contrasts with [N/Fe], which starts out positive, then flattens, and finally becomes negative over time. Figure 3.7 shows that the central [C/Fe] is always deficient compared to the sun while steadily increasing from $\sim -0.4$ to $\lesssim -0.2$. Unlike what is seen in [C/Fe], the central [N/Fe] starts close to solar, but increases around 5.6 Gyr ago to about +0.1 dex and then a major increase around 2.2 Gyr ago.

Combining the C and N abundance into [(C+N)/Fe] and [C/N] produces interesting results. The [(C+N)/Fe] gradient has a similar downward trend analogous to what is seen

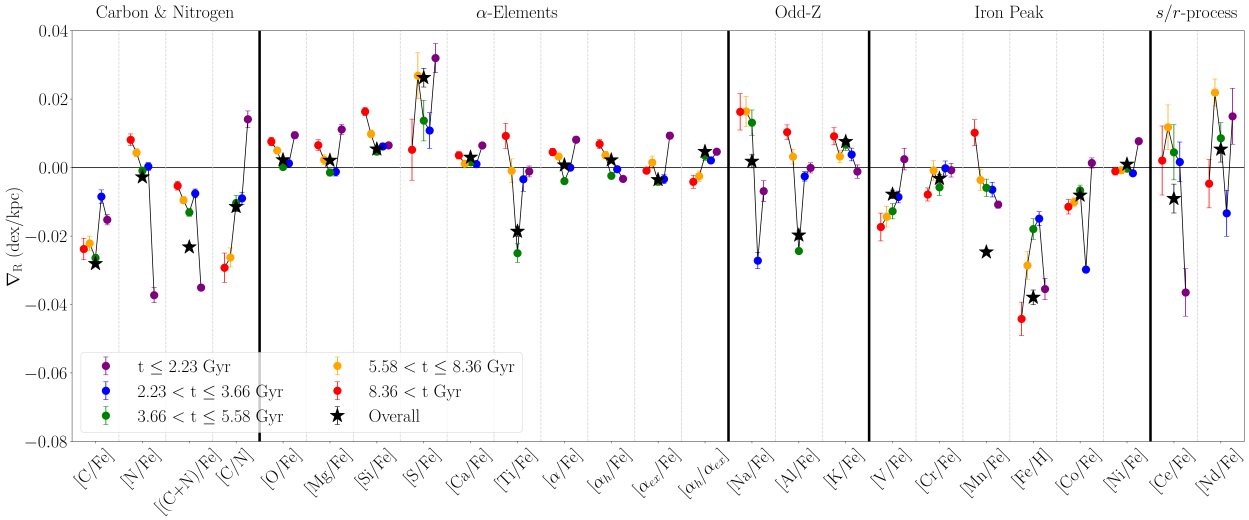



Figure 3.4: A figure showing each of the calculated [X/Fe] gradients are shown for each element. Also included here are [Fe/H], [C/N], $[\alpha_{\rm h}/{\rm Fe}]$, $[\alpha_{\rm ex}/{\rm Fe}]$ and $[\alpha_{\rm h}/\alpha_{\rm ex}]$. The abundances have been broken up into different groups of like elements with atomic number generally increasing to the right. The color of each dot corresponds to the different age bins for which a gradient was calculated. Black lines have also been added to make the trends in the gradients more clear. The value of each gradient here can be seen in Table 3.

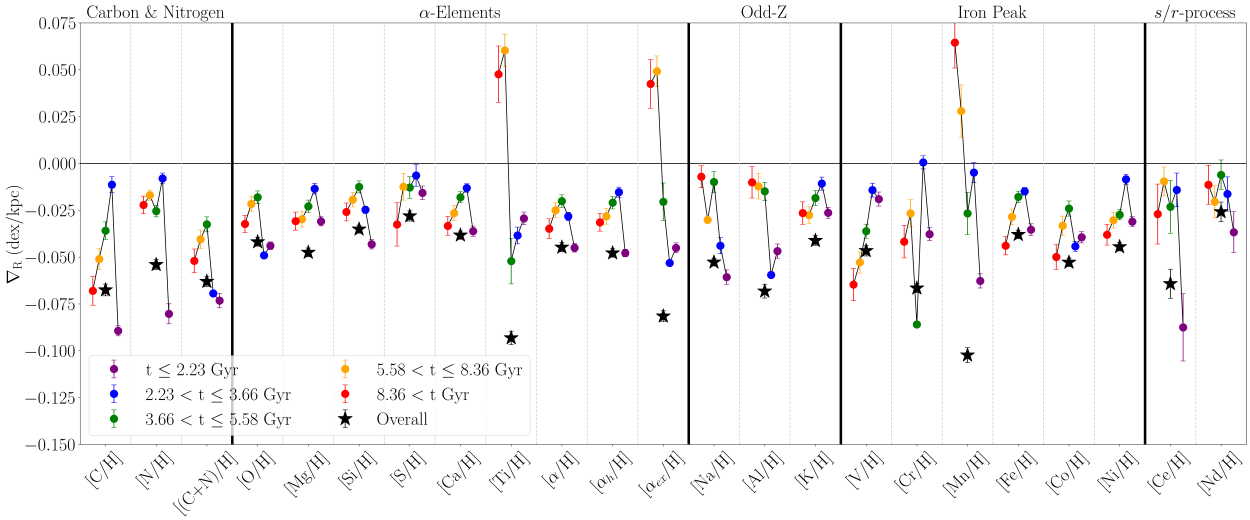



Figure 3.5: Same as Figure 3.4, but for the [X/H] gradients. The [Fe/H] has also been included here. The value of each gradient is given in Table 3.

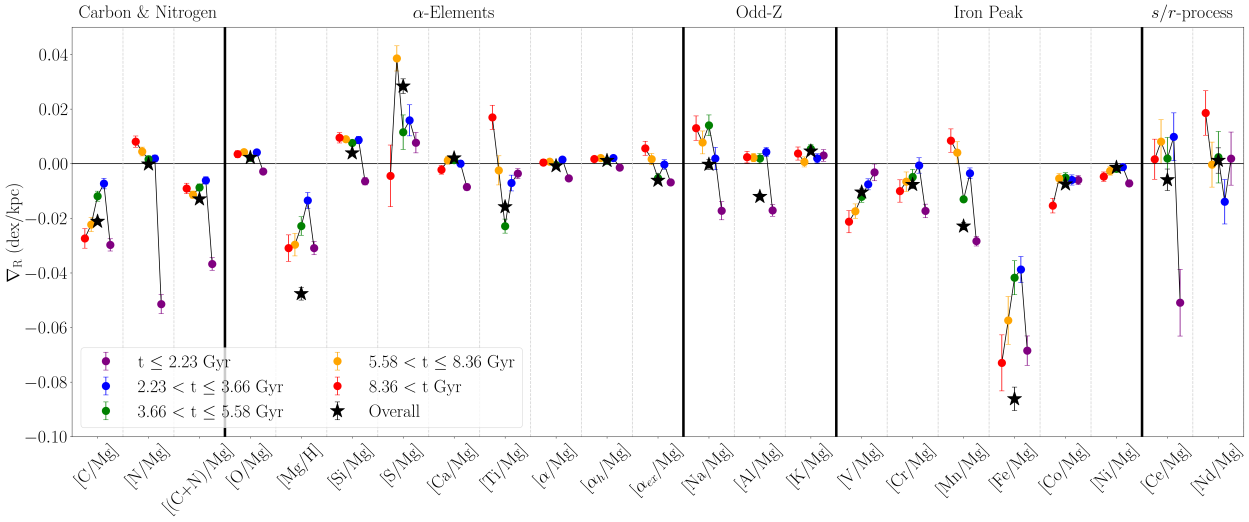



Figure 3.6: Same as Figure 3.4, but for the [X/Mg] gradients. The [Mg/H] gradient has also been included here. The value of each gradient is given in Table 3.

Table 3.7: A table of the gradients for each of the age bins. Horizontal lines have been added marking the division of the previously defined groups of elements. In general descending down the table corresponds to an increase in atomic number. Each age bin has its own separate column. This table also includes the evolution of the [Fe/H], [C/N] and $[\alpha_{\rm h}/\alpha_{\rm ex}]$.

| Element | $t \leq 2.23$ | $2.23 < t \leq 3.66$ | $3.66 < t \leq 5.58$ | $5.58 < t \leq 8.36$ | $8.36 < t$ |
|---|---|---|---|---|---|
| | $\nabla_{\rm R}$ | $\nabla_{\rm R}$ | $\nabla_{\rm R}$ | $\nabla_{\rm R}$ | $\nabla_{\rm R}$ |
| | (dex/kpc) | (dex/kpc) | (dex/kpc) | (dex/kpc) | (dex/kpc) |
| [C/Fe] | -0.0152 ± 0.0015 | −0.0085 ± 0.0020 | −0.0264 ± 0.0011 | −0.0222 ± 0.0022 | −0.0237 ± 0.0031 |
| [N/Fe] | −0.0373 ± 0.0022 | 0.0003 ± 0.0011 | −0.0009 ± 0.0010 | 0.0044 ± 0.0012 | 0.0081 ± 0.0017 |
| [(C+N)/Fe] | −0.0351 ± 0.0005 | −0.0076 ± 0.0013 | −0.0131 ± 0.0012 | −0.0095 ± 0.0010 | −0.0052 ± 0.0013 |
| [C/N] | 0.0141 ± 0.0026 | −0.0090 ± 0.0018 | −0.0103 ± 0.0023 | −0.0262 ± 0.0028 | −0.0291 ± 0.0042 |
| [O/Fe] | 0.0095 ± 0.0010 | 0.0012 ± 0.0007 | 0.0001 ± 0.0008 | 0.0050 ± 0.0009 | 0.0076 ± 0.0012 |
| [Mg/Fe] | 0.0111 ± 0.0014 | −0.0013 ± 0.0013 | −0.0015 ± 0.0010 | 0.0023 ± 0.0014 | 0.0065 ± 0.0016 |
| [Si/Fe] | 0.0065 ± 0.0010 | 0.0062 ± 0.0010 | 0.0047 ± 0.0010 | 0.0099 ± 0.0011 | 0.0164 ± 0.0012 |
| [S/Fe] | 0.0319 ± 0.0043 | 0.0108 ± 0.0051 | 0.0136 ± 0.0058 | 0.0270 ± 0.0066 | 0.0053 ± 0.0088 |
| [Ca/Fe] | 0.0065 ± 0.0007 | 0.0010 ± 0.0006 | 0.0016 ± 0.0007 | 0.0012 ± 0.0009 | 0.0035 ± 0.0010 |
| [Ti/Fe] | −0.0011 ± 0.0017 | −0.0035 ± 0.0036 | −0.0250 ± 0.0027 | −0.0009 ± 0.0034 | 0.0092 ± 0.0037 |
| [$\alpha$/Fe] | 0.0081 ± 0.0009 | 0.000 ± 0.0006 | −0.0040 ± 0.0007 | 0.0032 ± 0.0008 | 0.0045 ± 0.0011 |
| [$\alpha_{\rm h}$/Fe] | −0.0033 ± 0.0005 | −0.0005 ± 0.0009 | −0.0025 ± 0.0008 | 0.0036 ± 0.0011 | 0.0069 ± 0.0013 |
| [$\alpha_{\rm ex}$/Fe] | 0.0093 ± 0.0010 | −0.0034 ± 0.0013 | −0.0041 ± 0.0012 | 0.0015 ± 0.0018 | −0.0009 ± 0.0006 |

| | | | | | |
|---|---|---|---|---|---|
| $[\alpha_{\rm h}/\alpha_{\rm ex}]$ | $0.0046 \pm 0.0007$ | $0.0021 \pm 0.0009$ | $0.0034 \pm 0.0014$ | $-0.0026 \pm 0.0015$ | $-0.0041 \pm 0.0019$ |
| [Na/Fe] | $-0.0069 \pm 0.0031$ | $-0.0271 \pm 0.0024$ | $0.0132 \pm 0.0037$ | $0.0166 \pm 0.0045$ | $0.0163 \pm 0.0053$ |
| [Al/Fe] | $-0.0001 \pm 0.0015$ | $-0.0026 \pm 0.0014$ | $-0.0244 \pm 0.0009$ | $0.0031 \pm 0.0021$ | $0.0103 \pm 0.0021$ |
| [K/Fe] | $-0.0012 \pm 0.0019$ | $0.0038 \pm 0.0019$ | $0.0068 \pm 0.0017$ | $0.0032 \pm 0.0019$ | $0.0092 \pm 0.0024$ |
| [V/Fe] | $0.0025 \pm 0.0031$ | $-0.0086 \pm 0.0017$ | $-0.0128 \pm 0.0022$ | $-0.0143 \pm 0.003$ | $-0.0174 \pm 0.0041$ |
| [Cr/Fe] | $-0.0008 \pm 0.002$ | $-0.0002 \pm 0.0021$ | $-0.0058 \pm 0.0024$ | $-0.0008 \pm 0.0029$ | $-0.0079 \pm 0.0019$ |
| [Mn/Fe] | $-0.0108 \pm 0.0011$ | $-0.0064 \pm 0.0021$ | $-0.0060 \pm 0.0026$ | $-0.0037 \pm 0.0030$ | $0.0101 \pm 0.0038$ |
| [Fe/H] | $-0.0353 \pm 0.0031$ | $-0.0150 \pm 0.0020$ | $-0.0180 \pm 0.0031$ | $-0.0286 \pm 0.0042$ | $-0.0441 \pm 0.0049$ |
| [Co/Fe] | $0.0013 \pm 0.0015$ | $-0.0298 \pm 0.0004$ | $-0.0067 \pm 0.0015$ | $-0.0101 \pm 0.0012$ | $-0.0114 \pm 0.0022$ |
| [Ni/Fe] | $0.0077 \pm 0.0009$ | $-0.0017 \pm 0.0008$ | $-0.0003 \pm 0.0007$ | $-0.0009 \pm 0.0009$ | $-0.0011 \pm 0.0011$ |
| [Ce/Fe] | $-0.0367 \pm 0.0069$ | $0.0017 \pm 0.0058$ | $0.0047 \pm 0.0085$ | $0.0121 \pm 0.0065$ | $0.0026 \pm 0.0099$ |
| [Nd/Fe] | $0.0150 \pm 0.0080$ | $-0.0133 \pm 0.0068$ | $0.0079 \pm 0.0045$ | $0.0220 \pm 0.0039$ | $-0.0046 \pm 0.007$ |

in [N/Fe], but there is a larger jaggedness (see Figure 3.4). Much like [N/Fe], there is a large increase in the central [(C+N)/Fe], but this is much less abrupt starting between 3.7 and 5.6 Gyr ago and gradually increasing up to the present day (see Figure 3.7). In contrast, [C/N] shows a different evolutionary behavior. The [C/N] gradient changes almost linearly from $-0.03$ at old ages to $+0.015$ at the youngest ages. We can understand this change by remembering that [C/N] is sensitive to age for RGB stars, since the dredge-up of material is sensitive to mass. [C/N] generally increases with [Fe/H] for RGB stars until [Fe/H]$\approx-0.6$ and then decreases. At the metal-rich end ([Fe/H]$>-0.5$), [C/N] increases with age relative to the [Fe/H] trend (see Figure 2 in Hasselquist et al. 2020). The age-behavior for metal-poor RGB stars has not been characterized yet. One possible interpretation of the age dependent behavior of the [C/N] gradient, is that it is merely a result of the metallicity evolution at different radii. However, the [Fe/H] gradient does not follow this pattern, as can be seen in Figure 3.5. Instead, the [C/N] is likely the result of the changing age distribution at different radii. Old stars exist at essentially all radii in the LMC, while the youngest stars are more centrally concentrated because the radius of the star forming region decreases over time.

As for the [X/H] gradients for C and N the [C/H], [N/H], and [(C+N)/H] gradients all show a peculiar trend in their evolution. Each of these abundances start steep, but flatten out over time until just after 2.2 Gyr ago when the gradients become steeper again. This U-shaped trend is interesting as the extremum point matches in each trend (see Figure 3.5). The [C/Mg] gradient also shares this behaviour, but the [N/Mg] and [(C+N)/Mg] gradients do not.

<u>$\alpha$-Elements</u> Many of the [X/Fe] gradients for the individual $\alpha$-elements show a curious U-shaped trend as well as some of the composite abundances (see Figure 3.4). Abundances that show a flattening positive gradient and then more recent steepening include [O/Fe], [Mg/Fe], [S/Fe], [Ca/Fe], [Ti/Fe], [$\alpha$/Fe], and [$\alpha_{\rm ex}$/Fe]. To a lesser extent, signs of this trend

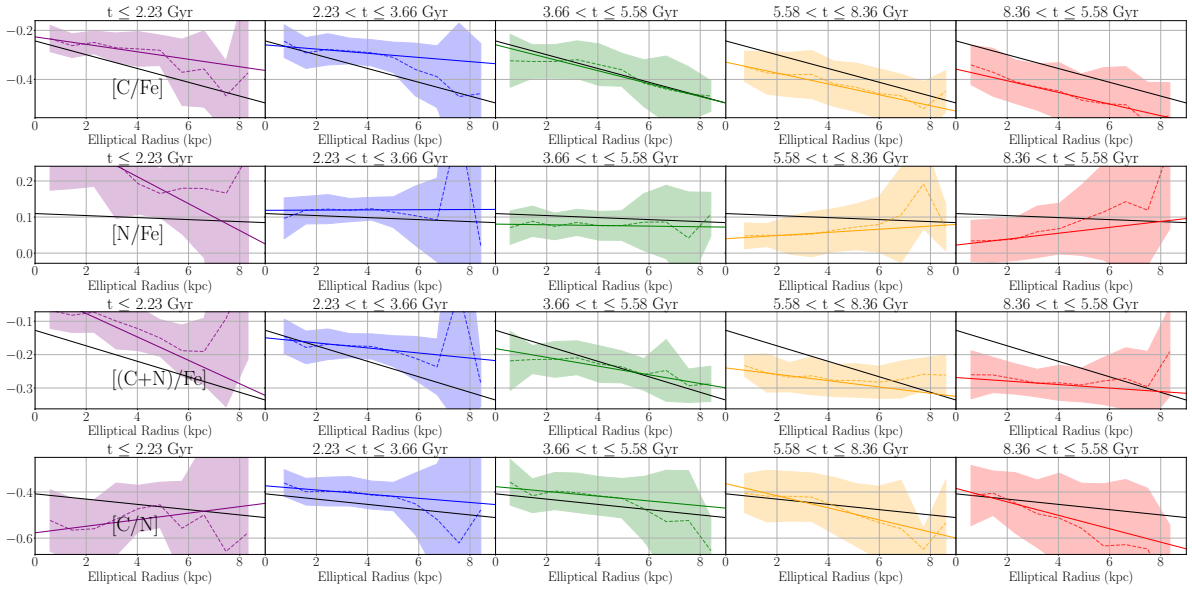



Figure 3.7: The radial abundance trends for the measured C and N abundances in the LMC. The particular abundance can be seen in the left more panel of each row. For each row, age increases from left to right with colored lines representing the linear model fits to the binned values. A correspondingly colored dashed line represents the binned median abundance value with the band showing the dispersion. A black line in a panel shows the overall radial abundance trend without age binning and functions as a fiducial here. These plots show that different C and N abundances increase over time in the galaxy, with the trends below the fiducial for older age bins and above for younger age bins. Also the [C/N] gradient clearly inverts for the youngest age bin. The range for each panel for a row is based on the fiducial line and does result in some trends being cut off in an effort to capture the overall differences among panels.

are seen in [Si/Fe], where its gradient flattens but then stays around +0.0060 dex/kpc. The [$\alpha_{\rm h}$/Fe] gradient shows a downward trend and inverts between 5.6 and 3.7 Gyr ago. For the most part, Figures 3.10 and 3.11 show that the radial trends evolve much in the same way regardless of the abundance.

The [X/H] gradients for the $\alpha$-element abundances all show similar evolutionary trends. All but [Ti/H] and [$\alpha_{\rm ex}$/H] show an inverted U-shaped trend with an extremum point around $\lesssim$2.2 Gyr (see Figure 3.4). Unlike the [X/Fe] gradients, there is much more consistency across different elements.

The [O/Mg], [Si/Mg], [$\alpha$/Mg], and [$\alpha_{\rm h}$/Mg], as well as potentially [Ca/Mg], gradients all evolve in a similar manner. For most of the history of the LMC, these gradients do not change until 2.2 Gyr ago. All of these elements have very slightly positive gradients, but the youngest stars have slightly negative ones.

Odd-Z Elements The evolution of the [Na/Fe] and [Al/Fe] gradients are quite interesting because they both start out positive but become negative and finally flatten out again (see Figure 3.4). Initially, the [Na/Fe] gradients do not evolve until more recently than 5.58 Gyr ago as the two oldest bins have gradients of +0.0163 $\pm$ 0.0053 dex/kpc and +0.0166 $\pm$ 0.0045 dex/kpc. Unlike [Na/Fe], the [Al/Fe] gradient immediately starts to flatten, going from +0.0103 $\pm$ 0.0021 dex/kpc to +0.0031 $\pm$ 0.0021 dex/kpc. In fact, it appears that the evolution in the [Na/Fe] gradient lags the analogous evolution in the [Al/Fe] gradient. This is somewhat reflected in the radial trends in Figure 3.12. The [K/Fe] gradient starts very similar to the [Al/Fe] gradient, but it jumps up becoming steeper in the third age bin before flattening out up to present day. The radial trend for [K/Fe] shows also that the central abundance does not change much over time.

As for the [X/H] gradients of the odd-Z elements, [K/H] evolves much like what is seen for the C and N gradients as well as the $\alpha$-element gradients (see Figure 3.5). The

evolutionary trend for [Na/H] has some jaggedness where the gradient for ages between 5.58 and 8.36 Gyr is steep with a value of $-0.0301 \pm 0.0015$ dex/kpc, while the oldest stars and stars ages 3.66–5.58 Gyr have gradients of $-0.0071 \pm 0.0058$ dex/kpc and $-0.0100 \pm 0.0056$ dex/kpc respectively. The youngest gradients for [Na/H] are then steeper and more negative than any of these values. The [Al/H] gradient does not experience much evolution until about 5.6 to 3.7 Gyr ago when there is an abrupt steepening in the gradient with a slight upturn for stars younger than 2.2 Gyr.

The [Na/Mg] gradient evolution is reminiscent of the [Na/H] evolution (see Figure 3.6). On the other hand, the [Al/Mg] gradient stays almost flat for the entire history of the LMC and then for the youngest stars the gradient becomes $-0.0172 \pm 0.0021$ dex/kpc. The [K/Mg] gradient shows even less evolution than [Al/Mg], by remaining flat even for the youngest ages.

Iron Peak Elements The iron peak [X/Fe] abundances show varied evolution in their gradients (see Figure 3.4). The [V/Fe] and [Cr/Fe] both show an upward trend, though this is more prominent for [V/Fe]. Interestingly, the radial trends of these elements reveal that there is not much change in their central abundance (see Figure 3.13). The [Mn/Fe] gradients stands out among the iron peak [X/Fe] gradients as it is the only one that has a downward trend. The [Mn/Fe] gradient starts at $+0.0101 \pm 0.0038$ dex/kpc for the oldest age, but then in the next age bin the gradient has inverted and become $-0.0037 \pm 0.0030$ dex/kpc. From there it continues to become even more negative over time. The radial trend for [Mn/Fe] also shows a large increase in the central abundance between the oldest and second oldest age bins, but then increases less drastically afterwards, corresponding to what is seen in the gradient. Unlike any other [X/Fe] gradient, the overall gradient without age binning falls outside the range suggested by the evolutionary trend of the gradient. The cause of this behavior is not clear, but is most likely due to some effects caused by the

binning. The evolution of the [Co/Fe] gradient is also quite unique with a clear increasing trend, but the gradient for the ages between 2.2–3.7 Gyr has an anomalous value of $-0.0298 \pm 0.0004$ dex/kpc.

Similarly to many other groups of elements, the majority of the [X/H] gradients for the iron peak show an inverted U-shaped with an extremum point at the same age (see Figure 3.5). [Cr/H] and [Mn/H] are the only abundances that do not show this trend, though [Mn/H] deviates more than [Cr/H] from the "normal" pattern. As with the overall [Mn/Fe] gradient, the overall [Mn/H] gradient is unusually negative with a value of $-0.1024 \pm 0.0040$ dex/kpc, which is $\sim$0.0400 dex/kpc from the closet gradient when binning by age.

The [X/Mg] for the [Cr/Mg] and [Fe/Mg] both show the previously mentioned inverted U-shaped trend while the other iron peak elements do not (see Figure 3.6). The [V/Mg] gradient shows a flattening over time becoming shallower. The [Mn/Mg] gradient shows a similar pattern, albeit scaled version, to the trend in [Mn/H]. The [Mn/Mg] gradient initially shows a downward trend until 2.23–3.66 Gyr ago, when it suddenly flattens before becoming relatively steep for the youngest stars with value of $-0.0284 \pm 0.0018$ dex/kpc. Now looking at [Co/Mg] and [Ni/Mg], these two elements show opposite behaviors in the evolution of their gradients. The [Co/Mg] gradient starts at $-0.0154 \pm 0.0027$ dex/kpc and then increases to $\sim -0.0060$ dex/kpc up to the present. Conversely, the [Ni/Mg] gradient shows little evolution remaining at $\sim -0.0020$ dex/kpc and then dropping to $-0.0072 \pm 0.0012$ dex/kpc for young ages.

Neutron Capture Elements For the neutron capture elements, there are not as many stars with well-measured abundances. The [Ce/Fe] and [Nd/Fe] gradients show an inverted U-shaped trend in their respective evolution (see Figure 3.4). For [Ce/Fe], the only gradient that decisively deviates from the general trend is the very steep youngest gradient with a value of $-0.0367 \pm 0.0069$ dex/kpc. There is a delay in the increase of the central [Ce/Fe]

value, which only slightly changes until the most recent ages where there is a sharp increase (see Figure 3.14). The [Nd/Fe] gradient evolution is similar to [S/Fe] but shifted to lower values.

Both the [Ce/H] and [Nd/H] abundance gradients show signs of the inverted U-shaped evolution present in the [X/H] gradients of almost all the elements (see Figure 3.5). This is not the case for the [X/Mg] gradients, as seen in Figure 3.6. The [Ce/Mg] gradient stays around +0.0015–0.0020 dex/kpc and then becomes quite steep at $-0.0507 \pm 0.0123$ dex/kpc. The [Nd/Mg] gradient does show what appears to be a U-shaped trend with an extremum point at the same time as seen in other abundance gradients.

Age-[X/Fe] Trends

So far we have discussed the behavior of radial abundance gradients and their temporal evolution. However, with our age information we can directly investigate how abundances change with age across the entire galaxy and also separated into different spatial regions. As shown in Figure 3.3, we break the spatial coverage into three radial zones and then into a North and South region.

Carbon & Nitrogen Figure 3.8 shows the age-[X/Fe] trends for [C/Fe], [N/Fe], and [(C+N)/Fe] separated into the six spatial zones. The age-[X/Fe] trends for [C/Fe], [N/Fe], and [(C+N)/Fe] are relatively flat, especially [N/Fe] and [(C+N)/Fe], up to 5 Gyr ago. For radii beyond 4.8 kpc, the LMC appears to be deficient in these abundances for both the north and south, although in the south, stars older than 12 Gyr follow the fiducial age-trend. The inner galaxy, on the other hand, is overabundant in these elements, especially for ages greater than 5 Gyr, while intermediate radii follow the fiducial age-trend quite well. The age-[N/Fe] trend follows the fiducial very well throughout the galaxy and appears to exponentially increase starting between 2 and 5 Gyr ago. Much like [N/Fe], [(C+N)/Fe] is nearly constant for the oldest ages and is deficient in the outer galaxy, much like [C/Fe].

The increase seen within the last 5 Gyr is quite linear similar to [C/Fe] but unlike [N/Fe].

The age-[C/N] trend is mostly flat throughout the LMC. The outer radial region shows that the periphery is low in [C/N] while the inner galaxy is rich in [C/N] except for the youngest stars with ages less than 2.5 Gyr. There is also a prominent downturn for young ages for the inner galaxy and especially for $3.3 < \mathrm{R} \leq 4.8$ kpc.

$\alpha$-Elements Most of the age-[X/Fe] trends for the $\alpha$-elements do not show much evolution (see Figure 3.15). An interesting feature shared by many of these elements ([O/Fe], [Mg/Fe], [Si/Fe], [Ca/Fe], and [Ti/Fe]) is a hump-like feature for younger stars. Each of the elements show an increase in the [X/Fe] abundance starting around $5.0-7.5$ Gyr ago with a peak $\lesssim 2.5$ Gyr ago followed by a drop off for the youngest stars. The only element for which this is not seen in the individual $\alpha$-elements is [S/Fe], which remains mostly constant with time. For the inner radii, stars older than about 7.5 Gyr are deficient in [O/Fe], [Si/Fe], and slightly in [Ti/Fe] as these trends fall below the fiducial trend. The outer LMC in the south is especially overabundant in [O/Fe] and the outer LMC is [Si/Fe]-rich.

The composite $\alpha$-element abundances as a function of age look very similar to the individual elements, which is not unexpected (see Figure 3.16). [$\alpha$/Fe], [$\alpha_{\mathrm{h}}$/Fe], and [$\alpha_{\mathrm{ex}}$/Fe] all show the hump seen in the individual $\alpha$-elements. The [$\alpha_{\mathrm{h}}/\alpha_{\mathrm{ex}}$] age-[X/Fe] trend evolves much like the [S/Fe] as it is flat over the lifetime of the LMC and there is potentially a slight downturn close to the present day.

Odd-Z Elements The age-[Na/Fe] trend is mostly flat suggesting [Na/Fe] production has been constant (see Figure 3.17). Curiously, the outer LMC is [Na/Fe]-rich as the trends in both the north and south show, though this is less true for more recent times. For $\mathrm{R} < 4.8$ kpc, the age-[Na/Fe] trend follows the fiducial in the south. Also, on average, the inner northern region seems to follow the fiducial.

Of the odd-Z elements, [Al/Fe] has the most dramatic change at younger ages, as seen

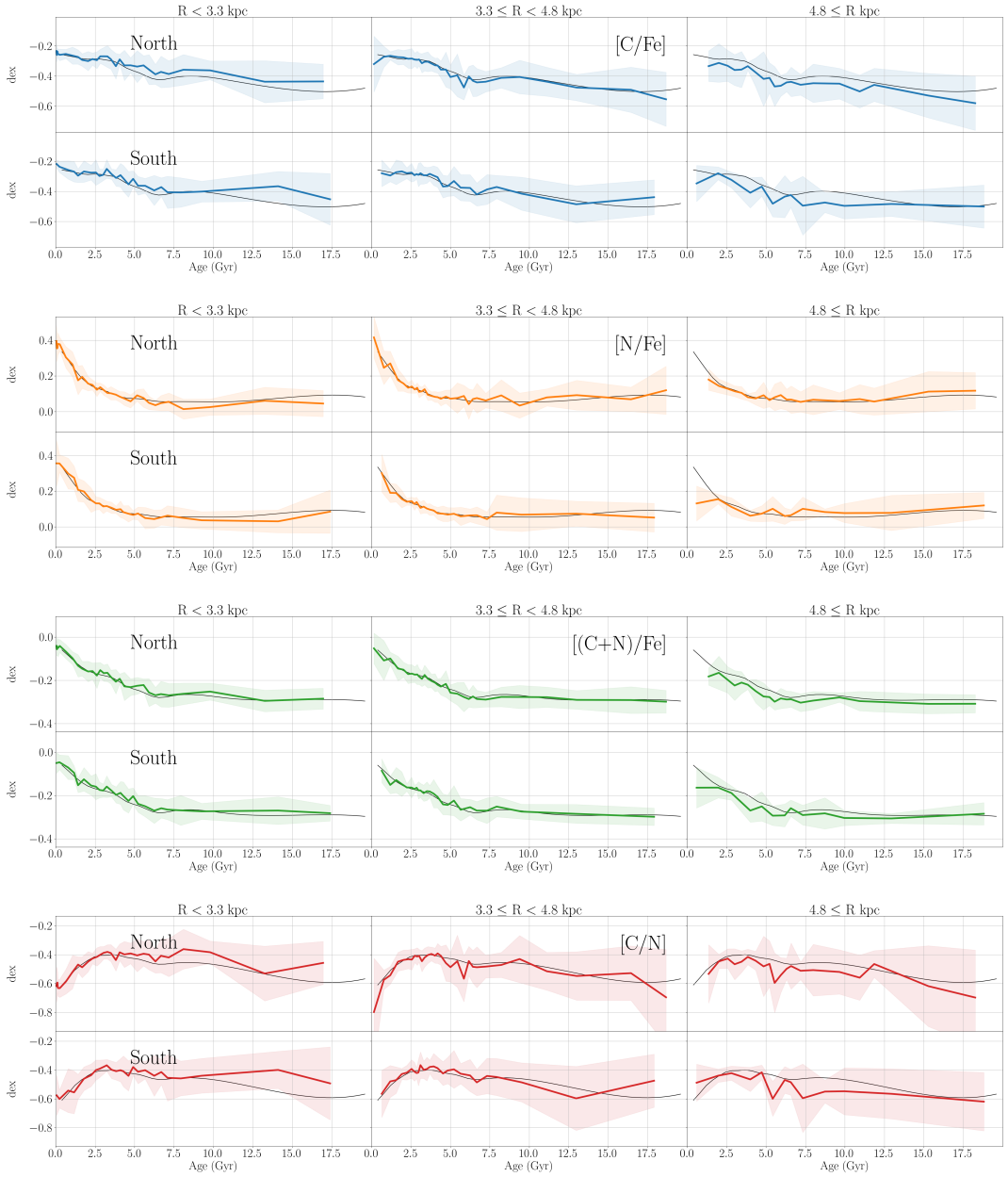



Figure 3.8: The age-[X/Fe] trends for the LMC for C and N. The top row in each panel shows the age-[X/Fe] trends for the northern part of the LMC and the bottom row shows the trends in the south. The LMC is split into three radial bins that contain an equal number of stars. For each sub-panel the age-[X/Fe] trend is included with a band of $1\sigma$ in addition the black fiducial line shows the age-[X/Fe] trend without any binning. Clearly the [N/Fe] and [(C+N)/Fe] have a sharp increase for recent times.

in the middle panel of Figure 3.17. Starting between 5.0 and 7.5 Gyr ago, the production of [Al/Fe] ramps up with a change of almost +0.2 dex. Before this, the age-[Al/Fe] trend is relatively flat. The inner northern LMC follows the fiducial trendline very closely, while, in contrast, the trend in the inner southern LMC shows the galaxy is slightly [Al/Fe]-poor. Both the north and south follow the fiducial trend in the intermediate radial annulus ($3.3 \leq$ R $< 4.8$ kpc), though at extremely old ages ($12 \leq$ age) the galaxy is [Al/Fe]-rich. For the outer galaxy, there is a small [Al/Fe] deficiency in the south as the age-[Al/Fe] trend falls slightly below the fiducial trendline, while the north is slightly above the trendline at the oldest ages.

While [Na/Fe] has a flat age trend and [Al/Fe] is mostly constant with an increasing trend for more recent times, [K/Fe] is fairly constant for older ages and within the last few Gyr has a hump (slow increase with sudden drop at the youngest ages; see bottom panel of Figure 3.17). For ages older than $5.0-7.5$ Gyr, the age-abundance trend is flat and slightly overabundant, though younger stars appear to be somewhat deficient. The intermediate radii ($3.3 \leq$ R $< 4.8$ kpc) for the north and south follow the fiducial trendline. The inner radii (R $< 3.3$ kpc) show a distinctive hump at young ages. This hump tends to be weaker in the south than in the north.

Iron Peak Elements The age-[X/Fe] trends for the iron-peak elements are very flat except for [Mn/Fe] and [Fe/H]. While [Mn/Fe] tends to follow its fiducial trendline very closely, this is not true for [Fe/H]. The outer galaxy is lacking in [Fe/H] for the north and the south. More often than not, the other LMC positional regions are [Fe/H]-rich for older ages. This makes sense as a general enrichment of Fe over time.

[Co/Fe] shows a hump like many of the other non-iron peak elements. There are some faint hints of a hump in other iron peak elements, but nowhere as strong as for Co. Like the other elements with the hump, it is the most prominent in the inner galaxy.

[V/Fe], [Cr/Fe] and [Ni/Fe] have flat trends, but a downturn that is strongest in the inner galaxy for [V/Fe] and [Ni/Fe], but not for [Cr/Fe]. [Cr/Fe] is flat and remains flat while also matching the fiducial trendline. Contrary to the other flat age-[X/Fe] trends, [V/Fe] is low in the outer galaxy.

Neutron Capture Elements For the neutron capture elements, we only use two radial bins due to the low number of stars with good neutron capture abundance measurements. The first radial bin corresponds to the inner disk region with R $<$ 3.5 kpc and the second radial bin includes everything outside of 3.5 kpc. The 3.5 kpc boundary was chosen based on Choi et al. (2018a), specifically, the fact that the inner disk corresponds to radii that are $\lesssim$ 3.5 kpc.

The [Ce/Fe] abundance increases with time, though a dramatic change happens for stars born around 2.5 Gyr ago (see Figure 3.19). Generally, the age-[Ce/Fe] trend for each of the radial bins follows the fiducial trendline. The outer galaxy in the south seems to have the largest deviation from the fiducial.

Unlike [Ce/Fe], the age-[Nd/Fe] trend is mostly flat for all ages with no noticeable increase (see Figure 3.19). Compared to [Ce/Fe], there are even less stars with reliable values of [Nd/Fe], which is obvious when looking at the trends. Each of the northern bins has $\sim$130 stars, while the southern bins only have $\sim$60 each. The age-[Nd/Fe] trends seem to follow the fiducial, but the inner southern field shows a [Nd/Fe] deficiency.

## Discussion

Here we discuss the relationship between the abundance gradients, the age-[X/Fe] trends and the chemical evolution for the LMC.

LMC Metallicity Gradient

The LMC was found to have an overall metallicity gradient of $-0.0380 \pm 0.0022$ dex/kpc. This value agrees with the value of $-0.035 \pm 0.0020$ dex/kpc found using ratios of C- and M-type AGB stars, the value of $-0.0500 \pm 0.0370$ dex/kpc found by Feast et al. (2010) using photometric metallicities of a sample of AGB stars, and the value of $-0.0300 \pm 0.0070$ dex/kpc found by Haschke et al. (2012) also using photometric metallicities (see Table 3.8 and Figure 3.9).

Cioni (2009) explores the metallicity gradients of Clouds and M33 using the C/M ratio. It was shown that the ratio of C- to M-type AGB stars in a region corresponds to the average [Fe/H] by Battinelli & Demers (2005). Calculating the [Fe/H] gradient in the LMC with the C/M ratio gives a value of $-0.035 \pm 0.0020$ dex/kpc out to $\sim$10 kpc. This agrees quite well with the derived gradient in this work. By removing all [Fe/H] measurements for which $\sigma_{[Fe/H]} > 0.2$ gives a value of $-0.0470 \pm 0.0030$ dex/kpc for the subset. This gradients does not overlap with the calculated overall gradient here, but it does agree with the gradient found for the oldest stars.

It has been shown that there is a relation between the period and [Fe/H] of RR Lyrae stars (e.g. Layden, 1995; Sandage, 1993; Sarajedini et al., 2006). In Feast et al. (2010), they make use of two different [Fe/H]-Period relations to calculate the metallicity gradient in the LMC. Their dataset comes from OGLE (Soszyński et al., 2009) and extends out to 5 kpc in the LMC with stars brighter than an I magnitude of 13.8. They also calculate the metallicity gradient for a sample of AGB stars. Only one of the gradients calculated for the [Fe/H]-Period relation overlaps with the calculated gradients. The gradient derived using Equation 2 in that work agrees with the youngest two [Fe/H] gradients, but not the overall calculated one. The AGB gradient actually overlaps with the overall gradient as well as all of the gradients for each age bin, but the AGB gradient does have a large uncertainty.

Haschke et al. (2012) and Wagner-Kaiser & Sarajedini (2013) also derive metallicity

gradients using RR Lyrae and obtain similar values to each other. The Haschke et al. (2012) gradient has a value of $-0.0300 \pm 0.0070$ dex/kpc and the Wagner-Kaiser & Sarajedini (2013) gradient of $-0.0270 \pm 0.02$ dex/kpc, meaning these both match very well to the $5.58 <$ age $\leq 8.36$ [Fe/H] gradient of $-0.0286 \pm 0.0042$ dex/kpc. The Haschke et al. (2012) gradient also overlaps with the youngest [Fe/H] in addition to the overall gradient as previously mentioned. Also, the globular cluster gradient in Wagner-Kaiser & Sarajedini (2013) is much flatter than the one found with RR Lyrae stars (see Table 3.8 and Figure 3.9).

Another paper that calculates metallicity for the LMC is Grady et al. (2021). Grady et al. use photometric [Fe/H] calibrated with the APOGEE [Fe/H] values for 3,077 RGB stars out to 40° from the LMC center. The large difference between their value of $-0.0480 \pm 0.0010$ dex/kpc and our $-0.0380 \pm 0.0022$ dex/kpc value probably has to do with different selection criteria.

Another photometric study using the VMC data out to a radius of ∼6 kpc in the LMC (Choudhury et al., 2021) does not find radial gradients consistent with any calculated in our work. Using the total VMC LMC data and the slope of the RGB branch, a gradient of $-0.0080 \pm 0.0010$ dex/kpc was found and repeating the analysis for a calibration set found a slightly different gradient of $-0.0010 \pm 0.0010$ dex/kpc.

It is clear that there is considerable variation amongst different calculated metallicity gradients, even when using the same source type. This is also similar to the tension in the MW abundance gradients (e.g. Bragança et al., 2019). But with the high resolution of APOGEE as well as the number of observed stars and its coverage, the metallicity gradient in this work is the most reliable to date.

The Evolution of Abundance Gradients of the LMC

This is also one of the first studies to explore the evolution of abundance gradients in the LMC. In order to do this the ages of 6130 field RGB stars were derived in Paper I. The

Table 3.8: Table of literature values for the LMC [Fe/H] gradient. In the last column, RR Eq 1 and RR Eq 2 refer to two different period-[Fe/H] which are Equations 1 and 2 in Feast et al. (2010) respectively. Also for Choudhury et al. (2021) VMC corresponds to the gradient using the VMC survey data and Calibration is the gradient derived for the dataset used to calibrate the [Fe/H]-RGB slope relation. Grady et al. (2021) derives the gradient from [Fe/H] isochrones and calibrates them with APOGEE.

| Source | $\nabla_R$ (dex/kpc) | $\nabla_R$ Error (dex/kpc) | Method |
|---|---|---|---|
| Cioni et al. 2009 | −0.0350 | 0.0020 | C/M |
| —"— | −0.0470 | 0.0030 | C/M Subset |
| Feast et al. 2010 | −0.0104 | 0.0021 | RR Equation 1 |
| —"— | −0.0145 | 0.0029 | RR Equation 2 |
| —"— | −0.0500 | 0.0370 | AGB |
| Haschke et al. 2012 | −0.0300 | 0.0070 | RR |
| Wagner-Kasier et al. 2013 | −0.0270 | 0.0020 | RR |
| —"— | −0.0022 | 0.0013 | GCs |
| Grady et al. 2021 | −0.0480 | 0.0010 | RGB |
| Choudhury et al. 2021 | −0.0080 | 0.0010 | VMC |
| —"— | −0.0100 | 0.0010 | Calibration |

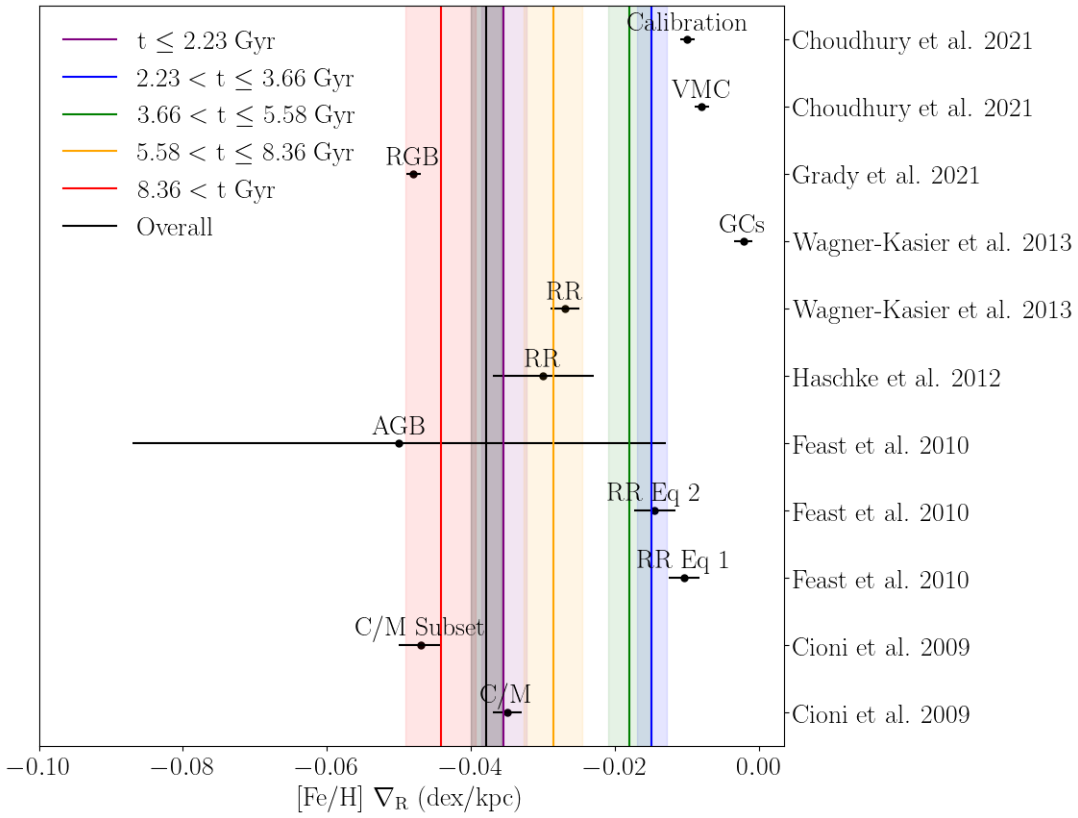



Figure 3.9: A comparison of the overall metallicity gradient found in this work for various literature values. The vertical black line represents the overall metallicity gradient and the black band represents the calculated error in the gradient. The gradient for each of the age bins is similarly shown. Choudhury et al. (2021); Cioni (2009); Feast et al. (2010) show agreement with the overall gradient, while other sources agree with the gradients found with different age bins in this work. In many cases, many of these sources calculate the gradient multiple ways. For more information see Section 3 and the references therein.

stars were then placed into five different age bins for each of which an abundance gradients was found. In the analysis, it was determined that changing the binning scheme did not greatly affect the results other than minor differences unless large scale changes were made.

Many gradients show a U-shaped trend in their abundance evolution with an extremum point between 2.33 and 3.66 Gyr ago. These abundances include: [O/Fe], [Mg/Fe], [Ca/Fe], [Ti/Fe], [$\alpha$/Fe], [$\alpha_{\rm ex}$/Fe], and [Al/Fe], most of the [X/H] gradients, [C/Mg], [Cr/Mg], and [Nd/Mg]. In addition, a similar trend is seen, albeit earlier, in the [Ti/Fe] and [Ti/Mg] gradients. With so many gradients sharing this feature, this is most likely due to a major event that shaped the overall chemical evolution of the LMC.

In addition, a majority of the age-[X/Fe] trends show an increase in the abundance values that starts around the same time as the beginning of this U-shaped trend, regardless of if there is a U-shaped trend in the respective gradient evolution. Also, this ramping up of abundance happens throughout the galaxy with the strongest effect in the central part of the LMC. Some of the age-[X/Fe] trends turn over and start to show a decrease in some abundances and the point of this critical point happens $\sim$1$-$2 Gyr ago which lines up with the extremum point in the gradient evolutionary trends. This provides additional evidence of a major chemistry altering event. Due to the proximity of the extremum point in the U-shaped gradient evolution trends and the increase in abundance seen in the age-[X/Fe] trends, these probably have a common cause.

The LMC is known to have experienced a starburst $\sim$2 Gyr ago due to a close interaction between the LMC and SMC (e.g. Harris & Zaritsky, 2009; Nidever et al., 2020). The LMC and SMC both show an increase in [$\alpha$/Fe] with respect to [Fe/H] for recent times, which indicates an increase in star formation in both galaxies. Based on the timing, this starburst event is the most likely cause for what is seen in the LMC abundance gradients and age-[X/Fe] trends. Galaxy interactions are known to induce bursts of star formation which have profound effects on the chemistry of the constituent galaxies. Observationally this has been

seen before in systems such the interacting dwarf pair dm1647+12, which show increased star formation (Privon et al., 2017). Further it can be inferred that the steepening of many gradients after the interaction with the SMC creating the U-shape is most likely due to metal poor gas being deposited onto the galaxy.

The Clouds are not in isolation and are two satellites of the MW. It turns out that the infall or crossing time of the Clouds was $\sim$1.5 – 2.0 Gyr ago when they entered the MW potential (Besla et al., 2007; Gómez et al., 2015; Kallivayalil et al., 2013; Patel et al., 2017). It is definitely possible that an interaction with the MW halo has shaped the evolution of the abundance gradients in the LMC. In Besla et al. (2012) it is was shown that many structures with recent star formation in the LMC are mainly due to a recent interaction with the SMC and less so the MW. This is taken as evidence that the LMC-SMC interaction is indeed more important for the evolution of the abundance gradients in the LMC than interactions with the MW.

As stated prior there is a possibility that radial migration has had an effect on the abundance gradients of the LMC. This means that the use of the term "evolutionary trend" is somewhat of a misnomer and it would be better to use "age-dependence trend" instead. It is expected that older stars will be affected more by radial migration as they have been around longer, so the gradients calculated for these stars are less likely to match their birth gradients.

In Lu et al. (2022) the affect of radial migration on the metallicity gradient for the MW was explored. In that work it was found that over time the metallicity gradient will flatten out starting with the oldest stars. Interestingly it was found that the MW metallicity gradient steepened 11–8 Gyr ago and that corresponds to a former dwarf galaxy merging with the MW leading to the creation of the present Gaia-Sausage-Enceladus (GSE) structure. Even with radial migration, a merger is still evident in the age-dependence of the metallicity gradient. The steepening in the MW is reminiscent of the LMC gradient steepening starting

$\sim$2 Gyr ago.

Specifically in simulations of dwarf galaxies it has been shown that radial migration only plays a minor role in metallicity gradients compared to larger galaxies (Schroyen et al., 2013). So it can be inferred that the gradients calculated for the LMC are much more reflective of reality than for large galaxies such as the MW or Andromeda.

## Summary

This paper presents the radial abundance trends for 25 abundance ratios and the evolution of their respective gradients. The main results of this paper are as follows:

- Using APOGEE data, the radial abundance gradients and their temporal evolution of 25 abundance ratios are presented.
- The LMC was found to have an overall metallicity gradient of $-0.0380 \pm 0.0022$ dex/kpc, which agrees with several literature values (e.g., Cioni, 2009; Feast et al., 2010; Haschke et al., 2012).
- Many of the abundance gradients have a U-shaped trend and share an extremum point 2.2–3.7 Gyr ago that corresponds to an interaction between the LMC and SMC (Hasselquist et al., 2021; Nidever et al., 2020).
- Many age-[X/Fe] trends show an increase in abundance just before the known LMC-SMC interaction and some of these trends show a hump with a maximum at the time of the interaction, further pinpointing it to $\sim$2 Gyr ago.

In the future, gradients and age-[X/Fe] trends could be used to study more dwarf galaxy interactions. With these results and similar results in the future, it may be possible to constrain dwarf galaxy simulations that handle mergers and interactions. Also, with a

larger sample size the relationship between the evolution of abundance gradients and galactic parameters can be explored.

This paper is the second in a series of three. In Paper I of the series, ages are determined for RGB stars in the LMC and used in this work to determine the evolution of radial abundance trends. Paper III will analyze the same trends as this work but in the SMC. To obtain the evolution of these trends for the SMC, a modified version of the age-determination method in Paper I will be used.

## Acknowledgements

J.T.P. acknowledges support for this research from the National Science Foundation (AST-1908331) and the Montana Space Grant Consortium Graduate Fellowship.

D.L.N. acknowledges support for this research from the National Science Foundation (AST-1908331)

D.G. gratefully acknowledges the support provided by Fondecyt regular n. 1220264. D.G. also acknowledges financial support from the Dirección de Investigación y Desarrollo de la Universidad de La Serena through the Programa de Incentivo a la Investigación de Académicos (PIA-DIDULS).

R. R. M. gratefully acknowledges support by the ANID BASAL project FB210003.

Funding for the Sloan Digital Sky Survey IV has been provided by the Alfred P. Sloan Foundation, the U.S. Department of Energy Office of Science, and the Participating Institutions.

SDSS-IV acknowledges support and resources from the Center for High Performance Computing at the University of Utah. The SDSS website is www.sdss.org.

SDSS-IV is managed by the Astrophysical Research Consortium for the Participating Institutions of the SDSS Collaboration including the Brazilian Participation Group, the Carnegie Institution for Science, Carnegie Mellon University, Center for Astrophysics

| Harvard & Smithsonian, the Chilean Participation Group, the French Participation Group, Instituto de Astrofísica de Canarias, The Johns Hopkins University, Kavli Institute for the Physics and Mathematics of the Universe (IPMU) / University of Tokyo, the Korean Participation Group, Lawrence Berkeley National Laboratory, Leibniz Institut für Astrophysik Potsdam (AIP), Max-Planck-Institut für Astronomie (MPIA Heidelberg), Max-Planck-Institut für Astrophysik (MPA Garching), Max-Planck-Institut für Extraterrestrische Physik (MPE), National Astronomical Observatories of China, New Mexico State University, New York University, University of Notre Dame, Observatário Nacional / MCTI, The Ohio State University, Pennsylvania State University, Shanghai Astronomical Observatory, United Kingdom Participation Group, Universidad Nacional Autónoma de México, University of Arizona, University of Colorado Boulder, University of Oxford, University of Portsmouth, University of Utah, University of Virginia, University of Washington, University of Wisconsin, Vanderbilt University, and Yale University.

This work has made use of data from the European Space Agency (ESA) mission *Gaia* (`https://www.cosmos.esa.int/gaia`), processed by the *Gaia* Data Processing and Analysis Consortium (DPAC, `https://www.cosmos.esa.int/web/gaia/dpac/consortium`). Funding for the DPAC has been provided by national institutions, in particular the institutions participating in the *Gaia* Multilateral Agreement.

*Software:* Astropy (Astropy Collaboration et al., 2013, 2018), Matplotlib (Hunter, 2007), NumPy (Harris et al., 2020), SciPy (Virtanen et al., 2020)

## Data Availability

All APOGEE DR17 data used in this study is publicly available and can be found at: `https://www.sdss4.org/dr17/data_access/`.

Table 3.9: A table of the gradients for each of the age bins using H as the fiducial element. Horizontal lines have been added marking the division of the previously defined groups of elements. In general descending down the table corresponds to an increase in atomic number. Each age bin has its own separate column.

| Element | $t \leq 2.23$ $\nabla_R$ (dex/kpc) | $2.23 < t \leq 3.66$ $\nabla_R$ (dex/kpc) | $3.66 < t \leq 5.58$ $\nabla_R$ (dex/kpc) | $5.58 < t \leq 8.36$ $\nabla_R$ (dex/kpc) | $8.36 < t$ $\nabla_R$ (dex/kpc) |
|---|---|---|---|---|---|
| [C/H] | $-0.0893 \pm 0.0027$ | $-0.0113 \pm 0.0042$ | $-0.0359 \pm 0.0047$ | $-0.0510 \pm 0.0056$ | $-0.0680 \pm 0.0077$ |
| [N/H] | $-0.0803 \pm 0.0054$ | $-0.0080 \pm 0.0029$ | $-0.0255 \pm 0.0031$ | $-0.017 \pm 0.0028$ | $-0.0222 \pm 0.0047$ |
| [(C+N)/H] | $-0.0732 \pm 0.0038$ | $-0.0694 \pm 0.0013$ | $-0.0325 \pm 0.0040$ | $-0.0405 \pm 0.0049$ | $-0.0520 \pm 0.0063$ |
| [O/H] | $-0.0439 \pm 0.0021$ | $-0.0491 \pm 0.0011$ | $-0.0181 \pm 0.0034$ | $-0.0216 \pm 0.0041$ | $-0.0323 \pm 0.0046$ |
| [Mg/H] | $-0.0309 \pm 0.0024$ | $-0.0135 \pm 0.0028$ | $-0.0229 \pm 0.0033$ | $-0.0297 \pm 0.0042$ | $-0.0308 \pm 0.0049$ |
| [Si/H] | $-0.0432 \pm 0.0025$ | $-0.0248 \pm 0.0019$ | $-0.0125 \pm 0.0032$ | $-0.0194 \pm 0.0039$ | $-0.0259 \pm 0.0048$ |
| [S/H] | $-0.0157 \pm 0.0036$ | $-0.0064 \pm 0.0058$ | $-0.0129 \pm 0.0058$ | $-0.0125 \pm 0.0071$ | $-0.0326 \pm 0.0116$ |
| [Ca/H] | $-0.0362 \pm 0.0027$ | $-0.0131 \pm 0.0023$ | $-0.0181 \pm 0.003$ | $-0.0266 \pm 0.004$ | $-0.0334 \pm 0.0051$ |
| [Ti/H] | $-0.0294 \pm 0.0034$ | $-0.0385 \pm 0.0045$ | $-0.0522 \pm 0.0121$ | $0.0603 \pm 0.0086$ | $0.0476 \pm 0.0151$ |
| [$\alpha$/H] | $-0.0451 \pm 0.0022$ | $-0.0283 \pm 0.0022$ | $-0.0201 \pm 0.0033$ | $-0.025 \pm 0.0041$ | $-0.0348 \pm 0.0052$ |
| [$\alpha_h$/H] | $-0.0479 \pm 0.002$ | $-0.0154 \pm 0.0027$ | $-0.0210 \pm 0.0033$ | $-0.0283 \pm 0.0042$ | $-0.0315 \pm 0.0047$ |
| [$\alpha_{ex}$/H] | $-0.0451 \pm 0.0026$ | $-0.0531 \pm 0.0014$ | $-0.0205 \pm 0.01$ | $0.0491 \pm 0.0082$ | $0.0424 \pm 0.013$ |
| [Na/H] | $-0.0607 \pm 0.0038$ | $-0.0439 \pm 0.0043$ | $-0.0100 \pm 0.0056$ | $-0.0301 \pm 0.0015$ | $-0.0071 \pm 0.0058$ |
| [Al/H] | $-0.0468 \pm 0.0038$ | $-0.0595 \pm 0.0015$ | $-0.0149 \pm 0.0048$ | $-0.0122 \pm 0.0068$ | $-0.0101 \pm 0.0083$ |

| | | | | | |
|---|---|---|---|---|---|
| [K/H] | $-0.0264 \pm 0.003$ | $-0.0108 \pm 0.0035$ | $-0.0185 \pm 0.0040$ | $-0.0276 \pm 0.0044$ | $-0.0265 \pm 0.0060$ |
| [V/H] | $-0.0190 \pm 0.0038$ | $-0.0143 \pm 0.0037$ | $-0.0362 \pm 0.0037$ | $-0.0529 \pm 0.0057$ | $-0.0647 \pm 0.0086$ |
| [Cr/H] | $-0.0378 \pm 0.0035$ | $0.0005 \pm 0.0035$ | $-0.086 \pm 0.0017$ | $-0.0267 \pm 0.0073$ | $-0.0418 \pm 0.0087$ |
| [Mn/H] | $-0.0627 \pm 0.0038$ | $-0.0049 \pm 0.0053$ | $-0.0267 \pm 0.0112$ | $0.0279 \pm 0.014$ | $0.0644 \pm 0.0136$ |
| [Fe/H] | $-0.0354 \pm 0.0031$ | $-0.0149 \pm 0.002$ | $-0.0179 \pm 0.0031$ | $-0.0286 \pm 0.0042$ | $-0.0439 \pm 0.0049$ |
| [Co/H] | $-0.0394 \pm 0.003$ | $-0.0443 \pm 0.0027$ | $-0.0241 \pm 0.0041$ | $-0.0333 \pm 0.0052$ | $-0.0499 \pm 0.0066$ |
| [Ni/H] | $-0.0311 \pm 0.0026$ | $-0.0085 \pm 0.0026$ | $-0.0274 \pm 0.0027$ | $-0.0304 \pm 0.0042$ | $-0.0381 \pm 0.0055$ |
| [Ce/H] | $-0.0875 \pm 0.0180$ | $-0.0142 \pm 0.0090$ | $-0.0232 \pm 0.0141$ | $-0.0096 \pm 0.0077$ | $-0.0270 \pm 0.0160$ |
| [Nd/H] | $-0.0367 \pm 0.0109$ | $-0.0163 \pm 0.0091$ | $-0.0061 \pm 0.0079$ | $-0.0205 \pm 0.0086$ | $-0.0114 \pm 0.0104$ |

Table 3.10: A table of the gradients for each of the age bins using H as the fiducial element. Horizontal lines have been added marking the division of the previously defined groups of elements. In general descending down the table corresponds to an increase in atomic number. Each age bin has its own separate column.

| Element | $t \leq 2.23$ $\nabla_R$ (dex/kpc) | $2.23 < t \leq 3.66$ $\nabla_R$ (dex/kpc) | $3.66 < t \leq 5.58$ $\nabla_R$ (dex/kpc) | $5.58 < t \leq 8.36$ $\nabla_R$ (dex/kpc) | $8.36 < t$ $\nabla_R$ (dex/kpc) |
|---|---|---|---|---|---|
| [C/Mg] | -0.0296 ± 0.0023 | -0.0073 ± 0.002 | -0.012 ± 0.0019 | -0.0223 ± 0.0025 | -0.0276 ± 0.0035 |
| [N/Mg] | -0.0514 ± 0.0035 | 0.0019 ± 0.0013 | 0.0016 ± 0.0012 | 0.0044 ± 0.0016 | 0.0081 ± 0.002 |
| [(C+N)/Mg] | -0.0368 ± 0.0024 | -0.0060 ± 0.0014 | -0.0087 ± 0.0013 | -0.0114 ± 0.0014 | -0.0091 ± 0.0019 |
| [O/Mg] | -0.0028 ± 0.0009 | 0.0041 ± 0.0007 | 0.0022 ± 0.0008 | 0.0042 ± 0.001 | 0.0035 ± 0.0013 |
| [Mg/H] | −0.0309 ± 0.0024 | −0.0135 ± 0.0028 | −0.0229 ± 0.0033 | −0.0297 ± 0.0042 | −0.0308 ± 0.0049 |
| [Si/Mg] | -0.0065 ± 0.0014 | 0.0087 ± 0.0013 | 0.0076 ± 0.0008 | 0.0089 ± 0.0011 | 0.0095 ± 0.0018 |
| [S/Mg] | 0.0075 ± 0.0038 | 0.0159 ± 0.0056 | 0.0120 ± 0.0062 | 0.0383 ± 0.0047 | -0.0045 ± 0.0112 |
| [Ca/Mg] | -0.0085 ± 0.0013 | 0.0000 ± 0.0012 | 0.0013 ± 0.0012 | 0.0013 ± 0.0014 | -0.0022 ± 0.0016 |
| [Ti/Mg] | -0.0037 ± 0.0019 | -0.007 ± 0.0029 | -0.0229 ± 0.0026 | -0.0023 ± 0.0054 | 0.0170 ± 0.0044 |
| [$\alpha$/Mg] | -0.0054 ± 0.0009 | 0.0015 ± 0.0009 | -0.0005 ± 0.0008 | 0.0007 ± 0.0011 | 0.0004 ± 0.0012 |
| [$\alpha_h$/Mg] | -0.0014 ± 0.0004 | 0.0021 ± 0.0004 | 0.0011 ± 0.0004 | 0.0021 ± 0.0005 | 0.0017 ± 0.0006 |
| [$\alpha_{ex}$/Mg] | -0.0068 ± 0.0012 | -0.0002 ± 0.0018 | -0.0053 ± 0.0017 | 0.0016 ± 0.0020 | 0.0056 ± 0.0026 |
| [Na/Mg] | -0.0173 ± 0.0033 | 0.0020 ± 0.0041 | 0.0141 ± 0.0038 | 0.0079 ± 0.0042 | 0.0131 ± 0.0046 |
| [Al/Mg] | -0.0172 ± 0.0021 | 0.0044 ± 0.0017 | 0.0019 ± 0.0018 | 0.0022 ± 0.0015 | 0.0024 ± 0.0021 |

| | | | | | |
|---|---|---|---|---|---|
| [K/Mg] | 0.0029 ± 0.0021 | 0.002 ± 0.0016 | 0.0054 ± 0.0017 | 0.0007 ± 0.0018 | 0.0037 ± 0.0024 |
| [V/Mg] | -0.0032 ± 0.003 | -0.0076 ± 0.0020 | -0.0121 ± 0.002 | -0.0173 ± 0.0026 | -0.0212 ± 0.004 |
| [Cr/Mg] | -0.0172 ± 0.0025 | -0.0006 ± 0.0028 | -0.0049 ± 0.0028 | -0.0066 ± 0.0036 | -0.0099 ± 0.0041 |
| [Mn/Mg] | -0.0284 ± 0.0018 | -0.0035 ± 0.0020 | -0.013 ± 0.0012 | 0.0041 ± 0.004 | 0.0086 ± 0.0043 |
| [Fe/Mg] | -0.0685 ± 0.0052 | -0.0388 ± 0.0048 | -0.0417 ± 0.0062 | -0.0575 ± 0.0084 | -0.0727 ± 0.0103 |
| [Co/Mg] | -0.0060 ± 0.0017 | -0.0059 ± 0.0019 | -0.0050 ± 0.0018 | -0.0054 ± 0.0018 | -0.0154 ± 0.0027 |
| [Ni/Mg] | -0.0072 ± 0.0012 | -0.0013 ± 0.0013 | -0.0019 ± 0.0013 | -0.0027 ± 0.0016 | -0.0048 ± 0.0017 |
| [Ce/Mg] | -0.0507 ± 0.0123 | 0.0103 ± 0.0088 | 0.0017 ± 0.0076 | 0.0075 ± 0.0081 | 0.0018 ± 0.0075 |
| [Nd/Mg] | 0.0020 ± 0.0099 | -0.0141 ± 0.0082 | 0.0022 ± 0.0097 | -0.0001 ± 0.0087 | 0.0188 ± 0.0082 |

## $\nabla_R$[X/H] & $\nabla_R$[X/Mg] Tables

The tables for the [X/H] and [X/Mg] gradients, which do not appear in the main body of the paper.

## Radius-[X/Fe]-Age Trends

The radius-[X/Fe]-age trends for the $\alpha$-elements, odd-Z elements, iron peak elements and neutron capture elements, which do not appear in the main body of the paper.

## age-[X/Fe] Trends

The age-[X/Fe] trends for the $\alpha$-elements, odd-Z elements, iron peak elements and neutron capture elements, which do not appear in the main body of the paper.

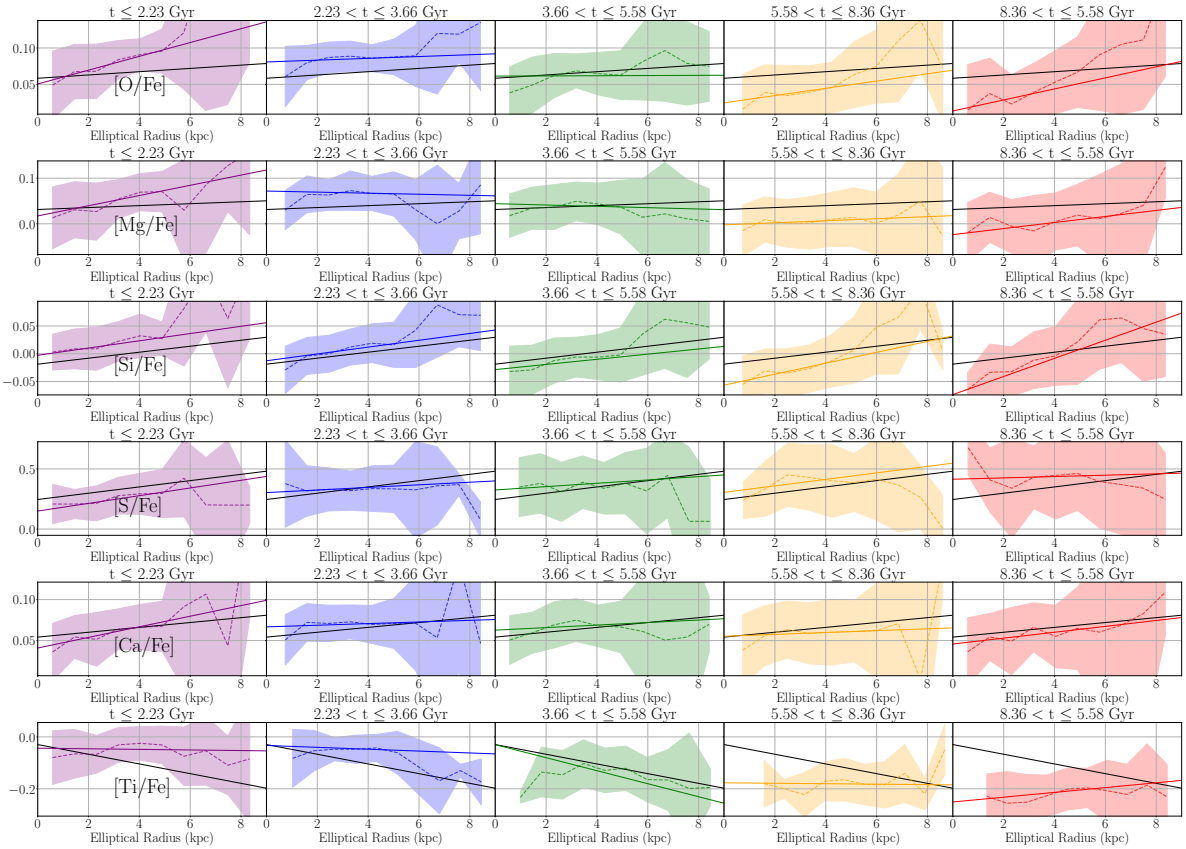



Figure 3.10: The same as for Figure 3.7, but with the individual $\alpha$-element abundances.

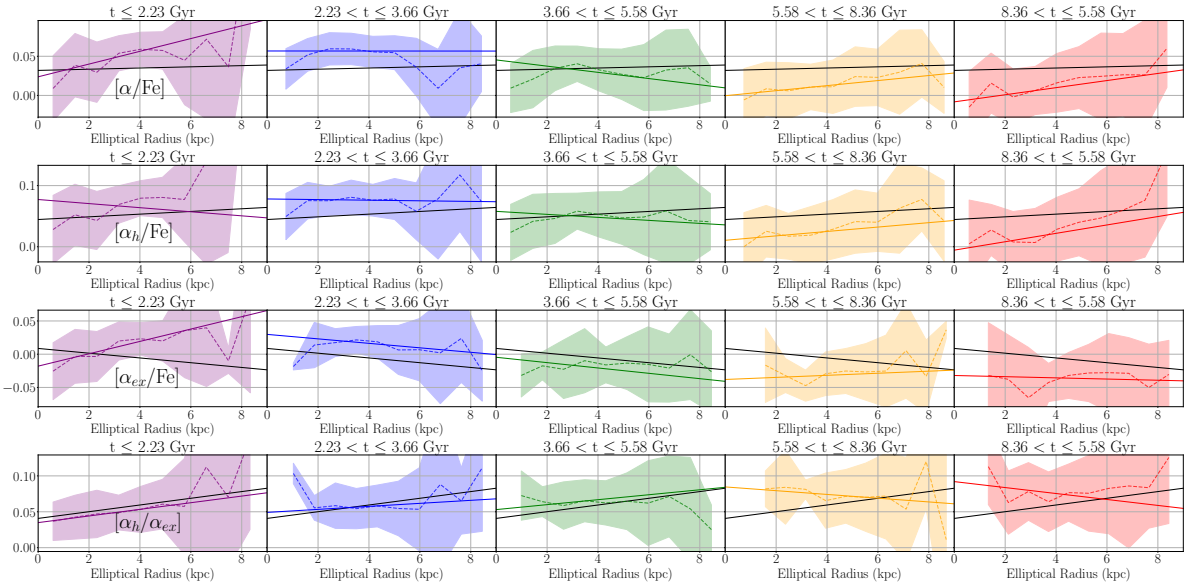



Figure 3.11: The radial abundance trends for the composite $\alpha$-element abundances.

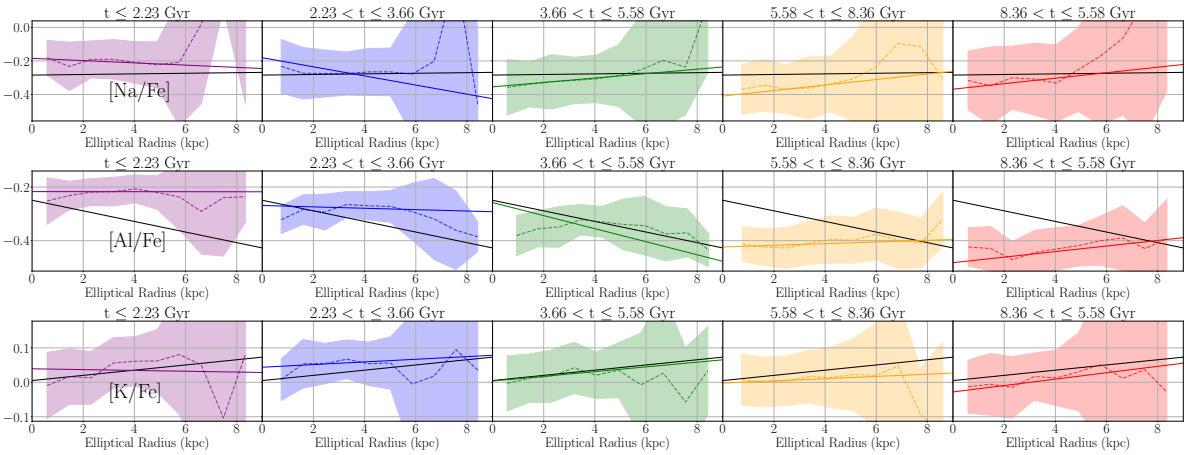



Figure 3.12: The radial abundance trends for the odd-Z abundances.

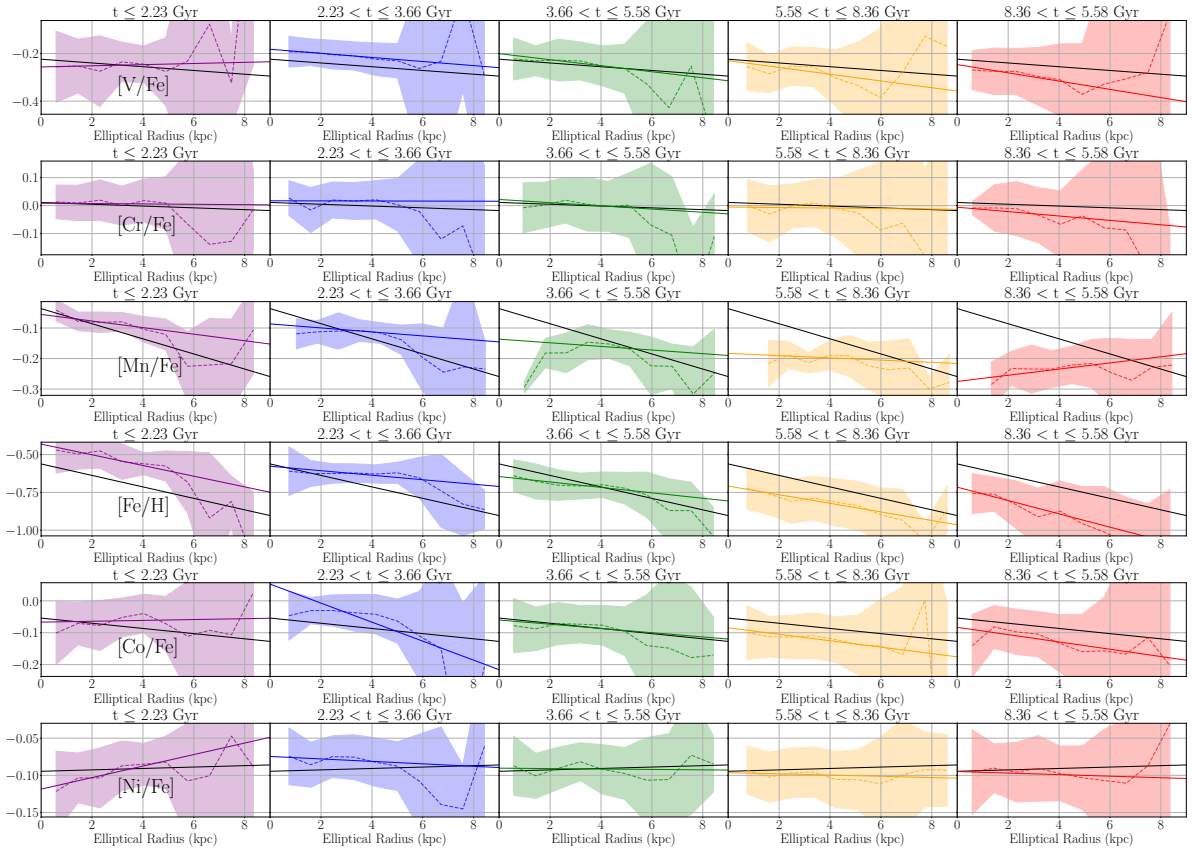



Figure 3.13: The radial abundance trends for the iron peak abundances.

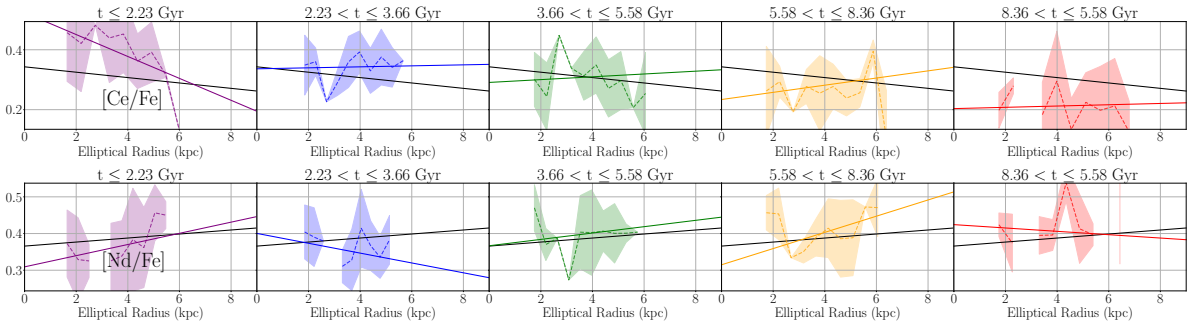



Figure 3.14: The radial abundance trends for the neutron capture abundances.

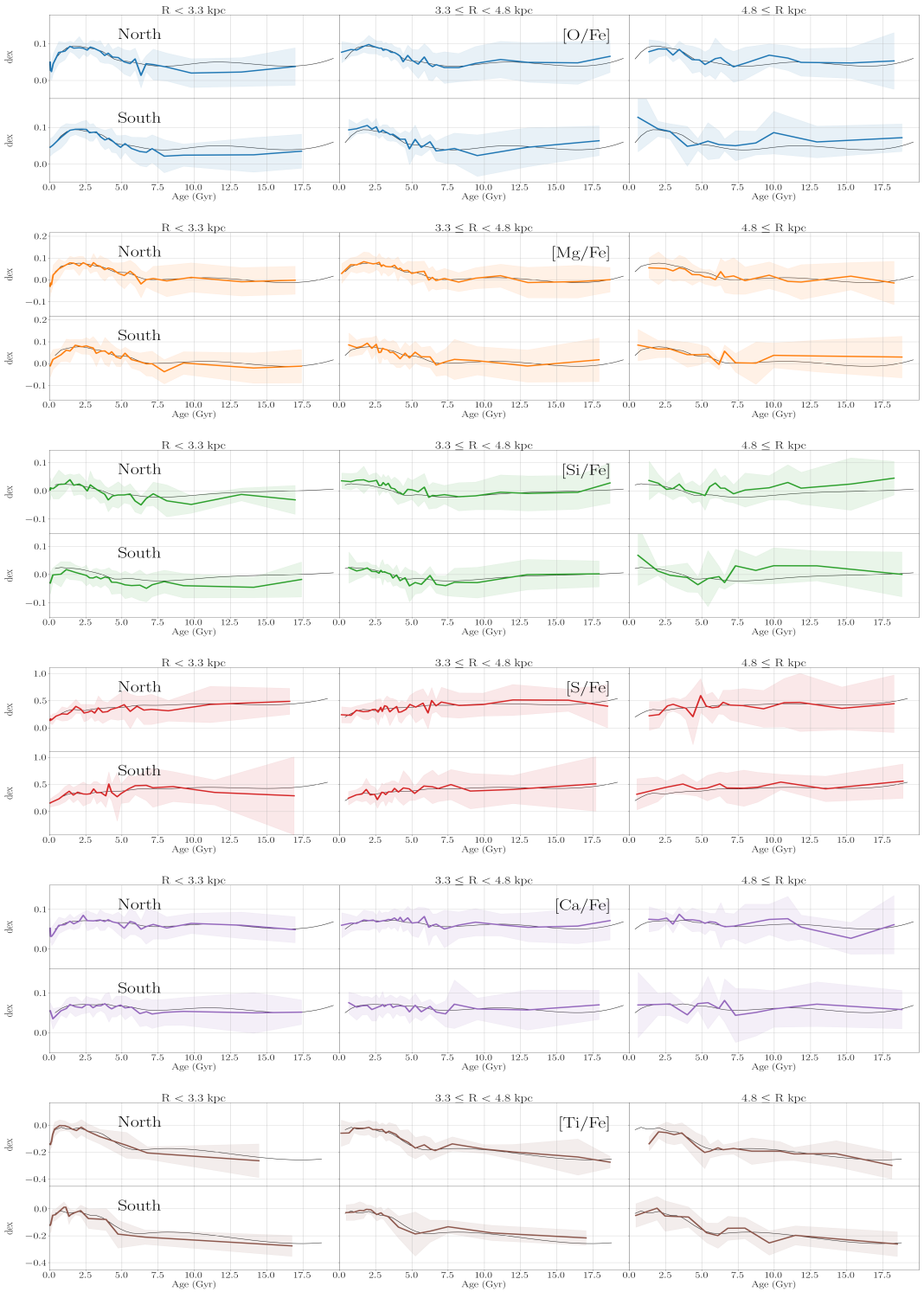



Figure 3.15: The age-[X/Fe] trends for the individual $\alpha$-elements.

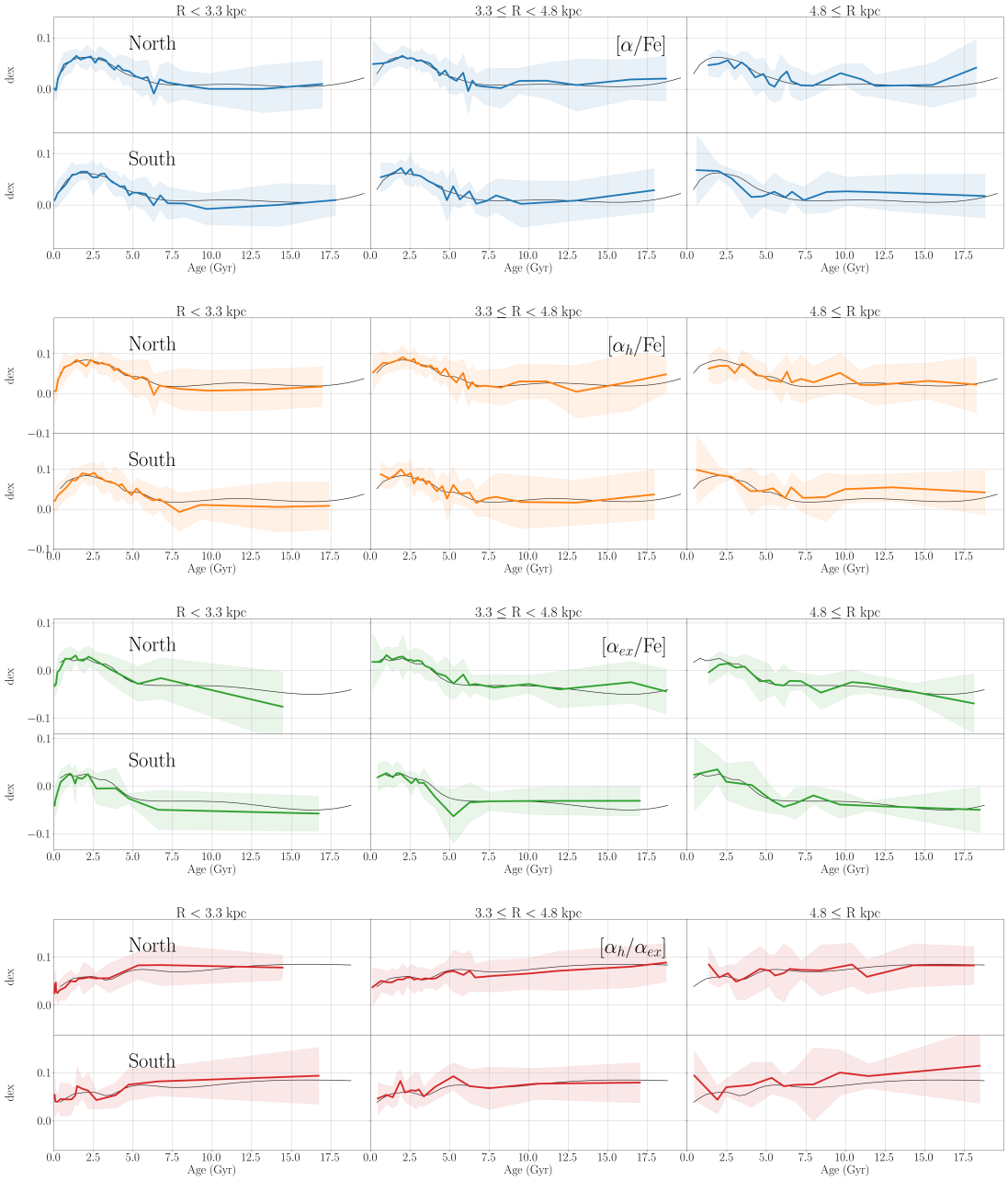



Figure 3.16: The age-[X/Fe] trends for the composite $\alpha$-elements.

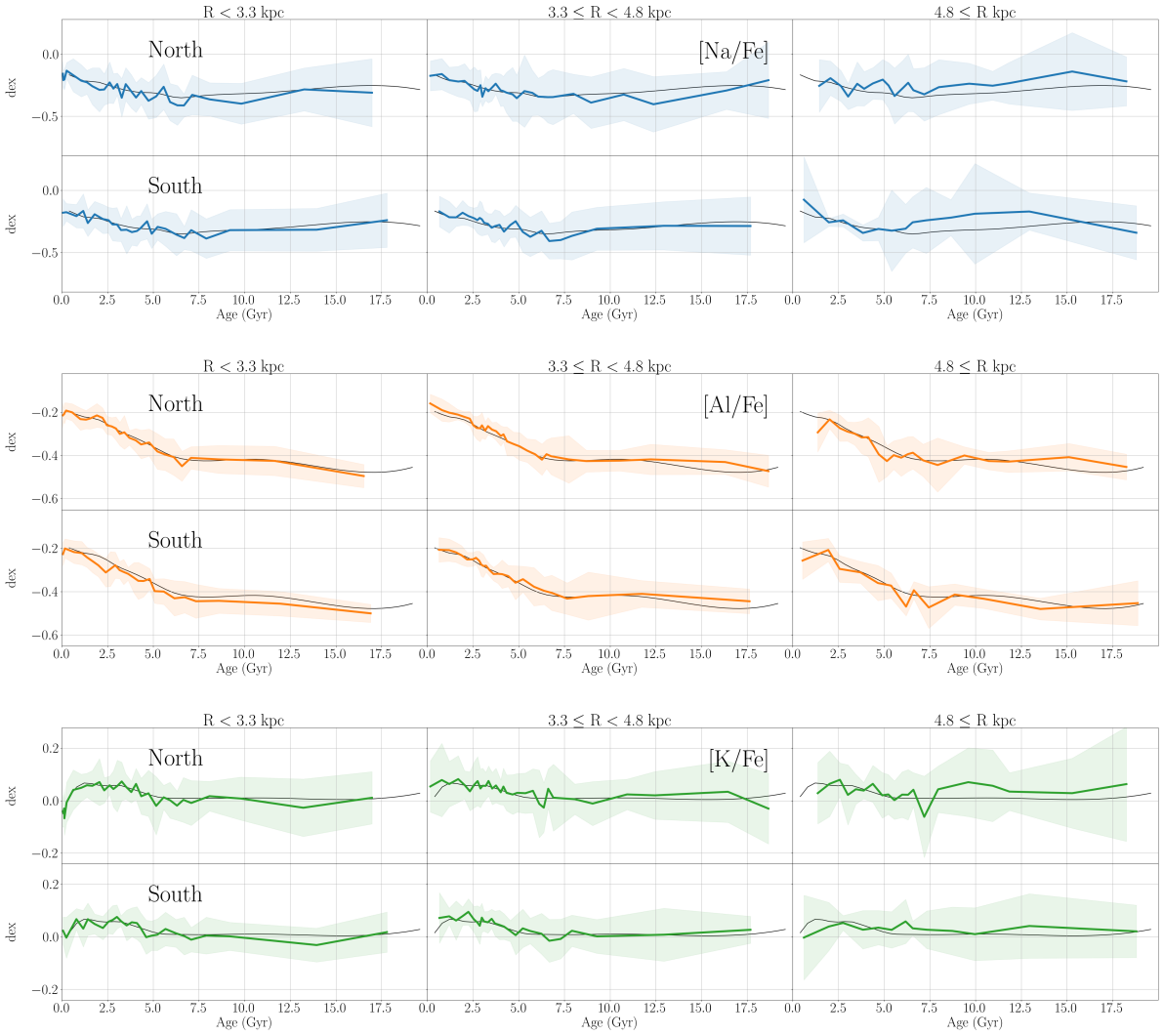



Figure 3.17: The age-[X/Fe] trends for the odd-Z elements.

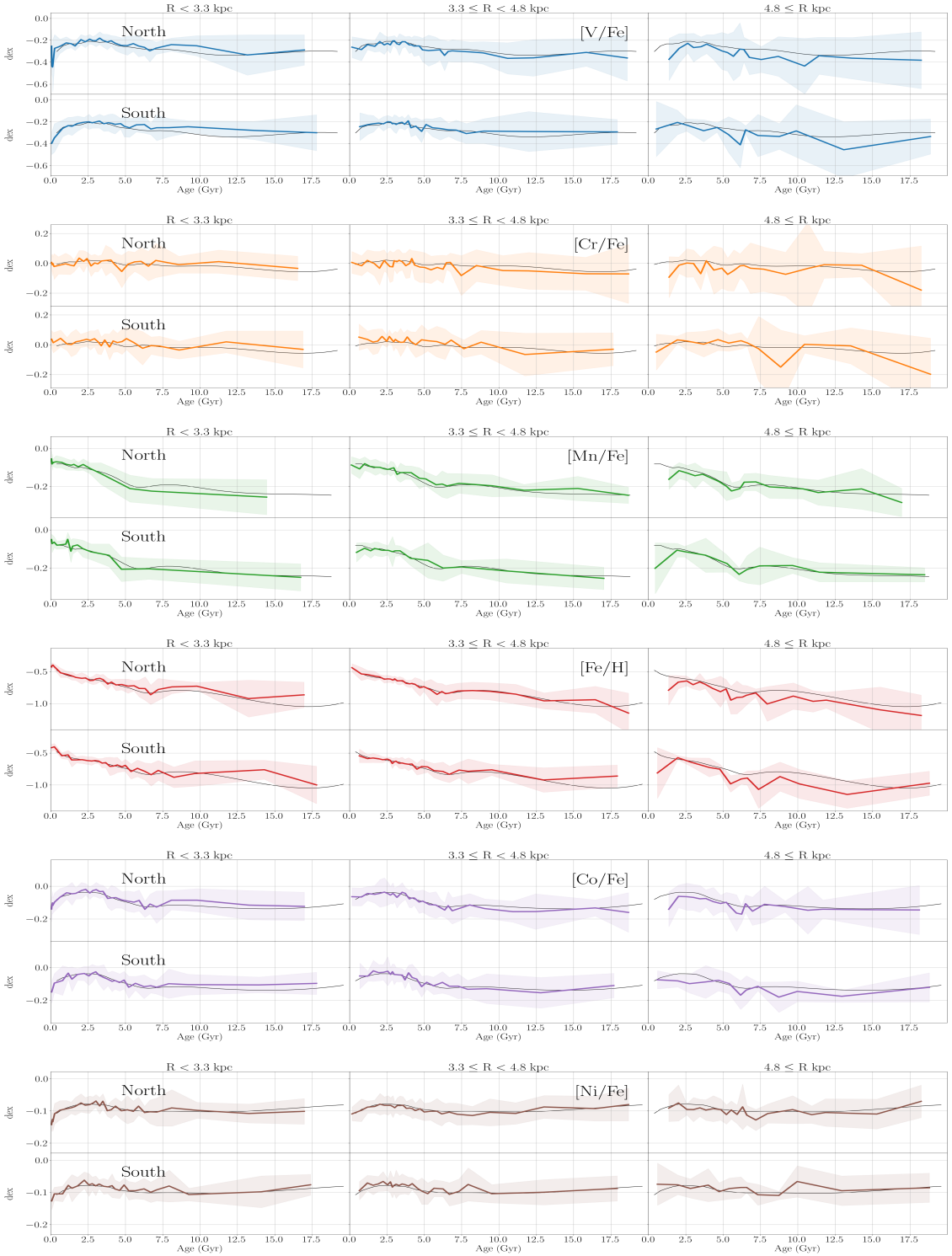



Figure 3.18: The age-[X/Fe] trends for the ironpeak elements.

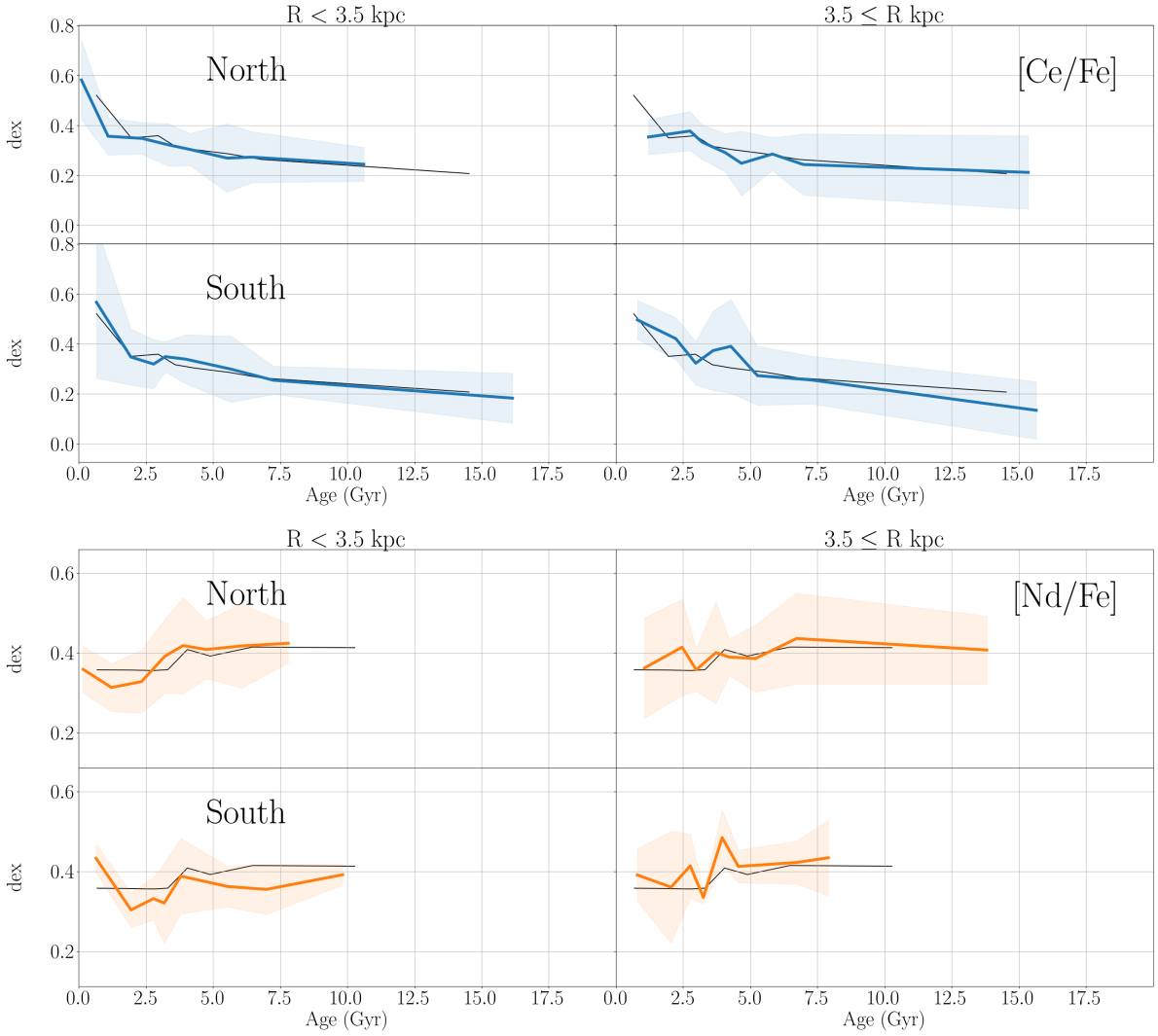



Figure 3.19: The age-[X/Fe] trends for the neutron capture elements.

# REVEALING THE CHEMICAL STRUCTURE OF THE MAGELLANIC CLOUDS WITH APOGEE. III. ABUNDANCE GRADIENTS OF THE SMALL MAGELLANIC CLOUD

## Contribution of Authors and Co-Authors

Manuscript in Chapter 4

Author: Joshua T. Povick

Contributions: Lead author of the manuscript who carried out the calculation of abundance trends and age-abundance trends.

Author: David L. Nidever

Contributions: Provided general advice, helped edit the manuscript, and gave comments on the manuscript.

Author: Pol Massana

Contributions: Provided general advice, helped edit the manuscript, and gave comments on the manuscript.

Author: Yuxi (Lucy) Lu

Contributions: Provided comments and feedback on the draft of the manuscript.

Author Steven R. Majewski

Contributions: Provided comments and feedback on the draft of the manuscript.

Author: Andrés Almeida

Contributions: Lead observer for the APOGEE-2S survey. Provided comments and feedback on the draft of the manuscript.

Manuscript Information

Joshua T. Povick, David L. Nidever, Pol Massana, Yuxi (Lucy) Lu, Steven R. Majewski, Andrés Almeida

Monthly Notices of the Royal Astronomical Society

Status of Manuscript:
_X_ Prepared for submission to a peer-reviewed journal
____ Officially submitted to a peer-reviewed journal
____ Accepted by a peer-reviewed journal
____ Published in a peer-reviewed journal

## Abstract

We determine radial- and age-abundance gradients of the Small Magellanic Cloud (SMC) using spectra of 2,062 red giant branch (RGB) field stars observed by SDSS-IV / APOGEE-2S. With coverage out to ∼9 kpc in the SMC, the high resolution (R ∼ 22,500) APOGEE $H$-band spectrograph is an excellent instrument to measure abundances throughout the SMC. Radial gradients are measured for each of the 24 abundance ratios. The SMC has an overall radial abundance gradient of $-0.0546 \pm 0.0043$ dex/kpc. Ages for each of the SMC stars are calculated to explore the evolution of the different abundance gradients. The evolutionary trends of the gradients exhibit a U-shaped trend with an extremum point around 3.66–5.58 Gyr ago, which is especially evident in the absolute [X/H] gradients. We previously detected these same types of patterns in the Large Magellanic Cloud (LMC). Starbursts are known to have occurred in both SMC and LMC, though the SMC burst precedes the one in the LMC by a few Gyr (as seen in the chemistry). These bursts are likely due to a close encounter between the two galaxies. Overall, the age-[X/Fe] trends in the SMC galaxy are relatively flat, signifying a relatively slow enrichment history. Comparing the SMC to the LMC and Milky Way (MW) reveals that [X/Fe] and [X/Mg] gradients tend to be similar for all three galaxies while the [X/H] gradients demonstrate a striking separation between the two dwarfs and the MW. The MW has a median [X/H] gradient around $-0.125$ dex/$R_d$ whilst the Clouds have a gradient around $-0.075$ dex/$R_d$.


## Introduction

The Small Magellanic Cloud (SMC) is the smaller of a pair of massive dwarf satellites of our own Milky Way (MW) known as the Magellanic Clouds (MCs). It has a stellar mass of ∼3–3.5 $\times$ $10^8$ $M_\odot$ (Skibba et al., 2012) and dark matter mass of $M_{DM}(R < 4 \text{ kpc}) =$ 1–1.5 $\times 10^9$ $M_\odot$ (Di Teodoro et al., 2019). The galaxy is also well within the virial radius

of the MW at a distance of 62.44 kpc (Graczyk et al., 2020), and, therefore, bright with an apparent $V$ magnitude of 2.2 $\pm$ 0.2 (McConnachie, 2012). Combined, these factors make the SMC a prime candidate for resolved stellar population analyses with high-resolution spectroscopic studies, using the numerous red giant branch (RGB) stars brighter than $V \sim$ 18 (e.g., Dobbie et al., 2014; Harris & Zaritsky, 2006; Nidever et al., 2020).

The SMC is a dwarf irregular galaxy (dIrr) with a complex geometry. The entire shape of the galaxy has been heavily affected by tidal interactions with the Large Magellanic Cloud (LMC), and continues to be a challenge to model. It has been shown that the SMC is very extended along the line-of-sight on the eastern side (towards the LMC), more than the extent it shows face-on and as much as 20 kpc based on observations standard of candles (Nidever et al., 2013; Scowcroft et al., 2016).

One of the most striking characteristics of the MCs as a whole is the trail of HI gas coming off the MCs, known as the "Magellanic Stream" (MS; e.g., Brüns et al., 2005; Mathewson et al., 1974; Nidever et al., 2008b; Putman et al., 2003), which was discovered to extend up to 200° across the sky (Nidever et al., 2010). The Stream is thought to be made mostly of stripped SMC gas (Besla et al., 2012; Lucchini et al., 2020) in a scenario where the MCs are in their first infall to the MW (Besla et al., 2007; Kallivayalil et al., 2013).

Interacting galaxies are known to experience starbursts leading to increased star formation in them for a period of time (e.g., Privon et al., 2017). The MCs are known to have had a close interaction in the recent past based on their kinematic data (Nidever et al., 2020; Zivick et al., 2018). The Magellanic Bridge (MB; Hindman et al., 1963), a bridge of gas and young stars (∼50 Myr old; Demers et al., 1991; Muller & Bekki, 2007) between the two galaxies (stretching ∼10° from the SMC to the LMC), has long been thought to be the result of their most recent interaction, only ∼200 Myr ago (e.g., Besla et al., 2012; Diaz & Bekki, 2012; Gardiner et al., 1994; Muller & Bekki, 2007). Additionally, the MCs are expected to have been interacting prior to that, based on the modelling of their tidal debris

(Cullinane et al., 2022) and star formation histories (Massana et al., 2022). Therefore, it is logical to expect that the chemistry of the MCs has been influenced by all these interactions and bursts of star formation. Naturally, abundance gradients of either galaxy should be expected to change as a consequence as well.

As mentioned in the previous paragraph, the MCs did experience a close interaction very recently. As a result there was a spike in star formation in the LMC about 2 Gyr ago (e.g., Nidever et al., 2020). That work used the `flexCE` code (Andrews et al., 2017) in order to model the chemical evolution of the LMC. To account for the possibility of a starburst, the star formation efficiency (SFE) was allowed to vary with time and a peak added $\sim$1 Gyr ago. Using similar modeling with `flexCE` and a time-evolving SFE, Hasselquist et al. (2021) was able to confirm the timeframe of the star formation burst in the LMC. That work also modelled the chemical evolution of the SMC and found that the burst was weaker and happened $\sim$3–4 Gyr earlier than in the LMC. With the delay between the star formation bursts in the MCs due to their close interaction, it is expected that changes in the chemistry of the SMC will predate the analogous changes in the LMC.

Interacting systems are important because they are the key to revealing how the MW and other larger galaxies formed. The prevailing galaxy formation paradigm called "hierarchical merging" (Searle & Zinn, 1978; White & Rees, 1978), states that galaxies merge and grow through processes involving many repeated interactions. Smaller, dwarf galaxies were the first type of galaxy to form, and, then, due to the influence of gravity from other dwarfs, they merged together to form galaxies in the large range of sizes and masses that we see today. However, our knowledge of the details of this process is still incomplete. The Universe is known to be full of dwarfs galaxies, which should make it easy to study. Nevertheless, the challenges with studying dwarf galaxies are that they are intrinsically faint and most are very distant. Therefore, the SMC (and the MCs more generally) is a good choice to study, as individual stars can be resolved in it, enabling a detailed study with

high-resolution spectroscopy.

Previously, most studies of the SMC only explored the metallicity gradient (e.g. Choudhury et al., 2020; De Bortoli et al., 2022; Dobbie et al., 2014; Li et al., 2023; Parisi et al., 2010, 2016) and not other abundances. This is because abundance gradient studies require high-resolution spectra to derive precise elemental abundances, while mean metallicity of stars is more readily measured with lower resolution (R$\sim$1000) data. In addition, for precise elemental abundances, higher resolutions are needed as well as high S/N. APOGEE is a great instrument and survey to carry out an abundance gradient study because it has a resolution of R $\sim$ 22,500 and S/N $>$ 100. This work goes further than previous studies, using APOGEE high-resolution spectroscopy to determine abundance gradients of 24 abundance ratios and their temporal evolution.

This work is part of a series of three papers on the Magellanic Clouds and their chemistry, as seen with the Apache Point Observatory Galactic Evolution Experiment (APOGEE, Majewski et al., 2017) data. Povick et al. 2023a (in prep.; hereafter Paper I), presents a method to calculate ages of individual red giant branch stars using high-resolution spectroscopy, multi-band photometry, and isochrones and applies it to the APOGEE-2S sample of the Large Magellanic Cloud. In Povick et al. 2023b (in prep.; hereafter Paper II), the abundance gradients of the LMC and their temporal evolution are determined. The focus of this third paper in the series is the abundance gradients of the Small Magellanic Cloud.

In this paper, we start by discussing the APOGEE and Gaia data in Section 4.2. Next, Section 4.3 outlines how we estimate distances and ages for the SMC stars. Section 4.4 outlines abundance trend calculations, while the results are presented in Section 4.5. From there, we discuss the implications of the results in Section 4.6. Finally, concluding remarks are given in Section 4.7.

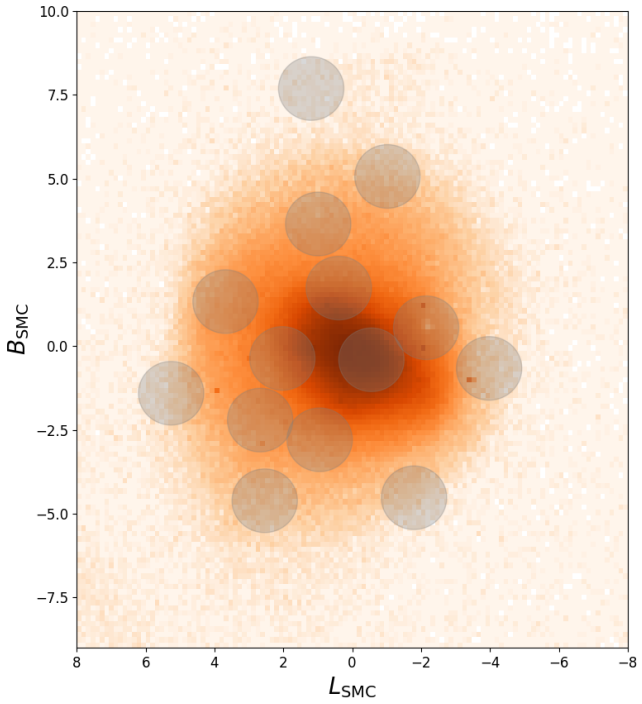



Figure 4.1: Stellar density map of the Gaia DR3 RGB with SMC-like proper motions in and SMC-centric coordinate system. The 14 APOGEE-2S SMC fields are highlighted in gray.

## Data

For our study of the SMC, we use high-resolution, high-S/N spectroscopic data from APOGEE as well as multi-band photometry and astrometry from Gaia.

### APOGEE

The Apache Point Observatory Galactic Evolution Experiment (APOGEE) survey is part of the wider Sloan Digital Sky Survey IV (SDSS-IV, Blanton et al., 2017), and is the source of the bulk of the SMC data analyzed in this work. The primary goal of APOGEE is to study the chemical enrichment and kinematics of the Milky Way and its environment. All the data are available as part of the public SDSS-IV data release 17 (DR17, Abdurro'uf et al., 2022).

Originally, the APOGEE survey was a single $H$-band spectrograph (Wilson et al., 2019) located at the Apache Point Observatory (APO, Gunn et al., 2006; Holtzman et al., 2010) in the state of New Mexico. With the most recent iteration of APOGEE (APOGEE-2), a second identical spectrograph was installed at the Las Campanas Observatory (LCO, Bowen & Vaughan, 1973) in Chile, making it possible for APOGEE to obtain data in the southern hemisphere. Specific information about the targeting for both APOGEE-2N and APOGEE-2S can be found in Zasowski et al. (2013) and Zasowski et al. (2017), while targeting information for the Magellanic Clouds survey is in Nidever et al. (2020).

Stellar parameters and abundances are derived from the observed spectra in a two-step process. First, the observed spectra are fed into the APOGEE pipeline (Nidever et al., 2015) for an initial reduction. Accurate stellar parameters are then calculated from the reduced spectra using the APOGEE Stellar Parameter and Chemical Abundance Pipeline (ASPCAP, Holtzman et al., 2015; Pérez et al., 2016). This second pipeline utilizes the `FERRE` (Allende Prieto et al., 2006) package to match the $T_{\rm eff}$, $\log(g)$, $v_{\rm micro}$, [M/H], [C/M], [N/M], [$\alpha$/M],

and $v_{macro}$ to a library of synthetic spectra created with `synspec` (Hubeny et al., 2021). Accurate elemental abundances that are obtained by ASPCAP include C, CI, N, O, Na, Mg, Al, Si, S, K, Ca, Ti, TiII, V, Cr, Mn, Fe, Co, Ni, and Ce. For DR17, the process is nearly identical to previous data releases except for some details outlined in Holtzman et al. (in prep.).

As with any observations, the APOGEE results have both statistic uncertainties and some systematic biases. The systematics for APOGEE are determined by inspecting stars in the solar neighborhood with solar metallicities. Offsets are then derived and applied to the APOGEE stars. The statistical uncertainties were calculated from the scatter from multiple visits of stars as functions of $T_{eff}$, [M/H], and SNR.

With coverage out to ∼9 kpc in 14 different fields (see Fig. 4.1), APOGEE was able to observe 2062 RGB stars in the SMC. This makes the survey perfect for determining the abundance gradients in the galaxy.

Gaia Data Release 3

The Gaia mission (Gaia Collaboration et al., 2016, 2022) is a massive all-sky photometric, astrometric and spectroscopic survey in optical wavelengths. The three photometric bands are $BP$, $G$, and $RP$, which are blue, green, and red, respectively. The Gaia Archive stores all the publicly available data and can be accessed through the website[1].

For this work, we use the Gaia red clump stars (RCs) in the APOGEE fields (see Section 4). The first step was to query the Gaia Archive for the SMC stars using a slightly modified version of the selection used by Gaia Collaboration et al. (2021b). For the full ADQL query, see Appendix 4. Next, the RC stars are selected by using a color-magnitude diagram criterion determined by eye:

1. $0.875 < BP - RP < 1.2$

[1] `https://gea.esac.esa.int/archive/`

2. $18.6 < G < 19.6$

Finally, for each APOGEE SMC field, all RC stars within 0.95° of the field center are selected, where 0.95° is the angular radius of the APOGEE plates.

## Calculating Distances and Ages

In Paper I, we determined ages for individual LMC RGB stars using spectroscopically-determined stellar parameters, multi-band photometry, and isochrones. In Paper II, we used these ages to determine the temporal evolution of the LMC elemental abundances and radial abundance gradients. An important ingredient of our age-determination method was that we knew the distances of the LMC RGB stars quite accurately because they lie in an inclined disk plane with observationally, well-determined parameters. This allowed us to calculate absolute magnitude which could be compared to isochrone photometry and constrain age. As previously mentioned, the SMC stars do not lie in an inclined disk plane, but, instead, have a complex, spheroidal geometry with a large line-of-sight depth on the eastern side. Therefore, another technique to obtain distances to SMC stars is needed so that our age-determination method can be utilized. We use a new technique called "proper motion distances" to accurately estimate the distances for individual SMC stars.

### SMC Distances

The kinematics of a star can be used to obtain an accurate distance, specifically by using the proper motion, because of its linear dependence on distance. The true velocity of an object is represented by its space velocity (v), which is defined by

$$\begin{aligned} v^2 &= v_r^2 + v_t^2, \\ v^2 &= v_r^2 + (4.74\mu d)^2 \end{aligned} \tag{4.1}$$

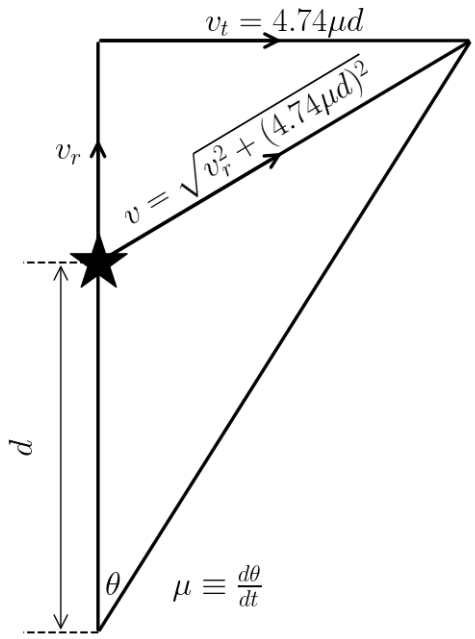



Figure 4.2: A schematic showing the relationship between true velocity ($v$), radial velocity ($v_r$), and tangential velocity ($v_t$). The time derivative of the angle $\theta$ is the proper motion. An observer would be at the bottom point in this diagram.

where $v_r$ is the radial velocity, $v_t$ is the tangential velocity, $\mu$ is the magnitude of the proper motion in units of mas yr$^{-1}$, and $d$ is the distance to the object in units of kpc (all quantities relative to the Sun). Figure 4.2 shows a schematic of the relationship between the space velocity of an object and its radial and tangential components.

For our APOGEE SMC RGB sample, the radial velocities are known from the APOGEE spectroscopy and the proper motions from Gaia astrometry. Although the tangential velocity ($v_t$) of any RGB star is unknown, it can be estimated by using the Gaia RC stars. These stars are standard candles, and, therefore, their distances can be accurately established simply from their photometry. While the RC absolute magnitude is fairly constant in near-infrared (NIR) magnitudes (Bovy et al., 2014), it has a metallicity-dependence in the optical

bands (Girardi, 2016). Using PARSEC isochrones, we determine that the $G$-band absolute magnitude of the RC for the mean metallicity of the SMC ([Fe/H]$=-1.1$) is $G_{\rm RC,SMC} = -0.21$. After determining the distance of each individual RC star, its tangential velocity can be calculated by using its distance and proper motion via $v_t = 4.74\mu d$. Next, we calculate the mean tangential velocity of all the Gaia RC stars in each APOGEE field separately. Finally, the distance of an individual RGB star can be calculated under the assumption that its tangential velocity is the same as the mean RC tangential velocity in its field, using

$$d_{\rm RGB} = \langle v_{t,\rm RC} \rangle / (4.74\mu) \tag{4.2}$$

The main steps in determining the "proper motion distances" for individual SMC RGB stars are summarized as follows:

1. Determine distances for individual RC stars in an APOGEE field using an absolute magnitude of $G_{\rm RC,SMC} = -0.21$, appropriate for the SMC mean metallicity.

2. Calculate the tangential velocity ($v_t$) for individual RC stars by using their distance (measured in the previous step) and their measured total proper motion with $v_t = 4.74\mu d$.

3. Calculate the mean tangential velocity of all RC stars in an APOGEE field.

4. Determine the distance to a single SMC RGB star by assuming its tangential velocity is the same as the mean RC tangential velocity and using its measured proper motion with $d_{\rm RGB} = \langle v_{t,\rm RC} \rangle / (4.74\mu)$.

We find that for the SMC RGB stars, the mean distance of the stars using this method is 66.21 kpc. An offset of 3.77 kpc is then applied so that the mean distance of the RGB stars is matches the 62.44 kpc found by Graczyk et al. (2020).

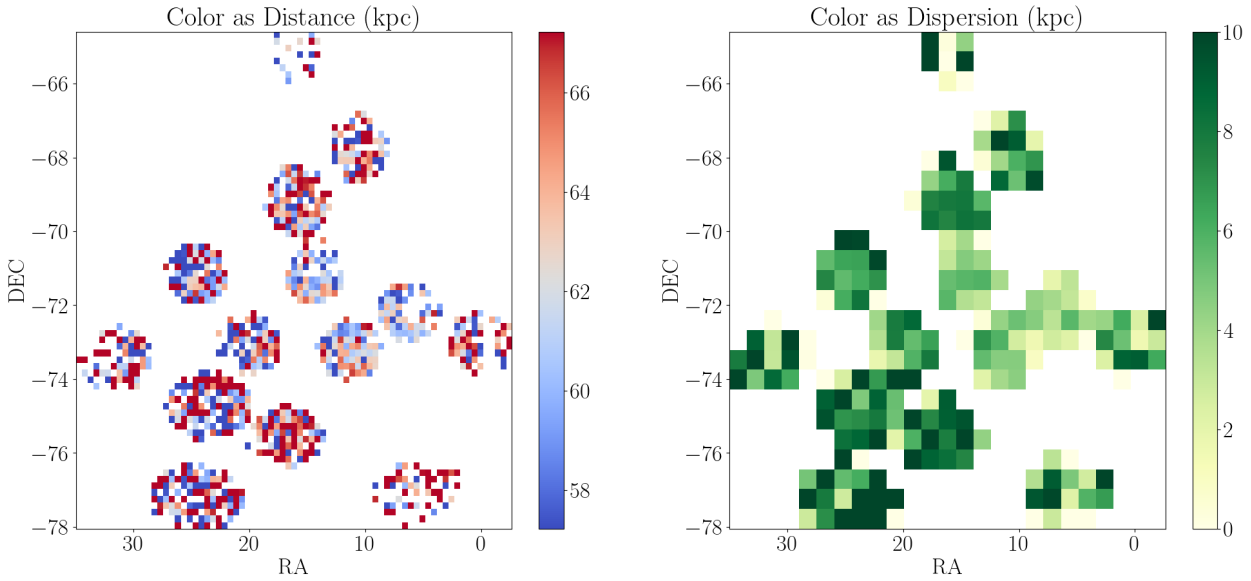



Figure 4.3: (*Left*) A map of the APOGEE SMC fields showing the mean distance in each spatial bin determined using our "proper motion distance" method. (*Right*) A dispersion map for the calculated distances. The larger line-of-sight depth is clearly visible on the eastern side of the galaxy.

Naturally, the actual tangential velocity of any given RGB star will deviate from the field-averaged mean. This will result in an error in our distance calculation. We can estimate this bias by using the measured radial velocity dispersion and assume that the tangential velocity dispersion is similar. The average $v_r$ dispersion of the 14 SMC fields is 22.7 km s$^{-1}$. Using propagation of errors, this $v_t$ dispersion translates to 3.25 kpc in distance. At an average SMC distance of 62.44 kpc, this amounts to a 5.2% uncertainty, which is quite good. The Gaia proper motions of the relatively bright individual SMC RGB stars have a fractional uncertainty of 4.2% which also translates to a fractional uncertainty in distance of 4.2% or 2.6 kpc. Combining these two sources of uncertainty in quadrature gives us an overall distance uncertainty of 4.16 kpc or 6.7% on a star-by-star basis. Figure 4.3 shows a map of the APOGEE SMC distances determined using this method showing a higher distance dispersion on the eastern side, as previously reported.

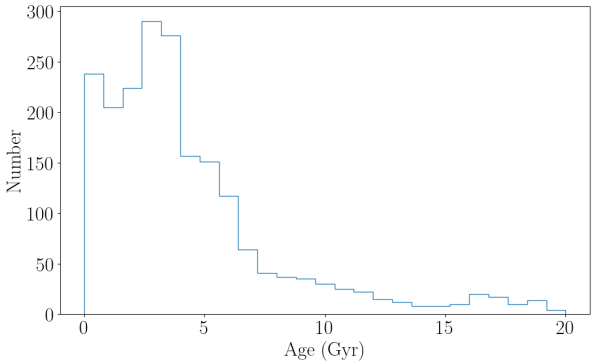



Figure 4.4: The distribution of calculated ages for the SMC stars. A large portion of the stars formed within the last ∼7.5 Gyr in the SMC with a peak ∼3–4 Gyr ago. This is similar to Figure 19 in Paper I, where most star formation happens

SMC Ages

Using the distances determined from our "proper motion distance" method, we can straightforwardly use the age-determination method described in Paper I. The distribution of our derived SMC ages is shown in Figure 4.4 and looks quite similar to the LMC age distribution shown in Figure 19 of Paper I.

The 6.7% or 4.16 kpc distance uncertainty that we calculated in Section 4 have an impact on the ages. They produce an average age uncertainty of 1.5 Gyr.

## Abundance Gradient Calculation

Here we discuss how the SMC radial abundance gradients are determined.

SMC Radius

Since the SMC does not have a well-shaped stellar disk, but rather a more spheroidal shape, we decide to simply use the radius of a star from the center of the SMC in the plane of the sky in kpc. The SMC radius of each star can be calculated by converting the provided equatorial coordinates ($\alpha$, $\delta$) into angular coordinates ($\rho$, $\phi$), where $\rho$ is the angular radius

and $\phi$ is the position angle. The angular coordinates in terms of $\alpha$ and $\delta$ are

$$\begin{aligned}
\cos\rho &= \cos\delta_0 \cos\delta \cos(\alpha - \alpha_0) + \sin\delta_0 \sin\delta, \\
\sin\rho \cos\phi &= -\cos\delta \sin(\alpha - \alpha_0), \\
\sin\rho \sin\phi &= \cos\delta_0 \sin\delta - \sin\delta_0 \cos\delta \cos(\alpha - \alpha_0),
\end{aligned} \tag{4.3}$$

where $(\alpha_0, \delta_0)$ is the center of the SMC at (13.18°, −72.83°) from Nidever et al. (2017). And converting the angular radius, $\rho$, to a linear radial is done by

$$R = D \tan\rho \tag{4.4}$$

where D is the distance to the center of the SMC and is 62.44 ± 0.44 kpc from Graczyk et al. (2020), and $\rho$ is the angular radius from the center of the SMC.

Determining Abundance Gradients with MCMC

Radial abundance gradients are determined by fitting abundance trends with radius in a galaxy. The convention is to use a simple linear model to accomplish this, and, therefore, the functional form of the model in this work is

$$[\mathrm{X/Fe}] = \nabla_R R + [\mathrm{X/Fe}]_0, \tag{4.5}$$

where [X/Fe] is the abundance, $\nabla_R$ is the gradient of the line, $R$ is the radius, and $[\mathrm{X/Fe}]_0$ is the central abundance.

Measuring abundances with hydrogen represents the "absolute" abundance and so it makes a natural choice for a fiducial element. However, it is often useful to remove the overall dependence of an abundance on metallicity by subtracting [Fe/H], i.e. [X/Fe] = [X/H] - [Fe/H]. This allows for deviations from the solar abundance ratios to be investigated. (Weinberg et al., 2019) suggests using magnesium as a fiducial element for abundances. This

is because it is released into the interstellar medium almost exclusively through type II SNe (Andrews et al., 2017), whereas iron has contributions from both SNe II and SNe Ia. Therefore, we determine gradients for [X/Fe], [X/H], and [X/Mg] with Fe, H and Mg as fiducial elements, as well as [C/N] and $[\alpha_{\rm h}/\alpha_{\rm ex}]$.

The gradients and central abundances in Equation 4.5 are found using maximum likelihood estimation with the likelihood function:

$$\ln \mathcal{L} = \frac{1}{2}\Bigg[\sum_i \frac{([\mathrm{X/Fe}]_i - \nabla_R R_i - [\mathrm{X/Fe}]_0)^2}{\sigma_i^2} - \ln 2\pi\sigma_i^2\Bigg], \tag{4.6}$$

where the radius of each individual star is $R_i$, the abundance of the star is $[\mathrm{X/Fe}]_i$, and the error in the abundance is $\sigma_i$.

For added robustness when fitting, all stars with S/N $>$ 100 are removed (only affected very few stars) and then the stars are binned in radius, and a model is fit to the median binned values with weighting using the median absolute deviation (MAD) of the median. After this fit, any outlier stars further than 3 $\times\sigma$ are rejected and the model is refit. This is done because there is large scatter at each radii in abundance, potentially due in part to some radial migration. Uncertainties in the gradients and central abundances are found by implementing a Markov chain Monte Carlo (MCMC) using the `emcee` (Foreman-Mackey et al., 2013) python package. This package is built upon the algorithms presented in Goodman & Weare (2010).

Stellar Age Binning

As mentioned above, we use the spectroscopic $T_{\rm eff}$, $\log g$, and [Fe/H] values as well as the distances calculated from Section 4 to determine ages using the method from Povick et al. 2023a. In order to make a comparison of the evolution of abundance gradients between the LMC and SMC, the same age bins from Povick et al. (2023b, in prep.) are used here. The particular age ranges for each bin can be found in Table 4.1.

Table 4.1: Table showing the different age bins used throughout this work. These are the same age bins from Povick et al. 2023b.

| Bin | Age Range (Gyr) |
|---|---|
| 1 | $t \leq 2.23$ |
| 2 | $2.23 < t \leq 3.66$ |
| 3 | $3.66 < t \leq 5.58$ |
| 4 | $5.58 < t \leq 8.36$ |
| 5 | $8.36 < t$ |

Age-[X/Fe] Trends

In addition to radial abundance trends, we also explore the different age-[X/Fe] trends for spatial regions in the SMC [X/Fe] abundances as well as [C/N] and $[\alpha_{\rm h}/\alpha_{\rm ex}]$. Stars were divided by their SMC position angle into east and west regions. In addition, each of these bins was further divided into two radial annular bins. Stars were classified as either inner SMC ($R < 3.3$ kpc) or outer SMC ($3.3 \leq R$ kpc). This radial cutoff was chosen as the inner SMC is morphologically more elliptical for $R < 3°$ compared to the outer portion of the galaxy (Nidever et al., 2011), which corresponds to 3.3 kpc.

The age-[X/Fe] trends are found by splitting the stars in different age bins and finding the abundance median and MAD scatter of each bin. Note that the age bins here are not the same as the ones used for the evolution of the radial abundance gradients. Here the number of age bins was set to 15 as it produced the best results by minimizing jaggedness without sacrificing the overall structure of the trends.

## Results

Below, we present the main results of the radial abundance gradient and age-abundance trends.

### The SMC Radial Abundance Gradients

The SMC radial abundance gradients are discussed separately in element groups.

Carbon & Nitrogen This work looks at the individual gradients for carbon and nitrogen, the composite C+N gradients, and the [C/N] abundance ratio. The largest contributor to measured carbon and nitrogen elements is intermediate mass stars that undergo type II SNe (Kobayashi et al., 2006; Ventura et al., 2013).

The radial trends fit to the [X/Fe] and [C/N] abundances can be found in Figure 4.8. The carbon gradients of [C/Fe], [C/H], and [C/Mg] all are steep especially the [C/H] gradient with a value $-0.0929 \pm 0.0077$ dex/kpc (see Table 4.2). On the other hand, the nitrogen gradients are very shallow, in comparison. The largest nitrogen gradient is $-0.0427 \pm 0.0046$ dex/kpc for [N/H]. The C+N gradients fall in between the carbon and nitrogen gradients, which is expected because the C+N abundances are calculated using a weighted average of the individual carbon and nitrogen abundances. Lastly, the [C/N] gradient is moderately steep, relatively speaking, with a value of $-0.0203 \pm 0.0040$ dex/kpc.

$\alpha$-Elements There is a wide number of $\alpha$ elements with abundances measured by APOGEE including O, Mg, Si, S, Ca, Ti, and overall $\alpha$. Enrichment of $\alpha$-elements in the interstellar medium (ISM) primarily occurs though type II SNe (Nomoto et al., 2013; Weinberg et al., 2019). From individual $\alpha$-elements, it is possible to calculate the average hydrostatic $\alpha$-abundance ([$\alpha_h$/Fe]=([O/Fe]+[Mg/Fe])/2), the average explosive $\alpha$-element abundance ([$\alpha_{\rm ex}$/Fe] = ([Si/Fe]+[Ca/Fe]+[Ti/Fe])/3), and the ratio of the average

Table 4.2: Radial gradients for the abundant metals carbon and nitrogen.

| Element | $\nabla_R$ [X/Fe] (dex/kpc) | $\nabla_R$ [X/H] (dex/kpc) | $\nabla_R$ [X/Mg] (dex/kpc) |
|---|---|---|---|
| C | $-0.0267 \pm 0.0029$ | $-0.0929 \pm 0.0077$ | $-0.0196 \pm 0.0033$ |
| N | $-0.0048 \pm 0.0018$ | $-0.0427 \pm 0.0046$ | $-0.0008 \pm 0.0031$ |
| C+N | $-0.0117 \pm 0.0017$ | $-0.0676 \pm 0.0059$ | $-0.0059 \pm 0.0022$ |
| [C/N] | $-0.0203 \pm 0.0040$ | ... | ... |

hydrostatic $\alpha$-abundance to the average explosive $\alpha$-abundance ($[\alpha_{\rm h}/\alpha_{\rm ex}] = [\alpha_h/{\rm Fe}]$-$[\alpha_{\rm ex}/{\rm Fe}]$). Hydrostatic $\alpha$-elements are so named because they are created from hydrostatic burning inside of a star while the explosive $\alpha$-elements are created during type II SNe itself (Carlin et al., 2018).

Regardless of the fiducial element, all of the $\alpha$-abundances have a wide range of values, as seen in Table 4.3. It is immediately clear that the [X/Fe] gradients are almost all positive, which is the opposite of what is seen in the [X/H] and [X/Mg] gradients. The only negative [X/Fe] gradients are for [Ti/Fe], with a value of $-0.0115 \pm 0.0018$ dex/kpc, and $[\alpha_{\rm ex}/{\rm Fe}]$, with a value of $-0.0001 \pm 0.0011$ dex/kpc. The $[\alpha_{\rm ex}/{\rm Fe}]$ is probably negative because of the the [Ti/Fe] values. Taking the average of the [Si/Fe], [Ca/Fe], and [Ti/Fe] gradients is negative due to the steep negative gradient of [Ti/Fe], so it would be expected that the $[\alpha_{\rm ex}/{\rm Fe}]$ would also be negative. For the [X/Fe] and $[\alpha_{\rm h}/\alpha_{\rm ex}]$ $\alpha$-element trends see Figures 4.15 and 4.13, where the global trends are shown in black.

Odd-Z Elements The next group of elements is the odd-Z elements. These elements are defined as having odd atomic numbers that do not fall into other groups. These elements are produced mostly in type II SNe with a slight metallicity dependence (Nomoto et al., 2013; Weinberg et al., 2019). Regardless of the fiducial element, the K gradients fall between the

Table 4.3: Table of radial abundance gradients for the $\alpha$-elements.

| Element | $\nabla_R$ [X/Fe] (dex/kpc) | $\nabla_R$ [X/H] (dex/kpc) | $\nabla_R$ [X/Mg] (dex/kpc) |
|---|---|---|---|
| O | $0.0024 \pm 0.0013$ | $-0.0635 \pm 0.0054$ | $0.0029 \pm 0.0010$ |
| Mg | $0.0074 \pm 0.0019$ | $-0.0643 \pm 0.0053$ | ... |
| Si | $0.0067 \pm 0.0016$ | $-0.0512 \pm 0.00482$ | $-0.0029 \pm 0.0015$ |
| S | $0.0172 \pm 0.0090$ | $-0.0502 \pm 0.0094$ | $0.0139 \pm 0.0084$ |
| Ca | $0.0001 \pm 0.0013$ | $-0.0668 \pm 0.005$ | $-0.0072 \pm 0.0019$ |
| Ti | $-0.0115 \pm 0.0018$ | $-0.0677 \pm 0.0057$ | $-0.0075 \pm 0.0022$ |
| $\alpha$ | $0.0004 \pm 0.0009$ | $-0.0681 \pm 0.0051$ | $-0.0023 \pm 0.0011$ |
| $\alpha_{\rm h}$ | $0.0051 \pm 0.0017$ | $-0.0648 \pm 0.0053$ | $0.0014 \pm 0.0005$ |
| $\alpha_{\rm ex}$ | $-0.0001 \pm 0.0011$ | $-0.0647 \pm 0.0055$ | $-0.0044 \pm 0.0017$ |
| $[\alpha_{\rm h}/\alpha_{\rm ex}]$ | $0.0040 \pm 0.0011$ | ... | ... |

Table 4.4: Table of radial abundance gradients for the odd-Z elements.

| Element | $\nabla_R$ [X/Fe] (dex/kpc) | $\nabla_R$ [X/H] (dex/kpc) | $\nabla_R$ [X/Mg] (dex/kpc) |
|---|---|---|---|
| Na | $0.0214 \pm 0.0084$ | $-0.0337 \pm 0.0086$ | $0.0140 \pm 0.0087$ |
| Al | $-0.0123 \pm 0.0028$ | $-0.0713 \pm 0.0066$ | $-0.0159 \pm 0.0018$ |
| K | $0.0061 \pm 0.0029$ | $-0.0541 \pm 0.0049$ | $0.0044 \pm 0.0026$ |

Na and Al gradients (see Table 4.4). The overall odd-Z abundance trends are shown as black lines in Figure 4.14.

Iron Peak Elements An important group of elements is the iron peak elements, which includes vanadium, chromium, iron, cobalt, and nickel. These elements are produced through type Ia SNe although there is some small contribution from type II SNe as well (Kobayashi et al., 2006).

The iron abundance or metallicity, is a very important property of a star as it is essentially a measure of the overall content of heavy-element content in a star. The [Fe/H] does not stand out among the [X/H] gradients even with its value of $-0.0546 \pm 0.0043$ dex/kpc, but the [Fe/Mg] is the steepest of the iron peak [X/Mg] gradient at $-0.1230 \pm 0.0097$ dex/kpc (see Table 4.5). As for the other gradients, there does not seem to be any discernible pattern with atomic number. The steepest [X/Fe] belongs to [V/Fe] with a value of $-0.0237 \pm 0.0107$ dex/kpc. At $-0.0339 \pm 0.0107$ dex/kpc, vanadium also has the steepest non-iron [X/Mg] gradient. The shallowest iron peak gradient is different for each fiducial element. The radial trends for the iron peak [X/Fe] and [Fe/H] can be found in Figure 4.15.

Neutron Capture Element One of the more massive elements with a measured abundance from APOGEE is cerium. It is an element created through the neutron capture

Table 4.5: Table of radial abundance gradients for the iron peak elements.

| Element | $\nabla_R$ [X/Fe] (dex/kpc) | $\nabla_R$ [X/H] (dex/kpc) | $\nabla_R$ [X/Mg] (dex/kpc) |
|---|---|---|---|
| V | $-0.0237 \pm 0.0107$ | $-0.0633 \pm 0.0101$ | $-0.0339 \pm 0.0107$ |
| Cr | $-0.0059 \pm 0.0037$ | $-0.0551 \pm 0.0064$ | $-0.009 \pm 0.0045$ |
| Mn | $-0.013 \pm 0.0014$ | $-0.0784 \pm 0.0049$ | $-0.0146 \pm 0.0033$ |
| Fe | ... | $-0.0546 \pm 0.0043$ | $-0.1230 \pm 0.0097$ |
| Co | $-0.0081 \pm 0.0033$ | $-0.0653 \pm 0.0061$ | $-0.0100 \pm 0.0034$ |
| Ni | $-0.0028 \pm 0.0006$ | $-0.0574 \pm 0.0048$ | $-0.0005 \pm 0.0021$ |

Table 4.6: Table of radial abundance gradients for cerium.

| Element | $\nabla_R$ [X/Fe] (dex/kpc) | $\nabla_R$ [X/H] (dex/kpc) | $\nabla_R$ [X/Mg] (dex/kpc) |
|---|---|---|---|
| Ce | $-0.0596 \pm 0.0021$ | $-0.1115 \pm 0.0094$ | $-0.0599 \pm 0.0039$ |

processes known as the $r$- and $s$-processes (Prantzos et al., 2020). It can be a difficult abundance to measure, so while gradients have been calculated for [Ce/Fe], [Ce/H], and [Ce/Mg], it is best not to make any strong conclusions due to the larger uncertainties. The [Ce/Fe] and [Ce/Mg] gradients have values of $-0.0596 \pm 0.0021$ and $-0.0599 \pm 0.0039$, respectively. The [Ce/H] abundance is very large at $-0.1115 \pm 0.0094$ dex/kpc. The [Ce/Fe] abundance trend can be seen in Figure 4.16.

The Evolution of the SMC Abundance Gradients

As previously mentioned, we have calculated ages for the individual RGB stars in the SMC subset of the APOGEE catalog (see Section 4). Using age bins from Table 4.1, the evolution of all the abundance gradients is determined.

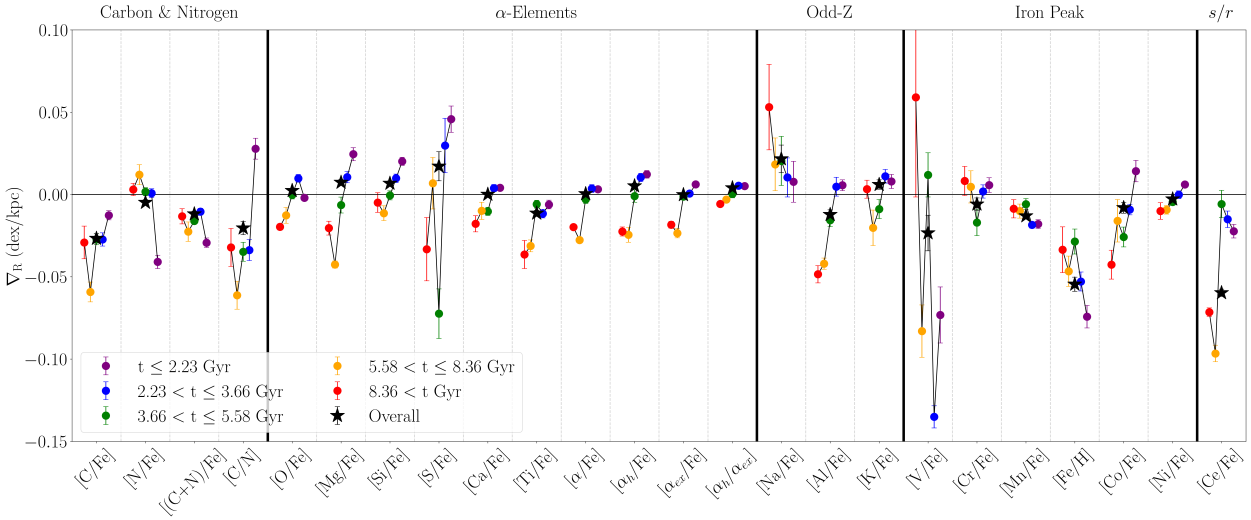



Figure 4.5: A figure showing each of the calculated gradients are shown for each element. The difference abundances have been broken up into different groups of like elements. The color of each dot corresponds to the different age bins that contain the same number of stars previously mentioned. The value of each gradient here can be seen in Table 4.

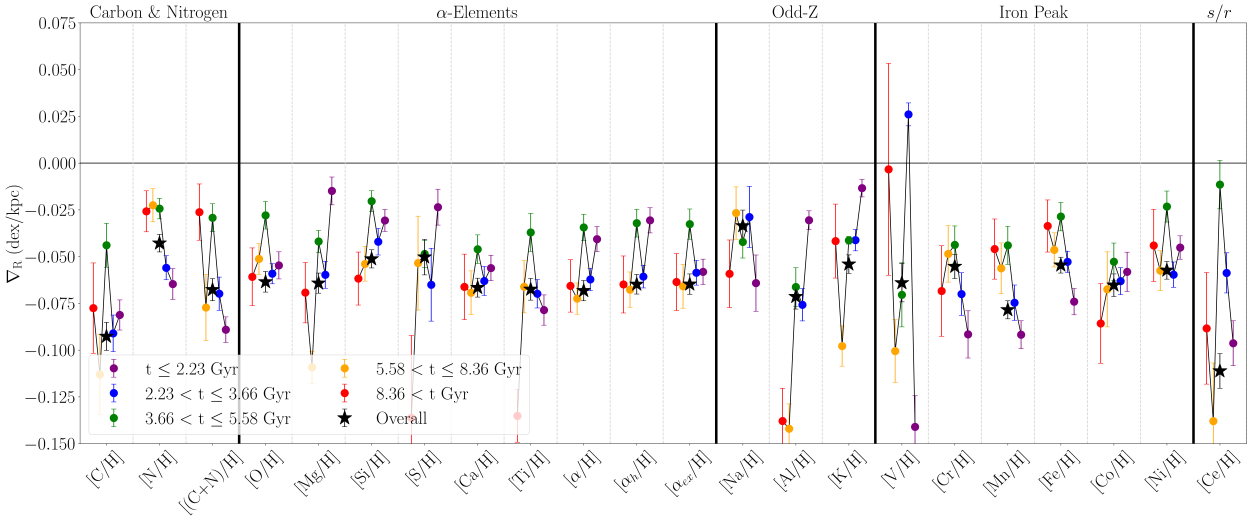



Figure 4.6: A figure showing each of the calculated gradients are shown for each element. The difference abundances have been broken up into different groups of like elements. The color of each dot corresponds to the different age bins that contain the same number of stars previously mentioned. The value of each gradient here can be seen in Table 4.

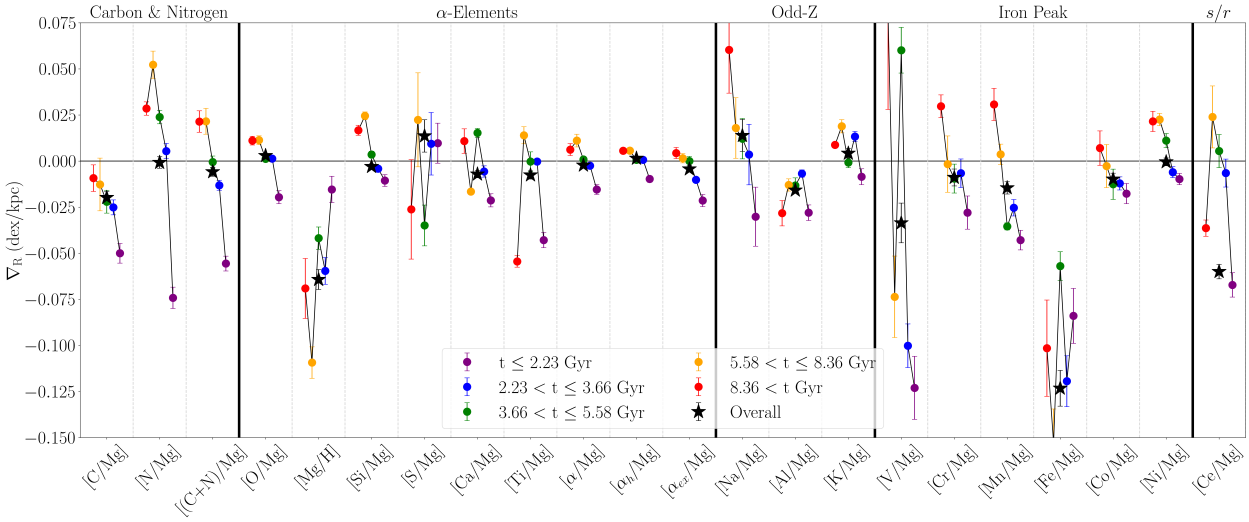



Figure 4.7: A figure showing each of the calculated gradients are shown for each element. The difference abundances have been broken up into different groups of like elements. The color of each dot corresponds to the different age bins that contain the same number of stars previously mentioned. The value of each gradient here can be seen in Table 4.

Table 4.7: Table of the [X/Fe] gradients for each of the age bins. Horizontal lines have been added marking the division of the previously defined groups of elements. In general descending down the table corresponds to an increase in atomic number. Each age bin has its own separate column. This table also includes the evolution of the [Fe/H], [C/N] and $[\alpha_{\rm h}/\alpha_{\rm ex}]$.

| Element | $t \leq 2.23$ $\nabla_R$ (dex/kpc) | $2.23 < t \leq 3.66$ $\nabla_R$ (dex/kpc) | $3.66 < t \leq 5.58$ $\nabla_R$ (dex/kpc) | $5.58 < t \leq 8.36$ $\nabla_R$ (dex/kpc) | $8.36 < t$ $\nabla_R$ (dex/kpc) |
|---|---|---|---|---|---|
| [C/Fe] | $-0.0126 \pm 0.0028$ | $-0.0273 \pm 0.0040$ | $-0.0272 \pm 0.0034$ | $-0.0592 \pm 0.0060$ | $-0.0291 \pm 0.0099$ |
| [N/Fe] | $-0.0409 \pm 0.0040$ | $0.0008 \pm 0.0026$ | $0.0017 \pm 0.0025$ | $0.012 \pm 0.0061$ | $0.0030 \pm 0.0037$ |
| [(C+N)/Fe] | $-0.0293 \pm 0.0028$ | $-0.0104 \pm 0.0020$ | $-0.0161 \pm 0.0008$ | $-0.0226 \pm 0.0059$ | $-0.0133 \pm 0.0046$ |
| [C/N] | $0.0278 \pm 0.0063$ | $-0.0338 \pm 0.0064$ | $-0.0348 \pm 0.0058$ | $-0.0612 \pm 0.0085$ | $-0.0321 \pm 0.0115$ |
| [O/Fe] | $-0.0020 \pm 0.0016$ | $0.0098 \pm 0.0024$ | $-0.0002 \pm 0.0024$ | $-0.0126 \pm 0.0048$ | $-0.0197 \pm 0.0019$ |
| [Mg/Fe] | $0.0245 \pm 0.0040$ | $0.0106 \pm 0.0034$ | $-0.0064 \pm 0.0048$ | $-0.0426 \pm 0.0022$ | $-0.0204 \pm 0.0042$ |
| [Si/Fe] | $0.0201 \pm 0.0025$ | $0.0099 \pm 0.0025$ | $-0.0005 \pm 0.0027$ | $-0.0114 \pm 0.0045$ | $-0.0049 \pm 0.0060$ |
| [S/Fe] | $0.0458 \pm 0.0080$ | $0.0298 \pm 0.0166$ | $-0.0724 \pm 0.0150$ | $0.0069 \pm 0.0156$ | $-0.0332 \pm 0.0192$ |
| [Ca/Fe] | $0.0041 \pm 0.0017$ | $0.0039 \pm 0.0022$ | $-0.0102 \pm 0.0025$ | $-0.0099 \pm 0.0052$ | $-0.0178 \pm 0.0049$ |
| [Ti/Fe] | $-0.0061 \pm 0.0026$ | $-0.0116 \pm 0.0026$ | $-0.0059 \pm 0.0024$ | $-0.0312 \pm 0.0036$ | $-0.0364 \pm 0.0086$ |
| $[\alpha/Fe]$ | $0.0032 \pm 0.0013$ | $0.0036 \pm 0.0024$ | $-0.0030 \pm 0.0025$ | $-0.0277 \pm 0.0012$ | $-0.0198 \pm 0.0013$ |
| $[\alpha_{\rm h}/Fe]$ | $0.0122 \pm 0.0023$ | $0.0104 \pm 0.0025$ | $-0.0010 \pm 0.0037$ | $-0.0245$ v $0.0045$ | $-0.0225 \pm 0.0027$ |
| $[\alpha_{\rm ex}/Fe]$ | $0.0062 \pm 0.0013$ | $0.0006 \pm 0.0019$ | $-0.0012 \pm 0.0019$ | $-0.0235 \pm 0.0028$ | $-0.0184$ v $0.0021$ |

| | | | | | |
|---|---|---|---|---|---|
| $[\alpha_{\rm h}/\alpha_{\rm ex}]$ | $0.0051 \pm 0.0015$ | $0.0053 \pm 0.0016$ | $0.0004 \pm 0.0024$ | $-0.0031 \pm 0.0019$ | $-0.0057 \pm 0.0016$ |
| [Na/Fe] | $0.0077 \pm 0.0124$ | $0.0104 \pm 0.0119$ | $0.0204 \pm 0.0149$ | $0.0183 \pm 0.016$ | $0.0531 \pm 0.0259$ |
| [Al/Fe] | $0.0057 \pm 0.0033$ | $0.0048 \pm 0.0057$ | $-0.0156 \pm 0.0039$ | $-0.0420 \pm 0.0034$ | $-0.0484 \pm 0.0052$ |
| [K/Fe] | $0.0079 \pm 0.0043$ | $0.0111 \pm 0.0042$ | $-0.0089 \pm 0.0058$ | $-0.0202 \pm 0.0108$ | $0.0032 \pm 0.0055$ |
| [V/Fe] | $-0.0732 \pm 0.0170$ | $-0.1351 \pm 0.0067$ | $0.0119 \pm 0.0134$ | $-0.0830 \pm 0.0159$ | $0.0591 \pm 0.0606$ |
| [Cr/Fe] | $0.0057 \pm 0.0045$ | $0.0019 \pm 0.0040$ | $-0.0170 \pm 0.008$ | $0.0047 \pm 0.0098$ | $0.0082 \pm 0.0089$ |
| [Mn/Fe] | $-0.0179 \pm 0.0026$ | $-0.0185 \pm 0.002$ | $-0.0059 \pm 0.0034$ | $-0.0101 \pm 0.0043$ | $-0.0087 \pm 0.0055$ |
| [Fe/H] | $-0.0742 \pm 0.0068$ | $-0.0529 \pm 0.0057$ | $-0.0286 \pm 0.0076$ | $-0.0466 \pm 0.0092$ | $-0.0335 \pm 0.0139$ |
| [Co/Fe] | $0.0142 \pm 0.0065$ | $-0.0091 \pm 0.0032$ | $-0.0258 \pm 0.006$ | $-0.0160 \pm 0.0129$ | $-0.0426 \pm 0.0088$ |
| [Ni/Fe] | $0.0061 \pm 0.0008$ | $-0.0001 \pm 0.0023$ | $-0.0045 \pm 0.0010$ | $-0.0093 \pm 0.0026$ | $-0.0101 \pm 0.005$ |
| [Ce/Fe] | $-0.0223 \pm 0.0041$ | $-0.0151 \pm 0.0051$ | $-0.0058 \pm 0.0083$ | $-0.0966 \pm 0.005$ | $-0.0714 \pm 0.0026$ |

Carbon & Nitrogen The carbon and nitrogen abundance gradients show different evolutionary trends depending on the particular fiducial element (see Figure 4.5). The [C/Fe] gradient has a U-shaped trend with a critical points for the stars aged 5.58–8.36 Gyr. For these stars 5.58–8.36 Gyr there is an increase in the central [C/Fe] abundance, after which it remains constant around $-0.4$ dex (see Figure 4.8). The [N/Fe] gradient hovers around 0.0 dex/kpc, but for the stars with the youngest ages the gradient becomes quite negative with a value of $-0.0409 \pm 0.0040$ dex/kpc. The [(C+N/Fe)] gradient hovers around $-0.0020$ dex/kpc. The [C/N] gradient has a similar behaviour to [C/Fe], though it does become positive for stars younger than 2.23 Gyr. When the [C/N] gradient becomes positive, it corresponds to a decrease in the central abundance.

The [X/H] gradients for carbon and nitrogen all become more steeply negative for ages less than 5.58 Gyr (see Figure 4.6). The [N/Fe] gradient has a U-shaped trend with an extremum point in the $5.58 < t \leq 8.36$ Gyr age bin. As for the [C/H] and [(C+N)/H], if the oldest age bin is not considered, these also show a U-shaped trend, but the extremum point happens later around 3.66–5.58 Gyr ago.

Lastly, for the [X/Mg] carbon and nitrogen gradients, [C/Mg] shows a steepening trend and the [N/Mg] and [(C+N)/Mg] gradients start out positive and then inverts, becoming negative (see Figure 4.7). The [N/Mg] gradient inversion lags the [(C+N)/Mg] gradient inversion, which happens in the 3.66–5.58 Gyr age bin.

$\alpha$-Elements The $\alpha$-element gradients have various evolutionary trends as seen in Figure 4.5. The [Mg/Fe] and [Si/Fe] gradients have parallel evolutionary patterns as evidenced by the same general shape of their gradient trends. The radial trends from Figure 4.12 also show evolution in parallel for [Mg/Fe] and [Si/Fe], though the 5.58–8.36 gradient is much steeper for [Mg/Fe]. The relative evolution of [Ca/Fe] and [Ti/Fe] are similar in that they both tend to flatten out, but the gradients for stars younger than 3.66 Gyr tend to be slightly

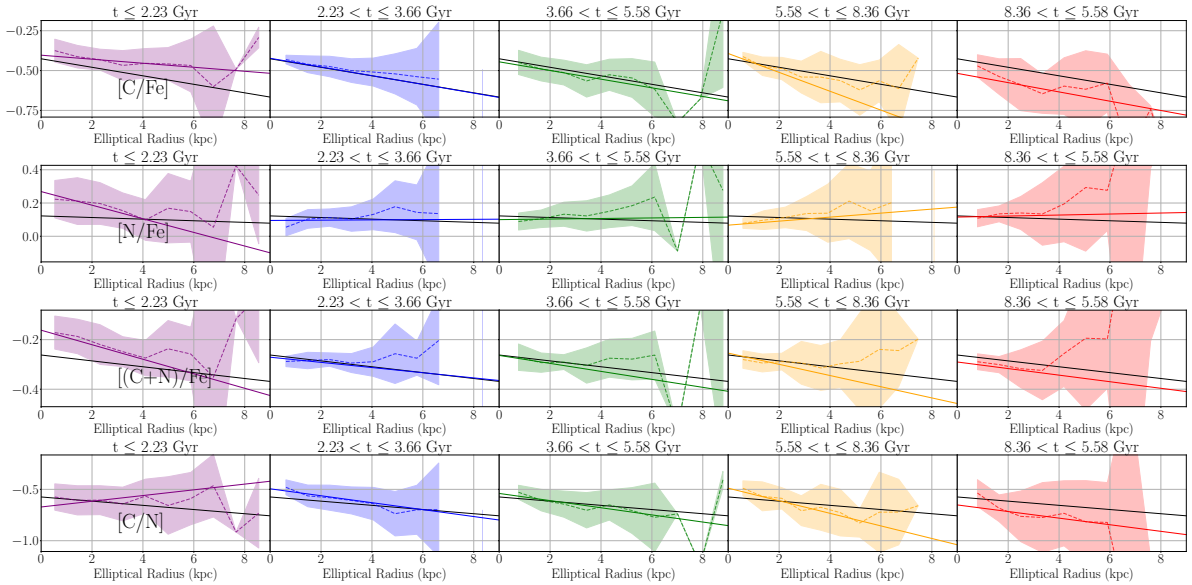



Figure 4.8: The radial abundance trends for the carbon and nitrogen abundances. For each row, age increases from left to right. The solid colored line is the fitted linear model, the dashed line follows the median abundance value for a given radius, and the color band shows the dispersion around the median. The black line is the fit to all the data without any age binning and serves as a fiducial. These plots show that the each of the different abundances increase over time, with the fit trend below the fiducial for older age bins and above for younger age bins. The youngest [N/Fe] and [C/N] trends standout showing much larger gradients than the other age bins. Also the [C/N] gradient clearly inverts for the youngest age bin.

positive and the corresponding [Ti/Fe] gradients are negative (see Figure 4.5). Both [O/Fe] and [S/Fe] evolve differently from the rest of the individual $\alpha$-element gradients, but [O/Fe] is similar to [Ca/Fe]. The composite $\alpha$-element gradients of [$\alpha$/Fe], [$\alpha_{\rm h}$/Fe], and [$\alpha_{\rm ex}$/Fe] evolve much like [Ca/Fe] or [Ti/Fe] (see Figure 4.5). The radial trends of these also evolve similarly (see Figure 4.13). The [$\alpha_{\rm h}/\alpha_{\rm ex}$] gradient does not show much evolution and remains fairly flat for the whole history of the SMC.

Many of the evolutionary trends for the [X/H] gradients of the $\alpha$-elements have a notable maximum for stars with ages between 3.66 and 5.58 Gyr (see Figure 4.6). While not necessarily a global extremum, these trends for the gradients show a significant change in the trajectory of the evolution. The [Mg/H], [Si/H], [$\alpha$/H], and [$\alpha_{\rm h}$/H] gradients have this maximum, but then turn downturn with the 2.23−3.66 Gyr gradients becoming steeper. These gradients then flatten to around the 3.66−5.58 Gyr value or even more for the gradients of the youngest star. The [O/H], [Ca/H], [Ti/H] and [$\alpha_{\rm ex}$/H] abundance ratios have global extrema for the 3.66−5.58 Gyr stars. The [Ca/H] evolutionary trend is also the only trend that shows a positive concave feature. The [S/H] gradient does not have a clear evolutionary trend and is fairly constant with time.

The individual $\alpha$-elements show quite a bit of variation in their evolution while the composite abundances are similar (see Figure 4.7). The evolution seen in [O/Mg] is comparable to the composite abundances. [S/Mg] does not have a clear evolutionary trend. The [Ti/Mg] gradients evolution has a U-shape with a critical point between 5.58–8.36 Gyr ago.

Odd-Z Elements Figure 4.5 shows that all of the odd-Z elements have different evolutionary trends. The [Na/Fe] gradient starts as significantly positive with a value of $+0.0531 \pm 0.0259$ dex/kpc and then flattens out to $+0.0077 \pm 0.0124$ dex/kpc for the youngest ages. The [Al/Fe] gradient starts around $\approx -0.0500$ dex/kpc before flattening for

more recent ages with very slightly positive gradients for stars younger than 3.66 Gyr. The [K/Fe] gradient has a U-shaped trend in its evolution, but its extremum point is between 5.58–8.36 Gyr ago, with these stars having a gradient of $-0.0202 \pm 0.0108$ dex/kpc. The central abundance values of the [X/Fe] abundance ratios show that the central value remains mostly constant regardless of the radial slope (see Figure 4.14).

For the odd-Z [X/H] gradients, both [Na/H] and [K/H] exhibit a U-shaped trend, while the [Al/H] flattens over time (see Figure 4.6). The [Na/H] has a potential extremum point at the same time as most other elements while the [K/Fe] extremum point happens for stars aged 5.58–8.36 Gyr.

The [X/Mg] gradients for the odd-Z elements evolve differently (see Figure 4.7). Much like the [Na/Fe] and [Na/H], the [Na/Mg] starts steep and positive and becomes shallower over time. Sometime between 2.23 and 3.66 Gyr ago the [Na/Mg] gradient inverts. The [Al/Mg] gradient shows a U-shaped trend in its evolution with a potential extremum point for the stars in the 3.66–5.58 Gyr age bin. Its trend is reminiscent of the shape seen for [Na/H]. The [K/Mg] gradient evolutionary trend shows an overall downward tendency, but oscillates as it flattens.

Iron Peak Elements Multiple [X/Fe] gradients show a potential U-shaped trend except for [V/Fe] (see Figure 4.5). While the trend is not as prominent, it is visible for [Cr/Fe], [Mn/Fe], and [Ni/Fe]. Both [Cr/Fe] and [Mn/Fe] have an extremum point around the 3.66–5.58 Gyr age bin, while the heavier iron peak elements ([Co/Fe] and [Ni/Fe]) have an extremum point earlier around the 5.58–8.36 Gyr age bin. The radial trends show that the central abundances for the lighter iron peak elements are fairly constant over time (see Figure 4.15). This is less true for the heavier iron peak elements and [Fe/H].

Many of the iron peak elements do have a U-shaped trend with an extremum point at the same time as most of the other element that also have a U-shaped trend (see Figure 4.6).

This is true for [Cr/H], [Mn/H], [Fe/H], and [Ni/H] as well as potentially [Co/H]. The [V/H] gradient's evolution shows a lot of large, sporadic excursions and, therefore, it is challenging to say what the gradient truly is doing over time.

The [X/Mg] gradients for Cr, Mn, Co, and Ni have similar evolutionary trends, but V and Fe are outliers (see Figure 4.7). The [Cr/Mg], [Mn/Mg], [Co/Mg], and [Ni/Mg] all show a downward trend. Each of these start positive for the oldest stars, but eventually thet invert becoming negative. The [V/Mg] gradient shows an evolution similar to the [V/H] gradient evolution. The [Fe/Mg] does have have a critical point in its evolution for stars aged 3.66–5.58 Gyr.

Neutron Capture Element For the [Ce/Fe] gradient, the oldest two ages have very negative values compared to the other age bins (see Figure 4.5). The radial trends show the dispersion in the [Ce/Fe] tends to be on the larger side (see Figure 4.16). The flattening and then subsequent steepening in the gradient evolution can also be seen in the radial trends quite clearly. This contrasts with what is seen in Figure 4.6, where the gradient potentially shows the U-shaped trend with an extremum point in the 3.66–5.58 Gyr age bin. The [Ce/Mg] gradient does show temporal evolution, though it is fairly complex.

Age-[X/Fe] Trends

Overall, the age-[X/Fe] trends for the SMC are mostly flat, though some show an increase in abundance for younger ages.

Carbon & Nitrogen The age-[X/Fe] trends for the carbon and nitrogen abundances are mostly flat (see Figure 4.8). The [C/Fe] abundance in the SMC very gradually increases over time throughout the galaxy. The western side of the galaxy for radii $< 3.3$ kpc is overabundant with the trend falling above the fiducial line found by calculating the age-[X/Fe] trend without any spatial binning. The outer galaxy is underabundant in both the

east and west.

The age-[N/Fe] trend reveals that throughout the SMC there was an increase in [N/Fe] within the last Gyr or so. Also, the outer galaxy is nitrogen-rich in both the eastern and western side for old stars, though the west is more nitrogen-rich. The inner west tends to be close to the fiducial or slightly underabundant. The [(C+N)/Fe] age-[X/Fe] trend looks analogous to the [N/Fe] trend because it matches the fiducial throughout the galaxy and the outer west is the most different.

An interesting feature with the age-[C/N] trend is the underabundance for all ages in the west for radii >3.3 kpc, but the overabundance for the inner radii of the west. There may also be a very slight hump between 0.0–5.0 Gyr.

$\alpha$-Elements Overall, the individual $\alpha$-elements have very flat age-[X/Fe] trends with somewhat larger deviations from this behaviour at recent times (see Figure 4.17). The lightest individual $\alpha$-element is [O/Fe] and the age-[O/Fe] trends in the east of the SMC follow the global fiducial, for the most part. There is actually a slight hump in the fiducial trendline and this is seen in the inner eastern region as well. The west is more complex with the younger stars in the inner region being oxygen-poor. The outer western region shows that the oldest stars are much more overabundant in [O/Fe] and the youngest stars are also slightly overabundant, but the ages between $\sim$5.5 Gyr and $\gtrsim$ 7.5 Gyr are underabundant in oxygen.

The age-[Mg/Fe] trend shows that the stars with radii $<$ 3.3 kpc have a downturn trend in magnesium. The outer SMC in the east has a flat age-[Mg/Fe] trend. The outer west has an age-[Mg/Fe] trend that is similar to the age-[O/Fe] trend in the same age bin, but the magnitude of the difference in the trends are smaller than what is seen in [O/Fe].

The next lightest individual $\alpha$-element is silicon. Both the inner and outer regions have flat age-[X/Fe] trends in the east. The inner western SMC appears to be deficient in

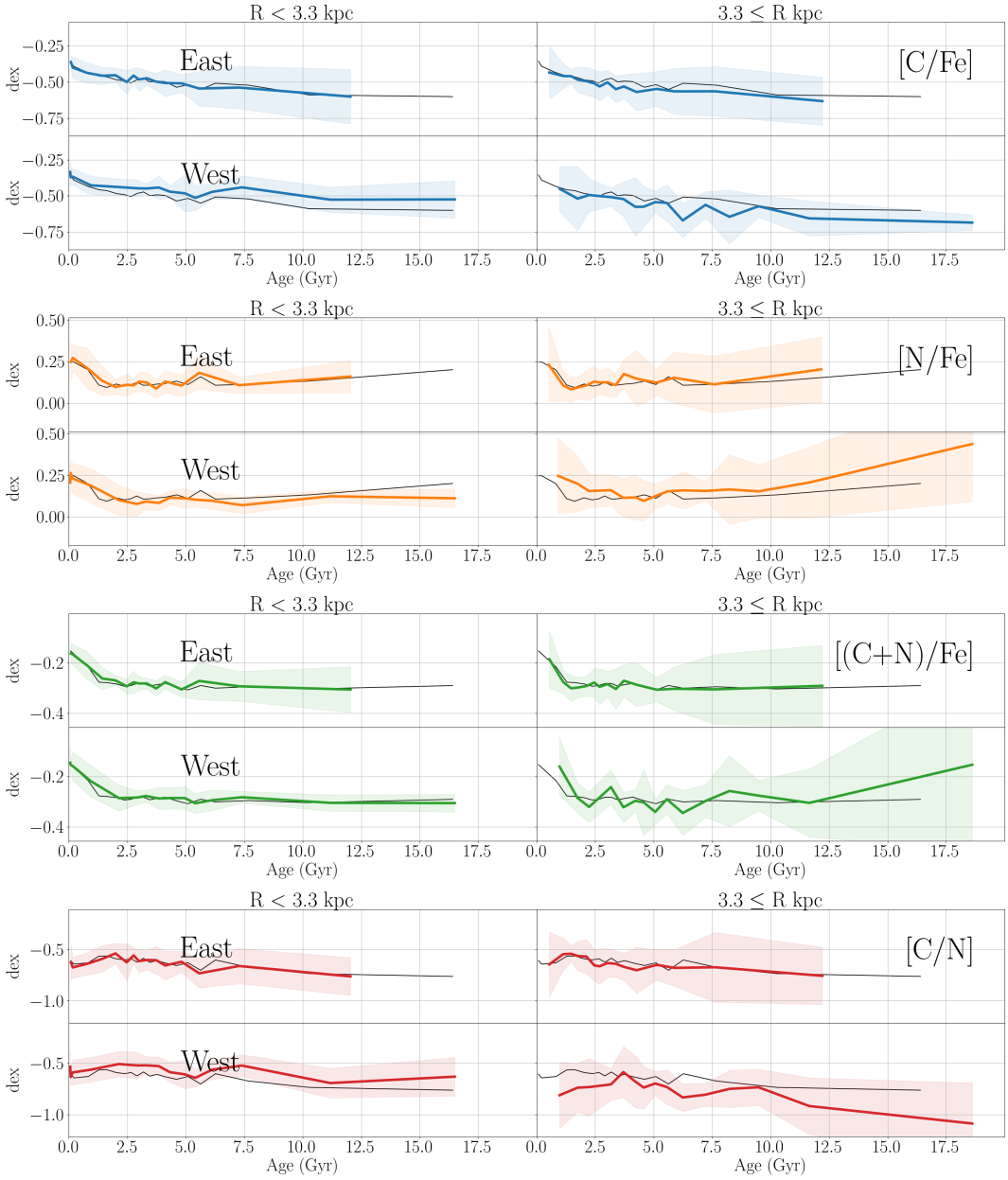



Figure 4.9: The age-[X/Fe] trends for the SMC for carbon and nitrogen. The top row in each panel shows the age-[X/Fe] trends for the northern part of the SMC and the bottom row shows the trends in the south. The SMC is split into two radial bins that contain an equal number of stars. For each sub-panel the age-[X/Fe] trend is included with a band of $1\sigma$ in addition the black fiducial line shows the age-[X/Fe] trend without any binning. Clearly the [N/Fe] and [(C+N)/Fe] have a sharp increase for recent times.

silicon for ages younger than 5 Gyr. The [Si/Fe] in the outer west looks very similar to the age-[Mg/Fe] trend in the same area.

Looking at the [S/Fe] and [Ca/Fe] age-abundance trends, both are very flat and do not show much deviation from the fiducial trendline or bin-to-bin. The [Ti/Fe] abundance is also quite flat like these abundances, except there is a slight tendency to increase over time.

The composite $\alpha$-abundance age-[X/Fe] trends look similar to the individual abundance ones (see Figure 4.18). The age-[$\alpha$/Fe] trend shows that the eastern SMC follows the fiducial trendline better than in the west. There is also a bump present in the abundance for ages less than 5 Gyr. For younger stars, with ages that are $\lesssim$2.5 Gyr in the inner western SMC, there is a deficiency in $\alpha$-abundance. Stars with similar ages in the outer west show an overabundance of [$\alpha$/Fe], while between $\sim$5 Gyr to $\sim$ 12.0 Gyr the stars are [$\alpha$/Fe]-poor. However, the oldest stars are [$\alpha$/Fe]-rich.

The age-[$\alpha_{\rm h}$/Fe] trend in the east, at all radii, looks a lot like the age-[$\alpha$/Fe] trend. This is also the case for stars at radii $<$ 3.3 kpc in the west as the age-[$\alpha_{\rm h}$/Fe] trend looks like the analogous trend in [$\alpha$/Fe]. The outer west of the SMC has a [$\alpha_{\rm h}$/Fe] trend similar to the outer west [$\alpha$/Fe], but the dip in [$\alpha_{\rm h}$/Fe] for intermediate ages only happens $\sim$4 Gyr to just past 7.5 Gyr. The explosive $\alpha$-element abundance, [$\alpha_{\rm ex}$/Fe], has similar behaviour to [$\alpha_{\rm h}$/Fe], but the age-[X/Fe] trend is flatter.

The age-[$\alpha_{\rm h}/\alpha_{\rm ex}$] trend shows a slight downturn in the inner galaxy for radii $<$ 3.3 kpc with a deficiency for younger stars in the west. The outer east has a slight overabundance compared to the fiducial trendline. Finally, the outer west SMC [$\alpha_{\rm h}/\alpha_{\rm ex}$] looks like [$\alpha_{\rm h}$/Fe], but with more exaggerated deviations from the fiducial trendline.

Odd-Z Elements For the odd-Z elements, the eastern SMC has essentially flat age-[X/Fe] trends for [Na/Fe], [Al//Fe], and [K/Fe] (see Figure 4.19). This is also true for stars with radii $<$ 3.3 kpc for [Al/Fe] and [K/Fe]. This not the case with the inner SMC which

is [Na/Fe]-poor especially for ages over 5 Gyr. The outer galaxy age-[Na/Fe] trend shows that it is rich in [Na/Fe] for most of the lifetime of the SMC. The western region for radii larger than 3.3 kpc shows that the galaxy is poor in [Al/Fe] for ages between ∼4 Gyr to ∼8 Gyr. The outer western part of the SMC has a more complicated age-[K/Fe] trend, but the average trend appears to somewhat follow the fiducial trendline.

Iron Peak Elements Much like other groups of elements, the iron peak age-[X/Fe] trends are also mostly flat, though some deviate from this pattern (see Figure 4.9). The [V/Fe] abundance for the youngest stars in the inner galaxy show an increasing abundance with age, while this is less so for the outer galaxy. The eastern outer galaxy does show this increase more than in the west, but nowhere near the inner galaxy. In the west, for stars of the inner galaxy that are older than ∼12.5 Gyr, show a deficiency in [V/Fe], but the outer western galaxy shows an overabundance for ages most ages.

The age-[Cr/Fe] trend stays close to solar for all times and radii <3.3 kpc. This is also the case for the stars at larger radii on the eastern side. The outer SMC in the west shows a different behavior with a [Cr/Fe] deficiency for ages ∼10 Gyr. The age-[Mn/Fe] trend looks similar to the [Cr/Fe] one. The average value is less then solar and is around −0.2 dex. The outer west is [Cr/Fe] poor for ages $\lesssim$ 8 Gyr.

There is a steady increase from $\approx -1.5$ dex up to $\approx -0.6$ at the current day for the inner galaxy. The outer eastern region also shows this trend although it only reaches up to $\approx -1.0$ dex at the present time. The outer west is the most divergent from the rest of the galaxy as evidenced by the deviation from the fiducial trendline. While the outer west does show an increase in [Fe/H], around 2.5 Gyr the trend turns down showing a decrease in [Fe/H] for that part of the galaxy. Also, the outer west galaxy is metal-poor compared to the fiducial trendline for the older stars.

The age-[Co/Fe] trend is very flat staying slightly under the solar value. This is also

case for [Ni/Fe], which is just under solar as well. The greatest deviations from the fiducial trendline happen in the outer west of the SMC. The average of the trends still follow the fiducial for both [Co/Fe] and [Ni/Fe].

Neutron Capture Looking at the age-[Ce/Fe] trend in Figure 4.21, it is clear that the SMC [Ce/Fe] abundance increases over time with a more substantial increase for ages less than 5 Gyr. The eastern part of the SMC is neither deficient nor overabundant in cerium as there is almost no difference between the global fiducial trend and those for each radial bin. On the other hand, the west shows an overabundance in cerium for the inner SMC for ages $\gtrsim$ 5 Gyr, but the outer galaxy is underabundant.

## Discussion

Below, we discuss the implications of our APOGEE abundance gradient results for the SMC.

### SMC Metallicity Gradient

It is important to note that many literature sources provide gradients in units of dex/deg and to compare to this work, these have been converted to units of dex/kpc[2]. Also, the literature sources discussed here are not exhaustive but demonstrate the range of measured values in the SMC radial metallicity gradient.

The overall metallicity gradient gradient of the SMC in this work was found to be $-0.0546 \pm 0.0043$ dex/kpc, which overlaps with gradients found by De Bortoli et al. (2022), Parisi et al. (2016) and Dobbie et al. (2014). Parisi et al. (2010) investigated the metallicity of RGB stars calculated from the near-infrared Ca II Triplet (CaT) for various samples out to a radius of $\sim$7.86°. Looking at exclusively field stars, the gradient was found to be $-0.0055$

[2]We multiply by $\frac{180}{62.44\pi}$ deg/kpc and make use of the small angle approximation.

$\pm$ 0.0083 dex/kpc and this overlaps with the gradient of the oldest stars found in this work. Interestingly, if globular clusters are included with the field stars, then the gradient moves away from the calculated gradients in this work becoming 0.0064 $\pm$ 0.0110 dex/kpc.

Looking at the RGB stars out to 5° in the galaxy, Dobbie et al. (2014) find quite different results from Parisi et al. Although Dobbie et al. also used field stars and CaT metallicities, they found a gradient of $-0.0688 \pm 0.0101$ dex/kpc, which is consistent with the gradient of the youngest stars in the APOGEE sample.

Revisiting the gradient of the SMC, Parisi et al. (2016) find a value of $-0.0734 \pm 0.0184$ dex/kpc using CaT-derived metallicities for field stars. This gradient does not overlap with the overall metallicity gradient found herein, but it does with the youngest metallicity gradient and also the Dobbie et al. value.

Choudhury et al. (2020) use a different metallicity-estimation technique to explore the metallicity distribution of the SMC. Metallicities were derived by relating the slope of the RGB branch in the $Y$ vs. $Y-K_{\rm s}$ color-magnitude diagram (CMD). The slopes were calculated for 1,180 subregions of the SMC. The calculated gradient using the RGB slope metallicities is $-0.0028 \pm 0.0046$ dex/kpc, which is similar to what was found by Parisi et al. (2010).

The CaT technique is used to derive metallicities in De Bortoli et al. (2022). In that work, they explore the gradient of the inner (R $< 3.4°$) and outer (R $> 3.4°$) SMC using both field stars and globular clusters. Both of the outer gradients fall far outside the range of any of the gradients calculated in this work. With the outer field stars having a gradient of $+0.0459 \pm 0.0184$ dex/kpc and the outer clusters having a slightly shallower gradient of $+0.0275 \pm 0.0184$ dex/kpc. Both of the inner gradients overlap with the overall metallicity gradient and many other ones calculated here.

The final literature source discussed here is Li et al. (2023). In that work, metallicities are found for RR Lyrae stars in Gaia by using $G$-metallicity relations and near–IR period–absolute magnitude–metallicity relations. The gradient found was $-0.0070 \pm 0.0030$

Table 4.8: Table of literature values for the [Fe/H]-gradient of the SMC. All but Li et al. (2023) and Choudhury et al. (2020) use CaT equivalent widths to the [Fe/H].

| Source | $\nabla_R$ (dex/kpc) | Method |
|---|---|---|
| Parisi et al. 2010 | $-0.0055 \pm 0.0083$ | CaT Field |
| —"— | $+0.0064 \pm 0.0110$ | CaT Field+GCs |
| Dobbie et al. 2014 | $-0.0688 \pm 0.0101$ | CaT Field |
| Parisi et al. 2016 | $-0.0734 \pm 0.0184$ | CaT Field |
| Choudhury et al. 2020 | $-0.0028 \pm 0.0046$ | RGB Slope |
| De Bortoli et al. 2022 | $-0.0734 \pm 0.0367$ | CaT Inner GCs |
| —"— | $+0.0275 \pm 0.0184$ | CaT Outer GCs |
| —"— | $-0.0734 \pm 0.0275$ | CaT Inner Field |
| —"— | $+0.0459 \pm 0.0184$ | CaT Outer Field |
| Li et al. 2023 | $-0.0070 \pm 0.0030$ | Gaia G Band RR |

dex/kpc, which is consistent with Choudhury et al. (2020), Parisi et al. (2010), and the old RGB star gradient calculated in this work.

This variation in the literature values for the SMC gradient is reminiscent of what is seen for the LMC gradient (Povick et al. 2023b, in prep.). Interestingly, the literature gradients seem to mostly agree with either younger gradient with some overlap with the oldest gradient in this work, with none overlapping with more intermediately aged gradients (see Figure 4.10). The metallicity gradient found in this work was derived with some of the largest coverage of the SMC with very high resolution compared to other studies making it one of the most accurate, to date.

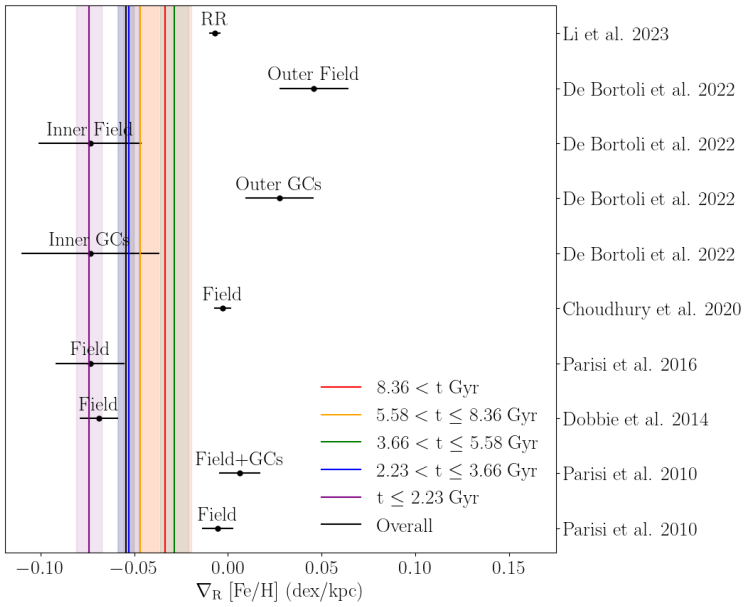



Figure 4.10: A comparison of the [Fe/H] gradients found in this work to multiple literature values. The vertical lines and bands correspond to the gradients for each of the age bins with the associated errors. The literature values are shown as points. The gradients calculated by De Bortoli et al. (2022) out to 3.4° overlap with the overall gradient as well as values found by Dobbie et al. (2014) and Parisi et al. (2016). Around half of the literature gradients overlap with any of the gradients calculated in this work.

Evolution of Abundance Gradients of the SMC

Abundance gradients for 24 abundance ratios were calculated using 2,062 field RGB stars in the SMC. Combining these gradients with ages calculated using the method in Povick et al. (2023b, in prep.) makes it possible to study the evolution of each of the gradients.

While there are extremum points in the trends of the gradients for most elements, many have one for stars aged 3.66–5.58 Gyr. Abundances with this critical point appear in their evolution includes [C/Fe], [N/Fe], [Na/Fe], [Cr/Fe], [Mn/Fe], most of the [X/H] gradients, [O/Mg], [Ca/Mg], [Na/Mg], [Mn/Mg], and [Fe/Mg]. The fact that this feature is so ubiquitous in many elements from different element groups, suggests a major galaxy-wide event caused it.

In Paper II, it was found that extremum points in the evolution of LMC abundance gradients are possibly connected to starbursts from intergalactic interactions. It is known that an LMC-SMC interaction produced a starburst in each galaxy (Dobbie et al., 2014; Hasselquist et al., 2021; Nidever et al., 2020). The starburst in the LMC was found to happen about 2 Gyr ago in Nidever et al. (2020) and is consistent with the change in the abundance trends in Paper II. The turnover in the gradient evolution for the SMC was found to happen earlier around 3.66–5.58 Gyr ago. This is consistent with the starburst in Dobbie et al. (2014) 5–6 Gyr ago. Hasselquist et al. (2021) found that the SMC did experience a burst of star formation 3–4 Gyr before the LMC. Qualitatively the results of that paper agree with this present work, but the time of the burst is somewhat different. Also, Massana et al. (2022) found bursts of star formation at $\sim$3 Gyr and $\sim$2 Gyr in the SMC, while the LMC star formation ramps up at $\sim$3 Gyr ago but doesn't peak until $\sim$2 Gyr ago. It is not entirely clear why these inconsistencies exist between the photometrically determined SFHs and the star formation bursts deduced from the chemistry. Nevertheless, the other results qualitatively support the SMC experiencing a star formation burst that precedes the one in

the LMC.

Radial migration is a process whereby stars move to a different radius because additional angular momentum is imparted on them (e.g. Sellwood & Binney, 2002). Naturally this will change the observed gradients especially for older stars so the present day gradients may not be representative of the gradients when the stars formed. But Schroyen et al. (2013) showed that dwarf galaxy metallicity gradients are less affected by radial migration than larger galaxies. It is best to keep in mind radial migration when ruminating about the results in this work and to think of the evolutionary trends as more age-dependent trends.

Additionally, in Paper II it was found that many of the age-[X/Fe] trends have a turnover with an extremum point due to an LMC starburst which further helps pinpoint the timeframe of the burst. This is not what is seen in the SMC. The trends for the SMC are essentially flat with a few showing some slight increase or decrease for extremely young ages. There is no feature in the trends at the time of the burst. Most trends stay close to the fiducial trendline regardless of the spatial bin. Any disparities with the global fiducial trend are mostly in the outer western region of the galaxy.

Comparing the SMC to the LMC and MW

In addition to comparing the calculated [Fe/H] gradient to other literature values, we also compare the SMC abundance gradients to those of the LMC and MW using the same method outlined in Section 4 and the same APOGEE data. This allows us to conduct an apples-to-apples comparison of abundance gradients across a factor of $\sim$500 in total galaxy mass (SMC: $2 \times 10^9$ $M_\odot$, Stanimirović et al. 2004; LMC: $1.38 \times 10^{11}$ $M_\odot$, Erkal et al. 2019; MW: $1.28 \times 10^{12}$ $M_\odot$, Watkins et al. 2019) in a uniform manner. Gradients for the LMC were previously calculated using the APOGEE data in Povick et al. (2023b, in prep.). We determine our own MW radial abundance gradients here.

MW RGB stars were selected from the APOGEE `allStar` file[3] using a slightly modified version of the selection from Jönsson et al. (2020):

1. $1.5 < \log g < 3.5$
2. [C/N] > 0.04 - 0.46[M/H] - 0.0028·$dT$

where

$$dT = \mathrm{T_{eff,spec}} - (4400 + 552.6 \cdot (\log \mathrm{g_{spec}} - 2.5) - 324.6 \cdot [\mathrm{M/H}])$$

and where $\mathrm{T_{eff,spec}}$, and $\log \mathrm{g_{spec}}$ are the `TEFF_SPEC` and `LOGG_SPEC` columns in the `allStar` summary file, respectively. After this initial selection, a second selection was used to pick out stars close to the MW midplane using:

1. $4.0 \leq \mathrm{R} \leq 15.0$ kpc
2. $|\mathrm{Z}| \leq 1.0$ kpc

where R is the galactic radius of a star, and Z is the vertical distance from the midplane. The selection criterion on R was chosen so that there is large radial coverage, but that structures of the inner MW (i.e., bar and bulge) did not "contaminate" the disk sample. Once the selection is done, the method in Section 4 is used to calculate the radial abundance gradients. Each of the galaxy gradients are scaled by the exponential disk radial scale length of each galaxy to remove the bias of different galaxy sizes. The radial scale of the disk for the SMC is 1.25 kpc (Gonidakis et al., 2009), for the LMC is 1.667 kpc (Choi et al., 2018b), and for the MW is 2.15 kpc (Bovy & Rix, 2013).

In the top panel of Figure 4.11, the SMC, LMC, and MW really stand out from each other in their [X/H] gradients. The LMC gradients appear the shallowest followed by the SMC and then the MW. While not exactly the same, both of the Clouds have more similar

[3] `https://www.sdss.org/dr17/irspec/spectro_data/`

gradients between themselves versus the MW. The clear separation between the Clouds and the MW for the [X/H] suggest that there may exist a mass dependence in these gradients. The median [X/Mg] gradients for the Clouds are $\sim -0.075$ dex/$R_d$ and the MW median gradient is roughly 50% steeper with a value of $-0.120$ dex/$R_d$.

In contrast, the patterns in the [X/Fe] gradients of the three galaxies look very similar (top panel of Figure 4.11). There are only a few elements for which a substantial difference occurs such as the case with [Ce/Fe]. For some elements, the gradients for the Clouds look alike (e.g. [N/Fe], [C/N], [O/Fe], [$\alpha$/Fe], etc.) while there are elements for which the LMC and MW look alike or the SMC and the MW do. Since the Clouds and the MW have had a very different accretion and formation history, the overall consistency of the patterns in the radial [X/Fe] gradients (in dex/$R_d$) may suggest that these are a fairly universal aspect of galaxies.

As for the [X/Mg] gradients (Figure 4.22), the three galaxies have comparable gradients except in a few elements. The largest separation between the galaxies occurs with [Fe/Mg] and [Ce/Mg] and is similar in many ways to what is seen for the [X/H] gradients. Possibly these gradients are galaxy mass sensitive. The median [X/Mg] gradients for all three galaxies is flat.

## Summary

We calculated radial abundance gradients for 24 abundance ratios and their temporal evolution with an MCMC technique using 2,062 APOGEE DR17 RGB stars in the SMC. In addition, age-abundance trends for [C/N] and [$\alpha_h/\alpha_{ex}$] were measured.

The SMC has an overall metallicity gradient of $-0.0546 \pm 0.0043$ dex/kpc, which is steeper than the LMC, but nowhere near as steep as the MW field star gradient. Accounting for disk scale length, the metallicity gradient of the SMC is $-0.0654 \pm 0.0067$ dex/$R_d$, the LMC is $-0.0525 \pm 0.0035$ dex/$R_d$, and the MW is $-0.1196 \pm 0.0009$ dex/$R_d$. The calculated




Figure 4.11: A comparison of the overall radial abundance gradients for the SMC, LMC and the MW. The LMC is shown in blue, the SMC in orange, and the MW in green. (*Top*) [X/H] gradients which show a clear separation between the MW and the dwarf galaxies. The MW has median abundance gradients (dotted horizontal lines) almost 50% larger then ($-1.20$ dex/$R_d$) than the MCs ($-0.80$ dex/$R_d$). (*Bottom*) [X/Fe] gradients where all three galaxies show much more consistent patterns and almost no difference in the median gradients.

SMC gradient agrees with gradients from Dobbie et al. (2014), Parisi et al. (2016), and De Bortoli et al. (2022). There is better agreement on the inner SMC metallicity gradient calculated in the literature, regardless of the source using GCs or field stars.

Further comparing the overall SMC gradients to the LMC and MW show that in many cases the gradients are too similar to distinguish between the three galaxies. This is true for the [X/Fe] and [X/Mg] gradients, but not with the [X/H] gradients. The radial iron gradients, regardless of the fiducial element, deviate from each other for all three galaxies, though the MCs have closer gradients. The median gradient for the [X/Fe] and [X/Mg] are very similar for all three galaxies, but this is not the case for [X/H]. For the [X/H] abundances, the median MW gradient is around $-0.125$ dex/$R_d$, while the Clouds have median gradients around $-0.075$ dex/$R_d$.

There are a substantial number of gradients with extremum points in their evolution for stars aged 3.66–5.58 Gyr old. As the LMC gradients in Paper II show, an extremum point appears in their evolution and corresponds to the starburst triggered by a close interaction between the LMC and SMC. As noted, the SMC experienced a starburst a few Gyr before the LMC and that corresponds to the slightly older extremum point in the evolution of the SMC gradients.

For the most part, the age-[X/Fe] trends are flat for the SMC. Even more so than what was found in Paper II with the LMC. In most cases with any discernible differences, the outer SMC in the west seems to be more chemically different compared to the rest of the galaxy. Unfortunately, there is no feature in the trends which can help pinpoint the starburst due to the LMC-SMC interaction like what was found in Paper II.

## Acknowledgements

J.T.P. acknowledges support for this research from the National Science Foundation (AST-1908331) and the Montana Space Grant Consortium Graduate Fellowship.

D.L.N. acknowledges support for this research from the National Science Foundation (AST-1908331)

Funding for the Sloan Digital Sky Survey IV has been provided by the Alfred P. Sloan Foundation, the U.S. Department of Energy Office of Science, and the Participating Institutions.

SDSS-IV acknowledges support and resources from the Center for High Performance Computing at the University of Utah. The SDSS website is www.sdss.org.

SDSS-IV is managed by the Astrophysical Research Consortium for the Participating Institutions of the SDSS Collaboration including the Brazilian Participation Group, the Carnegie Institution for Science, Carnegie Mellon University, Center for Astrophysics | Harvard & Smithsonian, the Chilean Participation Group, the French Participation Group, Instituto de Astrofísica de Canarias, The Johns Hopkins University, Kavli Institute for the Physics and Mathematics of the Universe (IPMU) / University of Tokyo, the Korean Participation Group, Lawrence Berkeley National Laboratory, Leibniz Institut für Astrophysik Potsdam (AIP), Max-Planck-Institut für Astronomie (MPIA Heidelberg), Max-Planck-Institut für Astrophysik (MPA Garching), Max-Planck-Institut für Extraterrestrische Physik (MPE), National Astronomical Observatories of China, New Mexico State University, New York University, University of Notre Dame, Observatário Nacional / MCTI, The Ohio State University, Pennsylvania State University, Shanghai Astronomical Observatory, United Kingdom Participation Group, Universidad Nacional Autónoma de México, University of Arizona, University of Colorado Boulder, University of Oxford, University of Portsmouth, University of Utah, University of Virginia, University of Washington, University of Wisconsin, Vanderbilt University, and Yale University.

This work has made use of data from the European Space Agency (ESA) mission *Gaia* (`https://www.cosmos.esa.int/gaia`), processed by the *Gaia* Data Processing and Analysis Consortium (DPAC, `https://www.cosmos.esa.int/web/gaia/dpac/consortium`). Fund-

ing for the DPAC has been provided by national institutions, in particular the institutions participating in the *Gaia* Multilateral Agreement.

*Software:* Astropy (Astropy Collaboration et al., 2013, 2018), Matplotlib (Hunter, 2007), NumPy (Harris et al., 2020), SciPy (Virtanen et al., 2020)

## Data Availability

All APOGEE DR17 data used in this study is publicly available and can be found at: `https://www.sdss4.org/dr17/data_access/`.

## Gaia ADQL Query

Here is the Gaia ADQL query used to get a sample of SMC stars from which the RC is selected for determining the APOGEE field RC proper motions.

```
SELECT * FROM gaiadr3.gaia_source_lite as g
WHERE 1 = CONTAINS(POINT(g.ra,g.dec),
CIRCLE(13.18333333,−72.82833333,11))
AND g.phot_g_mean_mag<20.5
AND g.parallax IS NOT NULL
AND g.phot_bp_mean_mag IS NOT NULL
AND g.phot_rp_mean_mag IS NOT NULL
AND g.phot_g_mean_mag IS NOT NULL
AND g.parallax<0.2
AND g.parallax>−0.2
AND g.pmra>=−3.0
AND pmra<=3.0
```

```
AND g.pmdec>=-3.0
AND pmdec<=3.0
AND g.phot_g_mean_flux_over_error>3.0
AND g.phot_bp_mean_flux_over_error>3.0
AND g.phot_rp_mean_flux_over_error>3.0
```

## $\nabla_R$[X/H] & $\nabla_R$[X/Mg] Tables

The tables for the [X/H] and [X/Mg] gradients, which do not appear in the main body of the paper.

Table 4.9: Table of the [X/H] gradients for each of the age bins. Horizontal lines have been added marking the division of the previously defined groups of elements. In general descending down the table corresponds to an increase in atomic number. Each age bin has its own separate column.

| Element | $t \leq 2.23$ $\nabla_R$ (dex/kpc) | $2.23 < t \leq 3.66$ $\nabla_R$ (dex/kpc) | $3.66 < t \leq 5.58$ $\nabla_R$ (dex/kpc) | $5.58 < t \leq 8.36$ $\nabla_R$ (dex/kpc) | $8.36 < t$ $\nabla_R$ (dex/kpc) |
|---|---|---|---|---|---|
| [C/H] | $-0.0812 \pm 0.0081$ | $-0.0910 \pm 0.0098$ | $-0.0440 \pm 0.0117$ | $-0.1131 \pm 0.0215$ | $-0.0776 \pm 0.0241$ |
| [N/H] | $-0.0647 \pm 0.0082$ | $-0.0560 \pm 0.0064$ | $-0.0244 \pm 0.0055$ | $-0.0225 \pm 0.0088$ | $-0.0258 \pm 0.0110$ |
| [(C+N)/H] | $-0.0891 \pm 0.0068$ | $-0.0698 \pm 0.0089$ | $-0.0292 \pm 0.0075$ | $-0.0772 \pm 0.0177$ | $-0.0262 \pm 0.0150$ |
| [O/H] | $-0.0547 \pm 0.0072$ | $-0.0591 \pm 0.0054$ | $-0.0279 \pm 0.0073$ | $-0.0513 \pm 0.0082$ | $-0.0608 \pm 0.0154$ |
| [Mg/H] | $-0.0149 \pm 0.0074$ | $-0.0597 \pm 0.0072$ | $-0.0419 \pm 0.0059$ | $-0.1092 \pm 0.0086$ | $-0.0693 \pm 0.0161$ |
| [Si/H] | $-0.0307 \pm 0.0059$ | $-0.0420 \pm 0.0071$ | $-0.0204 \pm 0.0056$ | $-0.0539 \pm 0.0092$ | $-0.0618 \pm 0.0142$ |
| [S/H] | $-0.0236 \pm 0.0096$ | $-0.0651 \pm 0.0195$ | $-0.0486 \pm 0.0072$ | $-0.0535 \pm 0.0251$ | $-0.1362 \pm 0.0441$ |
| [Ca/H] | $-0.0561 \pm 0.0068$ | $-0.0631 \pm 0.0078$ | $-0.0461 \pm 0.0077$ | $-0.0693 \pm 0.0117$ | $-0.0662 \pm 0.0175$ |
| [Ti/H] | $-0.0786 \pm 0.0081$ | $-0.0699 \pm 0.0076$ | $-0.0371 \pm 0.0102$ | $-0.0661 \pm 0.0140$ | $-0.1352 \pm 0.0141$ |
| [$\alpha$/H] | $-0.0407 \pm 0.0067$ | $-0.0622 \pm 0.006$ | $-0.0344 \pm 0.0071$ | $-0.0724 \pm 0.0084$ | $-0.0657 \pm 0.0141$ |
| [$\alpha_h$/H] | $-0.0306 \pm 0.0067$ | $-0.0607 \pm 0.0061$ | $-0.0321 \pm 0.0074$ | $-0.0677 \pm 0.0094$ | $-0.0649 \pm 0.0153$ |
| [$\alpha_{ex}$/H] | $-0.0582 \pm 0.0068$ | $-0.0586 \pm 0.0066$ | $-0.0326 \pm 0.0081$ | $-0.0658 \pm 0.0118$ | $-0.0636 \pm 0.0153$ |
| [Na/H] | $-0.0642 \pm 0.0151$ | $-0.0288 \pm 0.0164$ | $-0.0421 \pm 0.0086$ | $-0.0267 \pm 0.0140$ | $-0.0592 \pm 0.0181$ |
| [Al/H] | $-0.0305 \pm 0.0050$ | $-0.0758 \pm 0.0086$ | $-0.0663 \pm 0.0103$ | $-0.1421 \pm 0.0133$ | $-0.1379 \pm 0.0175$ |

| | | | | | |
|---|---|---|---|---|---|
| [K/H] | $-0.0134 \pm 0.0047$ | $-0.0412 \pm 0.0057$ | $-0.0413 \pm 0.0020$ | $-0.0978 \pm 0.0108$ | $-0.0417 \pm 0.0198$ |
| [V/H] | $-0.1411 \pm 0.0166$ | $0.0260 \pm 0.0061$ | $-0.0705 \pm 0.0171$ | $-0.1005 \pm 0.0168$ | $-0.0033 \pm 0.0566$ |
| [Cr/H] | $-0.0916 \pm 0.0126$ | $-0.0700 \pm 0.0114$ | $-0.0437 \pm 0.0101$ | $-0.0486 \pm 0.0151$ | $-0.0684 \pm 0.0242$ |
| [Mn/H] | $-0.0918 \pm 0.0074$ | $-0.0747 \pm 0.0095$ | $-0.0440 \pm 0.0102$ | $-0.0562 \pm 0.0136$ | $-0.046 \pm 0.0161$ |
| [Fe/H] | $-0.0741 \pm 0.0070$ | $-0.0528 \pm 0.0057$ | $-0.0286 \pm 0.0076$ | $-0.0464 \pm 0.0091$ | $-0.0336 \pm 0.0139$ |
| [Co/H] | $-0.0582 \pm 0.0105$ | $-0.0631 \pm 0.0072$ | $-0.0528 \pm 0.0100$ | $-0.0675 \pm 0.0201$ | $-0.0857 \pm 0.0213$ |
| [Ni/H] | $-0.0452 \pm 0.0063$ | $-0.0597 \pm 0.0068$ | $-0.0233 \pm 0.0083$ | $-0.0575 \pm 0.0107$ | $-0.0441 \pm 0.0193$ |
| [Ce/H] | $-0.0963 \pm 0.012$ | $-0.0587 \pm 0.0107$ | $-0.0115 \pm 0.0129$ | $-0.1380 \pm 0.031$ | $-0.0884 \pm 0.0298$ |

Table 4.10: Table of the [X/H] gradients for each of the age bins. Horizontal lines have been added marking the division of the previously defined groups of elements. In general descending down the table corresponds to an increase in atomic number. Each age bin has its own separate column.

| | | | | | |
|---|---|---|---|---|---|
| [C/Mg] | $-0.0500 \pm 0.0054$ | $-0.0252 \pm 0.0041$ | $-0.0221 \pm 0.0062$ | $-0.0127 \pm 0.0143$ | $-0.0093 \pm 0.0072$ |
| [N/Mg] | $-0.0742 \pm 0.0058$ | $0.0054 \pm 0.0041$ | $0.0239 \pm 0.0037$ | $0.0522 \pm 0.0074$ | $0.0285 \pm 0.0036$ |
| [(C+N)/Mg] | $-0.0556 \pm 0.004$ | $-0.0132 \pm 0.0027$ | $-0.0006 \pm 0.0033$ | $0.0215 \pm 0.0070$ | $0.0214 \pm 0.0058$ |
| [O/Mg] | $-0.0196 \pm 0.0035$ | $0.0013 \pm 0.0014$ | $0.0012 \pm 0.0008$ | $0.0113 \pm 0.0024$ | $0.0111 \pm 0.0024$ |
| [Mg/H] | $-0.0154 \pm 0.0072$ | $-0.0596 \pm 0.0073$ | $-0.0418 \pm 0.006$ | $-0.1094 \pm 0.0086$ | $-0.0691 \pm 0.0162$ |
| [Si/Mg] | $-0.0106 \pm 0.0032$ | $-0.0041 \pm 0.0011$ | $0.0035 \pm 0.0018$ | $0.0245 \pm 0.0021$ | $0.0167 \pm 0.0027$ |
| [S/Mg] | $0.0097 \pm 0.0109$ | $0.0094 \pm 0.0170$ | $-0.0349 \pm 0.0111$ | $0.0223 \pm 0.0255$ | $-0.0262 \pm 0.027$ |
| [Ca/Mg] | $-0.0213 \pm 0.0036$ | $-0.0057 \pm 0.003$ | $0.0153 \pm 0.0024$ | $-0.0166 \pm 0.0016$ | $0.0108 \pm 0.0066$ |
| [Ti/Mg] | $-0.0429 \pm 0.0042$ | $-0.0003 \pm 0.0011$ | $-0.0003 \pm 0.0053$ | $0.0140 \pm 0.0046$ | $-0.0545 \pm 0.0031$ |
| [$\alpha$/Mg] | $-0.0154 \pm 0.0027$ | $-0.0025 \pm 0.0012$ | $0.0008 \pm 0.0017$ | $0.0111 \pm 0.0034$ | $0.0062 \pm 0.0032$ |
| [$\alpha_{\mathrm{h}}$/Mg] | $-0.0097 \pm 0.0018$ | $0.0006 \pm 0.0007$ | $0.0006 \pm 0.0004$ | $0.0057 \pm 0.0012$ | $0.0055 \pm 0.0011$ |
| [$\alpha_{\mathrm{ex}}$/Mg] | $-0.0214 \pm 0.0033$ | $-0.0102 \pm 0.0008$ | $0.0000 \pm 0.0025$ | $0.0015 \pm 0.0025$ | $0.0043 \pm 0.0030$ |
| [Na/Mg] | $-0.0302 \pm 0.0160$ | $0.0035 \pm 0.0164$ | $0.0121 \pm 0.0109$ | $0.0179 \pm 0.0164$ | $0.0603 \pm 0.0234$ |
| [Al/Mg] | $-0.028 \pm 0.0042$ | $-0.0068 \pm 0.0020$ | $-0.0133 \pm 0.0041$ | $-0.0130 \pm 0.0033$ | $-0.0283 \pm 0.0069$ |
| [K/Mg] | $-0.0085 \pm 0.0043$ | $0.0133 \pm 0.0028$ | $-0.0008 \pm 0.0028$ | $0.0188 \pm 0.0036$ | $0.0088 \pm 0.0011$ |
| [V/Mg] | $-0.1231 \pm 0.0171$ | $-0.1002 \pm 0.0119$ | $0.0601 \pm 0.0124$ | $-0.0737 \pm 0.0221$ | $0.0799 \pm 0.0519$ |
| [Cr/Mg] | $-0.0280 \pm 0.0090$ | $-0.0066 \pm 0.0078$ | $-0.0095 \pm 0.0079$ | $-0.0017 \pm 0.0153$ | $0.0297 \pm 0.0062$ |

| | | | | | |
|---|---|---|---|---|---|
| [Mn/Mg] | $-0.0429 \pm 0.0053$ | $-0.0254 \pm 0.0044$ | $-0.0354 \pm 0.0019$ | $0.0036 \pm 0.0055$ | $0.0307 \pm 0.0087$ |
| [Fe/Mg] | $-0.0840 \pm 0.0149$ | $-0.1194 \pm 0.0138$ | $-0.0570 \pm 0.0078$ | $-0.1530 \pm 0.0185$ | $-0.1016 \pm 0.0261$ |
| [Co/Mg] | $-0.0177 \pm 0.0055$ | $-0.0121 \pm 0.0036$ | $-0.0126 \pm 0.0082$ | $-0.0028 \pm 0.0117$ | $0.0070 \pm 0.0093$ |
| [Ni/Mg] | $-0.0098 \pm 0.0030$ | $-0.0060 \pm 0.0030$ | $0.0111 \pm 0.0039$ | $0.0225 \pm 0.0033$ | $0.0215 \pm 0.0055$ |
| [Ce/Mg] | $-0.0672 \pm 0.0066$ | $-0.0065 \pm 0.0076$ | $0.0054 \pm 0.009$ | $0.0239 \pm 0.0168$ | $-0.0364 \pm 0.0044$ |

## Radius-Abundance-Age Trends

The radius-[x/Fe]-age trends for the $\alpha$-elements, odd-Z elements, iron peak elements and neutron capture elements that do not appear in the main body if the paper.

## Age-[X/Fe] Trends

The age-[X/Fe] trends for the $\alpha$-elements, odd-Z elements, iron peak elements and neutron capture elements that do not appear in the main body if the paper.

## Comparing to the LMC and MW Extra Plots

Plots comparing the SMC, LMC, and Milky Way that do not appear in the main body if the paper.

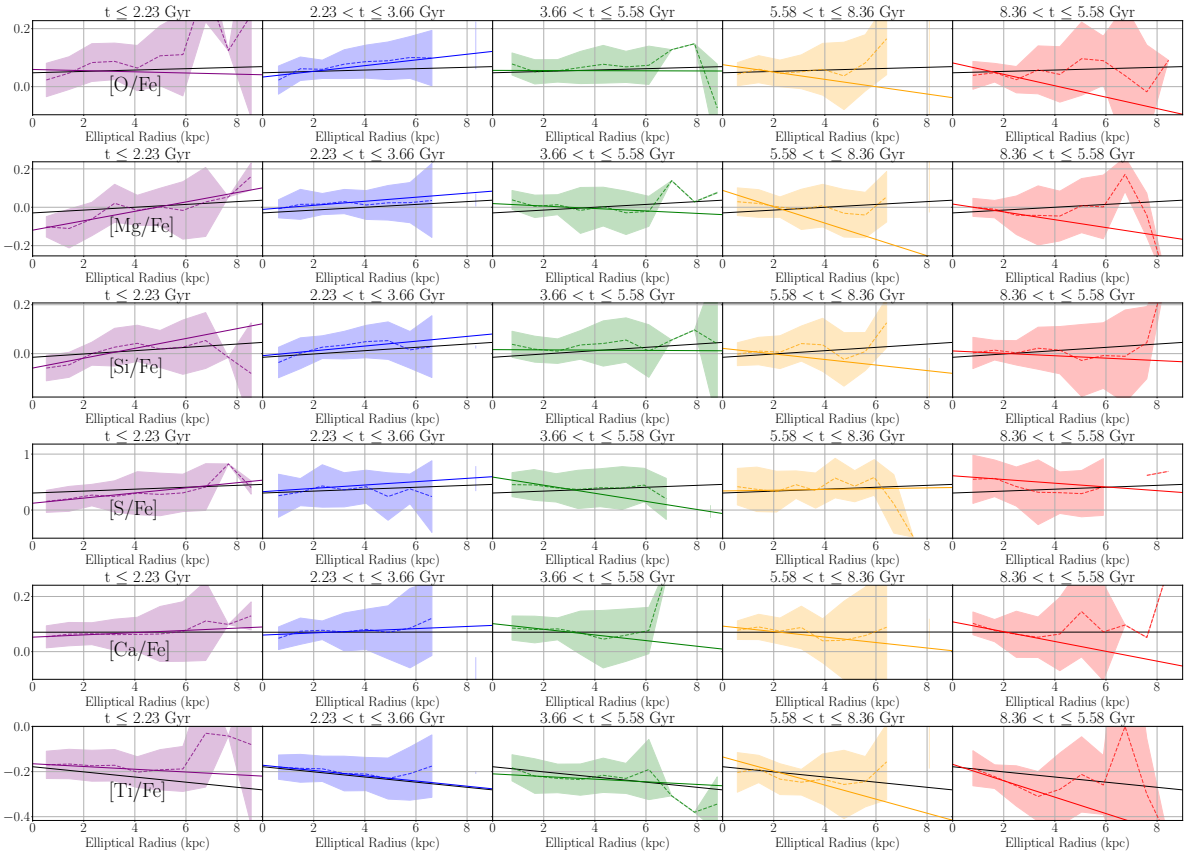



Figure 4.12: The same as for Figure 4.8, but with the individual $\alpha$-element abundances.

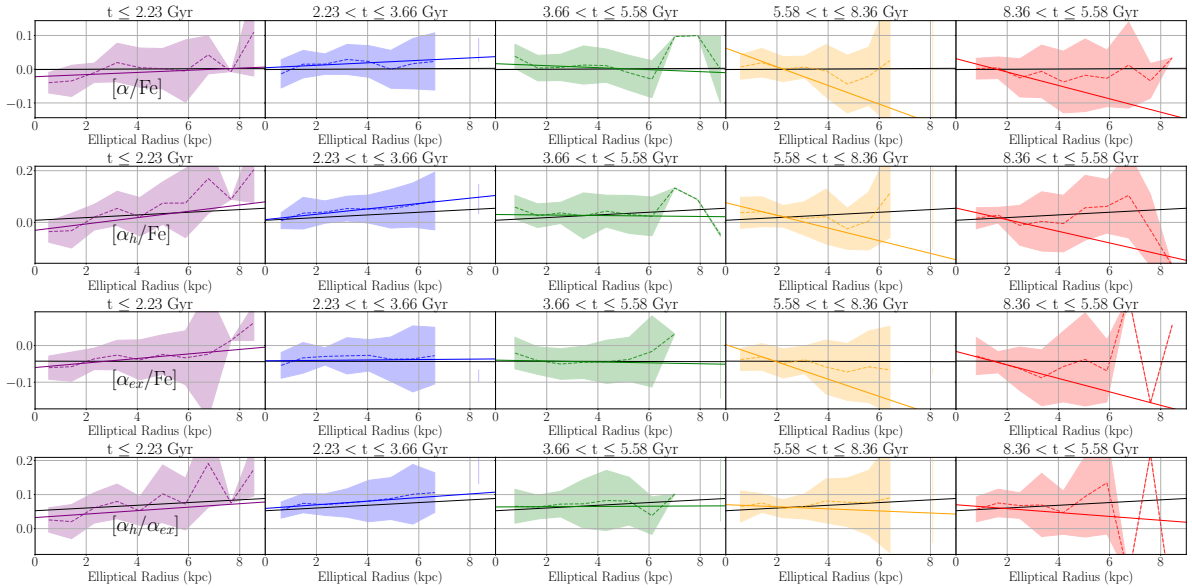



Figure 4.13: The radial abundance trends for the composite $\alpha$-element abundances.

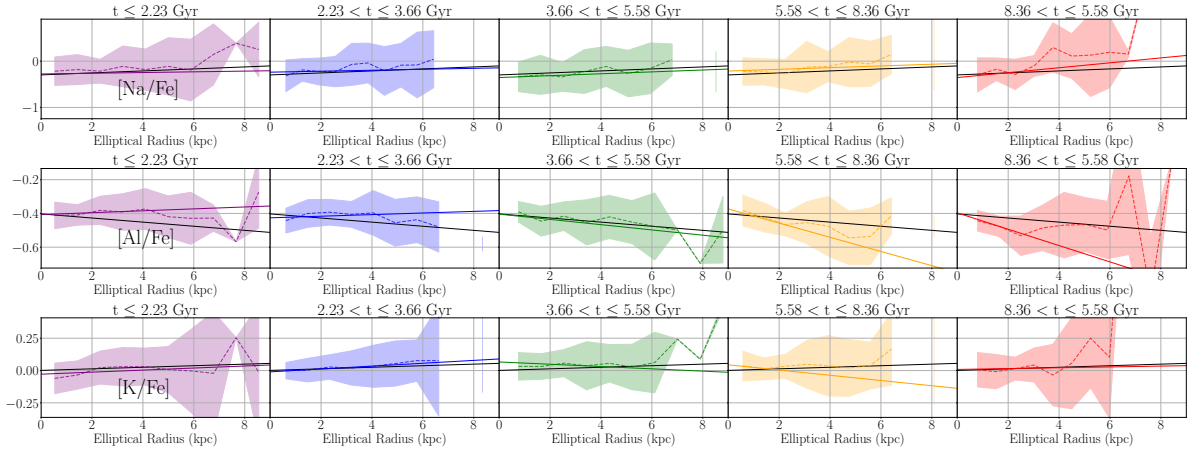



Figure 4.14: The radial abundance trends for the odd-Z abundances.

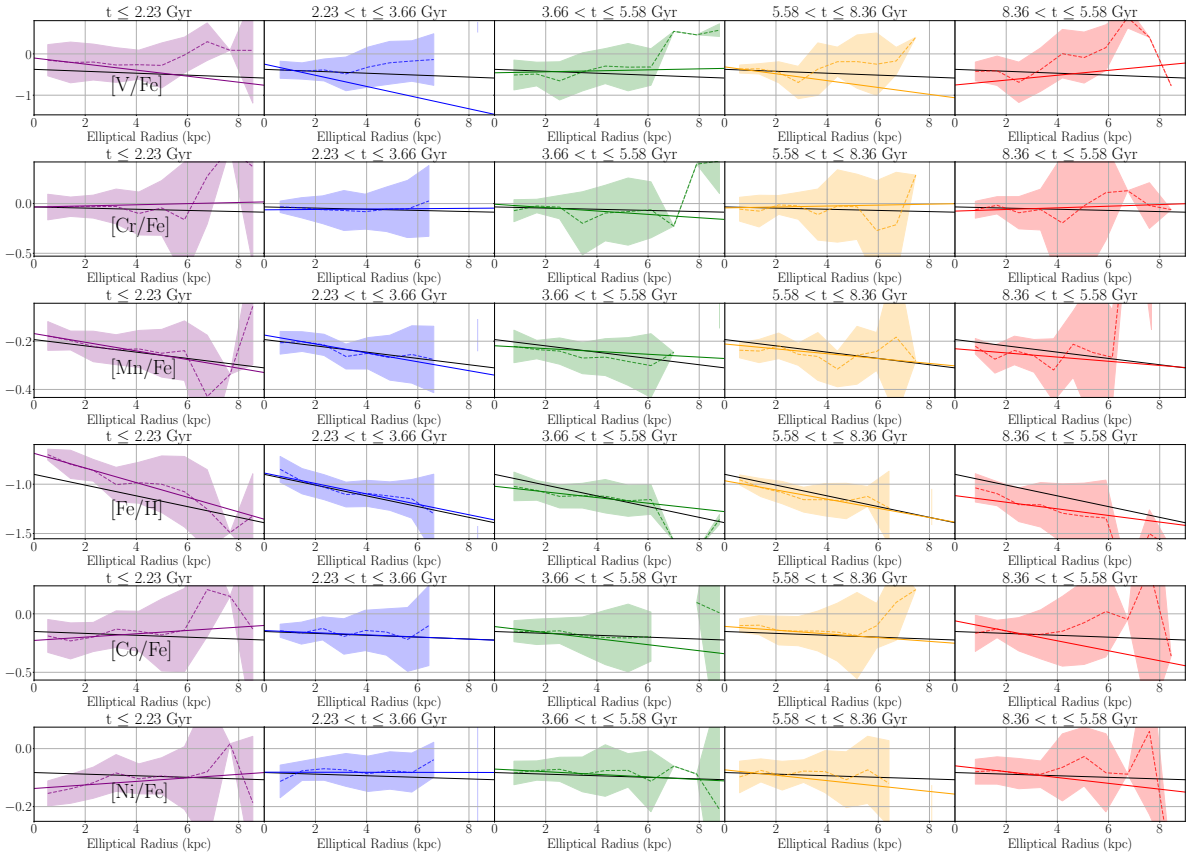



Figure 4.15: The radial abundance trends for the iron peak abundances.

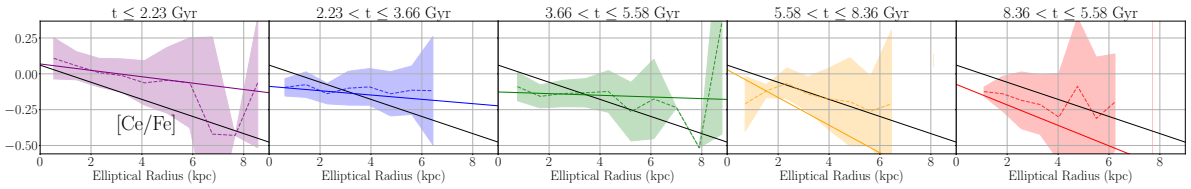



Figure 4.16: The radial abundance trends for the neutron capture abundances.

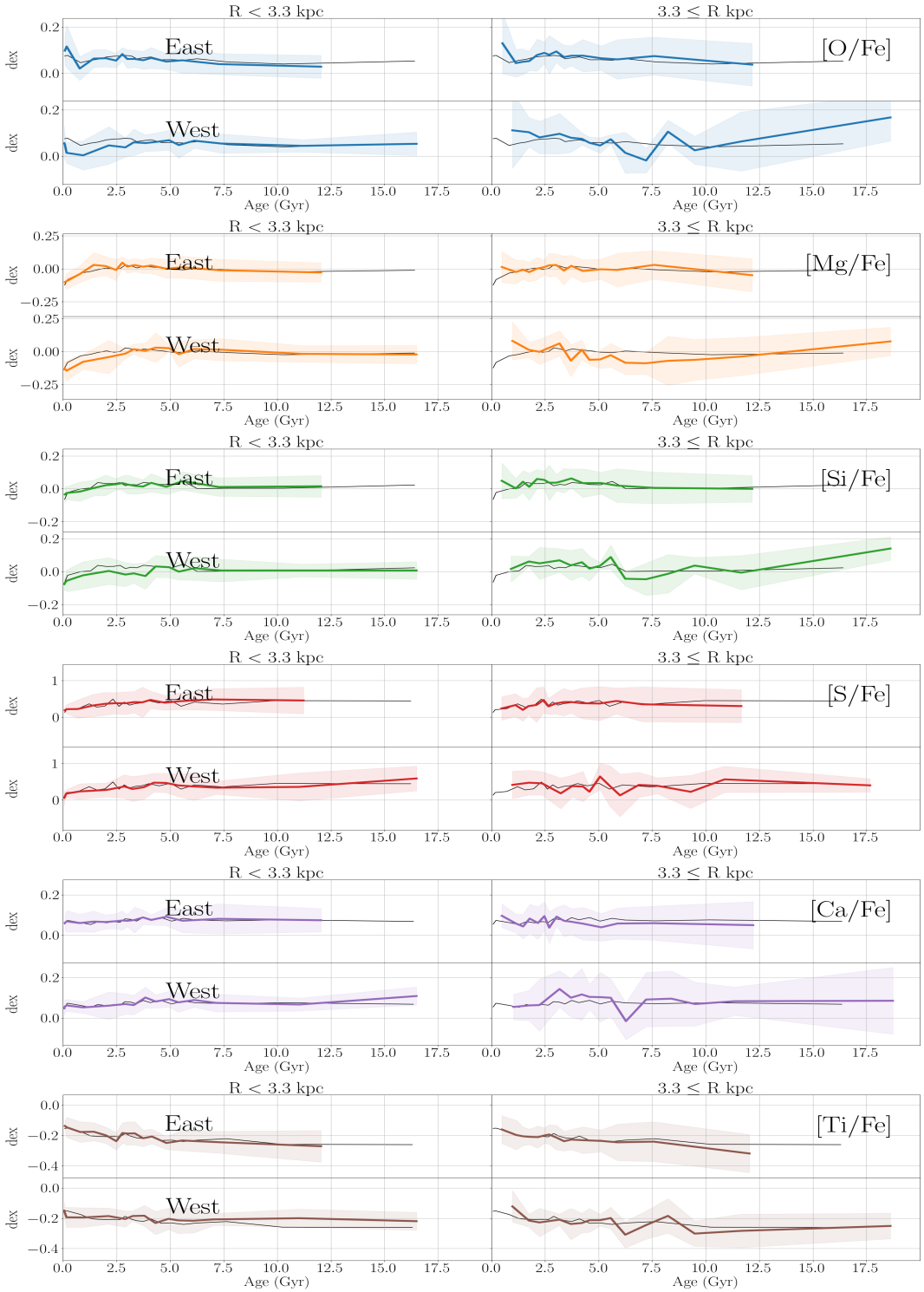



Figure 4.17: The age-[X/Fe] trends for the SMC for the individual $\alpha$-element abundances.

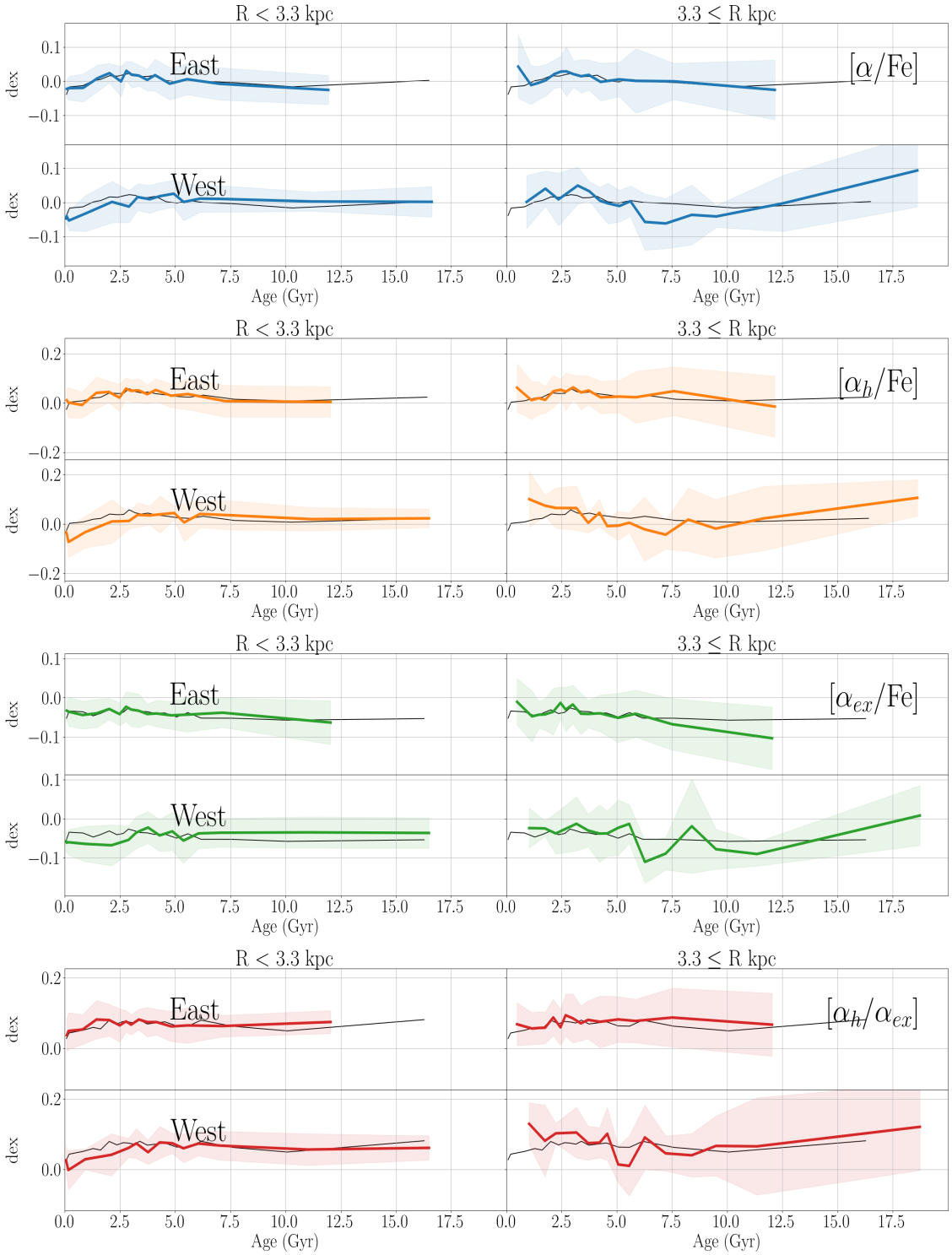



Figure 4.18: The age-[X/Fe] trends for the SMC for the composite $\alpha$-element abundances.

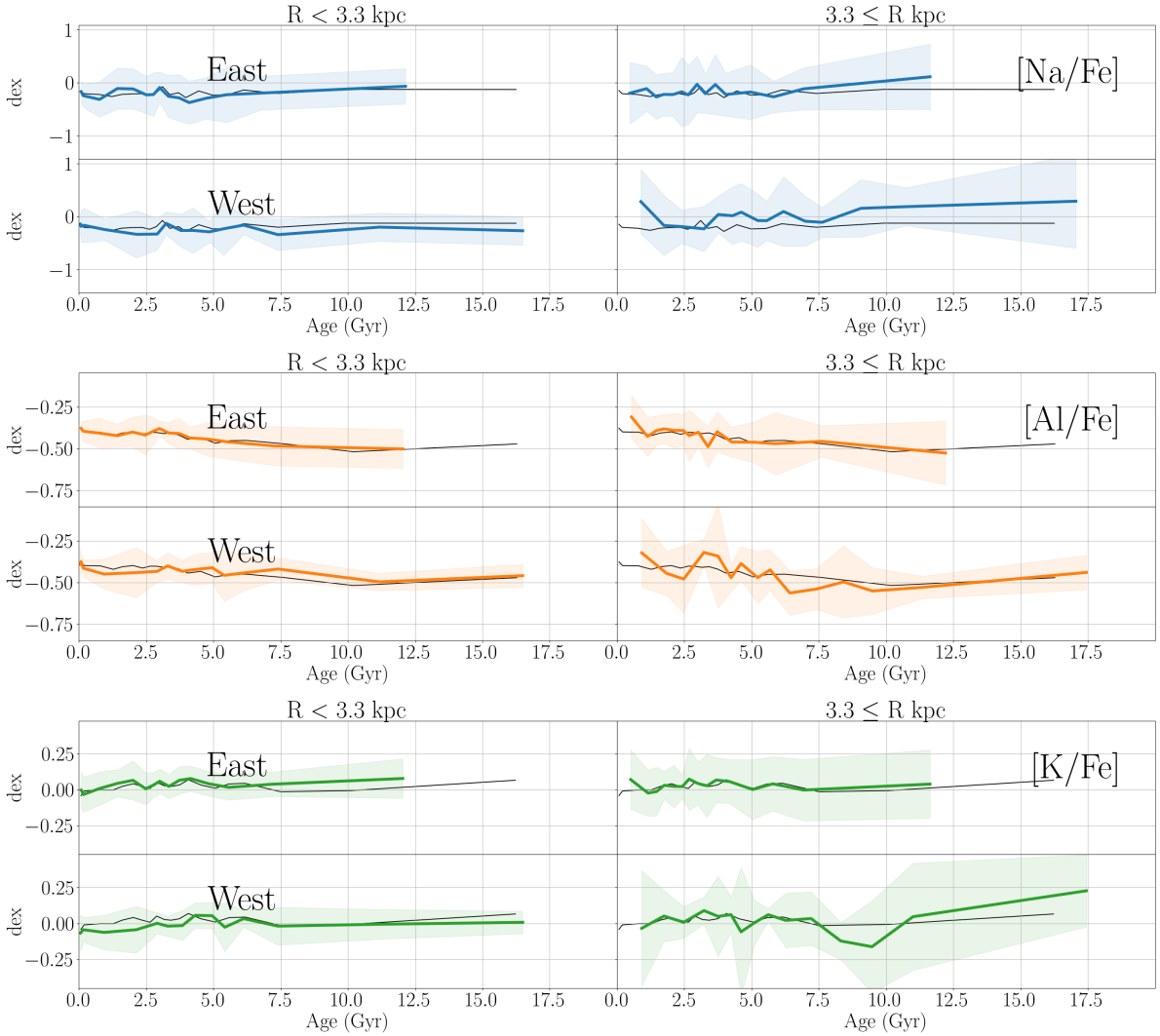



Figure 4.19

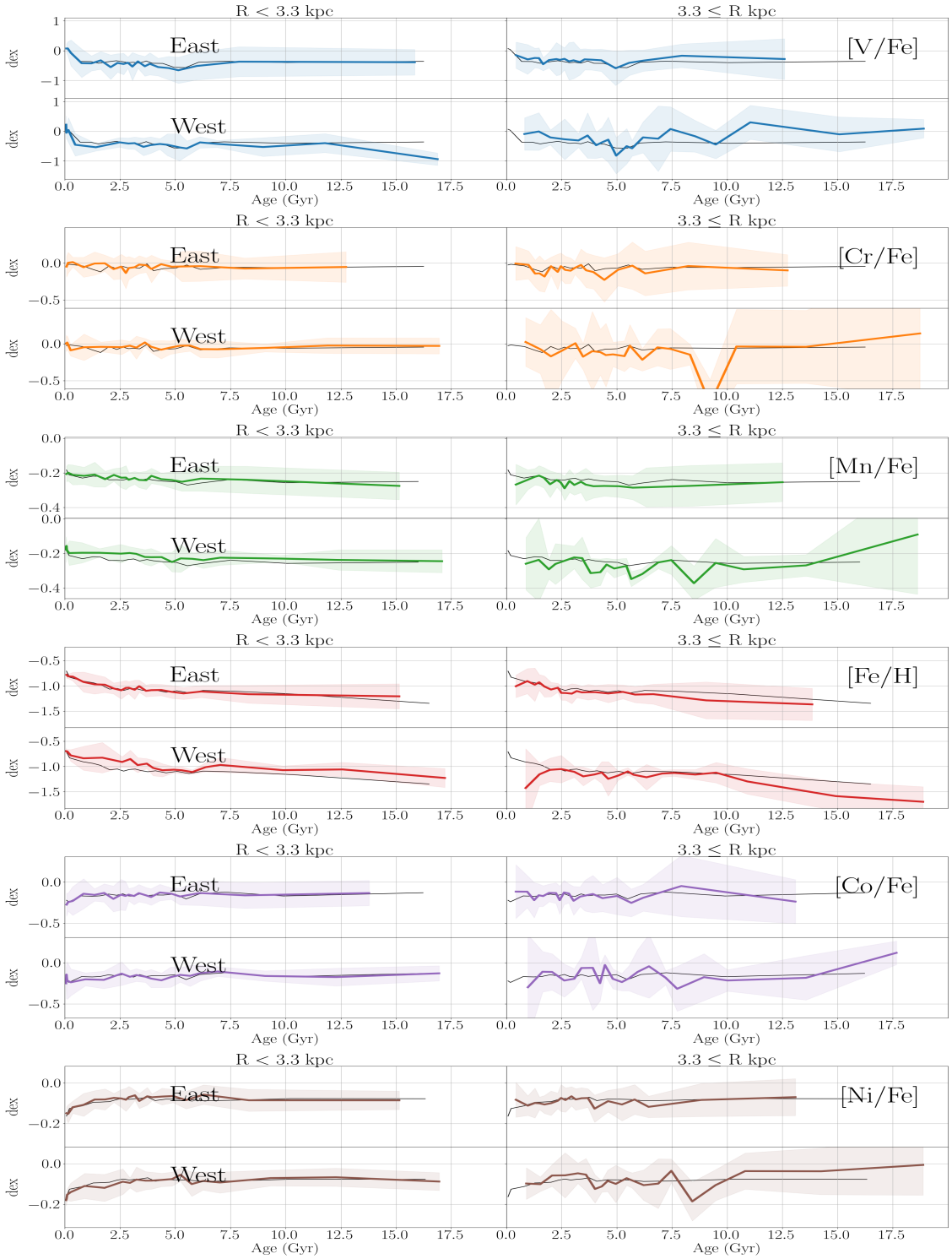



Figure 4.20: The age-[X/Fe] trends for the SMC for the individual iron peak abundances.

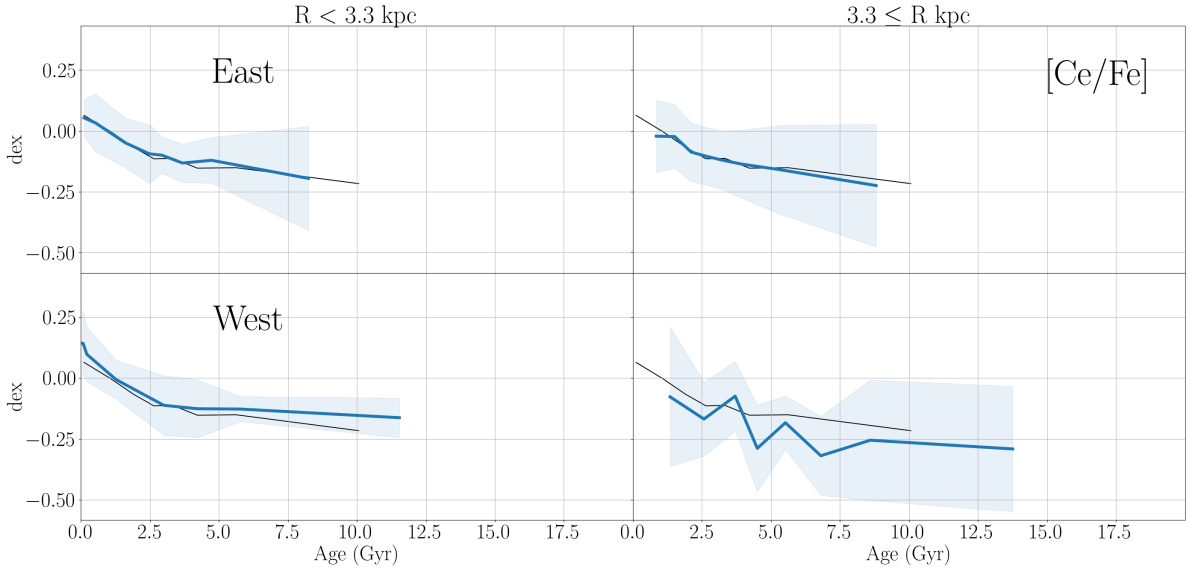



Figure 4.21: The age-[X/Fe] trend for the SMC for the neutron capture element cerium.

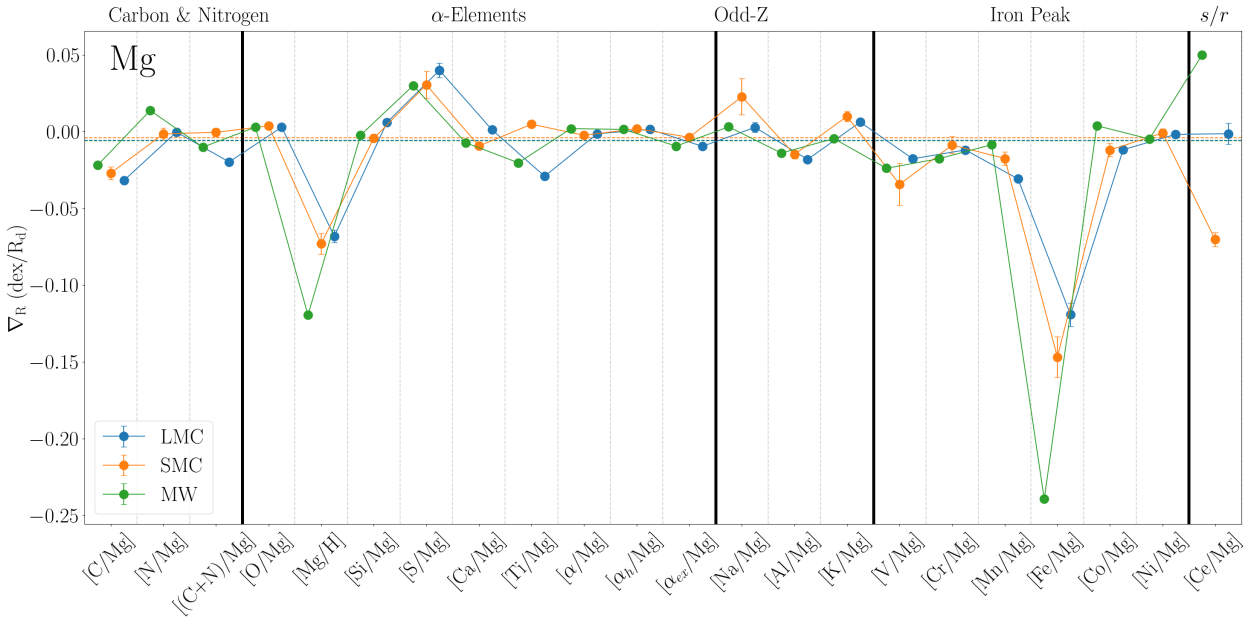



Figure 4.22: The same as Figure 4.11, but for the [X/Mg] gradients only. The median gradient value all three galaxies is quite similar.

# CONCLUSION

This work has explored the evolution of abundance gradients in the MCs in three different projects. The first project was to develop a method to calculate the ages of individual stars. The second project was to derive abundance gradients and investigate their evolutions in the LMC. The third and final project was the same as the second, but the analysis was carried out for the SMC.

In Chapter 2 the ages for individual RGB field stars were determined by comparing observed photometry to model photometry found using isochrones. The spatial distribution of ages suggests that star formation was more widespread in the past and is more centrally concentrated at recent times in the LMC. Also, there is a north-south dichotomy at radii R $<$ 4 kpc, with the northern fields being younger. These same northern fields cover a known spiral arm feature that may be connected to a close tidal interaction between the LMC and SMC, which caused new star formation in the northern fields. Finally, the AMR of the LMC using field stars tends to agree with globular clusters for younger ages but not as much for older clusters. There is a downturn in metallicity for the clusters that is not seen with the LMC field stars. Unfortunately, there are no known intermediate age clusters that are $\sim$3–12 Gyr old in the LMC. If the AMR is interpolated for the clusters it gives a lower than expected [Fe/H] compared to the AMR derived with field stars for the intermediate ages. There is also evidence of asymmetric drift present in the LMC.

The next project in Chapter 3 dealt with finding the abundance gradients and their evolutions as well as age-[X/Fe] trends in the LMC. Gradients were calculated for C, N, C+N, O, Mg, Si, S, Ca, Ti, $\alpha_{\rm h}$, $\alpha_{\rm ex}$, Na, Al, K, V, Cr, Mn, Fe, Co, Ni, Ce, and Nd for three different fiducials ([X/Fe], [X/H], and [X/Mg]). In addition, gradients for [C/N], and [$\alpha_h/\alpha_{ex}$] are calculated. All of the gradients were found by fitting a linear radial model to binned RGB abundance values. Using the ages calculated in Chapter 2, the evolution of

these gradients and age-[X/Fe] trends were also investigated.

The metallicity ([Fe/H]) gradient of the LMC was found to be $-0.0380 \pm 0.0022$ dex/kpc, which does agree with literature values such as the metallicity gradient calculated using the ratio of C- to M-Type AGB stars in different regions of the LMC, the gradient found using AGB stars from Feast et al. (2010), and the gradient found using RR Lyrae stars from Haschke et al. (2012). Looking at the gradients of [(C+N)/Fe], [O/Fe], [Mg/Fe], [Ti/Fe], [$\alpha$/Fe], [$\alpha_{ex}$/Fe], [Al/Fe], [C/Mg], [Ca/Mg], [Cr/Mg], [Fe/Mg], and [Nd/Mg] as well as a majority of the [X/H] gradients, there is a U-shaped trend in their evolutions with a critical point somewhere between 2.23 to 3.66 Gyr ago. This is coincident with a starburst $\sim$2 Gyr ago suggesting a common cause. Finally, the age-[X/Fe] trends show that many different elements experience an increase in the [X/Fe] starting $\sim$5 Gyr ago and continuing up to the present day, potentially demonstrating the lead up to the star formation from the starburst. Additionally some of the age-[X/Fe] trends show an increase in [X/Fe] starting at $\sim$5 Gyr ago but then there is a decrease in [X/Fe] in the last few Gyr. This is taken to be more evidence the LMC-SMC interaction. Finally the age-[X/Fe] trends show that the outer LMC is oftentimes deficient in [X/Fe].

In Chapter 4 the abundance gradients and the age-[X/Fe] trends are found for the SMC. The same list of abundances mentioned in the previous paragraph are also explored for the SMC, except for Nd. Unfortunately, APOGEE does not measure Nd and there are not enough SMC stars with measured [Nd/Fe] from Hayes et al. (2022) to calculate gradients or trends. Just like for the LMC, the radial abundance gradients are calculated using a linear model. Ages for the SMC RGB stars are calculated using the same method from Chapter 2. The same age bins are also calculated to compare the evolutions of gradients in the LMC and SMC more directly.

In the SMC, the metallicity gradient was found to be $-0.0546 \pm 0.0043$ dex/kpc, which is relatively steep compared to the LMC. Literature values, particularly with the work in

De Bortoli et al. (2022); Dobbie et al. (2014); Parisi et al. (2016), agree with the gradient calculated here. In De Bortoli et al. (2022), they look at globular clusters and field stars in both the inner ($R < 3.4°$) and outer ($R > 3.4°$) SMC. The inner clusters were found to have a metallicity gradient of $-0.0838 \pm 0.0314$ dex/kpc and the inner field stars have a metallicity gradient of $-0.0838 \pm 0.0419$ dex/kpc. As for Parisi et al. (2016) and Dobbie et al. (2014) they use the calcium triplet to derive gradients for field stars. There is less agreement with the outer clusters and outer fields stars. Many of the other literature sources (Choudhury et al., 2020; Li et al., 2023; Parisi et al., 2010) overlap with gradients calculated for different age bins and not the overall metallicity gradient. There is variation in the evolution of the abundance gradients in the SMC. Many of the gradients show a U-shaped trend in their evolution with a critical point happening 3.66–5.58 Gyr ago. This is consistent with what is found in Nidever et al. (2020) and Hasselquist et al. (2021), where it was determined that the SMC experienced a starburst a few Gyr before the LMC due to the same close interaction. On the other hand unlike the LMC, the different age-[X/Fe] in the SMC show little to no evolution. Most of the these trends are extremely flat, meaning they are unable to help constrain the critical point associated with the starburst in the SMC, which results in a wide range of possible times.

Chapters 2, 3, and 4 all show signs that correspond to a known interaction between the MCs. The age-radius relation for the APOGEE fields show that the single spiral arm feature in the LMC is younger than corresponding southern fields of similar radii. As mentioned previously, single spiral arms can be form due to the interaction between galaxies. Both the LMC and SMC display a critical point in the evolution of many of their gradients that corresponds to starbursts caused by the intergalactic interaction between the LMC and SMC. This work demonstrates that studying the evolution of abundance gradients in galaxies has to potential to unlock the merger history of those same galaxies. It is important to look at these systems to gain an understanding about how galaxies form and evolve.

There are two natural extensions of this work that could be investigated in the future. The first of these is using the results herein to help constrain simulations of interacting/merging Magellanic-like galaxies. To ensure that simulations are accurate, they must be able to reproduce observations and actually reflect reality. A GCE code should be able to reproduce the U-shaped trend found in this work with appropriate critical points. Second, the abundance gradients and their evolutions can be explored in other galaxies to derive relations to galactic parameters such as mass, morphology, median age, redshift, etc. These relations could help infer the gradients and their evolutions where abundances are not so easily measured.

# REFERENCES CITED

Abbott B. P., et al., 2017, Phys. Rev. Lett., 119, 161101

Abdurro'uf et al., 2022, ApJS, 259, 35

Afonso G. B., 2006, Scientific American Brasil, 14, 46

Ahumada R., et al., 2020, ApJS, 249, 3

Allende Prieto C., Beers T. C., Wilhelm R., Newberg H. J., Rockosi C. M., Yanny B., Lee Y. S., 2006, ApJ, 636, 804

Alpher R. A., Herman R., Gamow G. A., 1948, Physical Review, 74, 1198

Andreuzzi G., Bragaglia A., Tosi M., Marconi G., 2011, Monthly Notices of the Royal Astronomical Society, 412, 1265

Andrews B. H., Weinberg D. H., Schönrich R., Johnson J. A., 2017, ApJ, 835, 224

Arber E., Eden R., d'Anghiera Pietro Martire Sebastian M., Cabot S., 1885, The first three english books on america: (?1511)-1555 A.D.: Being chiefly translations, compilation, etc., by Richard Eden, from the writings, maps, &;c., of Pietro Martire, of Anghiera, Sebastian Münster, and Sebastian Cabot: With extracts, &;c., from the works of other Spanish, Italian, and German writers of the time. Turnbull & Spears, Edinburgh

Asplund M., Amarsi A. M., Grevesse N., 2021, A&A, 653, A141

Astropy Collaboration et al., 2013, A&A, 558, A33

Astropy Collaboration et al., 2018, AJ, 156, 123

Barnes S. A., 2007, ApJ, 669, 1167

Battinelli P., Demers S., 2005, A&A, 434, 657

Bekki K., Stanimirović S., 2009, MNRAS, 395, 342

Bekki K., Couch W. J., Beasley M. A., Forbes D. A., Chiba M., Da Costa G. S., 2004, ApJ, 610, L93

Belfiore F., et al., 2017, MNRAS, 469, 151

Bell C. P. M., et al., 2022, MNRAS, 516, 824

Berentzen I., Athanassoula E., Heller C. H., Fricke K. J., 2003, MNRAS, 341, 343

Besla G., 2015, The Orbits and Total Mass of the Magellanic Clouds (arXiv:1511.03346)

Besla G., Kallivayalil N., Hernquist L., Robertson B., Cox T. J., van der Marel R. P., Alcock C., 2007, ApJ, 668, 949

Besla G., Kallivayalil N., Hernquist L., van der Marel R. P., Cox T. J., Kereš D., 2012, MNRAS, 421, 2109

Bilitewski T., Schönrich R., 2012, MNRAS, 426, 2266

Binney J., Tremaine S., 1987, Galactic dynamics. Princeton university press

Blanton M. R., et al., 2017, AJ, 154, 28

Bouché N., et al., 2010, ApJ, 718, 1001

Bovy J., Rix H.-W., 2013, The Astrophysical Journal, 779, 115

Bovy J., et al., 2014, ApJ, 790, 127

Bowen I., Vaughan A., 1973, AJ, 12, 1430

Bower R. G., Benson A., Malbon R., Helly J., Frenk C., Baugh C., Cole S., Lacey C. G., 2006, Monthly Notices of the Royal Astronomical Society, 370, 645

Bragança G. A., et al., 2019, A&A, 625, A120

Bressan A., Marigo P., Girardi L., Salasnich B., Dal Cero C., Rubele S., Nanni A., 2012, MNRAS, 427, 127

Brüns C., et al., 2005, A&A, 432, 45

Burbidge E. M., Burbidge G. R., Fowler W. A., Hoyle F., 1957, Rev. Mod. Phys., 29, 547

Cardelli J. A., Clayton G. C., Mathis J. S., 1989, ApJ, 345, 245

Carlin J. L., Sheffield A. A., Cunha K., Smith V. V., 2018, ApJ, 859, L10

Carrera R., Gallart C., Hardy E., Aparicio A., Zinn R., 2008, AJ, 135, 836

Carrera R., Gallart C., Aparicio A., Hardy E., 2011, The Astronomical Journal, 142, 61

Cayatte V., Kotanyi C., Balkowski C., Van Gorkom J., 1994, The Astronomical Journal, 107, 1003

Chen H.-Y., Vitale S., Foucart F., 2021, ApJLetters, 920, L3

Choi Y., et al., 2018a, ApJ, 866, 90

Choi Y., et al., 2018b, ApJ, 869, 125

Choi Y., Olsen K. A. G., Besla G., van der Marel R. P., Zivick P., Kallivayalil N., Nidever D. L., 2022, ApJ, 927, 153

Choudhury S., et al., 2020, MNRAS, 497, 3746

Choudhury S., et al., 2021, MNRAS, 507, 4752

Cioni M. R. L., 2009, A&A, 506, 1137

Cioni M. R. L., et al., 2011, A&A, 527, A116

Cohen J. G., Blakeslee J. P., Ryzhov A., 1998, ApJ, 496, 808

Cole A. A., Tolstoy E., Gallagher John S. I., Smecker-Hane T. A., 2005, AJ, 129, 1465

Cullinane L. R., et al., 2020, MNRAS, 497, 3055

Cullinane L. R., Mackey A. D., Da Costa G. S., Erkal D., Koposov S. E., Belokurov V., 2022, MNRAS, 510, 445

Cunha K., Daflon S., 2003, in Charbonnel C., Schaerer D., Meynet G., eds, Astronomical Society of the Pacific Conference Series Vol. 304, CNO in the Universe. p. 172

Cunha M. S., et al., 2007, The A&A Review, 14, 217

Da Costa G. S., 1991, in Haynes R., Milne D., eds, IAU Symposium Vol. 148, The Magellanic Clouds. p. 183

Daflon S., Cunha K., 2004, ApJ, 617, 1115

Dalcanton J. J., et al., 2012, ApJS, 200, 18

Davé R., Finlator K., Oppenheimer B. D., 2011, MNRAS, 416, 1354

Davé R., Finlator K., Oppenheimer B. D., 2012, MNRAS, 421, 98

De Bortoli B. J., Parisi M. C., Bassino L. P., Geisler D., Dias B., Gimeno G., Angelo M. S., Mauro F., 2022, A&A, 664, A168

De Grijs R., Wicker J. E., Bono G., 2014, AJ, 147, 122

Demers S., Grondin L., Irwin M. J., Kunkel W. E., 1991, AJ, 101, 911

Dennefeld M., 2020, The Messenger, 181, 37

Di Teodoro E. M., et al., 2019, MNRAS, 483, 392

Diaz J. D., Bekki K., 2012, ApJ, 750, 36

Dirsch B., Richtler T., Gieren W., Hilker M., 2000, arXiv preprint astro-ph/0004009

Dobbie P. D., Cole A. A., Subramaniam A., Keller S., 2014, MNRAS, 442, 1680

Donor J., et al., 2020, AJ, 159, 199

Dufour R. J., 1975, ApJ, 195, 315

Erkal D., et al., 2019, MNRAS, 487, 2685

Escala I., Gilbert K. M., Wojno J., Kirby E. N., Guhathakurta P., 2021, AJ, 162, 45

Favata F., Morale F., Sciortino S., Micela G., 1997, Technical report, On the comparison between spectroscopic and photometric metallicity measurements in active solar-type stars. SCAN-9707071

Feast M. W., Abedigamba O. P., Whitelock P. A., 2010, MNRAS: Letters, 408, L76

Ferrarotti A., Gail H.-P., 2006, A&A, 447, 553

Feuillet D. K., Bovy J., Holtzman J., Girardi L., MacDonald N., Majewski S. R., Nidever D. L., 2016, ApJ, 817, 40

Fitzpatrick E. L., 1999, Publications of ASP, 111, 63

Flower P., Geisler D., Hodge P., Olszewski E., Schommer R., 1983, ApJ, 275, 15

Foreman-Mackey D., Hogg D. W., Lang D., Goodman J., 2013, PASP, 125, 306

Fraunhofer J., 1817, Annalen der Physik, 56, 264

Frebel A., Christlieb N., Norris J. E., Thom C., Beers T. C., Rhee J., 2007, ApJ, 660, L117

Gaia Collaboration et al., 2016, A&A, 595, A1

Gaia Collaboration et al., 2021a, A&A, 649, A1

Gaia Collaboration et al., 2021b, A&A, 649, A7

Gaia Collaboration et al., 2022, arXiv e-prints, p. arXiv:2208.00211

García-Pérez A. E., et al., 2016, AJ, 151, 144

Gardiner L. T., Sawa T., Fujimoto M., 1994, MNRAS, 266, 567

Gatto M., et al., 2020, MNRAS, 499, 4114

Geisler D., Bica E., Dottori H., Claria J. J., Piatti A. E., Santos Joao F. C. J., 1997, AJ, 114, 1920

Geisler D., Piatti A. E., Bica E., Clariá J. J., 2003, MNRAS, 341, 771

Girardi L., 2016, ARA&A, 54, 95

Girardi L., Bertelli G., Bressan A., Chiosi C., Groenewegen M., Marigo P., Salasnich B., Weiss A., 2002, A&A, 391, 195

Gómez F. A., Besla G., Carpintero D. D., Villalobos Á., O'Shea B. W., Bell E. F., 2015, ApJ, 802, 128

Gonidakis I., Livanou E., Kontizas E., Klein U., Kontizas M., Belcheva M., Tsalmantza P., Karampelas A., 2009, Astronomy & Astrophysics, 496, 375

Goodman J., Weare J., 2010, Communications in applied mathematics and computational science, 5, 65

Gordon K. D., et al., 2016, ApJ, 826, 104

Graczyk D., et al., 2020, ApJ, 904, 13

Grady J., Belokurov V., Evans N., 2021, ApJ, 909, 150

Grocholski A. J., Cole A. A., Sarajedini A., Geisler D., Smith V. V., 2006, AJ, 132, 1630

Gunn J. E., Gott J. Richard I., 1972, ApJ, 176, 1

Gunn J. E., et al., 2006, AJ, 131, 2332

Harkins W. D., 1917, Journal of the American Chemical Society, 39, 856

Harris J., Zaritsky D., 2006, AJ, 131, 2514

Harris J., Zaritsky D., 2009, AJ, 138, 1243

Harris C. R., et al., 2020, Nature, 585, 357

Haschke R., Grebel E. K., Duffau S., 2011, AJ, 141, 158

Haschke R., Grebel E. K., Duffau S., Jin S., 2012, AJ, 143, 48

Hasselquist S., et al., 2020, ApJ, 901, 109

Hasselquist S., et al., 2021, ApJ, 923, 172

Hayes C. R., et al., 2022, ApJS, 262, 34

Henry R., Kwitter K. B., Jaskot A. E., Balick B., Morrison M. A., Milingo J. B., 2010, The Astrophysical Journal, 724, 748

Hill V., et al., 2002, A&A, 387, 560

Hindman J. V., Kerr F. J., McGee R. X., 1963, Australian Journal of Physics, 16, 570

Höfner S., Olofsson H., 2018, The A&A Review, 26, 1

Holtzman J. A., Harrison T. E., Coughlin J. L., 2010, Advances in Astronomy, 2010, 193086

Holtzman J. A., et al., 2015, AJ, 150, 148

Hubeny I., Allende Prieto C., Osorio Y., Lanz T., 2021, arXiv e-prints, p. arXiv:2104.02829

Hunter J. D., 2007, Computing in Science & Engineering, 9, 90

Jia Y., Chen Y., Zhao G., Xue X., Zhao J., Yang C., Li C., 2018, ApJ, 863, 93

Jönsson H., et al., 2020, arXiv e-prints, p. arXiv:2007.05537

Kallivayalil N., van der Marel R. P., Besla G., Anderson J., Alcock C., 2013, ApJ, 764, 161

Karakas A. I., Lattanzio J. C., 2014, Publications of the Astronomical Society of Australia, 31, e030

Khokhlov A., Mueller E., Hoeflich P., 1993, A&A, 270, 223

Kirchhoff G., 1860, Annalen der Physik, 185, 275

Knapen J. H., Cisternas M., 2015, ApJLetters, 807, L16

Kobayashi C., Umeda H., Nomoto K., Tominaga N., Ohkubo T., 2006, ApJ, 653, 1145

Kontizas M., Kontizas E., Michalitsianos A. G., 1993, A&A, 269, 107

Kroupa P., 2001, MNRAS, 322, 231

Kroupa P., 2002, Science, 295, 82

Lada C. J., Lada E. A., 2003, Annual Review of A&A, 41, 57

Larson R. B., Tinsley B. M., 1978, ApJ, 219, 46

Layden A. C., 1995, AJ, 110, 2312

Li X.-Y., Huang Y., Liu G.-C., Beers T. C., Zhang H.-W., 2023, The Astrophysical Journal, 944, 88

Lianou S., Grebel E. K., Koch A., 2011, A&A, 531, A152

Lilly S. J., Carollo C. M., Pipino A., Renzini A., Peng Y., 2013, ApJ, 772, 119

Lu Y., Minchev I., Buck T., Khoperskov S., Steinmetz M., Libeskind N., Cescutti G., Freeman K. C., 2022, arXiv e-prints, p. arXiv:2212.04515

Lucchini S., D'Onghia E., Fox A. J., Bustard C., Bland-Hawthorn J., Zweibel E., 2020, Nature, 585, 203

Luck R. E., Gieren W. P., Andrievsky S. M., Kovtyukh V. V., Fouqué P., Pont F., Kienzle F., 2003, A&A, 401, 939

Maciel W. J., Koppen J., 1994, Astronomy and Astrophysics, 282, 436

Mackey A., Payne M., Gilmore G., 2006, MNRAS, 369, 921

Majewski S. R., et al., 2017, AJ, 154, 94

Mamajek E. E., Hillenbrand L. A., 2008, ApJ, 687, 1264

Marigo P., et al., 2017, ApJ, 835, 77

Massana P., et al., 2022, MNRAS, 513, L40

Mateo M. L., 1998, ARA&A, 36, 435

Mateo M., Hodge P., Schommer R., 1986, ApJ, Part 1 (ISSN 0004-637X), vol. 311, Dec. 1, 1986, p. 113-134., 311, 113

Mathewson D. S., Cleary M. N., Murray J. D., 1974, ApJ, 190, 291

Mazzi A., et al., 2021, MNRAS, 508, 245

McConnachie A. W., 2012, AJ, 144, 4

McWilliam A., 1997, Annual Review of Astronomy and Astrophysics, 35, 503

Meschin I., Gallart C., Aparicio A., Hidalgo S. L., Monelli M., Stetson P. B., Carrera R., 2014, MNRAS, 438, 1067

Minchev I., Chiappini C., Martig M., 2013, A&A, 558, A9

Monteagudo L., Gallart C., Monelli M., Bernard E. J., Stetson P. B., 2018, MNRAS, 473, L16

Muller E., Bekki K., 2007, MNRAS, 381, L11

Ness M., Hogg D. W., Rix H. W., Martig M., Pinsonneault M. H., Ho A. Y. Q., 2016a, ApJ, 823, 114

Ness M., Hogg D. W., Rix H.-W., Martig M., Pinsonneault M. H., Ho A., 2016b, ApJ, 823, 114

Nidever D., 2021, dnidever/doppler: Cannon and Payne models, Zenodo, doi:10.5281/zenodo.4906681

Nidever D. L., Majewski S. R., Burton W. B., 2008a, ApJ, 679, 432

Nidever D. L., Majewski S. R., Butler Burton W., 2008b, ApJ, 679, 432

Nidever D. L., Majewski S. R., Butler Burton W., Nigra L., 2010, ApJ, 723, 1618

Nidever D. L., Majewski S. R., Munoz R. R., Beaton R. L., Patterson R. J., Kunkel W. E., 2011, ApJLetters, 733, L10

Nidever D. L., Monachesi A., Bell E. F., Majewski S. R., Muñoz R. R., Beaton R. L., 2013, ApJ, 779, 145

Nidever D. L., et al., 2015, AJ, 150, 173

Nidever D. L., et al., 2017, AJ, 154, 199

Nidever D. L., et al., 2020, ApJ, 895, 88

Nidever D. L., et al., 2021, AJ, 161, 74

Nomoto K., Kobayashi C., Tominaga N., 2013, Annual Review of A&A, 51, 457

Oddo G., 1914, Zeitschrift für anorganische Chemie, 87, 253

Olsen K. A. G., Zaritsky D., Blum R. D., Boyer M. L., Gordon K. D., 2011, ApJ, 737, 29

Olszewski E. W., Schommer R. A., Suntzeff N. B., Harris H. C., 1991, AJ, 101, 515

Pagel B., Edmunds M., 1981, Annual Review of A&A, 19, 77

Pagel B., Edmunds M., Fosbury R., Webster B., 1978, MNRAS, 184, 569

Palma T., Clariá J. J., Geisler D., Ahumada A. V., 2015, in Points S., Kunder A., eds, Astronomical Society of the Pacific Conference Series Vol. 491, Fifty Years of Wide Field Studies in the Southern Hemisphere: Resolved Stellar Populations of the Galactic Bulge and Magellanic Clouds. p. 235

Parisi M. C., Geisler D., Grocholski A. J., Clariá J. J., Sarajedini A., 2010, AJ, 139, 1168

Parisi M. C., Geisler D., Carraro G., Clariá J. J., Villanova S., Gramajo L. V., Sarajedini A., Grocholski A. J., 2016, AJ, 152, 58

Patel E., Besla G., Sohn S. T., 2017, MNRAS, 464, 3825

Peña M., Ruíz M. T., Rubio M., 1987, Revista Mexicana de Astronomia y Astrofisica, 14, 178

Pearson S., et al., 2018, MNRAS, 480, 3069

Peng Y.-j., Maiolino R., 2014, MNRAS, 443, 3643

Pérez A. E. G., et al., 2016, AJ, 151, 144

Piatti A. E., 2022, MNRAS: Letters, 511, L72

Pietrzyński G., et al., 2019, Nature, 567, 200

Pinsonneault M., Kawaler S. D., Sofia S., Demarque P., 1989, The Astrophysical Journal, 338, 424

Pinsonneault M. H., et al., 2014, ApJS, 215, 19

Pinsonneault M. H., et al., 2018, ApJS, 239, 32

Pozo Menares G., Canio M., Neculfilu C., Pilquinao R. D., 2015, Wenumapu: Astronomía y cosmología mapuche. Ocho Libros Editores

Prantzos N., Abia C., Cristallo S., Limongi M., Chieffi A., 2020, MNRAS, 491, 1832

Privon G., et al., 2017, ApJ, 846, 74

Putman M. E., Staveley-Smith L., Freeman K. C., Gibson B. K., Barnes D. G., 2003, ApJ, 586, 170

Renaud F., Boily C., Naab T., Theis C., 2009, ApJ, 706, 67

Rich R. M., Shara M. M., Zurek D., 2001, AJ, 122, 842

Riello M., et al., 2021, A&A, 649, A3

Ripepi V., et al., 2014, MNRAS, 442, 1897

Ruiz-Lara T., et al., 2020, A&A, 639, L3

Saitoh T. R., Daisaka H., Kokubo E., Makino J., Okamoto T., Tomisaka K., Wada K., Yoshida N., 2009, Publications of the Astronomical Society of Japan, 61, 481

Salaris M., Chieffi A., Straniero O., 1993, ApJ, 414, 580

Sandage A., 1970, ApJ, 162, 841

Sandage A., 1993, AJ, 106, 687

Santoro F., Tadhunter C., Baron D., Morganti R., Holt J., 2020, Astronomy & Astrophysics, 644, A54

Sarajedini A., 2008, Proceedings of the International Astronomical Union, 4, 221

Sarajedini A., Barker M. K., Geisler D., Harding P., Schommer R., 2006, AJ, 132, 1361

Schlafly E. F., Finkbeiner D. P., Schlegel D. J., Jurić M., Ivezić Ž., Gibson R. R., Knapp G. R., Weaver B. A., 2010, ApJ, 725, 1175

Schlegel D. J., Finkbeiner D. P., Davis M., 1998, ApJ, 500, 525

Schroyen J., De Rijcke S., Koleva M., Cloet-Osselaer A., Vandenbroucke B., 2013, MNRAS, 434, 888

Schweizer F., 2005, Astrophysics and Space Science Library, 329, 143

Scowcroft V., Freedman W. L., Madore B. F., Monson A., Persson S. E., Rich J., Seibert M., Rigby J. R., 2016, ApJ, 816, 49

Searle L., 1971, The Astrophysical Journal, 168, 327

Searle L., Zinn R., 1978, ApJ, 225, 357

Sellwood J., 2014, RvMP, 86, 1

Sellwood J. A., Binney J., 2002, MNRAS, 336, 785

Serenelli A., et al., 2017, The Astrophysical Journal Supplement Series, 233, 23

Sharma S., Borissova J., Kurtev R., Ivanov V. D., Geisler D., 2010, AJ, 139, 878

Skibba R. A., et al., 2012, ApJ, 761, 42

Skrutskie M. F., et al., 2006, AJ, 131, 1163

Soszyński I., et al., 2009, Acta Astron., 59, 1

Stanimirović S., Staveley-Smith L., Jones P. A., 2004, ApJ, 604, 176

Staveley-Smith L., Kim S., Calabretta M. R., Haynes R. F., Kesteven M. J., 2003, MNRAS, 339, 87

Thielemann F.-K., et al., 2011, Progress in Particle and Nuclear Physics, 66, 346

Tinsley B. M., 1980, FCPh, 5, 287

Toomre A., Toomre J., 1972, Astrophysical Journal, Vol. 178, pp. 623-666 (1972), 178, 623

Treyer M., et al., 2018, Monthly Notices of the Royal Astronomical Society, 477, 2684

Twarog B. A., Ashman K. M., Anthony-Twarog B. J., 1997, AJ, 114, 2556

Van Saders J. L., Pinsonneault M. H., 2012, The Astrophysical Journal, 746, 16

Vasiliev E., Belokurov V., Erkal D., 2021, MNRAS, 501, 2279

Vassiliadis E., Wood P. R., 1993, ApJ, 413, 641

Ventura P., Di Criscienzo M., Carini R., D'Antona F., 2013, MNRAS, 431, 3642

Vickers J. J., Shen J., Li Z.-Y., 2021, ApJ, 922, 189

Virtanen P., et al., 2020, Nature Methods, 17, 261

Wagner-Kaiser R., Sarajedini A., 2013, MNRAS, 431, 1565

Watkins L. L., van der Marel R. P., Sohn S. T., Evans N. W., 2019, ApJ, 873, 118

Weinberg D. H., et al., 2019, ApJ, 874, 102

Weiss A., Schlattl H., 2008, Astrophysics and Space Science, 316, 99

Weisz D. R., Dolphin A. E., Skillman E. D., Holtzman J., Dalcanton J. J., Cole A. A., Neary K., 2013, MNRAS, 431, 364

White S. D., Rees M. J., 1978, MNRAS, 183, 341

Wilson J. C., et al., 2019, PASP, 131, 055001

Wollaston W. H., 1802, Philosophical Transactions of the Royal Society of London, 92, 365

Woosley S., Janka T., 2005, Nature Physics, 1, 147

Zaritsky D., Harris J., Thompson I., 1997, AJ, 114, 1002

Zaritsky D., Harris J., Thompson I. B., Grebel E. K., 2004, AJ, 128, 1606

Zasowski G., et al., 2013, AJ, 146, 81

Zasowski G., et al., 2017, AJ, 154, 198

Zivick P., et al., 2018, ApJ, 864, 55

van der Marel R. P., Cioni M.-R. L., 2001, AJ, 122, 1807

van der Marel R. P., Kallivayalil N., 2014, ApJ, 781, 121

van der Marel R. P., Kallivayalil N., Besla G., 2008, Proceedings of the International Astronomical Union, 4, 81